UNIVERSITY OF MANCHESTER

DOCTORAL THESIS

Precision measurements of vector boson fusion and vertex counting as a luminosity measure at ATLAS

Author:
Jonathan CRANE

Supervisors:
Prof. Andrew Pilkington
and Prof. Terry Wyatt

A Thesis submitted in fulfillment of the requirements for the degree of Doctor of Physics

in the

Faculty of Science and Engineering
Department of Physics and Astronomy
Particle Physics Group

March 11, 2020

Contents

UNIVERSITY OF MANCHESTER

Abstract

Faculty of Science and Engineering
Department of Physics and Astronomy

Doctor of Physics

Precision measurements of vector boson fusion and vertex counting as a luminosity measure at ATLAS

by Jonathan CRANE

This thesis presents two analyses of proton-proton collision data recorded by the ATLAS detector during the years 2015-2018 at the LHC with a centre of mass energy of $\sqrt{s} = 13$ TeV. The first analysis is an vertex counting algorithm designed to measure the luminosity delivered to ATLAS per 10 luminosity blocks. It contains a Monte Carlo closure test that is used to validate the method. Furthermore, it contains tests of the internal and external stability of the algorithm.

The second analysis in this thesis is the measurement of differential cross-section of the electroweak production of a Z boson in association with jets. It is performed using 138.42 ($\pm$1.7%) fb^{-1} of data collected by the ATLAS experiment. The electroweak Zjj signal is extracted in a fiducial region designed to enhance the electroweak Zjj contribution. The differential cross-section measurements are presented for four variables: the di-jet invariant mass, m_{jj}; the rapidity separation of the leading two jets, Δy_{jj}; the transverse momentum of the di-lepton system, p_{T}^{Z}, and the signed azimuthal angle between the two leading jets, $\Delta\phi_{jj}^{\mathrm{signed}}$.

Declaration of Authorship

I, Jonathan CRANE, declare that this Thesis titled, "Precision measurements of vector boson fusion and vertex counting as a luminosity measure at ATLAS" and the work presented within is my own. I confirm that:

- This work was done wholly or mainly while in candidature for a research degree at this University.
- Where any part of this Thesis has previously been submitted for a degree or any other qualification at this University or any other institution, this has been clearly stated.
- Where I have consulted the published work of others, this is always clearly attributed.
- Where I have quoted from the work of others, the source is always given. With the exception of such quotations, this Thesis is entirely my own work.
- I have acknowledged all main sources of help.
- Where the Thesis is based on work done by myself jointly with others, I have made clear exactly what was done by others and what I have contributed myself.

Signed:

Date:

Copyright

Acknowledgements

I would like to thank Andy and Terry for being my supervisors over the past 4 years. Additionally I would like to thank everyone in the Manchester HEP group as they were all very helpful and welcoming. They made the department lovely to work in. I would like to thank all of my friends and family that have helped me along the way.

Chapter 1

Introduction

This thesis presents the implementation and utilisation of an algorithm that calculates the luminosity delivered to the ATLAS detector during proton-proton collisions at the Large Hadron Collider (LHC). Additionally it also contains a differential measurement of the electroweak production of di-jets in association with a Z boson performed with 138.42 ($\pm$1.7%) fb^{-1} of data that was collected by the ATLAS detector between 2015-2018. All of the data used in this thesis was collected with a centre of mass collision energy of $\sqrt{s} = 13$ TeV.

This thesis comprises eight chapters. Chapter 2 provides an overview of the theoretical framework of particle physics known as the Standard Model. Chapter 3 covers the LHC and the ATLAS detector which are the experimental apparatus used to collect the data used in this thesis. Firstly it covers the LHC as a whole, and then it describes the design of all of the detectors that make up ATLAS. Chapter 4 describes how the algorithms work that reconstruct the particles that pass through the ATLAS detector. Chapter 5 contains an introduction to the mathematical formalism of luminosity followed by how this is implemented by ATLAS. Chapter 6 outlines the luminosity measuring algorithm that utilises vertex counting. It describes the development, optimization and implementation of this algorithm for the Run 2 dataset. The algorithm is tested using Monte Carlo data and it is calibrated by a comparison to an algorithm utilising the LUCID detector in a long physics run. Finally this chapter presents internal and external stability measurements. Chapter 7 presents a differential measurement of the electroweak production of a Z boson in association with two jets. It utilises a data-driven method to constrain Strong-Zjj production, which is the dominant background. Chapter 8 is a summary of the findings in this thesis.

Unless stated otherwise, this thesis uses natural units, which is the standard in high energy particle physics. Natural units have the reduced planks constant, $\hbar$, and the speed of light, c, set to unity and all energies are expressed in electron volts, eV. Furthermore the Einstein summation convention is used where an upper and a lower index using the same symbol implies a sum over that index.

Chapter 2

The theoretical framework for particle physics

This chapter will provide an overview of the theoretical framework used in this thesis. Section 2.1 provides an introduction to the theory. Section 2.2 will cover the particle content of the Standard Model. Section 2.3 gives an overview of the mathematical formalism of the Standard Model. Section 2.4 will cover the validation and open questions in the Standard Model. This is followed by section 2.5 which covers cross-section calculations in proton-proton collisions. Finally, the Monte Carlo event generator approach to simulating proton-proton collisions is discussed in section 2.6.

2.1 Introduction

It is a remarkable fact that all known particle interactions can be explained by only four fundamental forces: the electromagnetic interaction acting on the electrically charged particles; the gravitational interaction responsible for making all massive matter attract each other; the strong interaction which keeps atomic nuclei together, and finally the weak interaction which is the mediator for decays of the atomic nucleus.

The current theory of particle physics was born from a combination of Quantum Mechanics [1], Einstein's theory of Special Relativity [2] and Classical Field Theory [3]. This combination is called a Quantum Field Theory (QFT). QFTs currently successfully describe three out of the four fundamental forces of nature, with gravity being omitted. The name given to the QFT that describes particle physics is the Standard Model (SM) [4]. The latest confirmation of the SM was the discovery of the Higgs boson in 2012 by the ATLAS and CMS collaborations [5–7].

2.2 Particles in the Standard Model

A fundamental particle is defined as a particle that has no substructure. These fundamental particles are classified as either fermions or bosons, with half-integer or integer spin[1] respectively. All fermions have an antiparticle, a particle with identical mass but opposite quantum numbers, such as electrical charge.

Fermions are sub-categorised into three generations of particles. The first generation of particles are both stable and the lightest generation. Additionally they form the constituents of every day matter. All generations of fermions have the same properties with the main exception being that the particle masses are larger

[1] Spin is an intrinsic form of angular momentum.

for higher numbered generations. Additionally the lifetimes and decays of different generations differ, generally with higher generations having shorter lifetimes. Table 2.1 shows the masses and charges of all known fermions.

Fermions: Spin = 1/2						
	Leptons			Quarks		
Generation	Flavour	Charge	Mass	Flavour	Charge	Mass
1st	ν_e	0	≤ 2 eV	u	+2/3	2.2 MeV
	e	-1	0.511 MeV	d	-1/3	4.7 MeV
2nd	ν_μ	0	≤ 0.19 MeV	c	+2/3	1.28 GeV
	μ	-1	105.658 MeV	s	-1/3	95 MeV
3rd	ν_τ	0	≤ 18.2 MeV	t	+2/3	173.1 GeV
	τ	-1	1776.86 MeV	b	-1/3	4.18 GeV

TABLE 2.1: A list of some basic properties of all fermions in the SM. Neutrinos are treated as massless in the SM, which is a very good approximation despite the fact that current results show they have non-zero but very small masses [8].

Fermions are further sub-categorised into leptons and quarks, with two of each per generation. The primary difference is that quarks carry one of three "colour[2] charges" and so are able to interact via the strong force, whereas the leptons do not. Experimentally no free quarks have ever been observed, instead they combine to form colour-neutral combinations. This fact is referred to as confinement and these colour neutral particle combinations are called hadrons. Hadrons are further sub-categorised into baryons and mesons. Baryons contain three quarks or anti-quarks and mesons are a quark and anti-quark pair. Due to the fact that quarks are not observed in isolation one cannot easily define the mass of a quark. In experimental particle physics one typically uses the pole mass, which corresponds to the rest mass of the particle in the special theory of relativity.

Per generation, the lepton doublet consists of an electrically charged particle and an electrically neutral neutrino. Each generation of leptons is referred to as having a "flavour" which labels[3] the species of an elementary particle and this quantity is conserved in the SM. Observations of lepton flavour violation are covered in section 2.4.2. Analogously to the leptons, the quarks also have a flavour[4] which is conserved by the strong and electromagnetic interactions but not the weak interaction.

Gauge bosons mediate the interactions between the fermions. A list of all fundamental bosons in the Standard Model can be found in table 2.2. The electromagnetic interaction (EM) is described by the symmetry group[5] $U(1)_{EM}$, and is mediated by the massless spin 1 photon. The photon can couple to any particle that is electrically charged and so it does not couple to itself as it carries no electric charge. The range of the EM interaction is infinite as the photon is massless.

All fermions interact via the weak force, which is the only interaction that neutrinos participate in. The unification of the weak and the electromagnetic forces allow both of them to be described by the symmetry group $U(1)_Y \otimes SU(2)_L$, which is covered in section 2.3.4. The weak force is mediated by the neutral Z boson and the

[2]Colour is the name given to a quantum number that labels one of three states a quark can be in, generally the labels red, blue and green are used to describe the three possible states.

[3]The lepton flavours are electron, muon and tau.

[4]The quark flavours are up, down, strange, charm, bottom, and top.

[5]Note that $U(1)_{EM}$ is not the same as $U(1)_Y$, which is the symmetry used in the full SM. However the full unified electroweak symmetry $U(1)_Y \otimes SU(2)_L$ breaks down into $U(1)_{EM}$.

Bosons					
Name	Spin	Charge	Mass [GeV]	Force	Relative strength
Gluon, g	1	0	0	Strong	1
Photon, γ	1	0	0	Electromagnetic	10^{-2}
$W^{\pm}$	1	± 1	80.385	Weak	10^{-13}
Z	1	0	91.188		
H	0	0	125.09		

TABLE 2.2: Gauge bosons and fundamental forces in the SM. Particle masses obtained from [8].

charged $W^{\pm}$ boson. The weak equivalent of electromagnetic charge is weak isospin. Up-type quarks and neutrinos have a weak isospin of $1/2$; the remaining fermions have a value of $-1/2$. The apparent weakness of the weak interaction is due to the fact the W and Z bosons have mass and thereby the range is limited by Heisenberg's uncertainty principle.

The strong force is described by the symmetry group $SU(3)_C$ and is mediated by 8 bosons called gluons which couple to particles with a colour charge. The gluons have no mass, however, and unlike the photon their range is limited to ~10^{-15} m due to self interactions. Additionally the photon carries no electric charge. The gluon does carry colour charge and so can self interact. This is covered in section 2.3.3.

The remaining particle in the SM is the Higgs boson. The Higgs boson has zero electric charge and is the only particle in the SM with zero spin. It does not mediate any of the interactions covered previously in this section. The Higgs boson is a remnant of the Higgs mechanism, which is responsible for giving mass to all of the other particles in the SM. This is covered in section 2.3.5. Additionally, it introduces the Yukawa interaction into the SM, which is the coupling of the Higgs boson to all fermions.

2.3 Mathematical formalism of the Standard Model

The Lagrange formalism allows the calculation of the equations of motion of a system using the Euler-Lagrange equation obtained from Hamilton's principle [9].

2.3.1 Quantum field theory and Lagrangian formalism

The Euler-Lagrange equation is a second order partial differential equation. The general version of the equation used by QFTs is given by,

$$\partial_\mu \frac{\partial \mathcal{L}}{\partial(\partial_\mu \psi)} = \frac{\partial \mathcal{L}}{\partial \psi} \ , \tag{2.1}$$

where $\mathcal{L}$ is the Lagrangian density, ψ is a general field, μ is the coordinate index, and ∂_μ is the partial derivative with respect to coordinate μ. In the QFT formulation [10], the elementary particles are described by fields, the dynamics of which are described by Lagrangian densities. These fields are operators on the QM Fock space, which is used in QM to describe systems with more than one degree of freedom. The general form of the Lagrangian of a QFT is given by,

$$\mathcal{L} = \mathcal{L}(\psi, \partial_\mu \psi), \tag{2.2}$$

where the index μ describes the 4 elements of 4 dimensional space-time[6].

In the context of particle physics a vector is defined by its transformation. A vector is an object that transforms like a four-vector under a Lorentz transformation. A scalar is defined as an object which is invariant under Lorentz transformations. Vector fields describe spin 1 particles and scalar fields describe spin zero particles. The fermion field ψ does not transform like a vector or a scalar. Instead a Lorentz transformation will only rotate the fermion field through half the angle a vector would transform. Thereby, ψ is a third type of quantity known as a spinor and spinors describe spin half particles.

The dynamics of non-interacting fermions are described by the Dirac equation[11], for which the Lagrangian, $\mathcal{L}_D$, is given by,

$$\mathcal{L}_D = \bar{\psi}\left(i\gamma^\mu \partial_\mu - m\right)\psi \tag{2.3}$$

where ψ is the fermion field, $\bar{\psi} \equiv \psi^\dagger \gamma^0$ is the Dirac adjoint, γ^μ are the Dirac matrices and m is the mass of a fermion. The fermion field ψ here takes the form of a bispinor. The Dirac equation is a relativistic wave equation which can describe any spin-half particles such as the fermions. It is consistent with both Quantum Mechanics and Special Relativity.

2.3.2 Gauge structure of the Standard Model

The Standard Model (SM) of particle physics [12–15] is a relativistic non-abelian[7] gauge[8] quantum field theory that describes the interactions of all known fundamental particles. The SM is based on the local gauge symmetry group,

$$U(1)_Y \otimes SU(2)_L \otimes SU(3)_C \tag{2.4}$$

where $U(1)_Y \otimes SU(2)_L$ is the symmetry group of the unified electromagnetic and weak interactions. Y denotes hypercharge and L reflects the left-handed nature of the weak interaction [16, 17]. The remaining symmetry group, $SU(3)_C$, represents the strong interaction, with C denoting colour. These symmetry groups contain a set of unitary base matrices called generators, T_a. Any transformation for that group can be described by a linear combination of these generators.

The interactions of vector bosons with fermions [18] can be derived by requiring that the Lagrangian is invariant under the local gauge transformations[9] associated with the symmetries given in equation 2.4. A general local gauge transformation is parametrised by,

$$\psi(x^\mu) \rightarrow e^{i\alpha^a(x^\mu)T_a}\psi(x^\mu), \tag{2.5}$$

where $\alpha^a(x^\mu)$ is the local phase. If a local gauge transformation was applied to a Lagrangian, extra terms arise due to the fact the partial derivative terms in the Lagrangian act on the local dependence of the transformation. Consequently, that Lagrangian would not be invariant under the transformation and this can be demonstrated by substituting equation 2.5 into 2.3. To manage this problem, and thereby

[6] The four elements of 4 dimensional space time of a particle is defined to be $x^\mu \equiv (t, x, y, z)$.

[7] Non-abelian means that the generators of a given symmetry group do not commute with each other.

[8] A gauge theory means that there are degrees of freedom in the mathematical formalism which do not correspond to changes in the physical state.

[9] It is also possible to have global transformations where the value of $\alpha^a(x^\mu)$ in equation 2.5 is a constant.

restore local gauge invariance, one replaces the partial derivative in the Lagrangian, ∂_μ , with a covariant derivative, D_μ,

$$D_\mu = \partial_\mu - igT_a A^a_\mu, \tag{2.6}$$

where A^a_μ are additional vector fields that are designed to transform so that they cancel out the additional terms introduced. Done correctly, the Lagrangian will then be invariant under the local gauge transformation. The constant g is referred to as the coupling constant and it defines the strength of the interactions between the fermions and bosons. To ensure the invariance of the Lagrangian the additional field, A_μ, will transform as:

$$A^a_\mu \to A^a_\mu + \frac{1}{g}\partial_\mu \alpha^a(x^\mu) + f_{abc} A^b_\mu \alpha^c(x^\mu). \tag{2.7}$$

Here, f_{abc} is the symmetry group's structure constant and is given by the commutation relations between the group's generators,

$$\left[T_a, T_b\right] = i f_{abc} T_c. \tag{2.8}$$

These new fields describe the vector bosons that mediate a specific interaction. The introduction of the fields A_μ in the covariant derivative add new terms to the Lagrangian when the partial is replaced with the covariant derivative. These terms describe the interaction of the fermions, ψ, with vector bosons, A^a_μ. An example of what these terms would look like is given by,

$$\mathcal{L} \supset -g\bar{\psi}\gamma^\mu A^a_\mu t^a \psi. \tag{2.9}$$

Furthermore, gauge boson self interaction terms of the form,

$$\frac{1}{4} F^a_{\mu v} F^{\mu v}_a, \tag{2.10}$$

can be added to equation 2.3 provided that the structure constant of the group is non zero.

2.3.3 The strong interaction

The theory of the strong interaction is called quantum chromodynamics (QCD). This theory describes the interactions of quarks and gluons. The evidence for quarks and gluons can be obtained from deep inelastic scattering experiments [19]. The generators of $SU(3)_C$ represent rotations in colour space and are given by,

$$T_a = \frac{\lambda_a}{2}, \tag{2.11}$$

where λ_a are the Gell-Mann matrices. The conserved quantum number from this symmetry is referred to as colour. It labels one of three states a quark can be in; generally the labels red, blue and green are used. From equation 2.6, the covariant derivative for the strong symmetry group is given by,

$$D_\mu = \partial_\mu - \frac{1}{2} i g_s \lambda_a G^a_\mu, \tag{2.12}$$

where g_s is the strong coupling constant[10] and G^a_μ represents the vector bosons for the strong interaction. There are eight Gell-Mann matrices and so there are eight gauge bosons associated with QCD which are called gluons. The kinetic term for the gluons can be written in an analogous way to the one for electromagnetic case and is given by,

$$\mathcal{L}_{QCD,kin} = -\frac{1}{4} G^a_{\mu v} G^{\mu v}_a, \tag{2.13}$$

where $G^a_{\mu v}$ is the strong field strength tensor given by,

$$G^a_{\mu v} = \partial_\mu G^a_v - \partial_v G^a_\mu + g_s f_{abc} G^b_\mu G^c_v. \tag{2.14}$$

The structure constant of the $SU(3)_C$ symmetry is non zero and so self interactions of the gluons are allowed by QCD. Equation 2.13 describes the self interactions of the gluon fields and it shows that triple and quartic gluon interactions are possible.

The value of g_s becomes asymptotically smaller for a large energy scale; this fact is referred to as asymptotic freedom. The result of asymptotic freedom is that quarks and gluons can be described as independent particles provided that the energy scale is high enough. Conversely for lower energy scales the value of g_s increases. As the energy scale is lowered, the value of g_s eventually becomes so large that perturbative expansions in the coupling no longer converge.

2.3.4 The electroweak interaction

The electroweak (EW) interaction is the combination of the electromagnetic and the weak interactions. These two forces were unified by Glashow, Salam and Weinberg [20–22]. This unified theory includes the flavour changing, charged interactions via the W boson and the flavour conserving, neutral interactions mediated by the photon and the Z boson. The conserved quantum numbers associated with the electroweak interaction are weak hypercharge, Y_W, and isospin, I. They are related to each other by the Gell-Mann–Nishijima [23, 24] formula,

$$Q = I_3 + \frac{Y_W}{2}. \tag{2.15}$$

Here, Q is the particle's charge and I_3 is the third component of isospin. The electroweak unification is described by the symmetry group,

$$U(1)_Y \otimes SU(2)_L. \tag{2.16}$$

There are three generators of the $SU(2)_L$ group which result in the existence of three gauge boson fields labelled as $W^{1,2,3}_\mu$. These gauge fields only couple to left-handed fermions[11] by construction. Right-handed fermions are $SU(2)_L$ singlets and do not interact weakly within the SM. As neutrinos only interact weakly, right handed neutrinos do not exist in the SM. The generators of $SU(2)_L$ are given by,

$$T_a = \frac{\sigma_a}{2}, \tag{2.17}$$

[10] g_s is often denoted as $\alpha_s = \frac{g_s^2}{4\pi}$ for mathematical convenience.

[11] A particle is right handed if its spin points in the same direction as its momentum and left handed otherwise.

where σ^a are the Pauli matrices. The structure constant for the $SU(2)_L$ group is the totally anti-symmetric tensor ϵ_{ijk}, which allows for self interaction between the gauge bosons as it is non zero.

There is a single generator for the $U(1)_Y$ group, which is simply the identity matrix multiplied by a constant and is denoted as Y. Thereby there is only one vector field, B_μ, associated with the $U(1)_Y$ group. From equation 2.6, the covariant derivative for the electroweak symmetry group is given by,

$$D_\mu = \partial_\mu - \frac{1}{2} i g_w \sigma_a W_\mu^a - \frac{1}{2} i g_Y Y B_\mu, \tag{2.18}$$

where g_w is the weak coupling constant and g_Y is the electromagnetic coupling constant. The Lagrangian of the electroweak interaction is then given by,

$$\mathcal{L}_{EW} = \sum_f \bar{\psi} i \gamma^\mu D_\mu \psi - \frac{1}{4} F^a_{\mu v} F_a^{\mu v}. \tag{2.19}$$

Equation 2.19 contains a sum over all fermions, f, describing their kinetic terms and interactions with the gauge bosons. The second term contains the electroweak field strength tensor, $F^a_{\mu v}$, and describes the kinetic and self interaction terms of the electroweak gauge fields. The electroweak field strength tensor is defined by,

$$F^a_{\mu v} = \partial_\mu W^a_v - \partial_v W^a_\mu + g_W f^{abc} W^b_\mu W^c_v + \partial_\mu B^a_v - \partial_v B^a_\mu. \tag{2.20}$$

Substituting equation 2.18 into equation 2.19 gives the interaction term between the $W^{1,2,3}_\mu$ fields and a fermion field,

$$\mathcal{L}_{SM} \supset -g_w \bar{\psi} \gamma^\mu \frac{\sigma^a}{2} W^a_\mu \psi = -g_w \bar{\psi} \gamma^\mu \begin{pmatrix} W^3_\mu & W^1_\mu - i W^2_\mu \\ W^1_\mu + i W^2_\mu & W^3_\mu \end{pmatrix} \psi. \tag{2.21}$$

From here it is common[12] notation to write the off-diagonal elements of the W^i_μ field's matrix as,

$$W^\pm = \frac{1}{\sqrt{2}} (W^1_\mu \mp i W^2_\mu), \tag{2.22}$$

where $W^\pm$ correspond to the physical $W^\pm$ bosons. These terms in the matrix couples up-like and down-like elements of the left-handed fermions. Additionally they describe the observed universality of flavour-changing couplings for quarks and leptons as only one coupling parameter, g_w, is used.

Finally the photon, A_μ, and the Z bosons, Z_μ, are represented by linear combinations of the two remaining neutral fields, W^3_μ and B_μ,

$$\begin{pmatrix} A_\mu \\ Z_\mu \end{pmatrix} = \begin{pmatrix} \cos\theta_W & \sin\theta_W \\ -\sin\theta_W & \cos\theta_W \end{pmatrix} \begin{pmatrix} B_\mu \\ W^3_\mu \end{pmatrix}, \tag{2.23}$$

where θ_W is the weak mixing angle, and is defined by,

$$\cos\theta_W = \frac{g_W}{\sqrt{g_W^2 + g_Y^2}}. \tag{2.24}$$

By construction the photon is a mixture of the W^3_μ and B_μ fields and so it can have an equal interaction with both left and right-handed fermions.

[12] This is because it makes the mass matrix of the W boson diagonal.

It is worth noting that for the charged leptons, the flavour eigenstates[13] are the same as the mass eigenstates. However, in general, the flavour eigenstate of fermions are not the same as their mass eigenstates; linear combinations of the mass eigenstates are used instead. For the quarks, the CKM[14] matrix gives the appropriate linear factors to convert from mass to the flavour eigenstate [25, 26]. This matrix is a 3×3 unitary matrix and can be written in terms of four real parameters. As there are four independent parameters a 3×3 unitary matrix cannot be forced to be real-valued. Thereby Charge-Party (CP) violation arises due to the fact that the couplings for quarks and anti-quarks have different phases, i.e. $V_{CKM} \neq V^*_{CKM}$. An analagous matrix called the PMNS[15] matrix exists for the neutrinos [27].

In summary, the weak and EM interactions have been unified into a single symmetry group, $U(1)_Y \otimes SU(2)_L$, and the observed bosons in nature can be described as a mixture of the 4 gauge fields. Finally, experimental observations of the W and Z bosons have demonstrated that they have mass. However, adding mass terms for the electroweak gauge fields of the form,

$$\mathcal{L}_{SM} \supset mA^2 A_\mu A^\mu, \tag{2.25}$$

in equation 2.19 breaks the local gauge invariance. The solution to this problem requires the introduction of electroweak symmetry breaking, which is covered in the next section.

2.3.5 Electroweak symmetry breaking

For both gauge bosons and fermions, if one introduces a mass term into the Lagrangian it is no longer gauge invariant. To solve this problem one introduces a new complex scalar field, ϕ, with four degrees of freedom [28–30]. This field is a doublet under $SU(2)_L$ consisting of one electrically positive and one neutral field and is given by,

$$\phi = \begin{pmatrix} \phi^+ \\ \phi^0 \end{pmatrix} = \frac{1}{\sqrt{2}} \begin{pmatrix} \phi_1 + i\phi_2 \\ \phi_3 + i\phi_4 \end{pmatrix}, \tag{2.26}$$

where ϕ is the Higgs field. This field has electroweak quantum numbers $I^3 = \pm\frac{1}{2}$ and $Y = 1$. A new term is then added to the SM Lagrangian,

$$\mathcal{L}_{SM} \supset \mathcal{L}_{Higgs} = \left(\mathcal{D}_\mu \phi\right)^\dagger \left(\mathcal{D}^\mu \phi\right) - V(\phi), \tag{2.27}$$

where D_μ is the covariant derivative of the electroweak interaction given in equation 2.18. Here, the first term results in interactions with the $SU(2)_L$ gauge bosons and the final term is the potential of the Higgs field, and is defined as,

$$V(\phi) = \mu^2 \phi^\dagger \phi + \lambda \left(\phi^\dagger \phi\right)^2, \tag{2.28}$$

where μ and λ are constants and $\lambda > 0$. At this point one needs to make a choice on the sign of μ^2. The only interesting[16] sign choice is when $\mu^2 < 0$ as this results in the "Mexican hat" potential, depicted in figure 2.1. By taking the differential of equation 2.28 with respect to ϕ one can show that the potential is minimised along a

[13] An eigenstate is a quantum state whose wave function is an eigenfunction of the linear operator that corresponds with an observable.

[14] Cabibbo-Kobayashi-Maskawa

[15] Pontecorvo–Maki–Nakagawa–Sakata

[16] If it was the case that $\mu^2 > 0$, one would find the minimum of the potential was at $\phi = 0$.

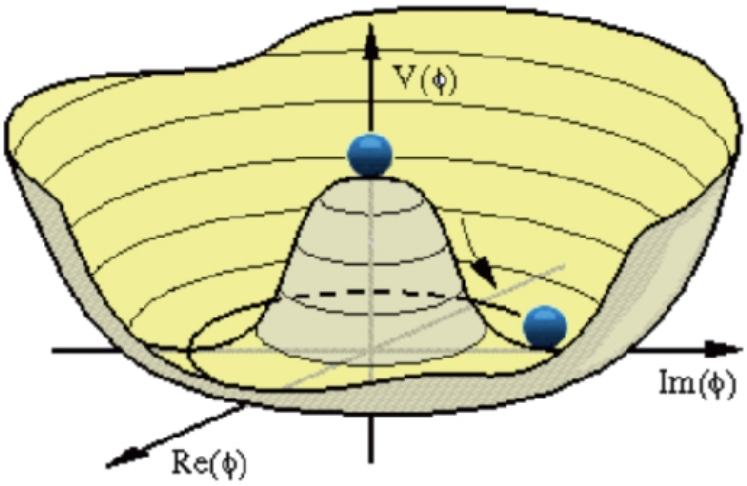

FIGURE 2.1: The Higgs potential, $V(\phi)$, for the case where $\lambda > 0$ and $\mu^2 < 0$. It has a minimum at $|\phi| = \sqrt{-\frac{\mu^2}{\lambda}}$. Figure obtained from reference [31].

series of points that satisfy the following equation,

$$\phi^\dagger\phi = \frac{1}{2}(\phi_1^2 + \phi_2^2 + \phi_3^2 + \phi_4^2) = -\frac{\mu^2}{2\lambda} = v. \tag{2.29}$$

The minimum of the Higgs potential is chosen so that the charged component of the Higgs doublet is zero, while the neutral one is equal to v. The choice of minimum is motivated by the fact that the Higgs field is not required to interact with the photon as it is known to be massless. Thereby the vacuum expectation value (VEV) of the Higgs field is given by,

$$\langle 0|\phi|0\rangle = \frac{1}{\sqrt{2}}\begin{pmatrix}0\\ v\end{pmatrix}. \tag{2.30}$$

Choosing a specific minimum breaks the $U(1)_Y \otimes SU(2)_L$ symmetry while leaving $U(1)_{EM}$ unbroken. This mechanism is called spontaneous electroweak symmetry breaking. From here the VEV from equation 2.30 can be substituted into the Higgs Lagrangian given in equation 2.27. With some careful rearrangement [32], one can identify a collection of mass terms,

$$\mathcal{L}_{SM} \supset \frac{1}{8}v^2 g_W^2\left[\left(W_\mu^1\right)^2 + \left(W_\mu^2\right)^2\right]^2 + \frac{1}{8}v^2\left[g_W W_\mu^3 - g_Y B_\mu\right] + 0\left[g_Y W_\mu^3 - g_W B_\mu\right]^2, \tag{2.31}$$

which can be re-written as,

$$\mathcal{L}_{SM} \supset \frac{1}{2}m_W^2\left(W^+\right)^2 + \frac{1}{2}m_W^2\left(W^-\right)^2 + \frac{1}{2}m_Z^2 Z_\mu^2 + \frac{1}{2}m_A^2 A_\mu^2 \tag{2.32}$$

From here one can obtain the masses of the W and Z bosons and the photon by substituting the definitions of the physical bosons given in equations 2.22 and 2.23. The masses are given by,

$$m_W = \frac{1}{2}v g_W, \tag{2.33}$$

$$m_Z = \frac{1}{2}v\sqrt{g_W^2 + g_Y^2}, \tag{2.34}$$

$$m_\gamma = 0. \tag{2.35}$$

The scalar Higgs field has four degrees of freedom (DoF), as seen in equation 2.26. Three of the 4 DoF are "eaten" by the $W^\pm$ and Z bosons, which results in them having a longitudinal polarisation mode which corresponds to a massive particle. The remaining DoF is the Higgs boson itself. This theory does not directly predict the mass of the Higgs boson; this was discovered experimentally to be $M_H = 125$ GeV [8]. Previous to its discovery its mass was predicted by using electroweak precision measurements.

2.4 Validation of the Standard Model and open questions

Despite having eighteen free parameters, the SM has been proven repeatedly to be a precise and reliable method to describe the phenomena of particle physics. This section will first cover the experimental validation of the SM and then move onto the remaining open questions.

2.4.1 Validation of the Standard Model

The Gfitter collaboration [33] fits the free parameters of the SM using a variety of precision measurements. A summary plot can be seen in figure 2.2, which shows that these fit results are in a good agreement with the measurements. This shows that the SM can simultaneously explain all of the measurements. In addition to these global fits, individual predictions of the SM can be tested as well. Figure 2.2 shows a summary of cross-section measurements taken by the ATLAS collaboration at different centre of mass energies. Here, the measured cross-sections agree with the SM prediction over a large range of cross-section sizes and interactions.

In cross-section calculations, radiative corrections[17] allow the masses of particles that are not in the initial or final state of an interaction to affect the calculation. The top quark has a non-small radiative correction to the calculation of the W boson mass and the $z \to b\bar{b}$ decay. Figure 2.3 shows that the recent direct and indirect measurements for the top quark masses are in good agreement with each other. This demonstrates the consistency of the SM.

2.4.2 Open questions in the Standard Model

It was previously covered that the SM does not include gravity, so we already know that it is an incomplete theory. The SM of particle physics does fall short in describing a number of observed phenomena. This section will be dedicated to some of the open questions in the SM.

From observing the rotation curves of galaxies and clusters [35–37], one can infer the existence of dark matter. Additional non-luminous matter is required to generate a strong enough gravitational field to explain these rotation curves. Only the gravitational effect of dark matter can be seen, so one can deduce it does not interact electromagnetically. Measurements of the cosmic microwave background radiation show that the mass density of dark matter is approximately 5 times higher than that of regular matter [38]. There are no particles in the SM that can describe dark matter or that can explain its abundance [8].

[17] Radiative corrections are higher order corrections applied to the cross-section when calculating using perturbation theory. Calculating cross-sections is covered in section 2.5.

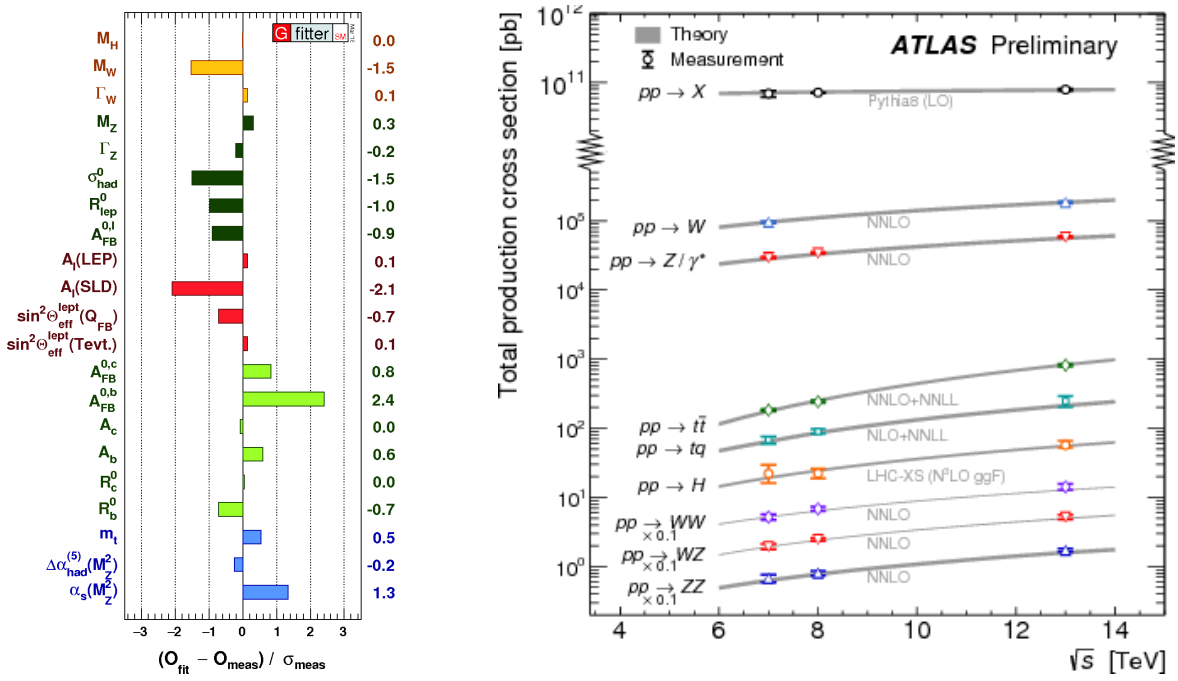

FIGURE 2.2: **Left:** a summary of the results from the Gfitter collaboration. Here the global fit results are in a good agreement with the measurements. Figure obtained from [33]. **Right:** Summary of total production cross-section measurements by ATLAS presented as a function of centre-of-mass energy $\sqrt{s}$ from 7 to 13 TeV for a few selected processes. The di-boson measurements are scaled by a factor 0.1 to allow a presentation without overlaps. Figure obtained from reference [34].

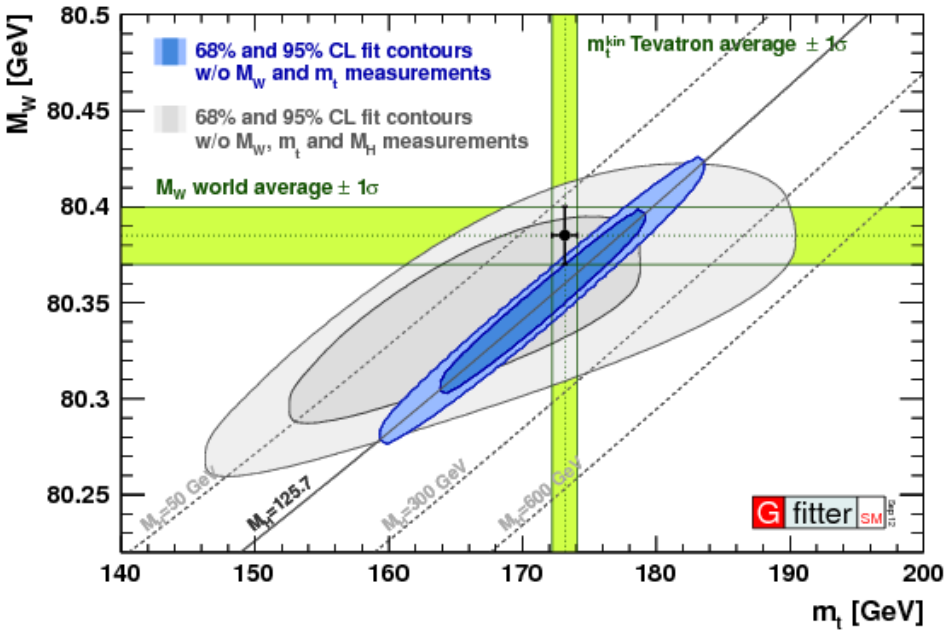

FIGURE 2.3: 68% and 95% CL contours in the $m_t - m_W$ plane for the fit including m_W (blue) and excluding m_H (grey). In both cases the direct measurements of m_W and m_t were excluded from the fit. The values of the direct measurements are shown as green bands with their one standard deviations. The dashed diagonal lines show the SM prediction for m_W as a function of m_t for different assumptions of m_H. Figure obtained from reference [33].

A second cosmological effect that is not explained by the SM is high ratio of matter to anti-matter in the universe [39]. Both the CKM and PMNS matrices of the SM include CP violating effects [40]. However these are not large enough to explain the size of this asymmetry.

A particle physics phenomena that is not described by the SM is neutrino oscillation [41]. Neutrino oscillation is the process during which a neutrino that was created with a specific lepton flavour can later be measured to be a different lepton favour at a later time. Neutrino oscillations imply that neutrinos have a non zero mass. However, the SM does not contain mass terms for the neutrinos that can be easily implemented by hand.

2.5 Cross-section calculations in hadron-hadron collisions

A cross-section is the effective area transverse to the relative motion of two particles that quantifies the likelihood of them interacting. This section will cover how cross sections are calculated using the SM to allow a comparison to the data collected by ATLAS.

2.5.1 Types of proton-proton scattering

There are three different types of proton-proton scattering that can occur. They are given below in order of likelihood:

- **Elastic scattering:** The proton acts as a single particle and no new particles are produced, thereby the inner structure cannot be probed. It occurs when there

is a small momentum transfer between the protons, and thereby they have a low[18] transverse momentum with respect to hard scatters.

- **Soft inelastic scattering:** One or both of the protons involved in the interaction are destroyed, but the momentum transfer between the two protons is still small. Primarily this produces pions and other light hadrons, again with low transverse momentum.
- **Hard scattering:** There is a large momentum transfer between the incoming protons and at least one of them is destroyed. This allows the production of new and high mass particles. Unlike for elastic scattering, the inner structure of the proton can be probed.

Of these three processes, typically in particle physics one is interested in the hard scattering process as this has the largest momentum transfer and so is able to produce higher mass particles than the other types of scattering.

2.5.2 Cross-section calculations

For the collision of two hadrons, labelled A and B, the differential cross-section can be written as,

$$d\sigma_{AB\to X} = \sum_{a,b} \int dx_a dx_b f_{a/A}(x_a, \mu_F^2) f_{b/A}(x_b, \mu_F^2) \times d\sigma_{ab\to X}(\alpha_s(\mu_R^2), Q^2). \quad (2.36)$$

For the LHC these hadrons are protons. Q^2 is the square of the four momentum transferred between the partons. The notation $AB \to X$ denotes the interaction between the two incoming protons producing any number of additional particles, X. The sum in equation 2.36 is over all partons in A and B. A parton is the name given to the constituents of the proton. Furthermore $d\sigma_{ab\to X}$ represents the cross-section for the collisions of parton a, from A, and parton b, from B. The parton distribution functions $f_{a/A}$ and $f_{b/B}$ describe the probability of finding a parton of a given momentum fraction inside a proton. This will be covered in section 2.5.4.

The terms $d\sigma_{ab\to X}(\alpha_s(\mu_R^2), Q^2)$ can be calculated directly from the SM and are dependent on the strong coupling, α_s, measured at the renormalisation scale, μ_R^2. Renormalisation scales are covered in section 2.5.5. Each parton is defined to have a fraction of the total proton's momentum, x, so the total energy, $\hat{s}$, of a specific hard scatter is given by,

$$\hat{s} = x_a x_b s, \quad (2.37)$$

and is always less than the collision energy, s.

2.5.3 Hard scatter

The hard scatter is described at parton level by a matrix element (ME) calculation. The ME gives information about whether a transition from an initial to a final state is possible and, if so, the likelihood of that transition. The SM allows one to calculate a ME using Feynman rules. Feynman rules provide a series of instructions about how to calculate a cross-section by drawing all possible Feynman diagrams for a process.

A Feynman diagram is a convenient pictorial representation of the mathematical expressions describing a particle interaction [42]. The lines in the diagram represent

[18] The protons in ATLAS essentially collide head on and so there is ~0 momentum transverse to the proton beams in the initial state.

particles; the points where they join are called vertices. A vertex is where the particles interact, and here they can emit or absorb new particles, or change type. The convention used in this thesis is such that the vertical displacement represents a spatial dimension and the horizontal displacement represents a displacement in time. An example Feynman diagram of the process $pp \to Zjj$ is shown in figure 2.4.

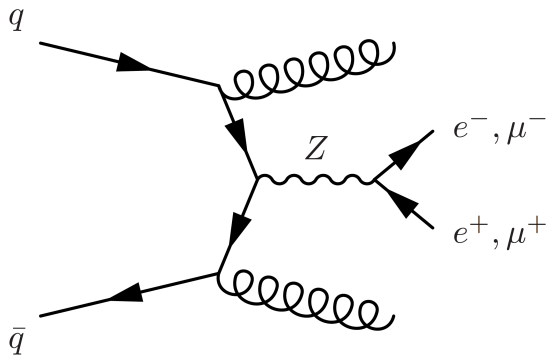

FIGURE 2.4: Feynman diagram depicting the process $pp \to Zjj$. In this diagram both the incoming quark and anti-quark emit a gluon, which will become the two jets in the final signature. Additionally the quarks annihilate to form a Z boson which decays leptonically to either an electron or a muon. Figure obtained from reference [43].

The full calculation of the partonic cross-section must take into account all possible Feynman diagrams for the relevant process. In principle there are an infinite number of Feynman diagrams for any process. In practice, one can truncate the perturbative expansion to allow manageable calculation. In terms of Feynman diagrams this results in ignoring all diagrams above a given complexity.

A leading order calculation (LO) only takes into account the most simple of these diagrams, i.e. it uses the first non-trivial term in the perturbative expansion[19]. A next-to-leading order (NLO) calculation will include the LO term and also the next non-trivial term in the expansion. The computational power required and accuracy of NLO calculations is higher than that of LO calculations. It is possible to extend this further with next-to-next-to-leading order (NNLO) calculation including a third term, and so on. As including additional terms increases the computational power required, it is uncommon for simulations to use a higher order of precision than NLO precision.

2.5.4 Parton distribution functions

Partons are sub-categorised into valence quarks, sea quarks and gluons. The proton contains three valence quarks (uud) which define the properties of the proton. These three quarks form a bound state which is held together by the strong interaction. Virtual[20] gluons are constantly exchanged between the valence quarks. Additionally these virtual gluons can form virtual quark-antiquark pairs which are referred to as sea quarks. So the proton is a highly complex environment with far more inside it than just the three valence quarks.

[19] For example in electron-electron scattering the first term in the expansion describes the case where the electrons do not interact, and so the second term is the one used for LO calculations. This results in the orders of a simulation not being equivalent to the order in α_s.

[20] A virtual particle is one that was created by a quantum fluctuation. It has its existence limited by the uncertainty principle.

Parton distribution functions (PDFs) are the probability density that a parton will carry a fraction, x, of the total momentum of the proton at a energy scale, Q. It is not currently possible to calculate PDFs purely from theory, and so they are extracted from experimental data. Most of this data is obtained by deep inelastic scattering experiments using electron-proton colliders. This can be supplemented with measurements of the Drell-Yan[21] process and with jet production cross-sections from proton-proton colliders.

If a PDF has been successfully determined for an energy scale it can be calculated for other scales using the DGLAP[22] equations [44–46]. Example PDFs are shown in figure 2.5 for the energy scales $Q = 2$ and $Q = 100$ GeV.

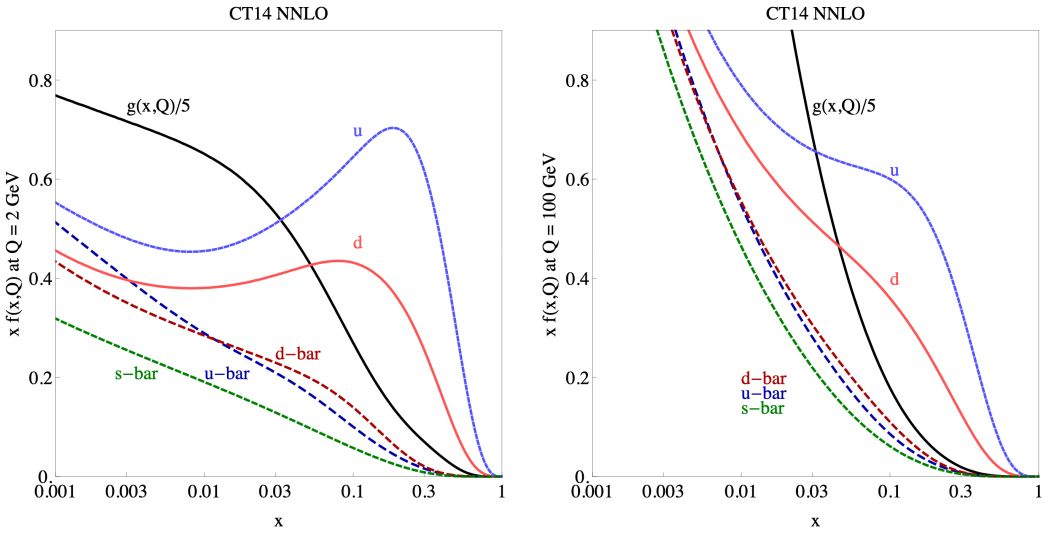

FIGURE 2.5: Parton distribution functions for all of the quarks, anti-quarks and the gluon for $Q = 2$ GeV, on the left, and $Q = 100$ GeV on the right. This measurement was performed by the CTEQ collaboration. Figure obtained from reference [47].

2.5.5 Factorisation and renormalisation scale

Factorisation is used in two different places in the calculation of the cross-section, given in equation 2.36. Firstly it used to separate the partonic cross-sections from the PDFs. Secondly it is used to separate the parton shower from the cross-section calculation itself. These stages are depicted in figure 2.6.

There are two scales associated with a matrix element calculation: the renormalisation scale, μ_R, and the factorisation scale, μ_R. These scales are limits on the energies that intermediate virtual particles are allowed to have. This can result in some loops[23] missing higher order virtual emissions. This is then approximated by additional terms which are given by the renormalisation group equation [49].

Most of the theoretical calculations used by ATLAS set both the factorisation and the renormalisation scale to the same value, i.e. $\mu = \mu_F = \mu_R$. The choice of scale, in

[21] Drell-Yan is the name given to the process where a quark-antiquark pair annihilate in a high energy hadron collision.

[22] DGLAP is short for Dokshitzer-Gribov-Lipatov-Altarelli-Parisi, after the scientists involved, some of whom came up with these equations independently.

[23] A loop is when one can draw a path through a Feynman diagram where one ends where one started. This can lead to divergences.

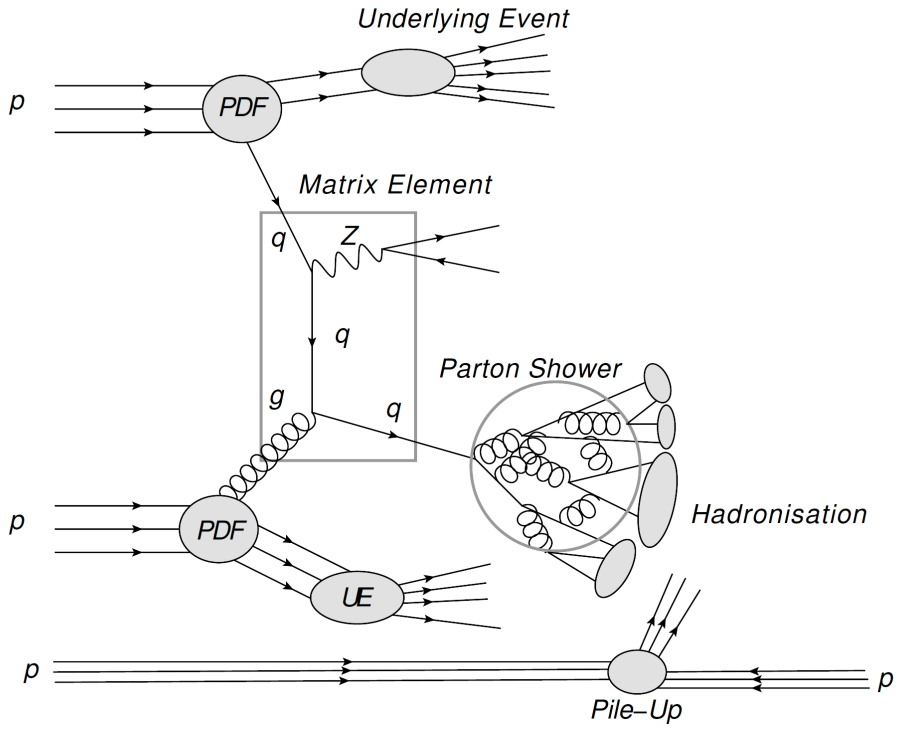

FIGURE 2.6: A schematic diagram of proton-proton collisions depicting the separate calculation steps in proton-proton collision simulations. Figure obtained from reference [48].

theory, should not matter if one expands to a high enough order. However there is some scale dependence for lower order calculations. From experience, μ is set to the same order as the scale of the hard scattering process that is being simulated. Some simulations will provide predictions for several values of μ to allow one to calculate the uncertainties arising from the scale choice [49, 50].

2.6 Monte Carlo event generator simulations

Once a cross-section is calculated for a particular partonic final state, it is necessary to turn this into a prediction for a hadronic final state. This is done with a Monte Carlo (MC) event generator. In this thesis, MC event generation is used to estimate the contributions from known physics processes in a fiducial region (Chapter 7) and to obtain pileup corrections for the Luminosity algorithm (Chapter 5).

2.6.1 Monte Carlo methods

Computational algorithms that rely on repeated sampling of random numbers to obtain numerical results are called Monte Carlo methods. For particle physics Monte Carlo methods are used to randomly sample events of the production and decay of a given process using its ME. If the number of samples is large enough, due to the law of large numbers the average outcome over all events approaches the expected one. Additionally, when the integral over a probability density function, f, is computed, the central limit theorem of statistics states that the mean value of f over these random experiments is an unbiased estimator of the integral.

2.6.2 Parton shower

Parton showering (PS) allows one to add higher order corrections to the perturbative calculation of a given hard scatter. The partons involved in a hard scatter transfer a large momentum to the particles in the final state of the scattering process. When an electrically charged particle is accelerated it will emit photons and produce Bremsstrahlung radiation. The same is true for accelerated particles with a colour charge, however, in this case the particle will emit gluons. Unlike the electromagnetic radiation the gluon carries a colour charge and so it will initiate new strong interactions. This results in a shower of particles being produced.

The parton shower algorithms simulate this emission of quarks and gluons from coloured particles. Additionally these algorithms can include EM radiation, which is suppressed by a factor of α_{EM}/α_s. The modelling of a PS begins at the energy scale of the hard process, Q_o, which provides an upper limit on the squared momentum transfer, t. During this shower evolution the algorithm will iterate over each of the final state particles. Then it will compute all possible parton branching fractions with a random number generator. This process continues until the infrared cut-off scale, t_o, is reached, which is normally of the order 1 GeV. This cut-off is required due to the running of the α_s coupling and removes both soft and collinear particles. Thereby emission with $t < t_0$ involves partons whose energy is too low to resolve[24].

When performing PS there is a choice to be made of which parton branchings to generate first. There are two choices that are primarily used for MC event generators, which are called coherent showering and dipole showering. For coherent showering the the parton branchings with a small opening angle are generated first. This leads to it being called an angular-ordered parton shower. For dipole showering, the emission of gluons is generated according to the dipole radiation pattern of a pair of partons.

It is possible to include double counting in the PS when the ME is calculated in a different simulation step to the PS. For example a NLO generator can include the radiation of an additional parton in its ME, which is also described in the PS for the case where this parton is not radiated. This overlap removal is performed using dedicated matching schemes. Finally the PS algorithms can be tuned using real data to compensate for neglected higher order effects [50].

2.6.3 Hadronisation

Hadronisation is the process by which hadrons are formed from quarks and gluons. After parton showering, there are many partons with a virtual mass-squared of the same order as the cut-off value, t_0, introduced in section 2.6.2. Due to the fact this cut off value is small, the value of α_s becomes too large to perform a perturbative calculation. There are two common simulation models used in MC event generators to describe hadronisation: the string fragmentation and the cluster fragmentation models. Both of these models contain several parameters that can be tuned with the use of data to match the observed relative fraction of different hadrons and their spins in the final jet.

[24] In this context resolvability is related to whether the parton will produce its own jet, or whether it will only contribute to the substructure of the jet of the parton that created it.

2.6.3.1 Hadronisation: The string fragmentation model

The string fragmentation model starts with a quark anti-quark pair produced by the PS. It then attaches a colour string with a linearly rising potential between these particles to represent the field generated by the strong force. For this model the gluons generated in the PS are described by kinks in these colour strings with two colour string pieces attached. As the quark anti-quark pair moves apart; the energy stored in the colour string increases. This continues until it is large enough for a new quark anti-quark pair to be created and the string "breaks". This process is repeated until all of the energy is absorbed and no further string breaking occurs. Finally the hadrons are created by grouping quark anti-quark pairs which are connected by short string segments [50].

2.6.3.2 Hadronisation: The cluster fragmentation model

The cluster fragmentation model starts by splitting all gluons produced by the PS into quark anti-quark pairs. It then clusters quark anti-quark pairs which neighbour each other in momentum space into colourless clusters. The decay of these new clusters via the creation of even more quark anti-quark pairs into hadrons is then calculated. The hadrons absorb the energy stored in the initially clustered quarkanti-quark pair [50].

2.6.4 Underlying event

In addition to the hard scatter, there is the extra activity from secondary scatters between spectator partons inside the proton, as well as beam-beam remnant activity. This is referred to as the underlying event (UE). These additional interactions generally have an energy scale of the order of 1 GeV, and so, they are small with respect to the hard scattering energy scale. As the underlying event has a low energy it generally does not form any additional high energy particles. Instead, it produces a uniformly distributed set of activity, normally in the form of hadrons.

Elastic gluon-gluon scattering has the largest cross-section out of all potential proton-proton interactions. In fact, it is larger than the total proton-proton scattering cross-section. This results in the mean number of gluon-gluon interactions being larger than the number of proton-proton collisions. To simulate the UE, a cut-off scale is introduced, similar to that of the PS algorithm in section 2.6.2. Interactions above this scale are covered by the PS and hadronisation. This cut-off scale can be estimated from the collision energy and from the proton's radius and impact parameter. These UE simulations can be tuned with results from real data [50].

2.6.5 Monte Carlo event generator programs

ATLAS uses a variety of different generator programs; this section will only cover the ones used in this thesis in detail. For a given process the ATLAS collaboration provides a recommendation on which MC to use for the highest possible precision. To evaluate the systematic uncertainties on the recommended MCs alternative choices are also provided.

The multi-purpose generators that can simulate a full event are PYTHIA [51], HERWIG [52, 53] and SHERPA[54]. Additionally there are specialised generators that only simulate the hard scatter, such as POWHEG [55] and MADGRAPH [56, 57]. These specialised generators have to be interfaced to one of the multi-purpose generators

for the PS and hadronisation steps. The main features of these generators are as follows:

- **Pythia:** PYTHIA is a multi-purpose MC generator. It provides LO precision MEs for many different processes. To model the hadronisation, PYTHIA uses the string model. Due to the fact PYTHIA only calculated the ME to LO it is no longer used as a stand-alone event generator inside of ATLAS. Instead a different MC generator is used to calculate the MEs. However, as PYTHIA's PS model shows a good agreement with data it is often still used.

- **Herwig:** HERWIG is a multi-purpose MC generator, however it is no longer used for this purpose. Instead its PS is used in combination with other MC generators. To model the hadronisation, HERWIG uses the cluster model. The difference between using purely PYTHIA and PYTHIA+HERWIG for the PS is used to asses the systematic error associated with the PS step in simulations.

- **Sherpa:** SHERPA is a multi-purpose MC generator. It provides NLO precision MEs for many different processes. It is, therefore, the generator of choice for any processes with additional jets as these can be included in the ME calculation. To model the hadronisation, SHERPA uses the cluster model. Unlike PYTHIA or HERWIG, SHERPA has no hybrid version where SHERPA is used in combination with another MC generator [54].

- **Powheg:** POWHEG calculates the ME to a NLO precision for many different processes. For the simulations used in this thesis, PYTHIA is used to provide the PS for Powheg. Like for PYTHIA, switching the PS algorithm to HERWIG can be used to evaluate systematics.

- **MadGraph5:** Like POWHEG, MADGRAPH calculates the ME to a NLO precision and either PYTHIA or HERWIG can be used to for the PS.

2.6.6 Detector simulation

A highly detailed model of the ATLAS detector [58] is used in conjunction with GEANT4 [59] to simulate the electromagnetic and hadronic interactions of long-lived particles as they pass through the detector. Then the detector response is calculated and the same reconstruction algorithms are implemented as the ones used for real data. These reconstruction algorithms are covered in Chapter 4.

Chapter 3

The ATLAS detector

This chapter will provide an overview of the LHC and the ATLAS detector. Firstly section 3.1 will cover the LHC and then section 3.2 will describe the ATLAS detector.

3.1 The LHC

The Large Hadron Collider (LHC) [60] is the largest and most powerful particle accelerator ever constructed. It is housed approximately 100 meters underground at the Swiss-French border at the European Organisation for Nuclear Research (CERN), just outside Geneva. It is made of two circular hadron accelerators with a circumference of approximately 27 km. The LHC is primarly used to collide protons. Since 2015, the proton-proton collisions had a centre of mass energy of $\sqrt{s} = 13$ TeV, which is just under the design energy of $\sqrt{s} = 14$ TeV. The LHC can also collide lead nuclei (and other ions) with lead–lead collisions as well as proton–lead collisions. These collision types are not covered in this thesis.

During Run 1, the LHC operated at a centre of mass energy of $\sqrt{s} = 7$ TeV in 2010 and 2011 and at $\sqrt{s} = 8$ TeV in 2012. It then underwent the planned long shutdown 1 (LS1) between 2013-14 [61]. Run 2 was started after LS1 at an energy of $\sqrt{s} = 13$ TeV during 2015-2018. The long shutdown 2 (LS2) will start in 2019 to prepare for Run 3.

There are four major experiments situated at the collision points of the LHC: ALICE [62], ATLAS [63], CMS [64] and LHCb [65]. CMS and ATLAS are general purpose detectors; ALICE was built to study lead ion collisions; LHCb was primarily designed to search for and study CPV and rare processes in beauty and charm quark interactions. This thesis uses data collected by the ATLAS experiment.

3.1.1 Accelerating the protons

To provide the protons for the LHC hydrogen gas is ionised by stripping the electrons off with an electric field. After ionisation, the protons are accelerated using a linear and several circular accelerators of increasing size. The layout of this accelerator chain is shown in figure 3.1. The first step of this process is the linear accelerator, LINAC2, which is used to accelerate the protons up to 50 MeV. Then the Proton Synchrotron Booster (PSB) is used to obtain an energy of 1.4 GeV. The PSB feeds into the Proton Synchrotron (PS) which then raises the energy to 25 GeV. The final accelerator before injecting into the LHC ring is the Super Proton Synchrotron (SPS) which raises the energy to 450 GeV. From here, two beams running in opposite directions are injected into the LHC. The remaining energy is gained inside the LHC ring to a maximum of 7 TeV per beam [60].

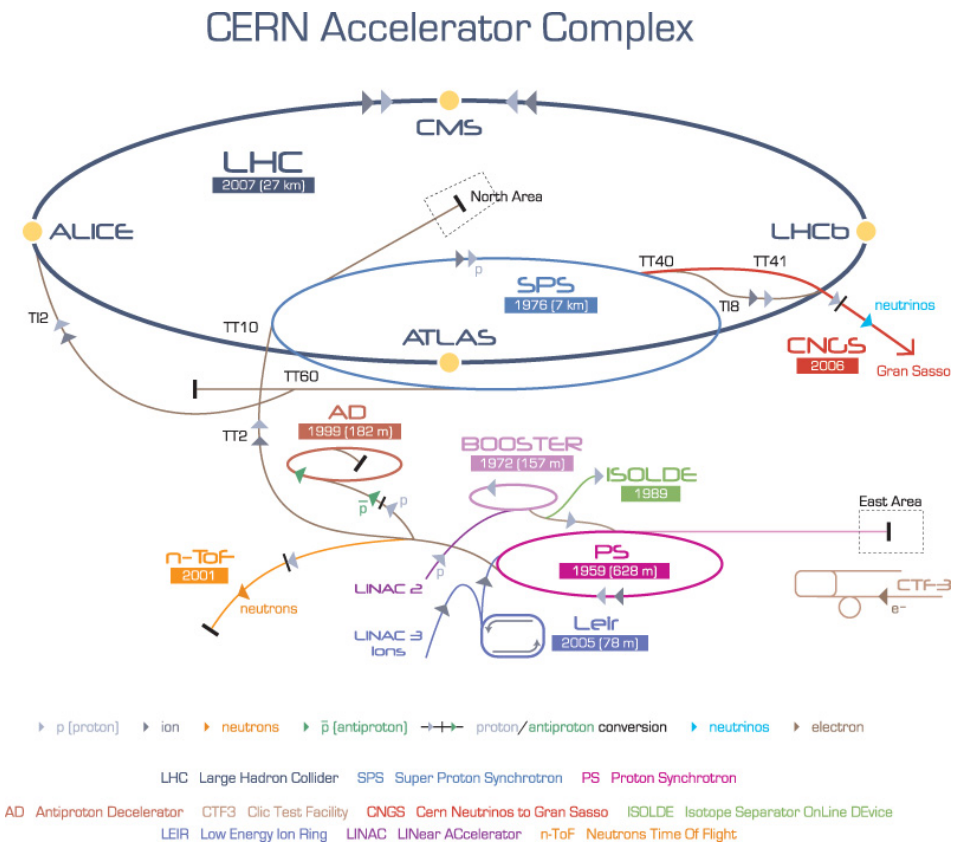

FIGURE 3.1: The accelerator complex at CERN which is used to inject the protons into the LHC. Figure obtained from [66].

3.1.2 LHC beam structure

The LHC operates with a radio frequency (RF) of 400 MHz and it can be filled once every 10 RF buckets. This leads to a 25 ns separation between proton bunches [67]. In principle, with this spacing between bunches it is possible to have a maximum of 3564 bunches in the ring at any one time. However, the actual number is lower for a number of reasons.

For a typical run in 2016 the SP injected a "train" of 72 bunches into the SPS. From here the SPS transferred 4 trains into the LHC, making 288 bunches in total (4×72) [68]. However, there are gaps between the bunches because there is a minimum kicker time for both the SP and SPS of 200 ns and 800 ns respectively. Thereby each train of 72 bunches must be separated by 200 ns (8 bunches) when injected into the SPS from the SP. An additional 32 empty bunches are caused when the SPS injects into the LHC. The process by which the LHC is filled with bunches is referred to as the "filling scheme". Another feature of most filling schemes is the inclusion of ~100 bunch gap for beam aborts. This is used to redirect the beam to the beam dump [69]. The total number of bunches that can be filled at the LHC after taking into account these limitations is 2808 at any one time.

3.1.3 Luminosity of the LHC

The luminosity, $\mathcal{L}$, of a particle collider such as the LHC relates R, the number of produced units per time and σ, the cross-section by [70],

$$\mathcal{L} = \frac{R}{\sigma}. \tag{3.1}$$

From equation 3.1 it can be seen that the units of luminosity are $m^{-2}s^{-1}$. The luminosity can be calculated from the following equation,

$$\mathcal{L} = \frac{n_b f_r n_1 n_2}{2\pi \Sigma_x \Sigma_y}, \tag{3.2}$$

where n_b is the number of bunches, f_r is the revolution frequency, $n_1 n_2$ is the bunch population product and $\Sigma_x \Sigma_y$ is the horizontal convolved beam and is defined in equation 5.14. Luminosity is covered in detail in Chapter 5 and so only a brief overview is given in this section.

3.1.4 Collisions inside the LHC

For the structure of this thesis it is convenient to define several concepts here. Firstly, the luminous region is the name given to the volume that the two counter-rotating proton beams intersect inside the detectors situated around the LHC ring. It is approximately ovoid in shape and is significantly longer in the direction of the beams than the direction transverse to the beam direction. Secondly, the hard scatter vertex is the name given to the proton-proton interaction with the highest energy in a given bunch crossing. Generally it is the only collision of interest as it has the potential to produce new high mass particles.

Finally, pileup is the name given to the additional proton-proton collisions that are not the hard scatter vertex. For all experiments at the LHC many of the subsystems have sensitivity windows longer than the time interval between proton-proton bunch crossings[1]. This results in many reconstructed objects being sensitive to the amount of pileup. An example of a pileup effect would be additional energy contributions in the reconstruction of a object. Pileup is discussed further in section 6.5.2.

3.2 The ATLAS detector

ATLAS stands for **A** **T**oroidal **L**HC **A**pparatu**S** and it is approximately cylindrical. ATLAS is 44 m long and 25 m in diameter. It is located at Point 1 on the LHC ring, which is near the main CERN site.

ATLAS contains many sub-detector systems that are optimised to measure different particle types. This can be seen in figure 3.2 which depicts a cutaway of the ATLAS detector. Starting from the outside of the detector and moving inwards one has the Muon Spectrometer (MS), responsible for measuring muon tracks as they leave the detector. Then we have the two calorimeters: the Hadronic Calorimeter (HCal) and the Electromagnetic Calorimeter (ECal) used for measuring hadronic and electromagnetic objects respectively. Closest to the beam-pipe lies the Inner Detector (ID) consisting of the Transition Radiation Tracker (TRT), the Semiconductor Tracker (SCT) and the Pixel Detector (PIX). These 3 are responsible for tracking charged particles near the beam-pipe.

[1] In ATLAS this interval was 25 ns for 2018

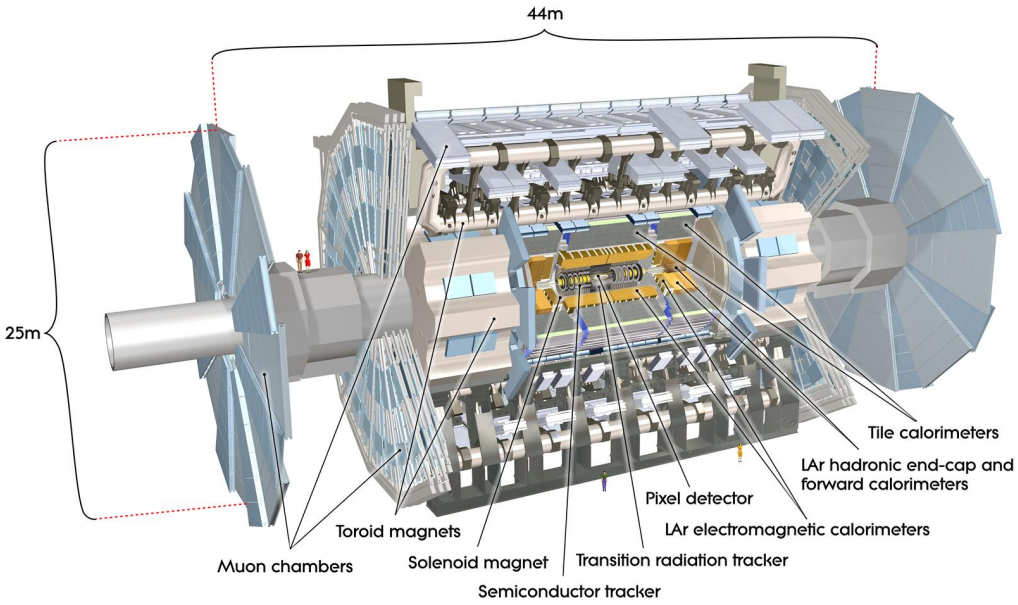

FIGURE 3.2: Cutaway view of the ATLAS detector. The dimensions of the detector are 25 m in height and 44 m in length. The overall weight of the detector is approximately 7000 tonnes. Figure obtained from reference [63].

3.2.1 Coordinate system

The ATLAS detector uses a right-handed coordinate system with the axes defined as follows: $\hat{x}$ is towards the origin of the LHC's ring; $\hat{y}$ is upwards, pointing away from the centre of the Earth and $\hat{z}$ is defined to be along the beam-pipe. The $\hat{x} - \hat{y}$ plane is referred to as the transverse plane.

The origin of the coordinate system is the nominal interaction point, where the protons collide. In addition, each point in the detector can be described using cylindrical coordinates, (r, θ, ϕ), where θ is the azimuthal angle around the bean lime ($\hat{z}$ direction) with $\theta = 0$ pointing along the $\hat{x}$ direction and ϕ is the polar angle with respect to the $\hat{z}$ axis.

Objects are defined by their 4-momentum, p^{μ},

$$p^{\mu} = \left(E, p_x, p_y, p_z\right), \tag{3.3}$$

where E is the particle's energy and $p_{x,y,z}$ is its momentum in the respective direction. As the initial momentum of the partons in the collision along the $\hat{z}$ axis is not known, the transverse momentum, p_T, is often used and is defined as,

$$p_T = p \cdot \sin\theta = \sqrt{p_x^2 + p_y^2}. \tag{3.4}$$

Additionally, it is often convenient to describe particles by their angle from the beam-pipe rather than using the Cartesian coordinates. It is convenient to make the following two definitions: rapidity, y, and pseudorapidity, η, defined as,

$$y = \frac{1}{2}\ln\left(\frac{E + p_z}{E - p_z}\right), \tag{3.5}$$

$$\eta = -\ln \tan \frac{\theta}{2}. \tag{3.6}$$

Differences in rapidity are also useful as they are invariant under Lorentz boosts along the $\hat{z}$ axis. Pseudorapidity is an approximation to rapidity that holds true if the particle's mass is negligible with respect to its momentum. Finally the geometrical distance between particles in the $\hat{\eta} - \hat{\phi}$ plane is usually given in terms of ΔR, where

$$\Delta R = \sqrt{(\Delta\phi)^2 + (\Delta\eta)^2}. \tag{3.7}$$

3.2.2 Detector components

The ATLAS detector can be broken up into three parts. These are the central region spanning $|\eta| < 1.4$, and the two end-caps spanning $1.4 < |\eta| < 4.9$. Each of these regions are broken up into several smaller detectors, the performance goals of which are given in table 3.1.

Sub-detector	Resolution	Coverage	Object
Inner Detector	$\sigma_{p_t}/p_t = 0.05\% \cdot p_t \oplus 1\%$	$\lvert\eta\rvert < 2.5$	Charged Particles
EM Calorimeter	$\sigma_E/E = 10\%/\sqrt{E} \oplus 0.7\%$	$\lvert\eta\rvert < 3.2$	e, γ, Jets
Hadronic Calorimeter	$\sigma_E/E = 50\%/\sqrt{E} \oplus 3\%$	$\lvert\eta\rvert < 3.2$	Jets
Forward Had. Calorimeter	$\sigma_E/E = 100\%/\sqrt{E} \oplus 10\%$	$3.1 < \lvert\eta\rvert < 4.9$	Jets
Muon Spectrometer	$\sigma_{p_t}/p_t = 10\%$ at $p_T = 1$ TeV	$\lvert\eta\rvert < 2.7$	Muons

TABLE 3.1: Performance goals of the detectors inside ATLAS [63].

3.2.3 Magnet systems

ATLAS contains four different magnet systems: one is a solenoid and is used in the inner detector; the other three are toroids with one located in the barrel region and the remaining two situated in each end-cap. The solenoid produces a field of 2.0 T and is responsible for bending the tracks of charged particles in the inner detector to allow for charge and momentum measurements. The toroids are used to further bend the tracks of muons to provide a more accurate momentum measurement for these particles. Each of these magnet systems will be covered in more detail in the sub-detector section in which they are used.

3.2.4 The inner detector

The inner detector (ID) is designed to measure the momentum and charge of charged particles [71, 72]. To allow for momentum measurements and charge identification the charged particles are bent by a superconducting solenoid magnet that produces a 2 T magnetic field. The charge can be defined from the direction of curvature and the momentum determined from the following equation [73],

$$p_{\mathrm{T}} = qBr_c, \tag{3.8}$$

where q is the charge, B is the magnetic field strength and r_c is the radius of curvature.

The ID spans the rapidity interval $|\eta| < 2.5$. The ID has a diameter of 2.1 m and a length of 6.2 m. There are three sub-detectors in the ID: the Semi-Conductor Tracker (SCT), The Silicon Pixel Detector, and the Transition Radiation Tracker (TRT). How these detectors are orientated spatially is shown in figure 3.3. The remainder of

this section will cover each of these detectors in the order of closeness to the proton beams.

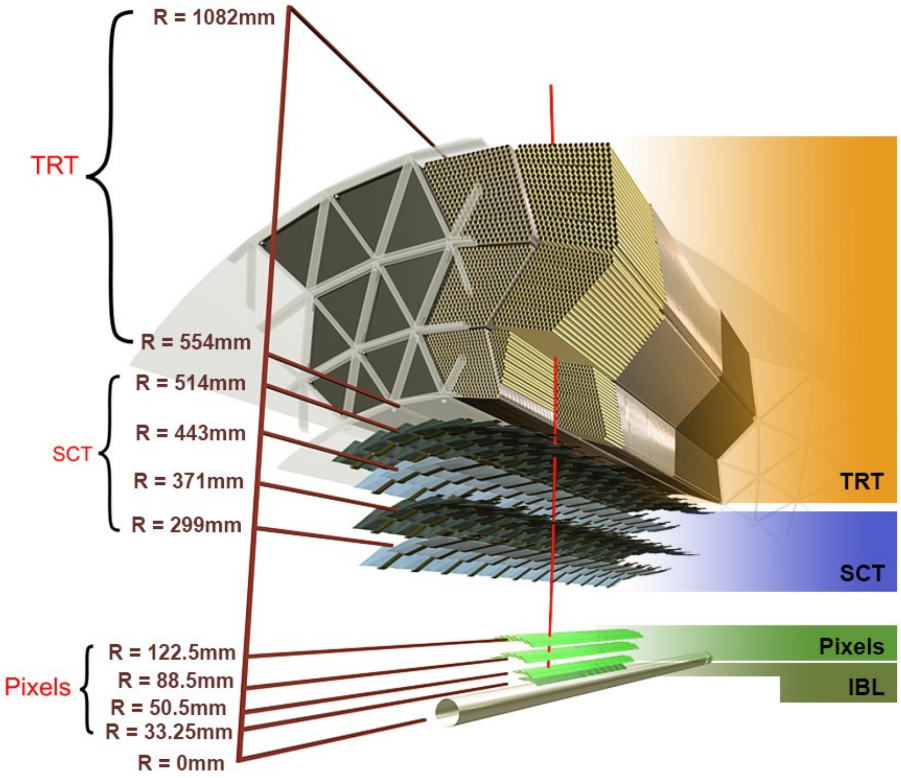

FIGURE 3.3: A cutaway of the ATLAS inner detector showing the three main sub-detectors, the IBL and their distances to the interaction point. Figure obtained from reference [74].

3.2.4.1 Silicon pixel detector

The silicon pixel detector comprises four cylindrical layers of silicon semi-conductor sensors, called pixels, along with three disks in each end-cap [75]. It covers the region $|\eta| < 2.5$. The layer nearest the beam-pipe, at a distance of 33 mm, is referred to as the Insertable b-layer (IBL) and it was added to ATLAS during the LS1 of the LHC to improve the resolution of the tracking system [76, 77]. It is made up of pixels with a size of 50 μm $\times$ 250 μm. All the other layers outside the IBL and the end-caps have a pixel size of 50 μm $\times$ 400 μm. The furthest layer from the beam sits at a radius of 122.5 mm. The whole of the pixel detector has 86.8 million readout channels.

The precision of the location measurements of particles by the silicon pixel detector is 10 μm in the $\hat{R} - \hat{\phi}$ plane and 70 μm in the $\hat{z}$ direction. Before the addition of the IBL it was 115 μm in the $\hat{z}$ direction. The combination of the smaller pixel size and distance to the beam results in more accurate measurements of the impact parameters, vertex reconstruction and the jet b-tagging. The IBL also contains newer technologies than the rest of the pixel system which allow it to withstand the harsh radiation close to the beam-pipe. This will allow the IBL to continue performing well as the innermost layer as the older pixel system layers degrade due to radiation.

3.2.4.2 Semiconductor tracker

The semiconductor tracker surrounds the pixel detector and employs a similar technology. The main difference is that instead of using silicon pixel sensors, larger sensors referred to as silicon strips are used. These strips are grouped into pairs which are glued back-to-back with a relative rotation of ± 20 mrad. This improves the resolution of momentum, impact parameter and vertex position and reduces the hit ambiguity.

The SCT spans a radius, r, of 30 cm $< r <$ 52 cm in the barrel region and covers $|\eta| < 2.5$. Additionally each of the end-caps contain 9 disks. The whole of the pixel detector has 6.3 million readout channels. The resolution of this sub-detector is 17 μm in the $\hat{R} - \hat{\phi}$ plane and 580 μm along the $\hat{z}$ axis. The resolution is worse in the $\hat{z}$ due to the fact that the strips are thicker in this direction.

3.2.4.3 Transition radiation tracker

The TRT is the outermost sub-detector in the ID. It uses a different method of detection technology to the previous detectors [78–80]. It covers the region $|\eta| < 2.0$, which is slightly less than the pixel and semiconductor trackers. Additionally it spans a radius of $55 < r < 108$ cm.

The TRT combines a drift tube tracker with transition radiation[2] detection, which assists with electron identification. The drift tubes, which are referred to as straws, are 4 mm in diameter and contain a tungsten wire running through the centre. There is a voltage applied between the straw and the wire. This is what causes the current to flow when an ionising particle passes through.

The TRT contains approximately 100,000 straws in the barrel region and 250,000 in the end-caps. These straws are filled with a gas mixture containing argon and xenon. These gases can be ionised by emitted transition radiation or when a charged particle passes through. This ionisation is then measured as a current in the wire which indicates a hit in that straw.

To encourage the particles to emit transition radiation photons, polyethylene fibres and polypropylene foil are placed between the straws in the barrel and end-caps respectively. Transition radiation is more likely to be emitted by a lower mass particle. This feature can be used for particle identification. The TRT signal output is categorised using a ternary output: zero, low-threshold and high-threshold. High-threshold events are generally caused by electrons due to their low mass.

The resolution of the TRT is 130 μm in the $\hat{R} - \hat{\phi}$ plane. The TRT does not provide any measurement along the $\hat{z}$ axis due to the fact the drift tubes are insensitive along the direction of the wire.

The TRT is to be removed as part the ATLAS Phase 2 upgrade program commencing in 2025. This is due to the fact that the high pileup in Run 4 of the LHC is expected to create occupancies of ~100% rendering the detector useless.

3.2.5 Calorimeters

Calorimeters measure the energy of particles that travel through them. There are two different types of calorimeters inside ATLAS: the Liquid Argon (LAr) and the Tile Calorimeters which cover the range up to $|\eta| < 4.9$, [81, 82]. The ECal uses LAr

[2] Transition radiation is a type of electromagnetic radiation which is emitted when a charged particle crosses the boundary between two different materials.

calorimeters whereas the HCal uses a combination of both. The Hadronic Calorimeter consists of three sub-detectors, the tile calorimeter, the LAr Hadronic end-cap Calorimeter (HEC) and the LAr Forward Calorimeter (FCal). The electromagnetic calorimeter consists of the electromagnetic barrel (EMB) and end-caps (EMEC). Figure 3.4 shows a cutaway of the ATLAS calorimeters.

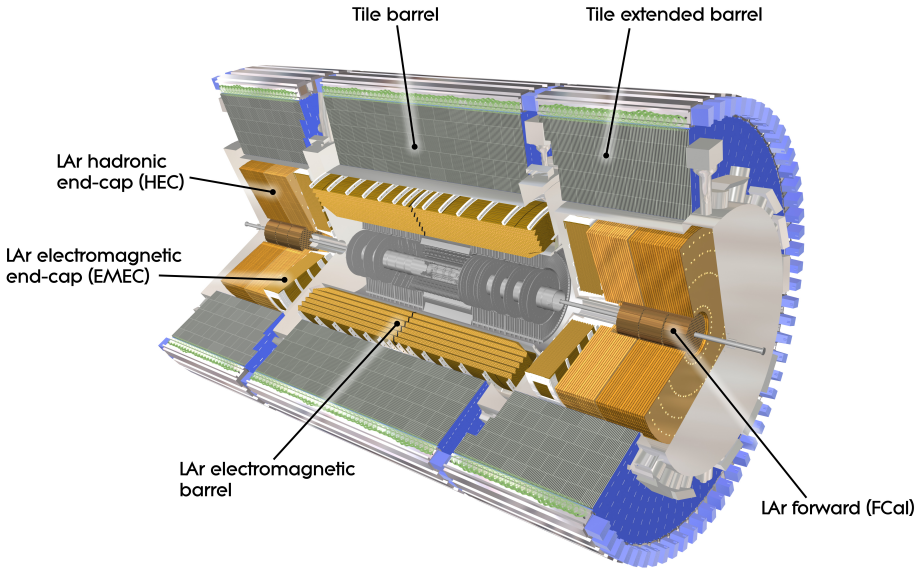

FIGURE 3.4: The layout of the ATLAS calorimeters. Figure obtained from Ref. [83].

Both of these calorimeters operate on the same general principle: an incoming particle initiates a particle shower as it passes through, and the resulting energy deposits are recorded. A particle shower is when a high-energy particle interacts with dense matter causing a cascade of secondary particles. Particle showers can be categorised as electromagnetic or hadronic depending on how the secondary particles are produced.

These calorimeters are categorised as sampling calorimeters as they contain alternating layers of an absorbing material and an active material. The reason for this multi-layered design is that it enables a shorter shower length than if only an active material were used.

The absorbing material is designed to induce particle showers and the active material is used to measure the energy of the shower. These showers ionise the active material and this in turn releases electrons which are accelerated by an electric field and are picked up by electrodes. As the total energy measured by the electrodes is much less than the total energy of the shower, it must be calibrated by comparing to test beam data with a known particle energy.

It is often convenient to talk about materials in terms of their radiation length. The radiation length, X_0, is defined to be the mean distance that a particle's energy takes to fall to $1/e$ of its original value. The relation between the particle's energy and the distance it has travelled is given by,

$$E(x) = E_0 e^{-x/X_0}. \tag{3.9}$$

From equation 3.9 it can be seen that the majority of the energy is therefore deposited in the first few radiation lengths. The radiation length of a given material is in general much smaller for electrons and photons than for hadrons. This allows the calorimeters to be optimised so that electrons and photons deposit all their energy in the electromagnetic calorimeter, and the hadrons do the same for the hadronic calorimeter.

3.2.5.1 Liquid argon calorimeter

There are 4 sub-detectors that are LAr calorimeters: the electromagnetic barrel and end-caps, and the hadronic end-cap and forward calorimeter. All 4 of these calorimeters are temperature controlled to 90 K by an enclosing cryostat.

The EMB covers the barrel region of the detector with a range of $|\eta| < 1.475$ and the two EMECs cover the end-cap region for the range $1.375 < |\eta| < 3.2$. These calorimeters comprise accordion shaped absorbers of steel-backed lead. The thickness of the lead varies depending on its location inside the detector and ranges between 1.1-2.2 mm. The liquid argon is used as the active material. This was chosen due to radiation-hardness requirements. As the LAr radiation length is too high to stop the electromagnetically interacting particles in a reasonable distance, lead is used to slow down the particles as its radiation length is approximately 20 times smaller than LAr. The thickness of the EMB is greater than 22 radiation lengths in the barrel region and 24 for the EMEC.

There are 4 layers in the EMB and EMEC. The first is a pre-sampler that is used to correct for the energy that is lost in the dead material and the ID. The next three layers in the ECal have different cell-structures in the $\hat{\eta} - \hat{\phi}$ plane. The layer closest to the beam-pipe has cell sizes of 0.003×0.1 in $\hat{\eta} - \hat{\phi}$, which is the finest granularity. The next two layers have the same granularity of 0.025×0.025 in $\hat{\eta} - \hat{\phi}$. The second layer is primary used to measure the shower energy precisely, whereas the outer (third) layer is used to constrain the tails of the EM showers. Both the sizes and the accordion shapes of these layers can be clearly seen in figure 3.5.

The HEC is located directly behind the EMEC in the end-caps and covers a range of $1.5 < |\eta| < 3.2$. Instead of lead it uses thick copper plates as the absorber material between 25-50 mm in thickness. The other main difference is that the HEC cells are rectangular, rather than accordion shaped. The FCal is used to provide coverage for hadronic jets in the range $3.2 < |\eta| < 4.9$. There are three layers in each of the FCal end-caps. The first is designed as an EM calorimeter with copper absorbing plates. The next two layers are designed as hadronic calorimeters and so have tungsten absorbers.

3.2.5.2 Tile calorimeter

The tile calorimeter is positioned just outside the EMB. It measures the residual energy from the hadrons which will have deposited a fraction of their energy in the LAr calorimeter if they are charged. It is constructed from scintillating polystyrene tiles and steel absorbing layers. A traversing hadron interacts with the nuclei in the steel causing a particle shower. This shower produces ultraviolet photons in the scintillating medium which are picked up by wavelength shifting fibres and then passed on to PMTs. The light read by the PMTs is proportional to the initial energy deposits of the hadron.

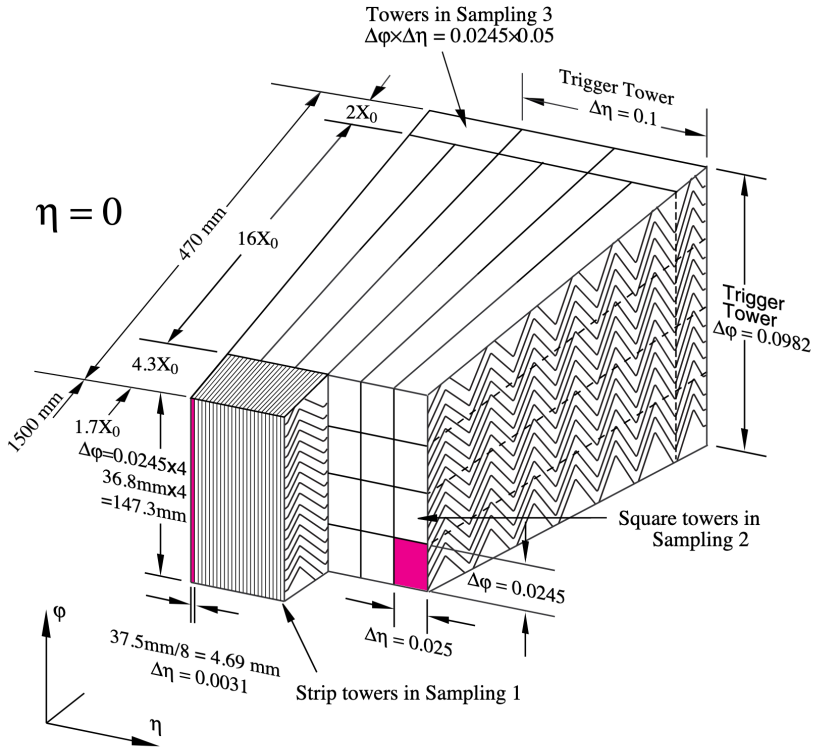

FIGURE 3.5: Diagram of the cells within the LAr barrel. Figure obtained from reference [81].

Again this calorimeter is split into a barrel region, $|\eta| < 1.7$, and an end-cap, $1.5 < |\eta| < 3.2$. The HCal has a much lower granularity then the ECal, and its granularity is 0.1×0.1 in $\hat{\eta} - \hat{\phi}$ and 0.2×0.2 in $\hat{\eta} - \hat{\phi}$ in the barrel region and end-caps respectively. The HCal is approximately 8-12 hadronic interaction lengths thick[3]. This is enough to stop all but the most energetic of hadronic showers.

3.2.6 Muon spectrometer

The muon spectrometer (MS) is a high-resolution spectrometer which provides tracking for muon reconstruction within $|\eta| < 2.7$ [84]. It has two functions: firstly it is used to trigger on events containing muons and secondly it is used to measure the muons' trajectories precisely, and from this their momentum using equation 3.8. The MS comprises three barrel layers and three wheels placed in each end-cap and is situated within the toroid magnet. There are 4 different main technologies that are used for triggering and momentum measurement:

- **Monitored Drift Tubes (MDT)** span the whole η range. They are used to take measurements of the muons' trajectories with a precision of 60-80 μm. Each MDT is made from an aluminium tube filled with an Argon and xenon gas mixture that is ionised when a muon passes through. Once the gas is ionised by the muons, the ions drift towards and are collected by a central tungsten-rhenium anode wire which is kept at a potential. This will register a hit which

[3]The hadronic interaction length is the mean distance over which the energy of a hadron is reduced to $1/e$ of the initial energy.

provides precision measurements of the track coordinates. They have a long drift time of approximately 700 ns.

- **Cathode Strip Chambers (CSC)** span the forward region, $|\eta| > 2$, in the end-caps. They use a similar technology to the MDTs, however, they have a strip with a mesh of anode wires running in parallel instead of a single wire. The gas used here is an argon-CO_2 mixture.
- **Resistive Plate Chambers (RPC)** are gaseous parallel electrode-plate detectors and are situated in the barrel region. The RPC is primarily used an as input to the ATLAS trigger systems as they provide a much faster response than the MDTs. They comprise two plastic resistive plates, separated by 2 mm and filled with a gas mixture. In this case the gas mixture is $C_2H_2F_4$, Iso-C_4H_{10} and SF_6. An electric field between the plates allows avalanches[4] to form along the ionised tracks towards the anode, which is read out by capacitive coupling to metallic strips.
- **Thin Gap Chambers (TGC)** are the RPC end-cap equivalent, consisting of two rings. They contain a different gas mixture to the PRCs which is CO_2 and n-pentane.

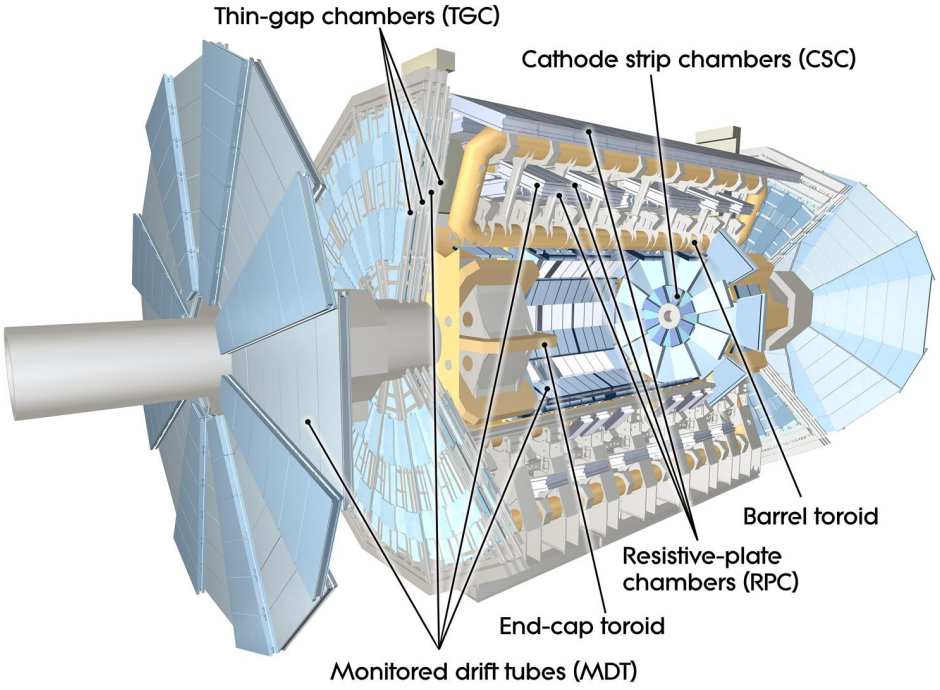

FIGURE 3.6: A cutaway of the muon spectrometer. Figure obtained from Ref. [85].

3.2.7 Forward detectors

There are several sub-detectors separate from the main body of ATLAS [86]. A diagram of their positions can be found in figure 3.7.

[4] An avalanche is when a electron collides with other atoms in a transmission medium and ionises them after experiencing a large acceleration by an electric field.

LUCID[5] is specifically designed to measure the luminosity delivered to ATLAS. It is situated 17 m from the interaction point on each side down the beam-pipe [87]. LUCID is made of photomultiplier tubes attached to quartz fibre bundles which are used to detect Cherenkov radiation. This radiation is created when charged particles pass through the quartz. The quantity of radiation produced is proportional to the number of proton-proton interactions inside ATLAS. Thereby LUCID can be used to measure the instantaneous luminosity.

The Beam Conditions Monitor (BCM), comprises four 8×8 mm^2 diamond sensors arranged in a cross pattern around the beam-pipe located 1.84 m either size of the IP [88]. It was originally designed to monitor the background levels in the beam-pipe in case the radiation levels got high enough to damage ATLAS.

The Zero Degree Calorimeter (ZDC) sits 140 m from ATLAS. It is used to measure the fraction of neutral particles (photons/neutrons) inside the proton beam before and after the beams have crossed. The ALFA detector uses Roman Pots to detect protons at angles very close to the beam-line, and is situated 240 m from the interaction point down the beam-pipe. In dedicated runs it is used to measure the total and elastic proton-proton cross-section. The final forward detector covered in this section is the AFP detector, which was installed in Run 2 and is used to look at diffractive physics in low luminosity runs [87].

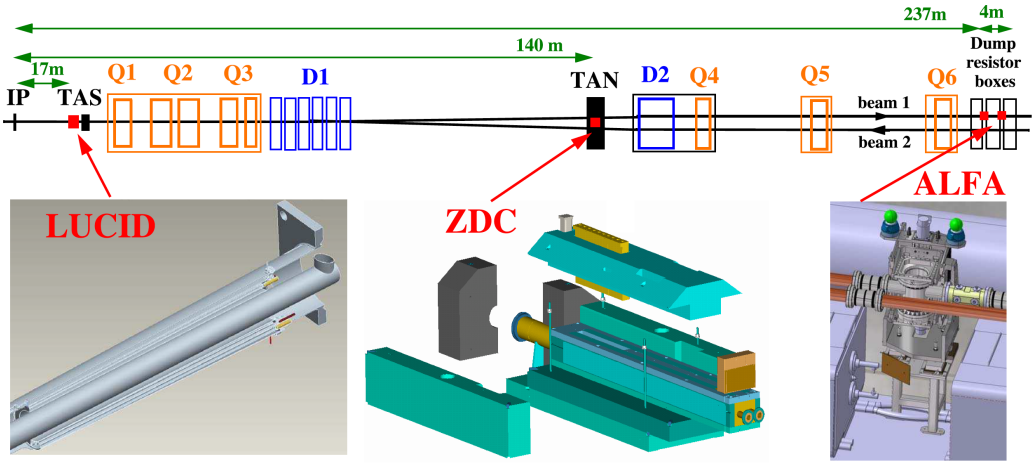

FIGURE 3.7: Location of ATLAS's forward detectors. Figure obtained from Ref.[86]. In this diagram ATLAS is situated at the far left side of the figure where the interaction point (IP) is marked.

3.2.8 Trigger system and data acquisition

During normal running conditions the LHC collides protons at a rate of 40 MHz [89]. A single event in ATLAS is approximately 2 MB of data and so it is impossible to write every event that ATLAS measures to a disk. To reduce the number of events that ATLAS records to a manageable level, only the events with the most interesting physics are saved. This is achieved by the use of a two stage triggering system that decides which events to keep. The level-1 (L1) triggers are applied first and then the high level triggers (HLT) are used in the final selection of events to be written to disk.

[5]LUCID stands for the LUminosity measurement using Cerenkov Integrating Detector.

L1 triggers make a decision if an event should be written to disk within ~3.5 μs. They are a hardware-based system and primarily use information from the calorimeters and the muon spectrometer. For Run 2, the L1 triggers reduce the rate of possible events to save to disk to a maximum of 100 kHz. Several different L1 triggers such as the L1 calorimeter and the L1 muon trigger are used to provide an input to the L1 Central Trigger, which was commissioned during 2016 [90]. This L1 Central Trigger makes a decision based on the geometric and kinematic association between the triggered objects.

Events that pass the L1 trigger selection are buffered in the Read-Out System (ROS) [91]. This buffered data is then used by the HLT to make a final decision on whether the event should be saved. In this step additional information is used, such as tracking information from the inner detector which would be too slow to use in the L1 triggers. Most of the HLT triggers initially do a faster first-pass reconstruction and then a more detailed reconstruction is performed on the events that pass the first one. This is done as many of the events will fail the faster first-pass reconstruction and so this allows the trigger to process events faster.

The HLTs cover all possible signatures relevant to the physics program at ATLAS. These triggers are set to as high a rate as possible within the constraints of bandwidth. Additionally ATLAS uses a large number of support triggers which are used for measuring the trigger efficiencies and detector calibrations. Some of the HLT triggers are pre-scaled. Pre-scaled triggers are ones where only a fraction of the events that pass the trigger are saved. This is done so that a single trigger only takes a small fraction of the total bandwidth.

3.2.9 Dead Time

There are a finite number of events that ATLAS can process per unit time. This causes dead time, where the detector cannot save or process any more events but it is still running normally and collisions are still occurring. There are two main causes of dead time. The first is called simple dead time which is caused by the L1 trigger selecting an event, as it takes about 100 ns (4 bunch crossings) for the readout from the detector to transfer to the front end buffers so that the HLT can analyse the event. The second is complex dead time which is caused by the fact that these the buffers for the individual sub-detectors can be filled to capacity.

3.2.10 Data Processing

Once the data acquisition system has decided to keep an event it is written to disk. From here, after the run has finished, it is processed by the Tier-0 computing facility at CERN. This is where the raw output from the detector is transformed into the physical objects used for analyses. More detail on this process can be found in Chapter 4. An express stream, containing a subset of the full dataset is first run through a calibration loop. This process is designed to calculate the geometry and conditions of the detector to allow the whole dataset to be processed.

After this calibration, the entire run has the object reconstruction algorithms applied to produce objects such as muons or jets. This new reconstructed dataset is called Analysis Object Data (xAOD). The final step after producing the xAOD is to produce the Derived Analysis Object Data (DxAODs) from the xAODs. DxAODs are always subsets of the xAOD and used for efficiency as they are smaller in size. A

specific DxAOD will contain all events with a process that a given analysis is looking for by applying a very loose selection. For example the DxAOD called STDM3 selects all events containing at least two electrons or muons and is used in chapter 7.

Chapter 4

Event reconstruction

Many of the particles that can be produced inside ATLAS have dedicated algorithms that use the readout of the detector to calculate the particles' properties, such as the 4-momentum[1]. This chapter will summarise the main algorithms used by ATLAS. Sections 4.1 and 4.2 cover the track and vertex reconstruction respectively. Then sections 4.3-4.5 cover lepton reconstruction. Jet reconstruction is then covered in section 4.6. Finally section 4.7 covers missing transverse energy.

4.1 Track reconstruction

Tracks are the name given to the line a particle traced through the ATLAS detector. The path traced by a charged particle inside ATLAS is bent by the magnetic field produced by the solenoids in the ID. They are reconstructed using the signals from the inner detector using a specialised algorithm. This algorithm has three main steps, which in order are: clusterization, track finding, and ambiguity solving [74].

Clusterization is designed to group together the hits from the SCT and Pixel detectors using a connected component analysis. These clusters are constructed so they represent a single point in space that intersected with the particle's path through the detector. As the SCT comprises a two layered strip structure (See section 3.2.4.2) the clustering algorithm combines each of the two layers to make single point in space. At this stage in the track reconstruction algorithm it is possible to have clusters that overlap due to multiple particles passing through a single sensor. These merged clusters are identified and managed by the clusterization algorithm.

Track finding starts with the formation of track seeds from sets of three of the space-points from the clusterization stage. Three sets are chosen as this is the lowest number that allows for a track curvature measurement. Then the impact parameters[2] are estimated by assuming the particle travels freely in a uniform magnetic field. Then selection criteria are applied to the track seed to ensure its quality. These criteria take into account the momentum and impact parameters. Additionally there is a criterion that the preliminary track crosses at least one more space-point than for the clusterization algorithm. The final step to track finding is the implementation of a combinatorial Kalman filter [92] which builds the track candidates from the preliminary tracks. It achieves this by adding more space-points to the track. At this stage it is possible for the filter to fit more than one track candidate to the same preliminary track. This can happen if there are two or more sets of space-points that are compatible with the preliminary track.

Ambiguity solving is the stage where the tracks are ordered by a track score describing its likelihood of being a well fitted and real particle track. This track score is

[1] The 4 momentum of a particle is defined to be $p^{\mu} = (E, p_x, p_y, p_z)$.

[2] Impact parameters quantify the the distance of closest approach to the collision.

calculated for each track candidate individually using the impact parameters. Any additional space-time points after the first three increases the track score proportionally to the resolution of the detector section that created the cluster. The reverse is also true, if a track candidate passes through a detector section and there is no hit the track score is reduced, using the same proportionality. The quality of the track candidate fit, χ^2, is also used as an input so one promotes high quality fits in the selection. The final input to the track score is the logarithm of the track's momentum as this suppresses tracks that have wrongly assigned clusters as these tracks typically have low momentum. Track candidates are accepted if the track score calculated by the ambiguity solver is high enough and the track also passes the basic set of quality cuts. The final criteria is that a maximum of only two tracks are allowed to share any one space-point and so the tracks with the two highest track scores are selected.

Once the tracks have been reconstructed using this algorithm the hits in the TRT can also be used to further refine the fit through a process called TRT track extension [93]. Here, the tracks that passed the ambiguity solving stage search for compatible sets of measurements from the TRT. This algorithm does not modify the track from the ambiguity solving stage, instead it extends the track further through the ATLAS detector.

The efficiency of reconstructing tracks is strongly dependent on $|\eta|$. This is because the quantity of material, and thereby the possible energy losses due to interaction with it, correlates with $|\eta|$. Tracks with a higher momentum have a higher reconstruction efficiency. This efficiency increases up to $85-90\%$ when the p_T of the tracks is greater than 5 GeV [75].

Finally there are two main algorithm types used in the reconstruction of tracks in ATLAS and only one of them is described in this section. The other algorithm starts with the information in the TRT and works "outside-in" from there. This approach is not covered in detail in this thesis as the process is very similar to what was described above.

4.2 Vertex reconstruction

A vertex is the name given to the location of a proton-proton interaction inside the ATLAS detector [94]. The vertex reconstruction algorithm is divided into two stages: vertex finding and vertex fitting [95]. Vertex finding uses a pattern recognition process where reconstructed tracks are associated to vertex candidates. The fitting stage then is responsible for reconstructing the vertex position.

Vertex reconstruction uses the tracks as the input to start. To begin the vertex reconstruction, a seed position for the first vertex is calculated. The tracks surrounding this seed are then used to calculate the vertex position using an iterative χ^2 minimisation. During each iteration, the tracks that have the worst fit have a lower weight associated to them when finding the vertex position in the next iteration. This individual track weight, $\omega(\hat{\chi}^2)$, is calculated according to,

$$\omega(\hat{\chi}^2) = \frac{1}{1+\exp\left(\frac{\hat{\chi}^2-\chi^2_{cutoff}}{2T}\right)}, \tag{4.1}$$

where $\hat{\chi}^2$ is the three dimensional χ^2 value for the compatibility of the current vertex position and the closest approach of the track. χ^2_{cutoff} is a constant that defines for what value of $\hat{\chi}^2$ the weight becomes equal to 0.5. T is the "temperature" and it controls how smooth this weighting procedure is. A low value of T results in

equation 4.1 approaching a step function, whereas for large values of T equation 4.1 flattens out, losing its $\hat{\chi}^2$ dependence. As this iterative procedure is applied, the value of T is progressively decreased to avoid a convergence in a local minima.

After this process converges on a vertex position, the tracks are incompatible if they lie more than seven standard deviations away from the fitted vertex and they are therefore removed. They are then available to be used in the determination of the next vertex, whereas the tracks that were fitted to the vertex are removed from further fits. This procedure is then repeated until all tracks have been associated to a vertex or no further vertices can be found.

The efficiency of reconstructing a vertex is dependent on the number tracks associated with the vertex. In figure 4.1 it can be seen that in the absence of pileup, once a vertex has five or more associated tracks its reconstruction efficiency is ~1. Vertex reconstruction is greatly complicated by pileup and this is covered in Chapter 6.

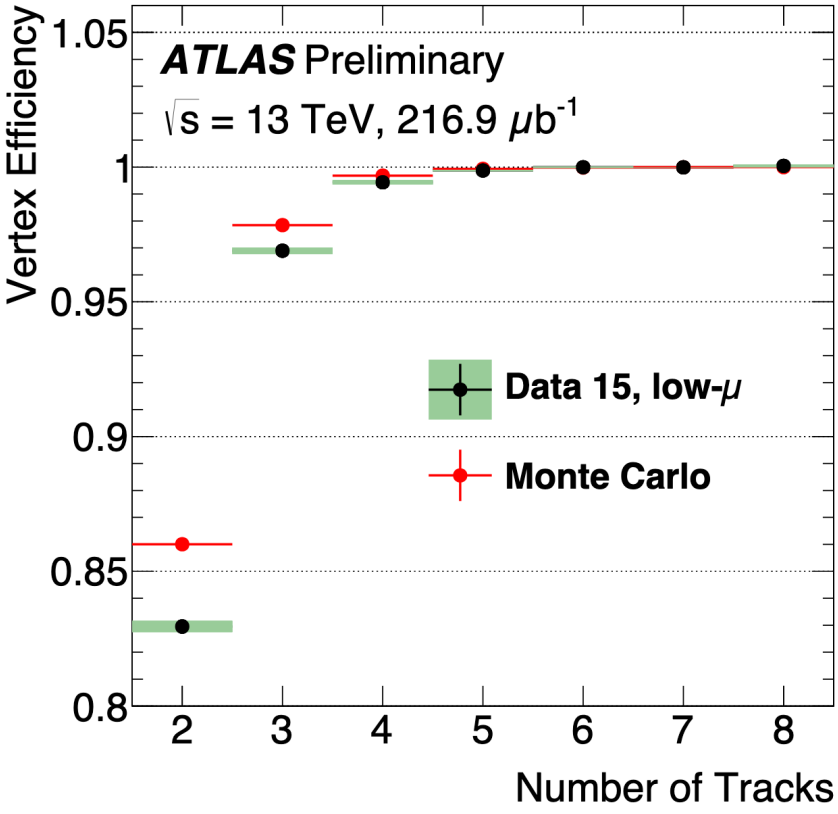

FIGURE 4.1: Efficiency of vertex reconstruction as a function of the number of tracks in the low-μ data. Figure obtained from Ref. [96].

4.3 Electron and photon reconstruction

Electrons produced inside ATLAS will pass through the inner detector and deposit their remaining energy in the ECAL. Figure 4.2 depicts the path an electron or photon takes inside ATLAS. Clusters of energy in the EM calorimeter along with an associated track from the ID are used to reconstruct the electron [97].

To obtain seeds the clustering algorithm uses a sliding-window of size 3×5 calorimeter cells in $\eta \times \phi$ to find regions in the calorimeter with a high local amount

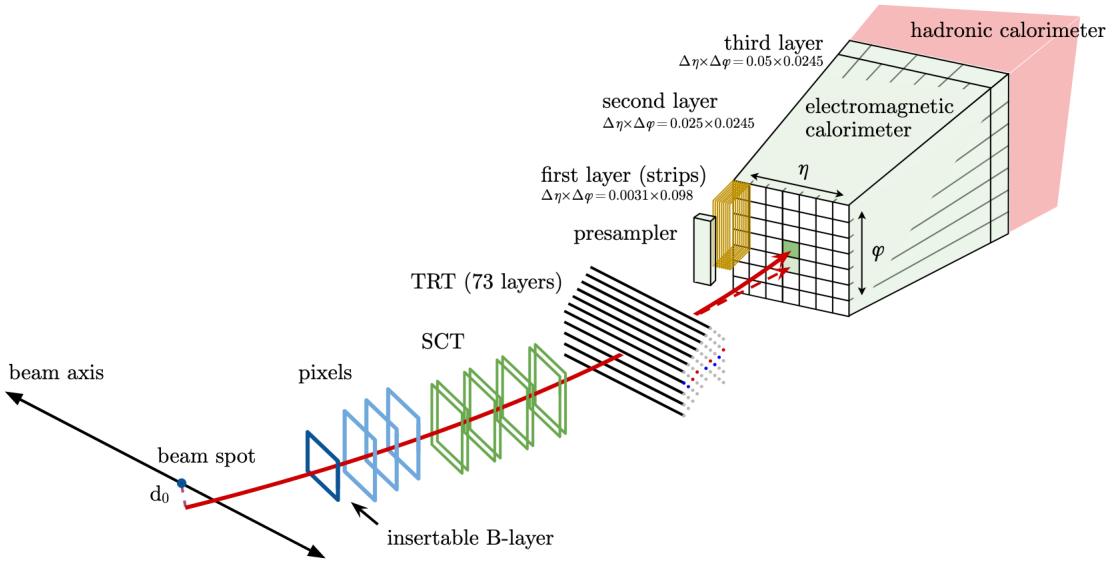

FIGURE 4.2: Schematic diagram of the path an electron or photon travels through the ATLAS detector. The red line shows the path of the electron which passes through the pixel detector, the SCT, the TRT and the ECAL. The red dashed line shows the path a photon would take. Figure obtained from reference [97].

of transverse energy, E_T [98]. If two clusters overlap the highest energy cluster of the two is kept if the E_T is within 10 % of each other, otherwise the cluster with the highest E_T in the central tower is kept.

Once these seeds have been found, a track (see section 4.1) is associated to any cluster with an E_T greater than 2.5 GeV. If a track cannot be fitted it is then considered to be a photon candidate, and so is no longer considered in this thesis. The criteria for matching a track to a cluster is shown in equation 4.2 and 4.3 below,

$$|\eta_{cluster} - \eta_{track}| < 0.05, \tag{4.2}$$

$$-0.10 < q \times \Delta\phi_{cluster,track} < 0.05, \tag{4.3}$$

where q is the particle's charge. If more than one track passes this selection criteria, a track is selected by another algorithm that factors in the centre of each of the cluster seeds with respect to the candidate track's parameters. If a track is found the clusters are re-calculated with a sliding-window size of 3×7 or 5×5 units in $\eta \times \phi$ in the barrel region or end-caps respectively. Finally tracks with a calorimeter cluster close by are re-processed with a Gaussian-sum filter to account for bremsstrahlung effects [99]. Once identified the 4-momentum of the electron can be derived from the energy in the ECAL cluster and the $\eta \times \phi$ of the associated track. This is calibrated using simulation [100, 101].

4.3.1 Electron identification

Once the reconstruction algorithm has been performed on the electron candidates a multivariate likelihood algorithm is used [97, 102]. This algorithm combines the track information from the TRT along with the calorimeter information, such as shower shape, to create a likelihood value for the electron candidate. This algorithm

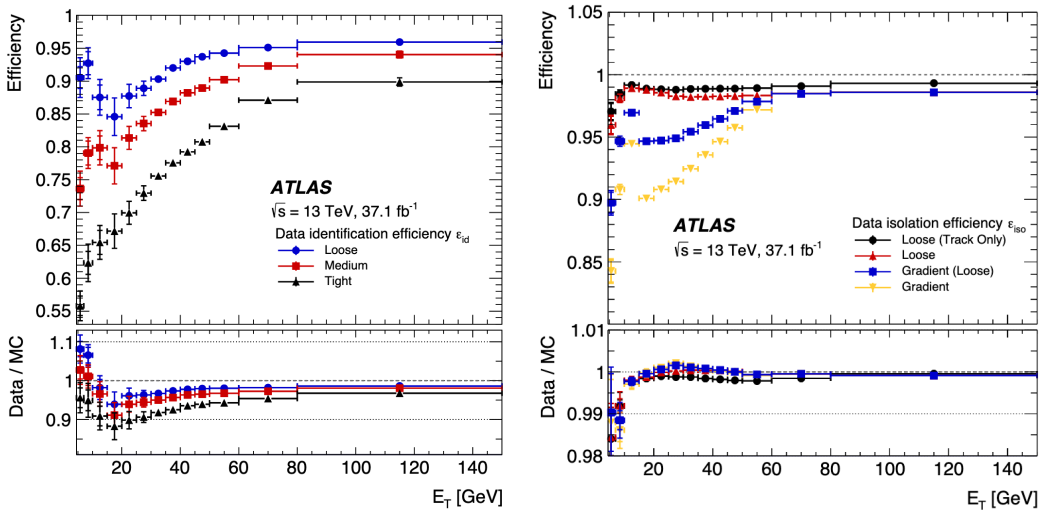

FIGURE 4.3: The measured likelihood (left) and isolation (right)electron efficiencies in $Z \rightarrow ee$ events per working point as a function of transverse energy. The bottom panel shows the ratio of data to simulation. Figure obtained from reference [97].

provides four working points as each physics analysis has its own requirements for performance. The four categories are `VeryLooseLH`, `LooseLH`, `MediumLH`, and `TightLH`. The tighter electron working points are subsets of the looser selections. Figure 4.3 shows the efficiencies for all the working points bar `VeryLooseLH` as a function of E_T.

4.3.2 Electron isolation

Electron isolation is a measure of how many additional particles are in the area surrounding the electron. Most signal electrons, for example electrons produced from a W boson decay, will have a small number of particles nearby [97]. The opposite is true for background electrons from sources such as photon conversion or jets. In these cases the electrons are produced in association with other particles. The fact that signal electrons are more isolated than their background counterparts allows one to reject background electrons by considering the electron's isolation.

To calculate electron isolation one constructs a variable that quantifies the energy surrounding an electron in a cone of a specific radius, ΔR, around the electron. This needs to be done separately for track-based and calorimeter-based isolation.

For track-based isolation one can calculate the sum of track p_{T} within a cone centred on the electron. The selection criteria for the tracks is that they must have a $p_{\mathrm{T}} >$ 1 GeV, be associated to the same vertex as the electron, and to have passed some basic quality requirements. Finally, any particles originating due to bremsstrahlung radiation are considered part of the original electron and so are also not counted in the sum. The cone used for the track-based isolation is of variable size and is defined to be,

$$\Delta R = \min\left(\frac{10\mathrm{GeV}}{p_{\mathrm{T}}}, R_{max}\right), \tag{4.4}$$

where R_{max} is defined to be the largest cone size allowed, which is typically 0.2.

Calorimeter-based isolation is a little more complicated than track-based as one does not have a discrete set of tracks to work with. Instead, as the energy deposits in the calorimeters clusters have a finite size, it is possible for a cluster to lie partially

outside the cone. To account for this, topological cluster [103] seeds are created using any calorimeter cell with a recorded energy four times larger than the noise-level of the cell. This seed is then extended to include all cells that record an energy of twice the noise-level of the respective cells. This process is repeated until there are no more adjacent cells that have an energy double that of the background noise-level. The isolation cone can then be calculated as the sum of E_T for all selected cells whose centre of mass fall inside a cone of $R < 0.2$ around the electron. Finally the energy deposited by the electron into the calorimeters is removed from the sum by subtracting all cells within a rectangle around the electron.

Higher energy electrons will generally have a higher energy in the cone surrounding them. To account for this, one defines relative isolation as the ratio of the energy in the cone to the p_{T} of the electron. As for the electron identification, there are four main working points for this algorithm: `Loose`, `LooseTrackOnly`, `Gradient` and `GradientLoose`. `Loose` and `LooseTrackOnly` have a fixed efficiency across electron's p_{T} and η distributions, the difference being that `LooseTrackOnly` does not use the information from the calorimeters. `Gradient` and `GradientLoose` instead have a p_{T}-dependent fixed efficiency that is uniform in η. Figure 4.3 shows the efficiencies for the four main working points as a function of E_T.

4.3.3 Electron efficiencies

The electron identification, reconstruction and isolation efficiencies are measured in J/ψ and $Z \to ee$ events using a tag and probe method. One electron must pass the tightest requirements (the tag) for the event to be tagged, then the second electron (the probe) can be selected using the requirement that the invariant mass of the dilepton pair matches the J/ψ or Z. This is done to avoid a bias on the measured quantities of the second lepton. The probe electron can then be used to measure the efficiencies. This method is used to calculate scale factors dependent[3] on η and/or p_T.

4.4 Muon reconstruction

Muon reconstruction primarily uses the Muon Spectrometer, however, it also uses tracking information from the ID [104, 105]. Muons in the ID are reconstructed like any other track from a charged particle and this is covered in section 4.1.

As described in section 3.2.6 the MS has four different detector systems. Each of these has separate algorithms to collect the hits as the muons pass through them. The track reconstruction in the MS starts with a search for hit patterns inside each of the muon chambers to form segments. A muon candidate is then created by taking all the segments in the middle layer and attempting to fit a track from this to the inner and outer layers. This is performed using a combinatorial search. To be selected at this stage a track is required to be fitted to at least two of the three layers, unless the track falls inside the transition region between the barrel and end-caps where candidates with only one layer are accepted. An overlap removal algorithm is used to decide which tracks to keep when multiple tracks are fitted to the same segment. The final stage is to perform a global χ^2 fit with each track candidate from the ID.

After this first stage the tracks from the ID and the MS need to be combined. There are 4 different reconstruction algorithms available to be used:

[3] A scale factor (SF) is used to correct the simulated data back to real data by applying a an additional scale to the weight of each simulated event.

- **Combined (CB):** CB muons use the information from the ID and the MS. The first step is to extrapolate the tracks in the MS back to the ID. Then a combined track can be fitted using both the ID and the MS, this allows one to add and/or remove hits to improve the quality of fit. Then the algorithm fits a track extrapolated from the ID to the MS.
- **Segment-tagged (ST):** ST muons use a combination of the ID and a track segment of the MS. This is primarily used for muons with a low momentum that only enter into one layer in the MS and can also be used to recover identification efficiency for regions where there is a low coverage in the MS.
- **Extrapolated (ME):** ME muons are identified in the forward region of the detector ($2.5 < |\eta| < 2.7$) and so cannot use the tracking information from the ID. These muons are reconstructed using a MS track which originates at the IP.
- **Calorimeter-tagged (CT):** CT muons can be reconstructed for $|\eta| < 0.1$. This is done because the sensitivity of the MS is low due to the detector layout. These muons are reconstructed using the ID tracks and a calorimeter signature consistent with a minimally ionising particle.

The CB muons are prioritised over the ST and the CT muons as CB muons generally calculate a better measurement of the muon's properties. The ME algorithm does not compete with the other 3 algorithms as it has a different acceptance in η.

4.4.1 Muon identification

As for the electrons in section 4.3.1 the muon candidates are classed by their likelihood to be a physical muon. This identification is designed to select signal muons while rejecting backgrounds like pions and kaons. Three variables are used in this selection for CB muons.

1. The difference between the value of charge to momentum obtained by the ID and the MS independently of each other divided by the errors added in quadrature.
2. The difference between the value of p_{T} obtained by the ID and the MS independently of each other divided by the p_{T} obtained from the combined track.
3. The χ^2 of the combined ID and MS track fit.
4. The number of hits within the ID.

There are four muon identification working points: `Loose`, `Medium`, `Tight` and Highp$_{\mathrm{T}}$. Highp$_{\mathrm{T}}$ is used for high mass searches, such as W' and will not be discussed further in this thesis. `Tight` muons only use CB muons that pass the `Medium` selection. `Medium` muons are the ATLAS recommendation and only include CB and ME tracks that pass `Loose`. `Loose` muons use all 4 muon types listed in section 4.4, however the CT and ST muons are restricted to $|\eta| < 0.1$. Figure 4.4 depicts the efficiencies for three of these WPs as calculated in $Z \to \mu\mu$ events.

4.4.2 Muon isolation

The muon isolation is calculated in a very similar way to the method for electrons outlined in section 4.3.2. The main difference for the track-based isolation variable

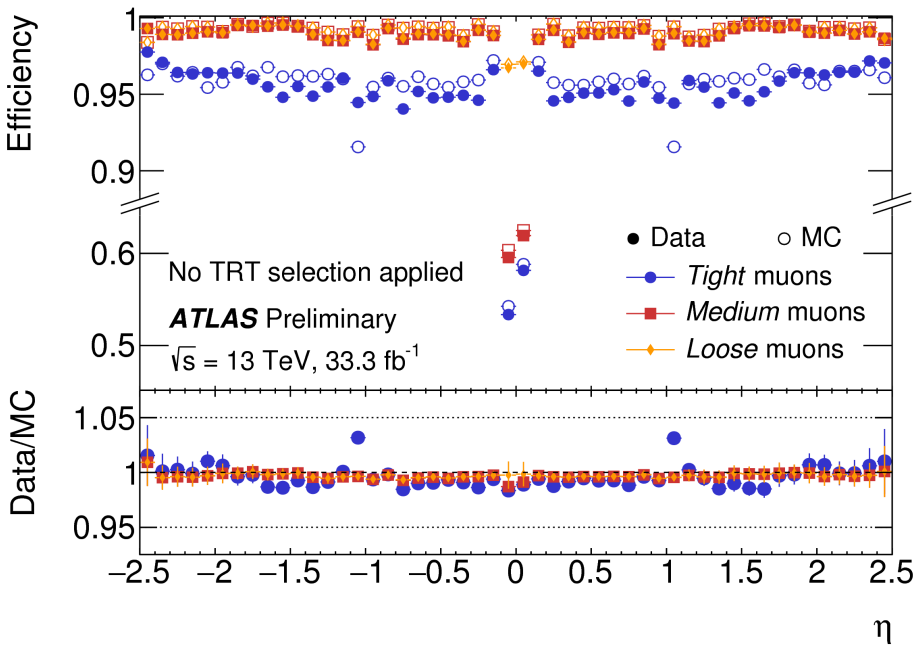

FIGURE 4.4: Muon reconstruction efficiencies for the `Loose`, `Medium` and `Tight` identification algorithms measured in $Z \to \mu\mu$ events as a function of the muon pseudorapidity for muons with a $p_{\mathrm{T}} > 10$ GeV. The prediction by the detector simulation is depicted as open circles, while filled dots indicate the observation in collision data with statistical errors. The bottom panel shows the ratio between expected and observed efficiencies, the efficiency scale factor. The errors in the bottom panel show the quadratic sum of statistical and systematic uncertainty. Figure obtained from reference [106].

is that the cone radius is $R < 0.3$. whereas the calorimeter-based isolation still uses a cone of radius of $R < 0.2$. Like the electron isolation, the muon isolation is categorised into working points such as `Loose` and `GradientLoose`. Figure 4.5 shows the efficiencies of four muon isolation working points as calculated in $Z \to \mu\mu$ events.

4.4.3 Muon efficiencies

Like the electrons an analogous tag and probe method is used to measure the identification, reconstruction and isolation efficiencies again with J/ψ and $Z \to \mu\mu$ events. Scale factors are also parametrised in terms of η and/or p_T.

4.5 Tau reconstruction

In this thesis tau leptons are not used and so only a brief overview is given. The τ-lepton has a large mass of 1.777 GeV with an average lifetime of 0.29 ps [8]. This results in the τ-lepton travelling a distance of order millimetres before it decays inside the ATLAS detector. A τ-lepton decays into a τ-neutrino and a W boson, which then decays in 65% of cases into hadrons and 35% of the time it will decay into the lighter lepton favours. The τ-lepton is not directly reconstructed inside ATLAS [107], instead the existence of the τ-lepton is inferred by reconstructing its decay products. This results in a different algorithms being used for hadronically and leptonically decaying τ-leptons. More detail can be found in [108, 109].

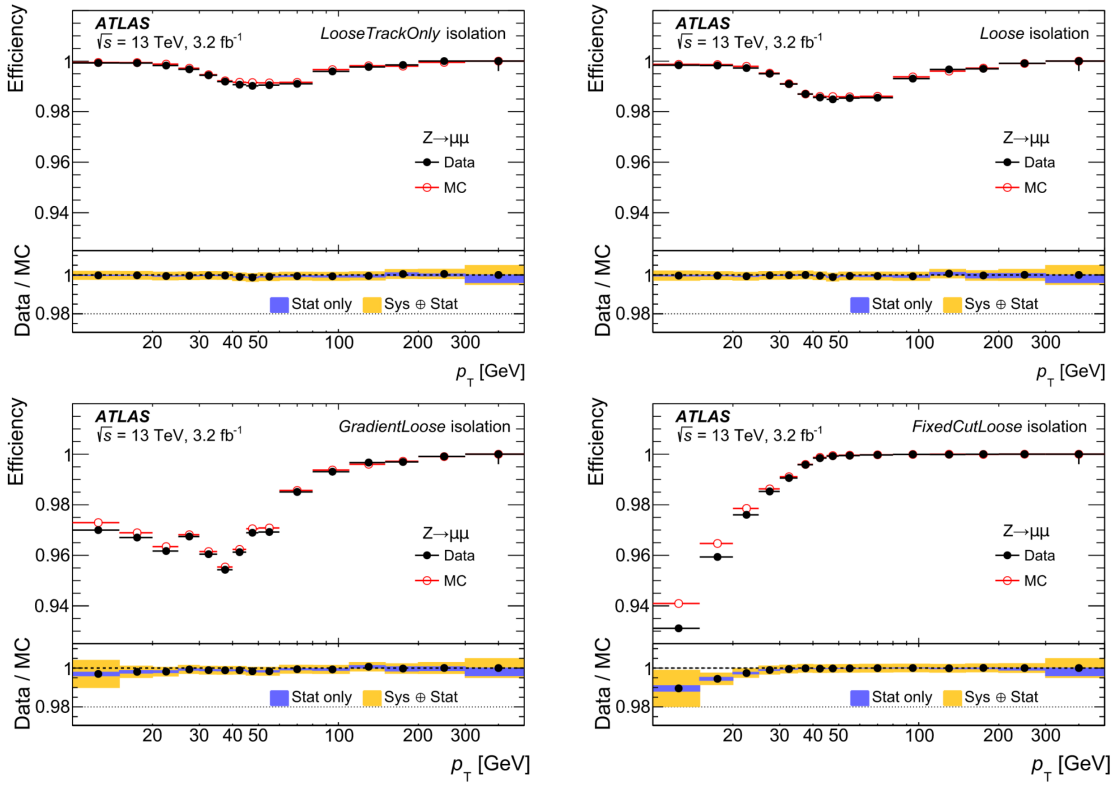

FIGURE 4.5: Isolation efficiency for the LooseTrackOnly (top left), Loose (top right), GradientLoose (bottom left), and FixedCutLoose (bottom right) muon isolation working points. The efficiency is shown as a function of the muon transverse momentum p_{T} and is measured in $Z \to \mu\mu$ events. The full (empty) markers indicate the efficiency measured in data (MC) samples. The errors shown on the efficiency are statistical only. The bottom panel shows the ratio of the efficiency measured in data and simulation, as well as the statistical uncertainties and combination of statistical and systematic uncertainties. Figure obtained from reference [105].

4.6 Jet reconstruction

Quarks or gluons produced during proton-proton interactions in ATLAS undergo a process called hadronisation[4] which produces a cone of collimated particles. These cones are referred to as jets and they can be reconstructed in the HCAL from their energy deposits. Jet reconstruction is a three step process: firstly the energy deposits in the HCAL are clustered; secondly an algorithm combines these clusters into jets and finally this combined cluster is calibrated to reconstruct the jet properties.

4.6.1 Formation of topo-clusters in the calorimeter

The energy deposits in the calorimeter are used as seeds if there is a signal to noise ratio[103] of,

$$|S/N| = E_{call}/\sigma_{cell} > 4. \tag{4.5}$$

[4]Hadronisation is the process where hadrons are formed from quarks and gluons after a high-energy collision. Due to colour confinement these quarks and gluons cannot exist in isolation and so they combine with quarks or antiquarks which are spontaneously created from the vacuum.

Then the neighbouring modules to the cluster are considered. These seeds are then clustered together with neighbouring modules in the HCAL if they have a signal to noise ratio of,

$$|S/N| > 2. \tag{4.6}$$

In this step connected clusters can be merged. Finally the process repeats itself but now with a signal to noise ratio of,

$$|S/N| > 0. \tag{4.7}$$

These clusters are referred to as topo-clusters. If the energy distribution inside a single cluster has more than one local maximum it is considered to have been formed by more than one particle, and so it is split into one cluster per local maximum. In theory, this should result in one cluster per particle that entered into the HCAL, but in practice this is not always the case due to distance between particles being small and the fact that the calorimeter modules have a finite resolution. Each calorimeter cluster is then treated as a pseudo-particle with zero mass, i.e.

$$E_{cluster} = |p_{cluster}|. \tag{4.8}$$

From this assumption the 4-momentum of the particle can be calculated from the total energy in all of the calorimeter cells in the cluster.

4.6.2 The anti-$k_t$algorithm

The topo-clusters are then grouped to form a jet using the anti-k_t algorithm [110] with a distance parameter of $R = 0.4$. The FastJet software package is used to implement the anti-k_t algorithm [111]. The anti-k_t algorithm is a specific version of a family of sequential recombination algorithms given by,

$$d_{ij} = \min\left(k_{t,i}^{2p}, k_{t,j}^{2p}\right)\frac{\Delta R_{i,j}^2}{R^2}, \tag{4.9}$$

$$d_{iB} = k_{t,i}^{-2}, \tag{4.10}$$

where $p = -1$ for the anti-k_t algorithm, k is the transverse momentum of the particles to be clustered, and R is the radius parameter which sets the jet size. Other values of p correspond to different algorithms [112, 113]. Regardless of the value of p the algorithm proceeds as follows: the smallest distance for all possible combinations of pseudo-particles i and j is calculated for d_{ij} and d_{iB}. If the smallest value is d_{ij}, the two pseudo-particles i and j are combined into a pseudo-jet, which is then included into the list of inputs for step 1. If the smallest value is d_{iB}, the input i (a pseudo-particle or jet) is declared to be a final input and is removed from the list of inputs. This process is repeated until all inputs have been declared to be final.

The $p = -1$ parameter in the anti-k_t algorithm means that small distances are assigned to close-by high-momentum particles, so that they are clustered at the start of the iterative procedure, creating seeds. This results in approximately circular jets being reconstructed in the $\eta \times \phi$ plane. Finally the vectorial sum of the energy in the topo-clusters is used to calculate the jet momentum and mass.

4.6.3 Jet calibration

The jets that are outputted by the anti-k_t algorithm require calibration which is performed in several steps. This is both shown in figure 4.6 and explained in this section. This calibration is designed to reconstruct the 4-momentum of the quark or gluon that initiated the hadronic shower [114].

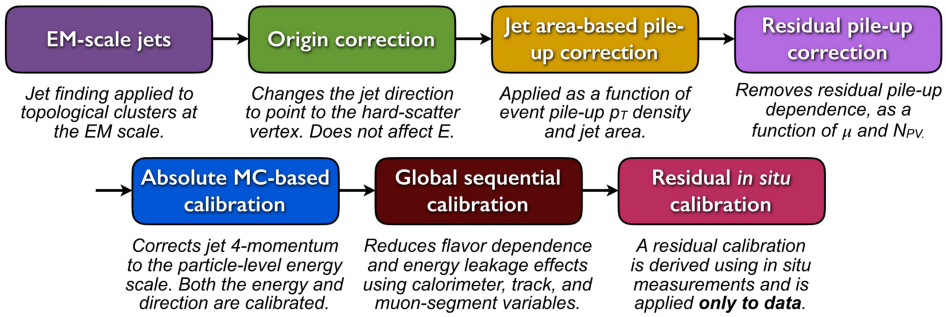

FIGURE 4.6: Overview of the stages taken during the ATLAS jet calibration scheme. Figure obtained from reference [114].

The origin correction is applied to the jet to account for the origin of the jet. In this step the 4-momentum is recalculated using the primary vertex as the origin of the jet, rather than the centre of the IP. This correction only effects the direction of the 3-momentum vector [5] and is used to improve the angular resolution of the jets.

After the origin correction, the effects from pileup are removed in the next two steps: the jet based pileup correction and the residual pileup correction. The jet based correction is a per event correction and subtracts an amount of energy from the jet, based on the pileup. This is calculated from the energy density in the event, ρ, which is calculated from the median of the energy density distribution and the jet area A. The jet area is calculated by adding uniformly distributed ghost particles with an infinitesimally small momentum to the event. The jet area is then defined by the ratio of ghost particles that get clustered into the jet to the total number. This method is used as it accounts for cases such as when two jets are close to each other leading to non-circular jets being reconstructed. Then the residual pileup correction is applied. The total correction is calculated as follows,

$$p_T^{corrected} = p_T - \rho A - \alpha\big(N_{PV} - 1\big) - \beta\langle\mu\rangle, \tag{4.11}$$

where N_{PV} is the number of reconstructed vertices in the event, and $\langle\mu\rangle$ is the mean number of interactions. The dependence of the jet momentum on these to variables is assumed to be linear and η dependent constants α and β are then used to quantify this linear behaviour. These constants are determined using MC simulations.

After the pileup correction, a Monte Carlo based calibration is applied to all jets. This calibration was obtained from the ratio, $\mathcal{R}$, between the reconstructed energy in the simulation to the truth[6] energy of the jet,

$$\mathcal{R} = \frac{E_{jet}}{E_{truth}}. \tag{4.12}$$

[5] 3-momentum is the classical momentum $p = (p_x, p_y, p_z)$

[6] Truth quantities are only available in Monte Carlo as they use the inputs before the detector response is simulated to get a perfect measurement.

The variable $\mathcal{R}$ is then parametrised in terms of η_{det}, the value of η from the centre of the detector, rather than the hard scatter vertex. A second Monte Carlo correction is applied due to a bias which is introduced when a jet spans two calorimeter regions that have different energy responses. After this calibration the jet energy and momentum corresponds to that of the particle that initiated the shower.

Some residual dependences remain on quantities such as jet shape. These dependencies are corrected for in the global sequence calibration (GSC). This calibration has several steps, each one is a correction for a different dependency. It was found that the order of these corrections has a negligible impact on the final result. Each of these corrections is parametrised in terms of η_{det} and p_T^{jet}. The GSC does not change the average energy of the jets, this is to preserve the jet energy scale (JES) so that changes to the GSC do not affect the JES.

The final step of the jet calibration procedure is the residual in situ calibration, which accounts for effects which are not well described by the Monte Carlo. This calibration uses measurements of events in data where the jet recoils against a well-measured object such as $Z \rightarrow ee+$ jet. This method is effective up to a jet p_T of 1 TeV after which the statistical error becomes too large for the method to be useful. Jets with $p_T > 1$ TeV are calibrated using a method called jet multi-jet balancing. A single hard jet in an event is compared to several recoiling softer jets using the principle of conversation of momentum to study the detector response. This procedure can be iterated to calibrate jets to energies of $p_T < 2$ TeV. For the highest p_T jets single particle response studies are used. Finally forward jets are calibrated by comparing them to well-measured central jets.

4.6.4 Jet vertex tagging

Jet vertex tagging [115, 116] is an algorithm designed to determine if a jet originated from the hard scatter vertex in an event. JVT is used to remove pileup jets, i.e. jets originating from other pp collisions inside of ATLAS. There are two separate JVT algorithms used in ATLAS, which are JVT and fJVT. These algorithms are used in the barrel region and end-caps respectively. For JVT, pileup removal is achieved by calculating a likelihood that the jet originated from the PV using properties such as the fraction of tracks that point back to the PV. fJVT provides identification and rejection of pileup jets beyond the tracking coverage of the inner detector($|\eta| \geq 2.5$). It uses the normalised projection of the missing transverse momentum on the transverse momentum.

4.6.5 c and b-tagging jets

In this thesis c and b-tagging is not used and so only a brief overview is given. b-tagging is the process used to distinguish jets produced from b-quarks from the lighter quarks [117]. All of the b-tagging algorithms make use of the fact that the b-quark has a long lifetime, 1.5 ps, and so will on average travel a couple of mm inside the detector before decaying and the charged decay products will be measured as tracks in the ID. The decay vertex of the b-quark can be separately resolved from the primary vertex and it is referred to as a secondary vertex (SV). The impact parameters of the resolved SV are used as inputs to the algorithms used for b-jet tagging.

The normal method ATLAS uses to tag b-jets is to input the jet's 4-momentum along with the impact parameter information about the tracks and the SV into a

Boosted Decision Tree (BDT) based multivariate algorithm. This class of b-tagging algorithm is called MV2c.

The process of c-jet tagging uses a very similar method to b-jet tagging. In addition the c-hadrons also have a relatively long lifetime, 0.5 - 1 ps. This makes it possible to distinguish them from light jets and b-jets.

4.7 Missing transverse energy

In this thesis missing transverse energy calculations are not used and so only a brief overview is given. There are particles that are un-detectable using the ATLAS experiment, for example the three flavours of neutrinos. The purpose of calculating MET is to allow one to detect these particles using conservation of momentum. The longitudinal momentum of the partons involved in a pp collision is unknown as they could contain any fraction of the proton's total momentum. However, the transverse momentum is known to be zero[7] and so the sum of transverse momenta in any pp collision should be zero. So thereby when the MET is calculated to be non zero, this "missing" energy implies there must have been at least one particle that was not detected by ATLAS.

At an analysis level missing transverse energy (MET) is defined to be the vectoral sum of the p_{T} of all objects associated to the primary vertex [118]. This is described in equation 4.13,

$$E_T^{miss} = -\sum_{i\in(\text{soft})} p_{t,i} - \sum_{j\in(\text{hard})} p_{t,j}, \tag{4.13}$$

where the hard objects are all objects that have been reconstructed inside ATLAS. The soft term includes all the remaining tracks in the ID that are not associated to a reconstructed object.

[7] Technically this traverse momentum is non zero, however it's value is negligible with respect to the collision energy.

Chapter 5

Luminosity

To measure rare processes, the LHC is required to collect a large quantity of data. The amount of data collected is defined in terms of the Luminosity. Nearly all of ATLAS's physics analyses requires an accurate measurement of Luminosity. For example, the differential cross section measurement presented in Chapter 7 uses the integrated luminosity in the denominator of the expression that defines the cross-section. Luminosity is normally one of the dominant systematic uncertainties on cross section measurements and so measuring it accurately is vital. Furthermore, the integrated luminosity is used to scale the MC backgrounds to match the number of predicted events in data. The measurement of luminosity is performed utilising several independent methods using different detectors and algorithms. The spread of predictions of these algorithms allows an estimation of the systematic error on the final luminosity measurement.

Section 5.1 covers the mathematical formalism of luminosity. Then section 5.2 will discuss the delivered luminosity inside ATLAS. After this, section 5.3 will deal with how luminosity measurements are calibrated. Finally section 5.4 will contain the main luminosity measurement algorithms used by ATLAS. In this thesis luminosity was briefly covered in section 3.1.3 and that information is repeated here for the reader's convenience.

5.1 Mathematical formalism of luminosity

The LHC is a proton-proton collider with bunched beams. The luminosity, $\mathcal{L}$, of a particle collider such as the LHC relates the number of produced events per unit of time, R, and the cross section, σ, by [70],

$$\mathcal{L} = \frac{R}{\sigma}. \tag{5.1}$$

From equation 5.1 it can be seen that the units of luminosity are $\mathrm{m}^{-2}\mathrm{s}^{-1}$. In the LHC, a single discrete packet of protons that travels around the ring is called a bunch. It is uniquely identified, per run, by its bunch crossing identifier (BCID). The luminosity can therefore be re-expressed in terms of the bunch luminosity, $\mathcal{L}_b$, which is the luminosity of a single pair of colliding bunches,

$$\mathcal{L}_b = \frac{\mu f_r}{\sigma_{inel}}, \tag{5.2}$$

where μ is the average number of inelastic interactions per bunch crossing, f_r is the bunch revolution frequency and σ_{inel} is the inelastic cross-section for pp collisions. In equation 5.2 one can replace 'inel' by any process 'x'. The inelastic process is used here is used as it a convenient choice. The total delivered luminosity is a sum over

all of the bunches and this is given by,

$$\mathcal{L} = \sum_{b=1}^{n_b} \mathcal{L}_b = n_b \langle \mathcal{L}_b \rangle = n_b \frac{\langle \mu \rangle f_r}{\sigma_{inel}}. \tag{5.3}$$

Here, n_b is the number of colliding bunches, $\langle \mu \rangle$ and $\langle \mathcal{L}_b \rangle$ are the bunch-averaged number of inelastic interactions and bunch luminosity respectively. Table 5.1 shows the operational conditions during Run 2 between 2015 to 2018.

Parameter	2015	2016	2017	2018
Maximum number of bunch pairs colliding	2232	2208	2544	2544
Bunch spacing [ns]	25	25	25	25
Typical bunch population [10^{11}protons]	1.1	1.1	1.1	1.1
Peak number of inelastic interactions [μ]	16	41	45	55
Peak luminosity delivered 10^{34} cm^{-2}s^{-1}	0.50	1.38	2.09	2.14
Total integrated luminosity delivered fb^{-1}	4.2	38.5	50.2	63.4

TABLE 5.1: Selected LHC parameters for pp collisions during the years 2015-2018. Values shown are for typical physics running conditions for that year. Table obtained from [119].

It is possible to determine the absolute luminosity from equation 5.1 by using a process for which the associated cross-section is well measured. An example would be a Z boson decaying to muons. However, the most common method used to determine the luminosity is to measure a visible interaction rate per bunch crossing, μ_{vis}, of a given process for an algorithm and detector combination. For this method to work it is required that the measured process is linearly proportional to the instantaneous luminosity. One obtains the delivered luminosity from the visible interaction rate per bunch crossing with the following equation,

$$\mathcal{L}_b = \frac{\mu_{vis} f_r}{\sigma_{vis}} \tag{5.4}$$

where

$$\mu_{vis} = \epsilon \mu, \tag{5.5}$$

and

$$\sigma_{vis} = \epsilon \sigma_{inel}. \tag{5.6}$$

Here, ϵ is the the efficiency of the detector and algorithm under consideration and σ_{vis} is the visible cross-section associated with μ_{vis}. The calibration of an algorithm and detector combination amounts to the calculation of the visible cross-section, this is because the visible interaction rate per bunch crossing is a directly measurable quantity. This calibration procedure is covered in section 5.3.

For physics analyses the integrated luminosity is required for some well-defined data samples. Integrated luminosity is defined as the time integral of the luminosity, as given by,

$$\mathcal{L}_{int} = \int \mathcal{L} dt. \tag{5.7}$$

To achieve this, the data collected at ATLAS is split into luminosity blocks (LBs) which have a duration of approximately 60 seconds. The LBs are defined by the ATLAS Central Trigger Processor (CPT). A new luminosity block is started if there are any configuration changes such as the pre-scaling of a trigger or if ~60 seconds

has passed. The ATLAS data is analysed under the assumption that each LB has the same instantaneous luminosity for its duration. This allows the time integral to be simply calculated.

5.2 Instantaneous and peak luminosities delivered

Initially the operational design of the LHC was to have an instantaneous luminosity of 1.0×10^{34} cm^{-2}s^{-1}. The operational design was exceeded by the end of the data taking period in 2016, which peaked at 1.38×10^{34} cm^{-2}s^{-1}. By December 2018 the LHC was collecting data at more than twice the original design luminosity. Figure 5.1 depicts the instantaneous luminosity as a function of time for the entirety of Run 2, separated by year [120]. The integrated luminosity collected by the ATLAS experiment for Run 2 is shown in figure 5.2 and 5.3.

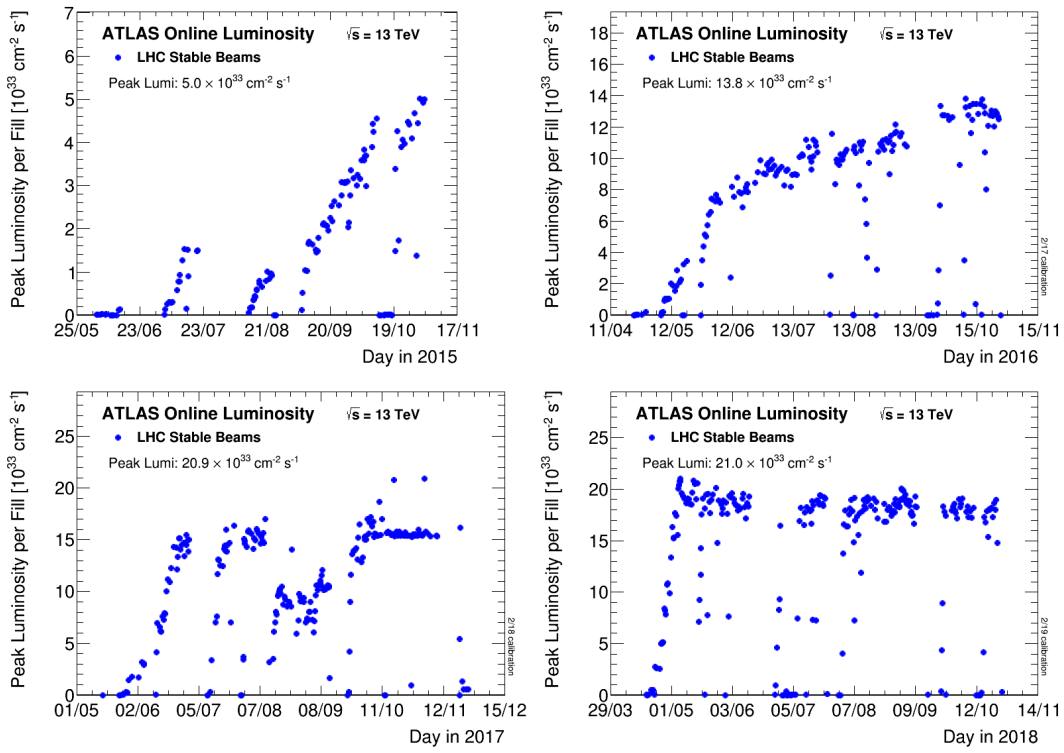

FIGURE 5.1: The peak instantaneous luminosity delivered to ATLAS during pp collisions during the years 2015 (top-left), 2016 (top-right), 2017 (bottom-left) and 2018 (bottom right). Figure obtained from Ref. [120].

The total amount of data collected at the LHC for the entirety of Run 2 (2015-2018) which can be used for physics analysis is 138.42 ($\pm$1.7%) fb^{-1} of data [120]. This is the same data collection period as used for the analysis detailed in chapter 7.

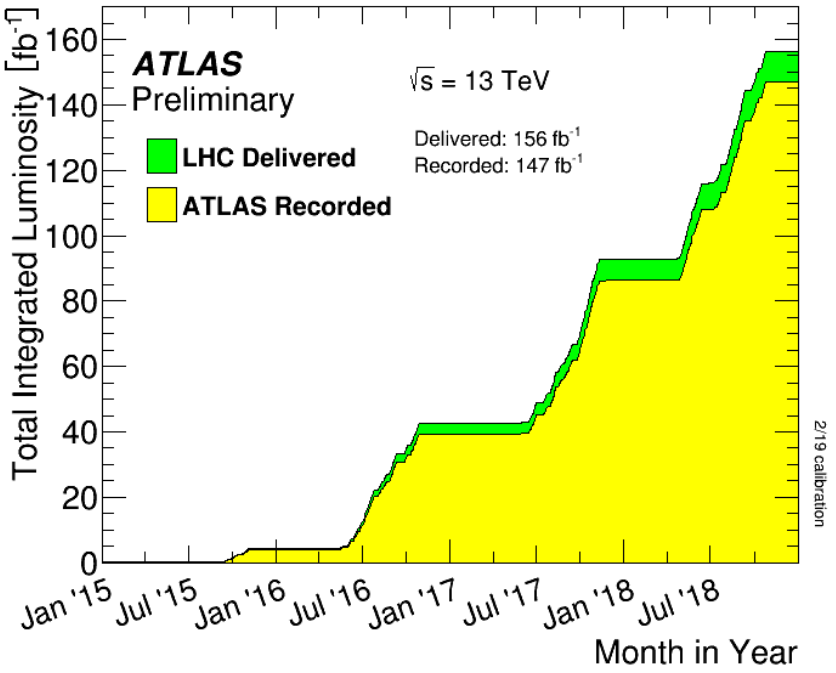

FIGURE 5.2: Cumulative integrated luminosity versus time delivered to (green) and recorded by ATLAS (yellow) during stable beams for pp collisions at 13 TeV centre-of-mass energy in Run 2. Figure obtained from Ref. [120].

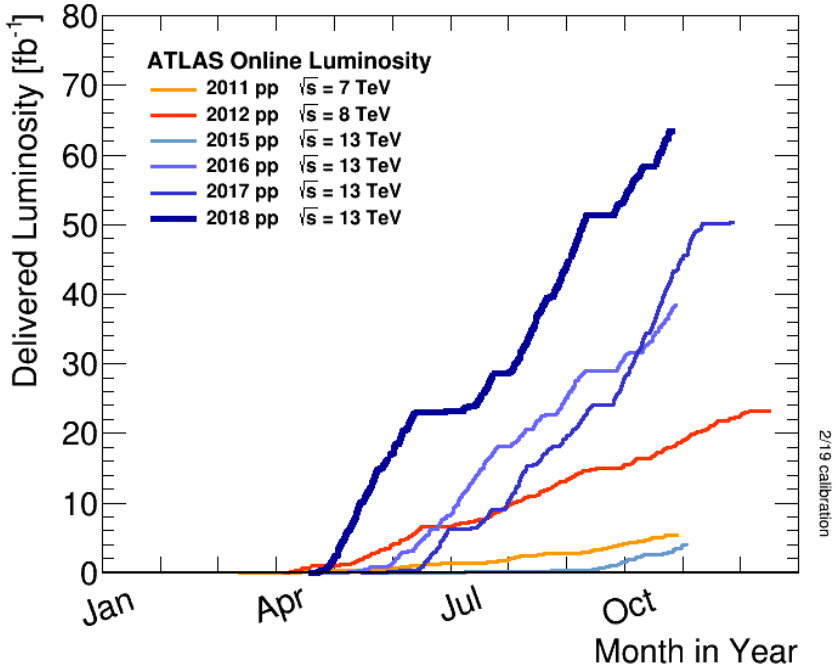

FIGURE 5.3: Cumulative integrated luminosity collected per year by the ATLAS detector at the LHC. Figure obtained from Ref. [120].

5.3 Van der Meer scans

As covered in section 5.1 the visible cross-section, σ_{vis}, must be obtained for a luminosity algorithm to be calibrated. The primary method of obtaining this calibration is the van der Meer (vdM) Scan. The vdM scan allows the instantaneous luminosity to be calculated directly from the beam parameters. This allows a calculation of the visible cross-section by using equation 5.2. The remainder of this section is dedicated to the mathematical formalism of vdM scans.

Assuming that the colliding beams have no crossing angle, the bunch luminosity can be expressed as,

$$\mathcal{L}_b = f_r n_1 n_2 \int \rho_1(x,y)\rho_2(x,y)dxdy, \tag{5.8}$$

where $n_{1(2)}$ is the the bunch-population and $\rho_{1(2)}$ is the normalised particle density in the transverse $(\hat{x}-\hat{y})$ plane of beam 1(2) at the interaction point. The vdM method requires the assumption that the particle density functions can be factorised into the vertical and horizontal components by,

$$\rho_n(x,y) = \rho_{xn}(x)\rho_{yn}(y)\ ;\ n = 1,2. \tag{5.9}$$

This assumption of factorisation is tested in ATLAS and a non-factorisation systematic is applied to the measured luminosity [70]. With this assumption equation 5.8 can be written as,

$$\mathcal{L}_b = f_r n_1 n_2 \Omega_x(\rho_{x1},\rho_{x2})\Omega_y(\rho_{y1},\rho_{y2}), \tag{5.10}$$

where

$$\Omega_\tau(\rho_{\tau 1},\rho_{\tau 2}) = \int \rho_{\tau 1}(\tau)\rho_{\tau 2}(\tau)d\tau\ ;\ \tau = x,y, \tag{5.11}$$

is the beam-overlap integral in the x or y direction. In the original method proposed by van der Meer [121, 122], this overlap integral can be calculated from,

$$\Omega_\tau(\rho_{\tau 1},\rho_{\tau 2}) = \frac{R_\tau(0)}{\int R_\tau(\delta)d\delta}\ ;\ \tau = x,y. \tag{5.12}$$

Here δ is the separation of the two incoming beams, $R_\tau(\delta)$ is the luminosity measured in arbitrary units and $R_\tau(0)$ is the value at zero beam separation. It can be seen from equation 5.12 that the luminosity is normalised by its value at zero beam separation, thereby any quantity linearly proportional to luminosity can be substituted here to replace R_τ. From here, using equation 5.10, the bunch luminosity can be defined as,

$$\mathcal{L}_b = \frac{f_r n_1 n_2}{2\pi\Sigma_x\Sigma_y}, \tag{5.13}$$

where Σ_i is the horizontal convolved beam size [123, 124] and is defined as,

$$\Sigma_\tau = \frac{1}{\sqrt{2\pi}}\frac{\int R_\tau(\delta)d\delta}{R_\tau(0)}\ ;\ \tau = x,y. \tag{5.14}$$

This allows the absolute bunch luminosity to be determined from the revolution frequency, f_r, the bunch population product $n_1 n_2$ and the product of $\Sigma_x\Sigma_y$ which can be directly measured during two orthogonal beam-separation (vdM) scans. For these two scans, the beams are displaced in the $\hat{x}$ and $\hat{y}$ direction.

If the functional form of the luminosity curve, $R_\tau(\delta)$, is a Gaussian distribution,

then Σ_x corresponds to the standard deviation of this Gaussian. The vdM method does not make any assumptions on the functional form of $R_\tau(\delta)$ and so can be calculated for any form of $R_\tau(\delta)$ using equation 5.14. Once the values of Σ_x and Σ_y are known, the luminosity can be calculated from equation 5.13

Once the luminosity is known for a given vdM scan it is possible to calibrate a luminosity algorithm. To achieve this one substitutes 5.4 into 5.13 to obtain

$$\sigma_{vis} = \mu_{vis}^{MAX} \frac{2\pi\Sigma_x\Sigma_y}{n_1 n_2}, \tag{5.15}$$

where μ_{vis}^{MAX} is the visible interaction rate per bunch crossing where the separation of the beams is zero, i.e. at the peak of the scan curve. Equation 5.15 then allows an absolute calibration of a luminosity algorithm and detector combination. This vdM scan method uses a low value of μ to reduce the systematic uncertainty brought about from pileup interactions. This results in a low instantaneous luminosity and so it is impractical to use for physics running. Thereby vdM scans are performed in dedicated runs.

To allow a comparison between the different algorithm and detector combinations, the specific luminosity is defined as the luminosity per bunch and per unit bunch population product. This is given by,

$$\mathcal{L}_{sp} = \frac{\mathcal{L}}{n_1 n_2} = \frac{f_r}{2\pi\Sigma_x\Sigma_y}. \tag{5.16}$$

As this depends only on the transverse beam it is a purely geometrical quantity and so it allows a direct test of the consistency of the absolute luminosity scale provided by these algorithms.

5.4 Luminosity measurements at ATLAS

ATLAS uses a variety of different detectors and algorithms to measure the luminosity. Comparisons on the different predictions allows one to calculate the systematic uncertainty on the final luminosity measurement. For each of these different algorithms the luminosity is calculated by measuring an observed interaction, μ_{algo}^{vis}, that is specific to the algorithm. The corresponding σ_{algo}^{vis} is then measured in the dedicated vdM scans and this is covered in section 5.3.

5.4.1 Luminosity algorithms

There are two main types of generalised luminosity algorithms that are used by ATLAS:

- **Event Counting:** The number of bunch crossings in which the detector registers an event is counted.
- **Hit Counting:** The number of hits per bunch crossings is counted.

The remainder of this section is dedicated to covering the mathematical formalism of these general algorithms.

5.4.1.1 Event Counting

There are two primary event counting algorithms [70] used to determine a μ^{vis}: the `EventOR` algorithm and the `EventAND` algorithm. The difference is that for an event to be counted, the `EventOR` algorithm only requires there to be a hit on one side of the detector, whereas the `EventAND` algorithm requires both sides to register a hit. Exactly what these hits are depends on the exact algorithm used. For now it suffices to say that a hit represents that a proton-proton inelastic scatter has taken place in the detector.

Assuming the number of proton-proton interactions in a given bunch crossing is Poisson distributed, the probability that a BCID passes the `EventOR` algorithm's criteria is given by,

$$P_{OR}(\mu_{vis}^{OR}) = \frac{N_{OR}}{N_{BC}} = 1 - P_0(\mu_{vis}^{OR}) = 1 - e^{-\mu_{vis}^{OR}}, \tag{5.17}$$

where N_{OR} is the number of bunch crossing where a hit was registered, N_{BC} is the total number of bunch crossings. $P_{OR}(\mu_{vis}^{OR})$ is equal one minus the probability of there being zero hits. Equation 5.17 can be solved for μ_{vis}^{OR} by re-arranging the terms to give,

$$\mu_{vis}^{OR} = -\ln\left[1 - \frac{N_{OR}}{N_{BC}}\right]. \tag{5.18}$$

A similar expression can be derived for the `EventAND` algorithm in an analogous manner. The probability that both sides of the detector register a hit is given by,

$$P_{AND}(\mu_{vis}^{AND}) = \frac{N_{AND}}{N_{BC}} = 1 - e^{-\mu_{vis}^{A}} - e^{\mu_{vis}^{C}} + e^{\mu_{vis}^{OR}}, \tag{5.19}$$

where N_{AND} is the number of bunch crossing where a hit was registered in both sides of the detector. Additionally $e^{-\mu_{vis}^{A}}$ and $e^{-\mu_{vis}^{C}}$ give the probabilities that no hit was registered in detector side A and C respectively. Relating the visible interaction rates of each algorithm gives,

$$\mu_{vis}^{OR} = \mu_{vis}^{A} + \mu_{vis}^{C} - \mu_{vis}^{AND}. \tag{5.20}$$

Using the relation given in equation 5.20, equation 5.19 can be written as,

$$\frac{N_{AND}}{N_{BC}} = 1 - 2\exp\left[-\left(\frac{\mu_{vis}^{AND} + \mu_{vis}^{OR}}{2}\right)\right] + \exp\left[-\mu_{vis}^{OR}\right]. \tag{5.21}$$

From here the use of equation 5.3 allows one to write equation 5.21 as a function of μ_{vis}^{AND} and the cross-sections σ_{vis}^{AND} and σ_{vis}^{OR},

$$\frac{N_{AND}}{N_{BC}} = 1 - 2\exp\left[-\left(1 + \frac{\sigma_{vis}^{OR}}{\sigma_{vis}^{AND}}\right)\frac{\mu_{vis}^{AND}}{2}\right] + \exp\left[-\left(\frac{\sigma_{vis}^{OR}}{\sigma_{vis}^{AND}}\right)\mu_{vis}^{AND}\right]. \tag{5.22}$$

Equation 5.22 cannot be calculated analytically so numerical methods are used.

5.4.1.2 Hit Counting

For the hit counting algorithms, the total number of hits registered in a specific detector is found per unit time [70]. It is assumed that the number of hits per bunch

crossing is binomially distributed and, as for event counting, that the number of proton-proton interactions is Poisson distributed.

From here one can say that the probability of having a hit in a given bunch crossing is given by,

$$P_{HIT}(\mu_{vis}^{HIT}) = \frac{N_{HIT}}{N_{BC}N_{CH}} = 1 - e^{-\mu_{vis}^{HIT}}, \tag{5.23}$$

where N_{HIT} is the number of hits per unit time and N_{CH} is the number of channels the detector has. Assuming that each of these detector channels has an equal probability to hit, this equation can be solved in the same way as equation 5.17, for μ_{vis}^{HIT},

$$\mu_{vis}^{HIT} = -\ln\left[1 - \frac{N_{HIT}}{N_{BC}N_{CH}}\right]. \tag{5.24}$$

5.4.2 Bunch-by-bunch luminosity algorithms

Bunch-by-bunch luminosity detectors allow a measurement of the luminosity at the per-bunch level for a given LB. The two primary algorithms of this form utilise the detectors LUCID and BCM, and they are both hit counting algorithms. Both the LUCID and BCM algorithms can be split into A and C sides allowing for both the `EventOR` algorithm and the `EventAND` algorithm to be used. In this thesis the LUCID and BCM detectors were briefly covered in section 3.2.7, however, the information is repeated here for the reader's convenience.

LUCID[1] is specifically designed to measure the luminosity delivered to ATLAS. It is situated 17 m from the interaction point on each side down the beam-pipe [87]. LUCID is made of photomultiplier tubes attached to quartz fibre bundles which are used to detect Cherenkov radiation. This radiation is created when charged particles pass through the quartz and the quantity of radiation produced is proportional to the number of pp interactions inside ATLAS. Thereby LUCID can be used to measure instantaneous luminosity. A hit is recorded for a bunch crossing if a PMT inside LUCID reads a signal over a given threshold.

The BCM, comprises four 8×8 mm^2 diamond sensors arranged in a cross pattern around the beam-pipe located 1.84 m either side of the IP [88]. It was originally designed to monitor the radiation levels inside ATLAS in case the level became high enough to damage ATLAS. A hit is recorded for a bunch crossing if a signal over a given threshold is read. This provides a low-acceptance measurement of luminosity for $|\eta| = 4.2$. The BCM is split up into the horizontal and vertical pairs of sensors, which are then read out separately. This results in two luminosity measurements called BCMH and BCMV that are treated independently of each other.

5.4.3 Bunch-integrating luminosity algorithms

Bunch integrated luminosity detectors do not provide a bunch-by-bunch resolution, instead they provide a luminosity measurement for all BCIDs for a given LB.

There are two main algorithms that use the assumption that the currents drawn in a given calorimeter should be proportional to the particle flux that passes through them. This is in turn proportional to the number of proton-proton interactions. The two main algorithms that use this assumption rely on the calorimeters TileCal and FCal. Details on these detectors can be found in section 3.2.5.

[1] LUminosity measurement using Cerenkov Integrating Detector

The measurement for TileCal algorithm uses the current drawn by the PMTs from specific cells in the region $|\eta| \approx 1.25$. This because this region was found to be the most sensitive to changes in instantaneous luminosity [125]. The current measured by the FCal algorithm is the one that is used to provide a stable field in the LAr cells in the modules that are closest to the IP [126].

As well as the calorimeters, the MPX system can be utilised as a bunch integrating luminosity algorithm. The MPX system comprises 13 Medipix pixel detectors, which are spaced through the ATLAS detector and they are all read out individually. The original design of the MPX system was to measure the radiation levels and its distribution inside ATLAS [127]. Using the same assumption about particle flux it can be used as a relative luminosity measure.

It is impossible to calibrate all of the bunch integrating algorithms covered in this section using a vdM scan as the response of the detectors in question is too low in the low μ runs used in vdM scans. To obtain a σ_{vis} for these algorithms a comparison is made to either BCDM or LUCID during a physics run [70].

Chapter 6

Measuring Luminosity using vertex counting

This chapter describes a method of measuring luminosity through counting the number of reconstructed vertices per event. It will document the method of counting the vertices, along with the corrections to account for imperfections in the vertex reconstruction algorithm.

Section 6.1 provides an introduction to the background of vertex counting. Section 6.2 covers the data and MC samples used. Section 6.3 describes working points used by the vertex counting algorithm. Section 6.4 contains the distributions of vertices along the $\hat{z}$ axis. Section 6.5 summarises the mathematical formalism of the vertex counting algorithm. Section 6.6 illustrated method used to optimise the cuts on the working points. Section 6.7 shows the results of the MC closure test. Section 6.8 describes how the algorithm was calibrated. Sections 6.9 and 6.10 cover the internal and external stability respectively. Section 6.11 presents the breakdown of the systematics that effect this algorithm. Finally section 6.12 is a summary of the results.

6.1 Introduction

Vertex counting as a method of determining the delivered luminosity has been previously studied inside ATLAS [43, 128, 129]. The previous iterations of this algorithm were used to measure the delivered luminosity for Run 1. This chapter will cover the development and implementation of the current iteration of the vertex counting algorithm for Run 2.

A primary vertex (PV) in the context of vertex counting is defined as a scattering of two protons in the LHC. If there are secondary interactions after the initial proton-proton scatter, such as the decay of a b quark, they can be reconstructed as different vertices, these are referred to as secondary vertices (SV).

The number of reconstructed vertices per event has a non-linear dependence on the instantaneous luminosity due to it being strongly effected by pileup. Additionally, the pileup in Run 2 is higher than that of Run 1 and so the challenge is greater. If the vertex reconstruction in ATLAS was perfect, simply counting the number of reconstructed vertices would give one the number of inelastic proton-proton scatters. In reality the pileup effects complicate this reconstruction process. If one counts the number of reconstructed vertices and applies corrections for the pileup effects it is possible to obtain a 2.2% accuracy on the prediction of the luminosity in a 10 LB time period.

In theory, vertex counting has the potential to surpass some of the other luminosity algorithms already employed at ATLAS as it is expected to be more stable than

some other measures. This is primarily for two reasons: firstly the vertex reconstruction is infrequently changed, meaning that the run to run consistency is expected to be good; secondly it should be less sensitive to detector conditions than some of the other measures. For example, track counting is highly sensitive to the status of the inner detector. This is because if a region of the inner detector is down for any reason the number of tracks counted is lower, whereas, if one counts the number of reconstructed vertices it is less likely to change as they are reconstructed from multiple tracks with each of these tracks being likely to be in a different region of the inner detector.

The motivation behind requiring multiple different independent luminosity algorithms is to allow the systematic error on the total integrated luminosity collected by the ATLAS experiment to be determined. As there is no way to directly measure the luminosity inside ATLAS outside of vdM scans, the independent algorithms can be compared against each other to measure their stability over a data taking year. For example, if three out of four luminosity algorithms are stable with each other and the fourth is shown to drift away from the others over a period several months it is highly likely that this fourth algorithm is not correctly accounting for some effect. An example of this would be the degradation of detector components due to radiation damage. Despite the fact that the vertex counting algorithm takes its absolute calibration from the LUCID algorithm it is still a valuable addition. This is because it can be used to measure the stability of all the other algorithms in use as its relative prediction is independent of LUCID outside of the initial calibration.

6.2 Data and MC samples

The vertex counting algorithm uses data taken in 2015 and 2016 with a proton bunch spacing of 25 ns. For data collected during 2015 and 2016, an integrated luminosity of 35.7 fb^{-1} was collected[1].

Two different data streams are used to obtain the data used by the vertex counting algorithm. First there is the `calibration_vdM` stream which uses a random L1 trigger for specific BCIDs which randomly triggers on events. This is used to obtain the quiescent period of vdM scans. For the physics runs the `calibration_PixelBeam` stream is used, again with a random trigger. This stream was initially used in 2012 and was designed to store minimal information to allow for a faster readout (~100 Hz) than the other streams.

Two custom MC datasets were generated to study the effect of pileup on vertex reconstruction and the GRID datasets are given in Appendix C.1. As these datasets were designed to study pileup, the primary interaction in the MC was the production of a single neutrino. This was done so that the primary interaction has a negligible effect on the vertex reconstruction. The first dataset was produced with a $\mu = 2$ to allow for the data-driven vertex merging correction to be evaluated in the MC. The second dataset had a flat μ profile between $1 \leq \mu \leq 60$ in steps of 1 to allow for the fake and merged vertex corrections to be evaluated. Details on these corrections can be found in section 6.5.

Both the MC and the data impose a set of quality cuts on the tracks called `VtxLumi` cuts. The requirements here are tighter than those used typically by ATLAS. The

[1]The 2015 dataset has an integrated luminosity of 3.22 fb^{-1}. The 2016 dataset suffers from the so-called BadBatMan problem that removes 1.66% of the luminosity (these events are flagged as bad). Prior to considering this, the 2016 luminosity was 32.99 fb^{-1}, becoming 32.44 fb^{-1}.

tracks are required to have $p_{\mathrm{T}} > 900$ MeV, zero pixel holes and less than two SCT holes in the tracks.

6.3 Working points

A working point (WP) is a set of criteria used to select which vertices are counted and which are ignored by the algorithm. There are three variables that can be changed in this algorithm to provide different working points:

1. There must be a minimum number of tracks associated to the reconstructed vertex, N.
2. The tracks associated to the vertex must pass a cut on their transverse momentum.
3. The position of the vertex with respect to the centre of the luminous region in the transverse plane must not exceed a value R.

For all working points the standard cuts applied are,

$$R < 0.3 \text{ mm}, \tag{6.1}$$

and

$$p_T > 900 \text{ MeV}, \tag{6.2}$$

unless otherwise specified. Furthermore, the working points will be hereafter referred to by `nVtxN_XXX` where `N` is the cut on the number of associated tracks and `XXX` is the cut on the track p_T in MeV. For example, the working point `nVtx5_950`, counts vertices with at least 5 tracks of $p_T > 950$ MeV.

This algorithm uses WPs that have between at least two and eight associated tracks. The other two cuts that define the WPs are optimised to maximise accuracy while maintaining statistical precision. The method used to optimise these cuts is covered in section 6.6. Furthermore the motivation behind adding this cut on R to the previous iteration of the algorithm is covered in Appendix A.

6.4 Distribution of vertices in the detector

The distribution of vertices in the detector is approximately Gaussian shaped in the $\hat{x}$, $\hat{y}$ and $\hat{z}$ directions. This distribution, however, is much wider in the $\hat{z}$ direction than for the $\hat{x} - \hat{y}$ plane. The distribution along the $\hat{z}$ axis is depicted in figure 6.1 for the quiescent period[2] of the vdM scan with run number 299390.

The distance in the $\hat{z}$ direction of all unique pairs of reconstructed vertices per event will hereafter be referred to as the Δz distribution of vertices. It is used in the data-driven vertex merging correction covered in section 6.5.4 and is depicted in figure 6.1. For now it is sufficient to note that the Δz distribution drops to ~0 for Δz~0. This is because the vertex reconstruction efficiency drops significantly for low values of Δz as the detector is not able to resolve the two vertices individually and so only one vertex is reconstructed.

[2]During the vdM scans there is time during the run where the other detectors at the LHC are performing their beam scans. ATLAS uses this time to collect some low μ data, this is refered to as the quiescent period.

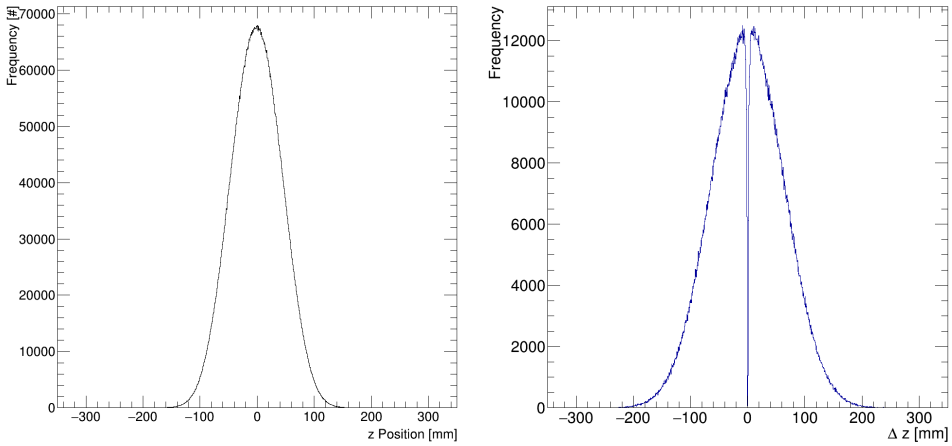

FIGURE 6.1: Observed $\hat{z}$ and Δz distribution of reconstructed vertices in the quiescent period of vdM scan 299390 for the working point `nVtx0_900`.

6.5 Mathematical formalism of the vertex counting

The next section will cover the three pileup effects that are corrected for in this algorithm. Then the remainder of this section will cover the mathematical formalism of these corrections. The corrections for this algorithm are applied to 10 LBs at a time. This is due to a statistical limitation in the method. Furthermore all plots in section 6.5 use a p_{T} cut of 900 MeV on the tracks because the effects of the pileup corrections are clearer to see when all the WPs use the same track p_{T} cut.

6.5.1 Summary of definitions

For the reader's convenience a summary of the different μ variables defined in this section are given below:

- μ_{rec}: The average number of reconstructed vertices per event. This is the input of the algorithm.
- μ_{vis}: The average number of vertices that could have been reconstructed if there were no pileup effects. This is the output of the algorithm.
- μ_{real}: The average number of reconstructed vertices per event that were real vertices, i.e. all of the reconstructed vertices that were not fakes or split.
- μ_{fake}: The average number of fake vertices per event.
- μ_{split}: The average number of split vertices per event.
- μ_{merged}: The average number of merged vertices per event.
- μ_{MC}: The average number of vertices that are reconstructed if MC truth information is used to match all of the vertex associated[3] tracks to the correct vertex. This is what μ_{vis}: is attempting to recover.
- μ_{truth}: The average number of proton-proton interactions obtained using MC truth information.

[3]The method by which tracks are associated to vertices is covered in section 4.2. A track is considered vertex associated if it was matched to any vertex during the reconstruction process.

6.5.2 Pileup effects

Per bunch crossing, there are generally multiple proton-proton interactions. The complications in reconstructing vertices due to this fact are referred to as pileup effects. These pileup effects result in a non-linear relationship between the number of reconstructed vertices and the instantaneous luminosity and this is demonstrated in figure 6.2. The two general types of pileup are given below:

- **In time pileup:** Where the complications arise from proton-proton interactions that happened within **the same** bunch crossing as the one currently being measured.
- **Out of time pileup:** Where the complications arise from proton-proton interactions that happened within **a different** bunch crossing as the one currently being measured.

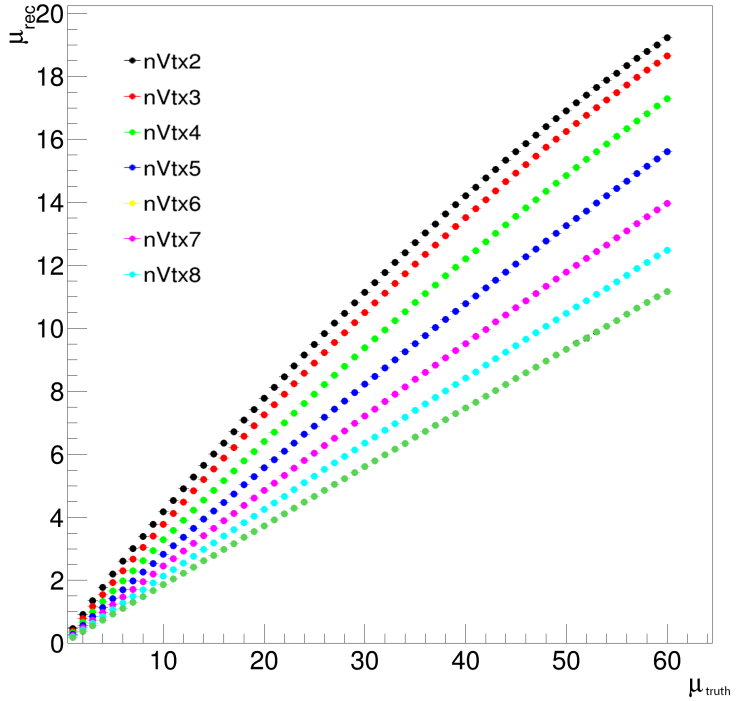

FIGURE 6.2: The average number of reconstructed vertices per event in Monte Carlo data as a function of μ obtained using truth information. All WPs use a p_T cut of 900 MeV.

The pileup corrections calculate how many vertices would have been reconstructed in the absence of pileup complicating the reconstruction process. There are three corrections for the "in time pileup'", and none for "out of time pileup", as it it does not have a large effect on this algorithm. Furthermore these corrections are evaluated for each working point individually. The three corrections applied to vertex counting are:

- **The split vertex correction:** A single vertex is mistakenly reconstructed as two vertices. This results in more vertices being reconstructed than should have been.

- **The merged vertex correction:** When two proton-proton collisions happen very close to each other the reconstruction algorithm can mistakenly reconstruct them both as one vertex, when there should have been two. This results in fewer vertices being reconstructed.
- **The fake vertex correction:** It is possible for a vertex that should have failed the cut on the number of associated tracks to pass due to a track (or tracks) being incorrectly assigned to the vertex. This results in more vertices being reconstructed.

6.5.3 Mathematical formalism of the pileup correction

The three pileup corrections are parametrised as a correction to the average number of reconstructed vertices per event, μ_{rec}, which is what the algorithm initially measures. Applying the corrections gives the average number of vertices that could have been reconstructed if there were no pileup effects, μ_{vis}, and this is the output of the algorithm.

The basic concept of this algorithm is as follows. Firstly the average number of fake vertices per event, μ_{fake}, and the average number of split vertices per event, μ_{split}, are subtracted from μ_{rec} as they increase the number of reconstructed vertices,

$$\mu_{real} = \mu_{rec} - \mu_{fake} - \mu_{split}. \tag{6.3}$$

Here, μ_{real} is the average number of real vertices that were reconstructed, i.e. all of the vertices that were not fake or split. Secondly, to correct for the vertices that were not reconstructed due to vertex merging, the number of real vertices are then added to the number of merged vertices to obtain μ_{vis},

$$\mu_{vis} = \mu_{real} + \mu_{merged}. \tag{6.4}$$

The quantity μ_{vis} should be linear with the instantaneous luminosity and this is tested in section 6.6.1. Additionally it is convenient to parametrise the merging correction as a multiplicative factor, f_{merge}, where a value of one would correspond to no merging. This factor f_{merge} is parametrised by,

$$f_{merge} = 1 + \frac{\mu_{merged}}{\mu_{real}}, \tag{6.5}$$

so thereby,

$$\mu_{vis} = \mu_{real} \times f_{merge}. \tag{6.6}$$

Both the split and fake vertex correction require truth MC information to be able to be calculated and the merging correction uses a data-driven technique.

Finally, there are two more definitions that are required for the discussion of this algorithm: firstly there is μ_{MC}, which is defined to be the average number of vertices that are reconstructed if MC truth information is used to match all of the tracks to the correct vertex; secondly there is μ_{truth}, which is the average number of proton-proton interactions obtained using MC truth information. The method used for the truth matching is covered in Appendix B.

6.5.4 The merged vertex correction

The merged vertex correction corrects for the case where two vertices are close enough to each other that they are mistakenly reconstructed as one vertex. This correction

is calculated in two stages and is the only one of the three corrections to use a data-driven technique, rather than MC truth information.

The first stage is to calculate the probability that one out of two vertices are merged as a function of their separation in Δz. This is done using a data-driven technique with low pileup data to reduce the effects of split and fake vertices. This probability is then assumed to be a constant for all runs and independent of μ.

In the second stage, the merging correction factor is calculated for groups of 10 LBs. This is because the width of the vertex distribution in z varies during a run and this in turn affects the merging probability. Ideally one would like to correct on a per LB basis, however, this is not possible due to the statistical precision of one LB.

6.5.4.1 Stage 1: The probability that two vertices merge

This section describes the process by which one calculates the probability that two vertices are merged, $p_{merge}(|\Delta z|)$, given their separation along the $\hat{z}$ axis. To improve the statistical precision, it is assumed that the functions used in vertex merging are symmetric in the variable Δz and this is tested in section 6.11.

There are two inputs to this calculation: the observed distribution of the vertices along the $\hat{z}$ axis, and the Δz separation between all unique pairs of vertices in the event, $f_{obs}(|\Delta z|)$. These inputs are taken from a low μ dataset such as the quiescent period of a vdM scan so that the contribution from fake and split vertices are small. This can be seen in figures 6.4 and 6.5. Additionally, this calculation is performed per working point.

1. The expected Δz distribution, $f_{exp}(|\Delta z|)$, of the vertices is defined to be what the Δz distribution would look like if there were no vertex merging. This can be estimated by randomly sampling pairs of points from the observed vertex z distribution and then calculating the absolute difference between these two points.

2. To obtain the correct normalisation for $f_{exp}(|\Delta z|)$, it is scaled by a constant, C_0, obtained by fitting to $f_{obs}(\Delta z)$ by,

$$f_{obs}(|\Delta z|) = C_0 \times f_{exp}(|\Delta z|) \; ; \; \Delta z \geq 50 \text{ mm}, \tag{6.7}$$

$$f'_{exp}(|\Delta z|) = C_0 \times f_{exp}(|\Delta z|). \tag{6.8}$$

   This fit is only performed in the tails of the distribution where the effect of vertex merging is negligible; in practice this is defined as $|\Delta z| > 50$ mm. This can be seen clearly in figure 6.3. Additionally a systematic is assigned to the region that is excluded from the fit and this is covered in section 6.11.2.

3. The function $p_{merge}(|\Delta z|)$ is calculated from the difference between the scaled expected, $f'_{exp}(|\Delta z|)$, and the observed case, $f_{obs}(|\Delta z|)$,

$$p_{merge}(|\Delta z|) = \frac{f'_{exp}|(\Delta z|) - f_{obs}(|\Delta z|)}{f'_{exp}(|\Delta z|)}. \tag{6.9}$$

   The quantity $p_{merge}(|\Delta z|)$ derived in the first stage is now assumed to be a constant for all runs and independent of μ. Figure 6.3 depicts the fit of $f_{exp}(|\Delta z|)$ to $f_{obs}(\Delta z)$ as well as $p_{merge}(|\Delta z|)$ for several of the WPs using data obtained from the quiescent period of the vdM scan with number 299390.

6.5.4.2 Stage 2: Applying the vertex merging correction

The next step is to calculate the total average per-event merging probability that any two vertices merge, P_{merge}, and from this the merging correction factor, f_{merge}. This correction is calculated for blocks of approximately 10 LBs at at time to account for changes in the z distribution of vertices during a run.

1. A new expected Δz distribution, $f_{exp,2}(|\Delta z|)$, is calculated using the same method as in the previous stage. However, now the input is the z distribution of vertices for the 10 LBs in the run that the correction it is to be calculated for. To obtain the total probability one integrates over $p_{merge}(\Delta z)$,

$$P_{merge} = 2 \times \int_0^\infty p_{merge}(|\Delta z|) \times C_1 f_{exp,2}(|\Delta z|) d\Delta z, \tag{6.10}$$

   where the factor of two arises as the modulus of Δz is used. C_1 is a normalisation constant so that $f_{exp,2}(|\Delta z|)$ has an integral of 1. This normalisation is given by

$$C_1 = \frac{1}{\int_{-\infty}^{\infty} f_{exp,2}(|\Delta z|) d\Delta z}, \tag{6.11}$$

   and it ensures that equation 6.10 is the multiplication of two probability distributions.

2. Using the total merging probability, P_{merge}, one can generate a function relating the average number of real reconstructed vertices per event, μ_{real}, to the number of vertices that could be reconstructed per event with no vertex merging, N_{gen}. To achieve this, the vertices are numbered in the order their reconstruction was attempted by the vertex finding algorithm, $1 \leq i \leq N_{gen}$. An iterative procedure is then used to calculate the probability that each vertex is reconstructed, p_i. This iterative procedure is required as one needs to account for the possibility that each vertex can merge with any other vertex.

3. The probability that the first vertex is reconstructed is defined to be 1, as there are no other vertices to merge with it,

$$p_1 = 1. \tag{6.12}$$

4. The probability that the second vertex is merged is given by the probability the first was reconstructed multiplied by the probability that it is not merged,

$$p_2 = p_1(1 - P_{merge}). \tag{6.13}$$

5. To calculate the probability that ith vertex is merged, an iterative procedure is applied. The probability for each vertex is now calculated after taking into account the probability that the previous vertices could be either have been merged or not,

$$p_k = \prod_{i=1}^{k-1} \left[p_i(1 - P_{merge}) + (1 - p_i) \right]. \tag{6.14}$$

   The first term in this equation, $p_i(1 - P_{merge})$, corresponds to the probability that the previous vertex i was reconstructed multiplied by the probability that it has not merged with vertex k. The second term, $(1 - p_i)$, corresponds to

the probability that the previous vertex i was merged and so cannot stop vertex k from being reconstructed. Equation 6.14 can be re-arranged to be more convenient for calculation so that each probability p_k only depends on p_{k-1},

$$\begin{aligned} p_k &= \prod_{i=1}^{k-1} \left[1 - p_i P_{merge}\right], \\ &= \left(1 - p_{k-1} P_{merge}\right) \prod_{i=1}^{k-2} \left[1 - p_i P_{merge}\right], \\ &= p_{k-1}\left(1 - p_{k-1} P_{merge}\right). \end{aligned} \tag{6.15}$$

6. A sum over the probabilities that each vertex is merged is then used to relate the average number of real reconstructed vertices per event, μ_{real}, to the number of vertices that could be reconstructed per event with no vertex merging, N_{gen}.

$$\mu_{real}\left(N_{gen}\right) = \sum_{i=1}^{N_{gen}} p_i \tag{6.16}$$

7. The total number of proton-proton interactions per event is a Poisson distributed process. To obtain the mean number of real reconstructed vertices per event, μ_{real}, as a function of the mean number of vertices that could be reconstructed if none were merged, μ_{vis}, one convolves the Poisson distribution, $P\left(N_{gen}; \mu_{vis}\right)$, with equation 6.16:

$$\mu_{real}\left(\mu_{vis}\right) = \sum_{N_{gen}=1}^{\infty} \left[P\left(N_{gen}; \mu_{vis}\right) \mu_{real}\left(N_{gen}\right)\right]. \tag{6.17}$$

8. From equation 6.6 and 6.17 one can obtain f_{merge} as a function of μ_{vis},

$$f_{merge} = \frac{\mu_{vis}}{\mu_{real}} = \frac{\mu_{vis}}{\sum_{N_{gen}=1}^{\infty} \left[P\left(N_{gen}; \mu_{vis}\right) \mu_{real}\left(N_{gen}\right)\right]}. \tag{6.18}$$

9. Finally a plot of f_{merge} against μ_{real} can be plotted. This is achieved by numerical methods and is then parametrised with a 4th order polynomial function so that it can be calculated for any value of μ_{real},

$$f_{merge} = \sum_{k=0}^{n=4} \left[c_k \times \mu_{vis}^k\right]. \tag{6.19}$$

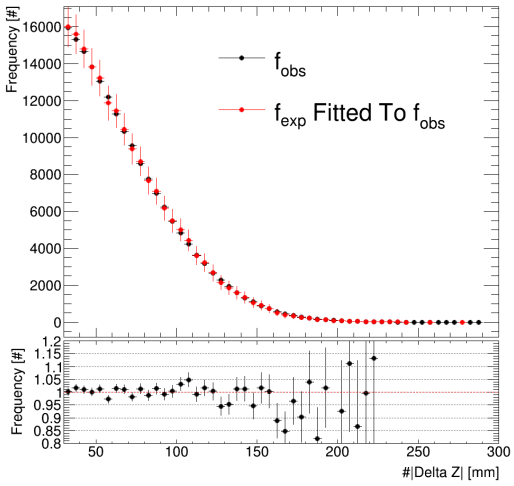

(a)$|\Delta z|$ template fit, `nVtx3_900`.

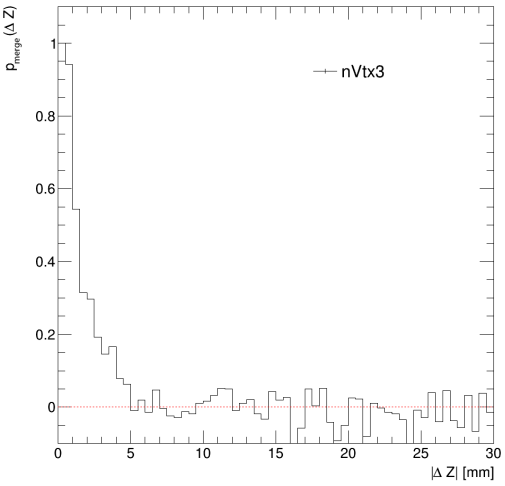

(b) $p_{merge}\left(|\Delta z|\right)$, `nVtx3_900`.

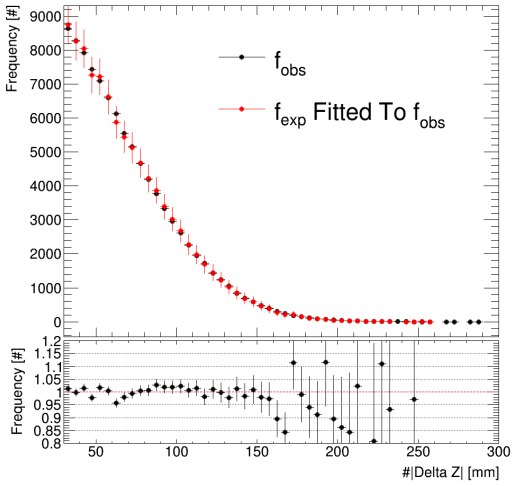

(c)$|\Delta z|$ template fit, `nVtx5_900`.

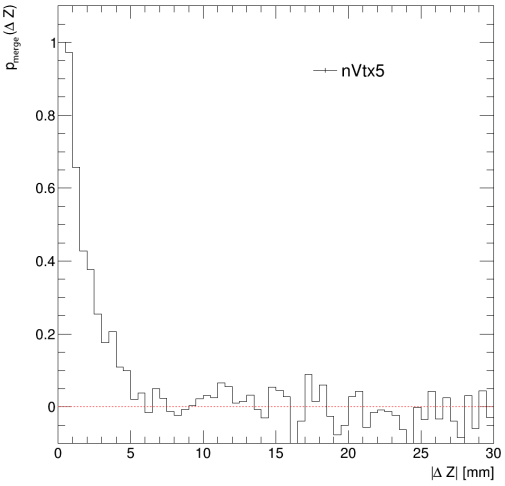

(d) $p_{merge}\left(|\Delta z|\right)$, `nVtx5_900`.

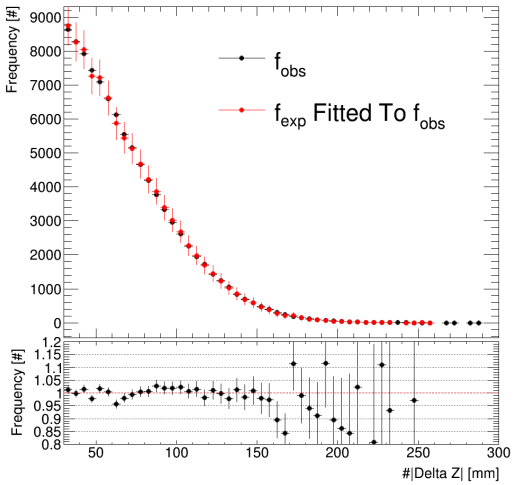

(e)$|\Delta z|$ template fit, `nVtx7_900`.

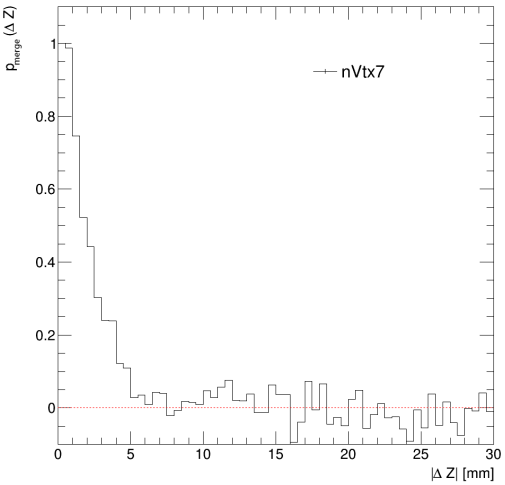

(f) $p_{merge}\left(|\Delta z|\right)$, `nVtx7_900`.

FIGURE 6.3: The working points shown here are `nVtx3`, `nVtx5` and `nVtx7`. The left three plots (a,c,e) show the fit of f_{exp} to f_{obs} in the Δz region where vertex merging has no effect. The right three (b,d,f) plots show the distribution of $p_{merge}\left(|\Delta z|\right)$. The data used in these plots was obtained from the quiescent period of run 299390. All WPs use a p_{T} cut of 900 MeV.

6.5.5 The split vertex correction

The split vertex correction is evaluated using MC truth information and more details on MC truth logic can be found in Appendix B.1. A vertex pair is classified as split if both of the vertices have the majority of their associated tracks truth-matched to the same proton-proton interaction. The split correction is parametrised in terms of μ_{vis},

$$\mu_{split} = \mu_{split}(\mu_{vis}). \tag{6.20}$$

Figure 6.4 depicts the average number of splits per event as a function of μ_{truth} and as a function of the number of vertices that could have been reconstructed with perfect track matching, μ_{MC}. The right hand side plot of figure 6.4 is then parametrised with an third order polynomial,

$$\mu_{split} = \sum_{k=0}^{3} \left[c_{k,split} \times \mu_{MC}^{k} \right]. \tag{6.21}$$

Then the substitution that $\mu_{MC} = \mu_{vis}$ is made, and this is tested in section 6.7. This gives,

$$\mu_{split} = \sum_{k=0}^{3} \left[c_{k,split} \times \mu_{vis}^{k} \right]. \tag{6.22}$$

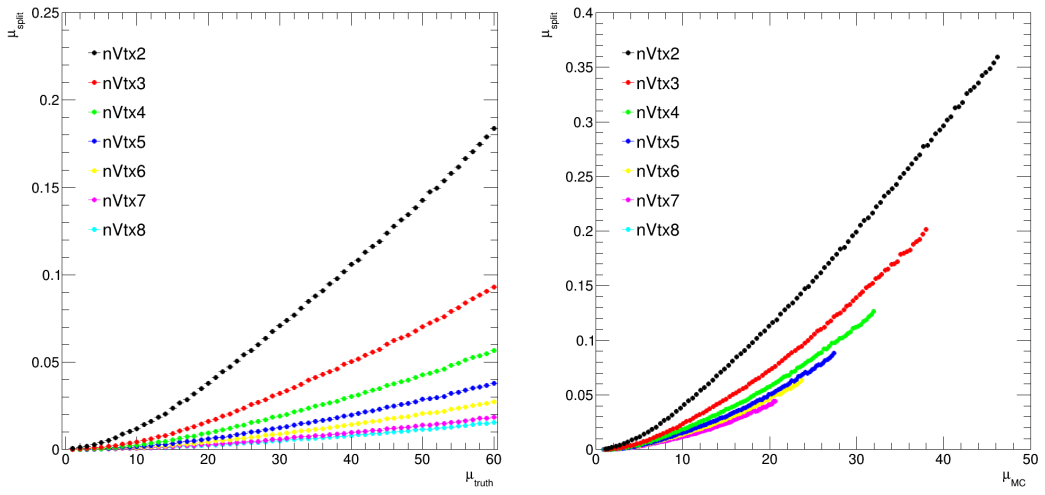

FIGURE 6.4: Left: The average number of split vertices, μ_{split}, per event as a function of μ_{truth}. Right: The average number of split vertices, μ_{split}, per event as a function of μ_{MC}. All WPs use a p_T cut of 900 MeV.

6.5.6 The fake vertex correction

The fake vertex correction is parametrised in an analogous manner to the split correction. Like the split vertex correction, the fake correction is also evaluated using MC truth information. More details on this can be found in Appendix B.2. A vertex pair is classified as fake if after using MC truth information to remove the incorrectly matched tracks it fails the cut on the number of associated tracks imposed by

the working point. The fake correction is parametrised in terms of μ_{vis},

$$\mu_{fake} = \mu_{fake}(\mu_{vis}). \tag{6.23}$$

From here one proceeds in exactly the same manner as for split vertices creating two plots of μ_{fake} as a function of μ_{truth} and μ_{MC} as a function of μ_{truth}. Again like the split correction these are combined into a plot of μ_{fake} as a function of μ_{MC}. Finally the distributions in figure 6.5 are parametrised with an third order polynomial and with the substitution that $\mu_{MC} = \mu_{vis}$ one obtains,

$$\mu_{fake} = \sum_{k=0}^{3} \left[c_{k,fake} \times \mu_{vis}^{k} \right]. \tag{6.24}$$

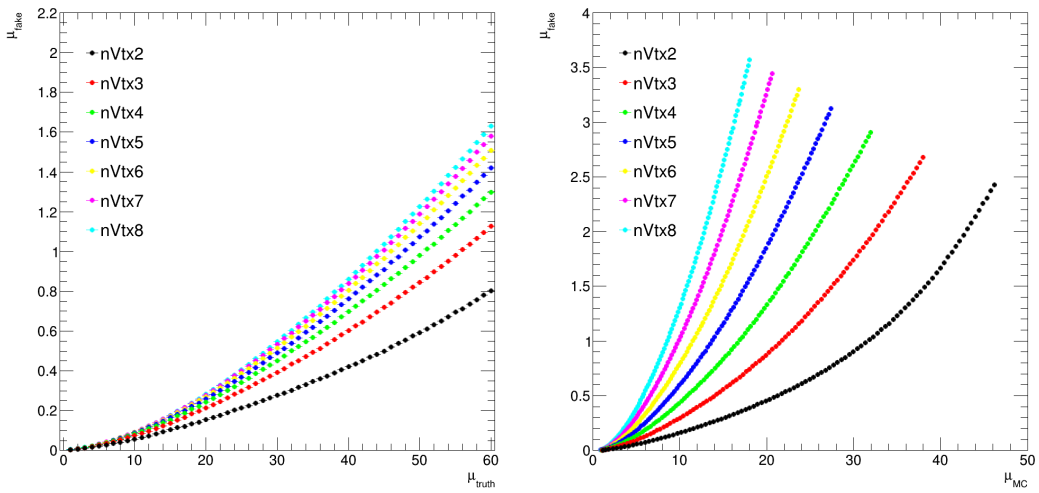

FIGURE 6.5: Left: The average number of fake vertices, μ_{fake}, per event as a function of μ_{truth}. Right: The average number of fake vertices, μ_{fake}, per event as a function of μ_{MC}. All WPs use a p_T cut of 900 MeV.

6.5.7 Final parametrisation

The vertex counting algorithm calculates a value of μ_{vis} for every 10 LBs in a run[4]. For the reader's convenience the parametrisation of the three pileup corrections are given below:

$$\mu_{merged} = \left[f_{merge}(\mu_{real}) - 1 \right] \times \mu_{real}, \tag{6.25}$$

$$\mu_{split} = \mu_{split}(\mu_{vis}), \tag{6.26}$$

$$\mu_{fake} = \mu_{fake}(\mu_{vis}). \tag{6.27}$$

The issue with this parametrisation is that the value of μ_{vis} is not yet known, as this is the output of the algorithm. The solution to this is to approximate μ_{vis} by $\mu_{vis,0}$. To obtain this, the vertex merging correction is applied to the number of reconstructed vertices,

$$\mu_{vis,0} = \mu_{rec} \times f_{merge}(\mu_{rec}). \tag{6.28}$$

[4]For runs with a number of LBs that is not divisible by 10 the remaining LBs are grouped with the final 10, so a run with 112 LBs will contain one calculation with 12 LBs.

Then an iterative procedure is used to find $\mu_{vis,\infty}$ where the output from n iterations, $\mu_{vis,n}$, is iterated:

$$\mu_{real,n+1} = \mu_{rec} - \mu_{fake}(\mu_{vis,n}) - \mu_{split}(\mu_{vis,n}), \tag{6.29}$$

$$\mu_{vis,n+1} = \mu_{real,n} \times f_{merge}(\mu_{real,n}). \tag{6.30}$$

This iterative procedure is repeated until the following condition is met,

$$\frac{|\mu_{vis,n+1} - \mu_{vis,n}|}{|\mu_{vis,n+1} + \mu_{vis,n}|} < 0.001, \tag{6.31}$$

as further iterations will no longer improve the accuracy of the algorithm. The result of the iteration is that one can parametrise the vertex merging corrections in terms of μ_{vis}.

6.6 Optimisation of the working points

This section describes the process by which the cuts on the WPs were optimised and each WP is optimised individually.

6.6.1 Linearity of μ_{vis} and μ_{MC}

The quantity μ_{MC} is the truth equivalent of μ_{vis} and so it is required to be linear with μ_{truth} for this algorithm to function properly. Figure 6.6 depicts the quantity μ_{MC} for `nVtx4_900` and `nVtx4_2000` as a function of μ_{truth} along with a fitted first order polynomial to demonstrate linearity. For the WP `nVtx4_900` it is clear that μ_{MC} is not linear with μ_{truth}. However, increasing the p_{T} cut on the tracks increases the linearity of μ_{MC}. In Run 1 this relationship was linear without increasing the p_{T}. The reason for this change is that the efficiency of associating tracks to a vertex is a μ dependent quantity. The higher pileup in Run 2 results in a lower efficiency for track to vertex association. Increasing the p_{T} on the associated tracks greatly reduces this effect. Ideally one would want to set this p_{T} cut as high as possible to reduce the effect of the non linearity of μ_{MC} with respect to μ_{truth}.

6.6.2 Radial cut optimisation

The radial cut was required to remove the effect of secondary vertices in the Δz distribution and more detail on this can be found in Appendix A. It was found that a cut of $R < 0.3$ mm was sufficient to negate the impact of secondary vertices on the Δz distribution. Further tightening of this cut had no effect other than to reduce the statistics.

6.6.3 p_{T} cut optimisation

The limiting factor on how tight cuts on the WPs can be set to was found to be the determination of $p_{merge}(|\Delta z|)$. If the cuts on the WPs are too tight it becomes impossible to resolve the dip to zero in the Δz distribution of vertices. The p_{T} cut was set as high as possible before the statistical error on the determination of P_{merge} was larger than 0.1%. This was tested in steps of 200 MeV[5]. Table 6.1 summarises

[5]The first step was 100 MeV.

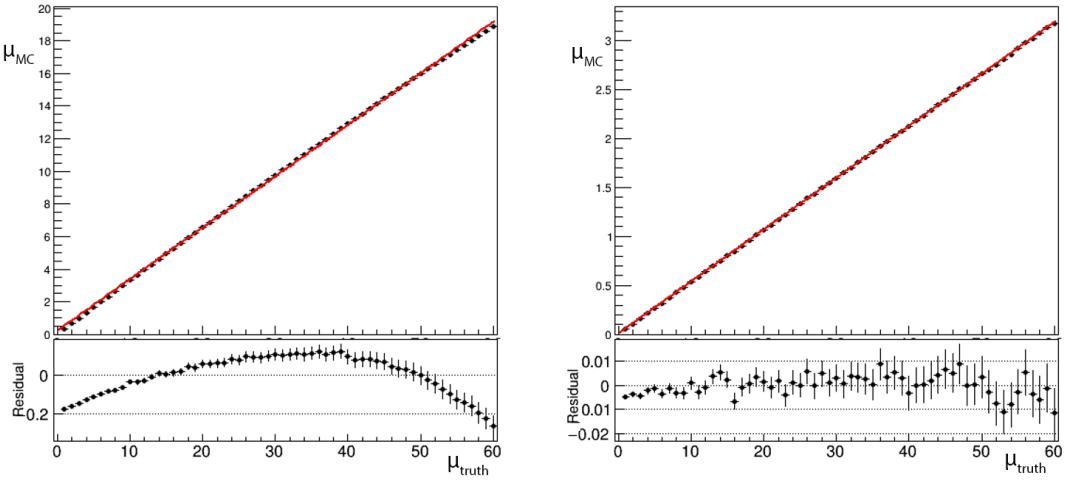

FIGURE 6.6: The top panel depicts the quantity $\mu_M C$ as a function of μ_{truth} for the WPs `nVtx4_900` (left) and `nVtx4_2000` (right). The red line is a first order polynomial fit and the bottom panel shows the residuals to this fit.

the value of the p_{T} and R cuts for all the WPs. It can be seen in section 6.7 that these p_{T} cuts are effective in restoring linearity to μ_{MC}.

Working Point	default p_T cut [MeV]	default R cut [mm]
`nVtx2`	1800	0.3
`nVtx3`	1600	0.3
`nVtx4`	1400	0.3
`nVtx5`	1200	0.3
`nVtx6`	1200	0.3
`nVtx7`	1000	0.3
`nVtx8`	900	0.3

TABLE 6.1: Table of default p_T cut for the vertex counting WPs. This has been optimised to be as high as possible while retaining enough statistics to determine $p_{merge}(|\Delta z|)$.

6.6.4 Changes to the original method

This section will cover the changes made to the algorithm since its previous iteration which is covered in [43]. The changes made to this algorithm were designed to improve upon the statistical precision and to better calculate the pileup corrections.

Previously the modulus of the Δz distribution was not used. This change effectively doubles the statistics available to calculate the merging correction. As no asymmetry has been previously observed in Δz, all the functions associated with the vertex merging correction are expected to be symmetric in this variable.

The split vertex correction was previously negated in other iterations of this algorithm. Although its effect is smaller than both the merged and fake vertex correction its inclusion provides a more accurate prediction of μ_{vis}. Additionally, the higher pileup in Run 2 with respect to Run 1 means that the split correction is larger than for previous iterations of this algorithm as they were designed for Run 1.

For the Run 1 iteration of this algorithm there was no variable cut on the p_T of the tracks associated to the vertex other than the ones imposed by the `VtxLumi` cuts covered in section 6.2. It was found that optimizing this p_T cut was required for the Run 2 version of the algorithm. The reason why this cut was required can be found in section 6.6.1.

6.7 Monte Carlo closure

A Monte Carlo closure test is performed to validate the three pileup corrections that are described in section 6.5. The same MC is used here as the one that was used to evaluate the fake and split corrections. Ideally one would want to use a statistically independent dataset, however, none were available. The merging correction was evaluated using the normal data-driven method on the $\mu = 2$ dataset. The WPs used in this section use the optimised cuts as described in section 6.6.

To have MC closure the output of the vertex counting algorithm, μ_{vis}, must correctly calculate the number of vertices that could have been reconstructed without pileup effects, μ_{MC}, which can be obtained using MC truth information. Furthermore it is required for the quantity μ_{vis} to be linear with μ_{truth}.

All of the following plots in this section show 4 quantities μ_{vis}, μ_{rec}, μ_{real} and μ_{MC} as a function of μ_{truth} fitted with a first order polynomial to allow a visualisation of the linearity. Figure 6.7 depicts the WPs `vNtx2_1800` and `vNtx3_1600`. It can be seen for the WP `vNtx2_1800` the method does not close as the black points (μ_{vis}) do not lie on top of the blue points (μ_{MC}). This is likely because the MC poorly describes vertex merging and fakes for this WP. For the WP `vNtx3_1600`, μ_{vis} does correctly recover μ_{MC}, however, neither quantity is linear with μ_{truth} and the reason for this is covered in section 6.6.1. With more statistics available to evaluate P_{merge} for higher values of the p_T cut it should be possible to get a linear relationship between μ_{vis} and μ_{MC} for `vNtx3_1600`.

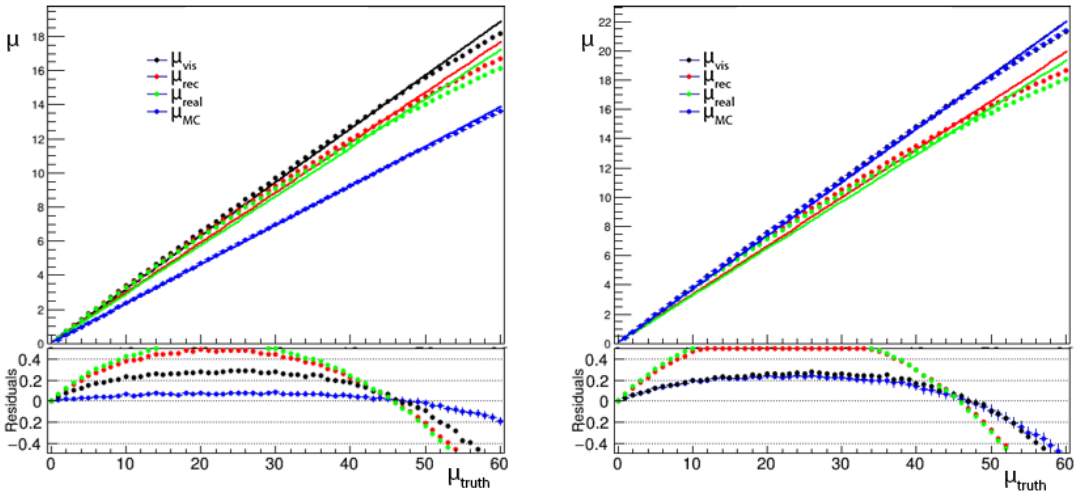

FIGURE 6.7: Closure test for the WPs `vNtx2_1800` (left) and `vNtx3_1600` (right). Top top panel shows the quantities μ_{vis}, μ_{rec}, μ_{real} and μ_{MC} as a function of μ_{truth} fitted with a first order polynomial. The bottom panel shows the residual to this first order polynomial fit. The value of μ_{vis} for the WP `nVtx2_1800` failed to recover μ_{MC}. The WP `vNtx3_1600` failed to have a linear μ_{vis}.

Figures 6.8 and 6.9 show the closure for the remaining WPs. Here, it can be seen that for the remaining WPs μ_{vis} does correctly recover μ_{MC} and that both quantities are linear with μ_{truth}.

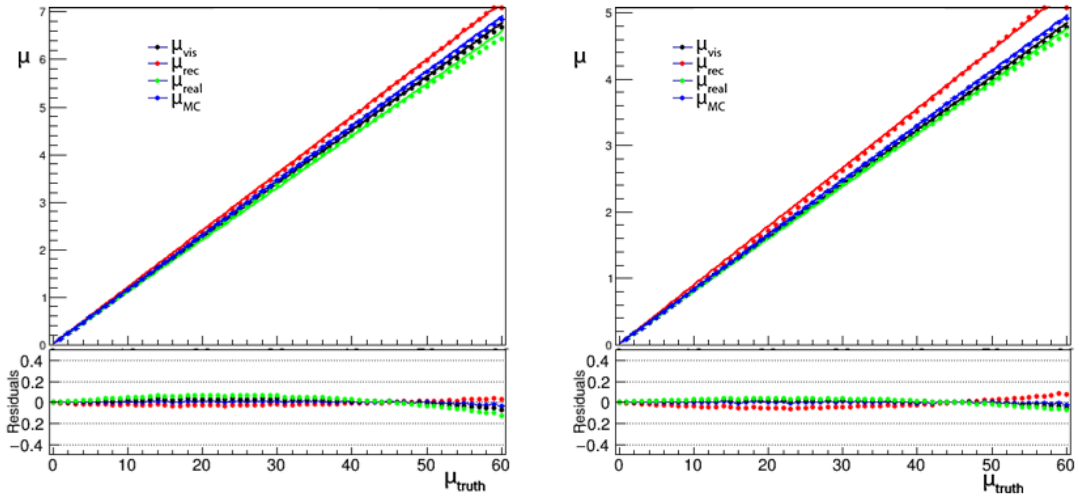

FIGURE 6.8: Closure test for the WPs `vNtx4_1400` (left) and `vNtx5_1200` (right). Top top panel shows the quantities μ_{vis}, μ_{rec}, μ_{real} and μ_{MC} as a function of μ_{truth} fitted with a first order polynomial. The bottom panel shows the residual to this first order polynomial fit.

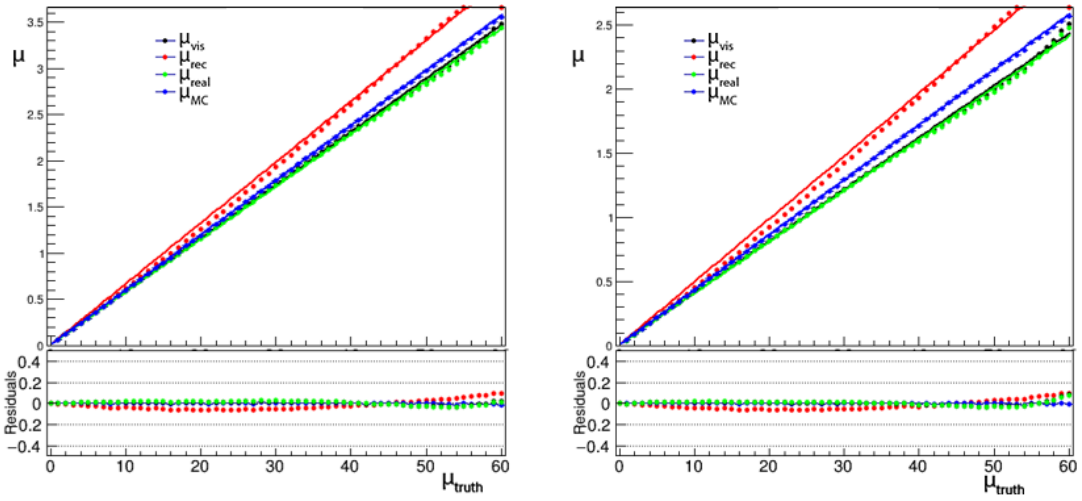

FIGURE 6.9: Closure test for the WPs `vNtx7_1000` (left) and `vNtx8_900` (right). Top top panel shows the quantities μ_{vis}, μ_{rec}, μ_{real} and μ_{MC} as a function of μ_{truth} fitted with a first order polynomial. The bottom panel shows the residual to this first order polynomial fit.

In summary MC closure has been demonstrated for all WPs `nVtx4-8`. The value of μ_{vis} for the WP `nVtx2_1800` failed to recover μ_{MC}. The WP `vNtx3_1600` failed to have a linear μ_{vis}.

6.8 Calibrating the algorithm

To calibrate the algorithm the reference long physics run 299584 is used. The choice of run is motivated by the fact that it was a long physics run that was measured very close in time to the vdM scan with run number 299390. The reference algorithm used to calibrate the vertex counting algorithm was chosen to be `LUCIDHitOR`. This calibration was performed per WP.

6.9 Internal consistency

Figures 6.10 and 6.11 depict the ratio of the luminosity predictions of the WPs `nVtx4-8` with respect to `nVtx6_1200` for two long physics runs in 2016. Each ratio is fitted with a first order polynomial to allow a visualisation of the "flatness". It can be seen that the working points that had MC closure are in very good agreement with each other after calibration. The WPs used in this section use the optimised cuts as described in section 6.6.

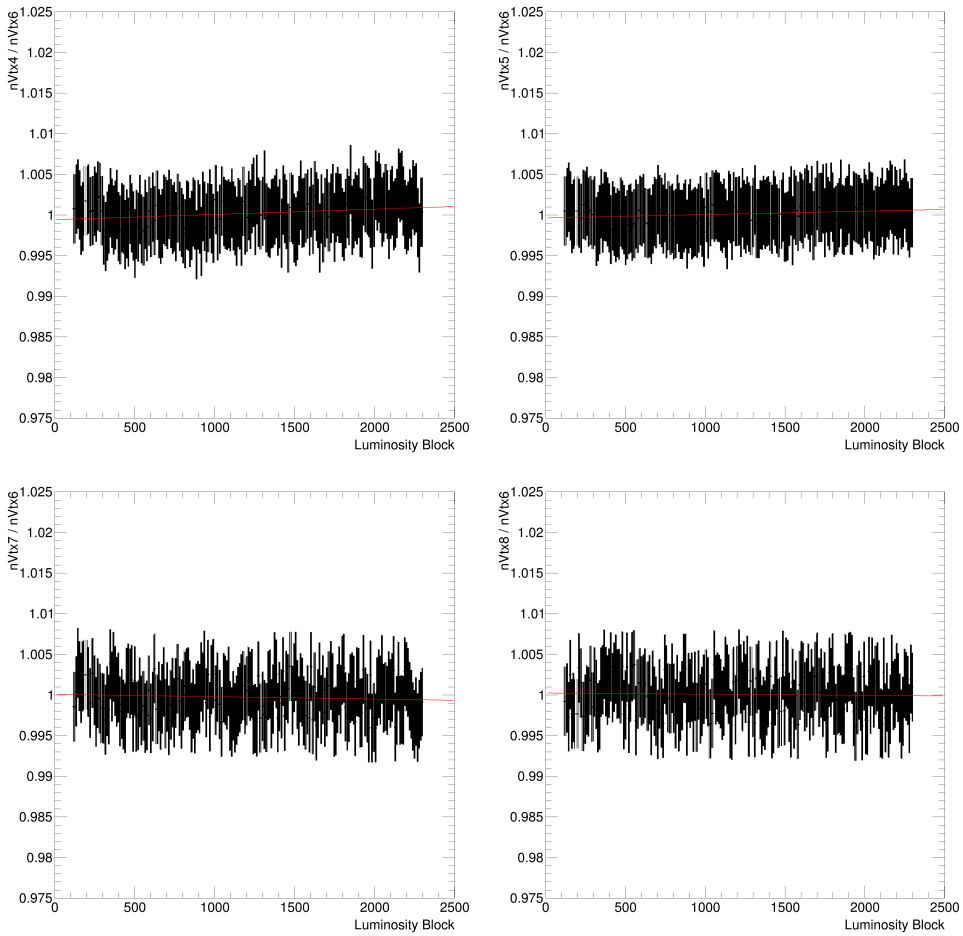

FIGURE 6.10: Internal stability ratios of the luminosity prediction with respect to `nVtx6_1200` for all WPs that have MC closure. The ratio in this figure is for the run number 299584. The working points `nVtx4-nVtx8` show good agreement with each other

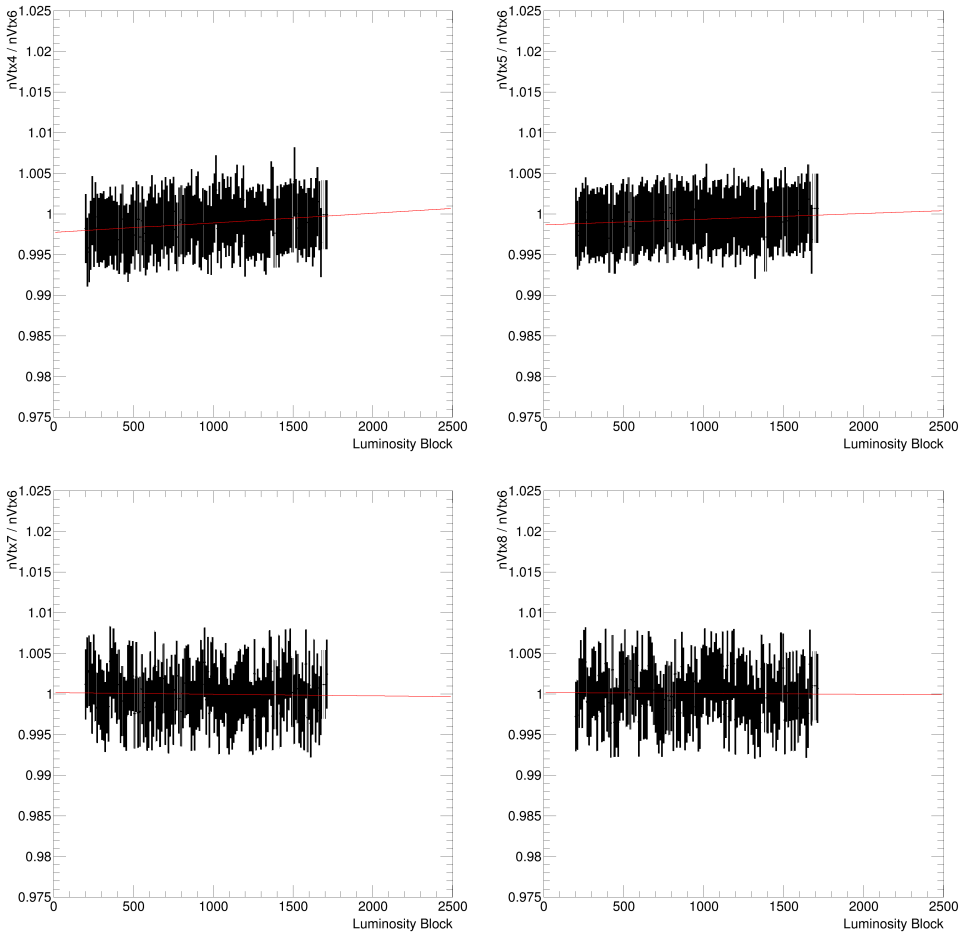

FIGURE 6.11: Internal stability ratios of the luminosity prediction with respect to `nVtx6_1200` for all WPs that have MC closure. The ratio in this figure is for the run number 302300. The working points `nVtx4`-`nVtx8` show good agreement with each other

The remainder of the runs that were analysed have a similar behaviour. As shown in section 6.5 the pileup corrections are very different for each WP. This suggests that the vertex counting algorithm demonstrates internal consistency as it has been shown to provide similar results over a large range of values for the p_{T} cut and the number of associated tracks cut.

Figure 6.12 shows the same ratios as figures 6.10 and 6.11, however now the WPs `nVtx2` and `nVtx3` are shown. It can be seen that these two WPs have a much poorer agreement with the other 5 WPs. This is to be expected as they did not have MC closure.

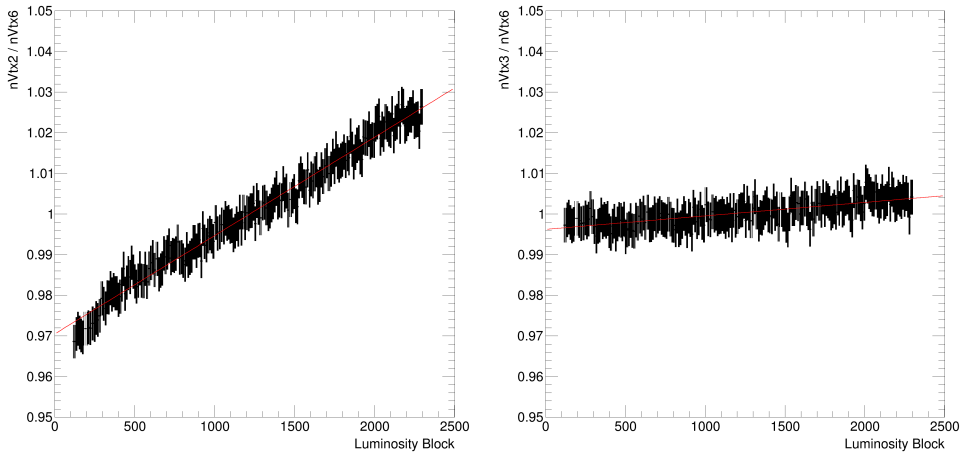

FIGURE 6.12: Internal stability ratios of the luminosity prediction with respect to `nVtx6_1200` for all WPs that do not have MC closure. The ratio in this figure is for the run number 299584. As expected the stability ratios are far worse for these working points than the others as they did not have MC closure.

6.10 External consistency

Figure 6.13 and 6.14 depict the ratio of the luminosity as predicted by the vertex counting algorithm with respect to other luminosity algorithms. Only the WP `nVtx6_1200` is used because all other considered WPs that had MC closure are consistent with it. The other algorithms that are compared to the vertex counting algorithm are `OR_BI_LUCID`, `Mean_EMEC`, `Mean_D5_TILE`, and `PIXELENHANCED2_TRACKS`. The calibration for the non vertex counting algorithms is the preliminary calibration update from February 2017. The WPs used in this section use the optimised cuts as described in section 6.6.

The figures 6.13 and 6.14 show that there is still a small residual μ dependence for vertex counting. It is of the order of 1%, which is an increase to the previous iteration of this algorithm in 2012. The behaviour of these two runs is typical for the whole of 2015-2016. The vertex counting algorithm is consistent with the four luminosity algorithms considered in this section to within its statistical and systematic errors. The WPs `nVtx2` and `nVtx3` are not shown in this section as they are known to be inconsistent and do not have MC closure.

Additionally it can be seen that the other algorithms do not perfectly agree with each other. The difference in the predictions between the different algorithms is taken as a systematic on the final luminosity measurement as it is not possible to determine if one is more correct than the others.

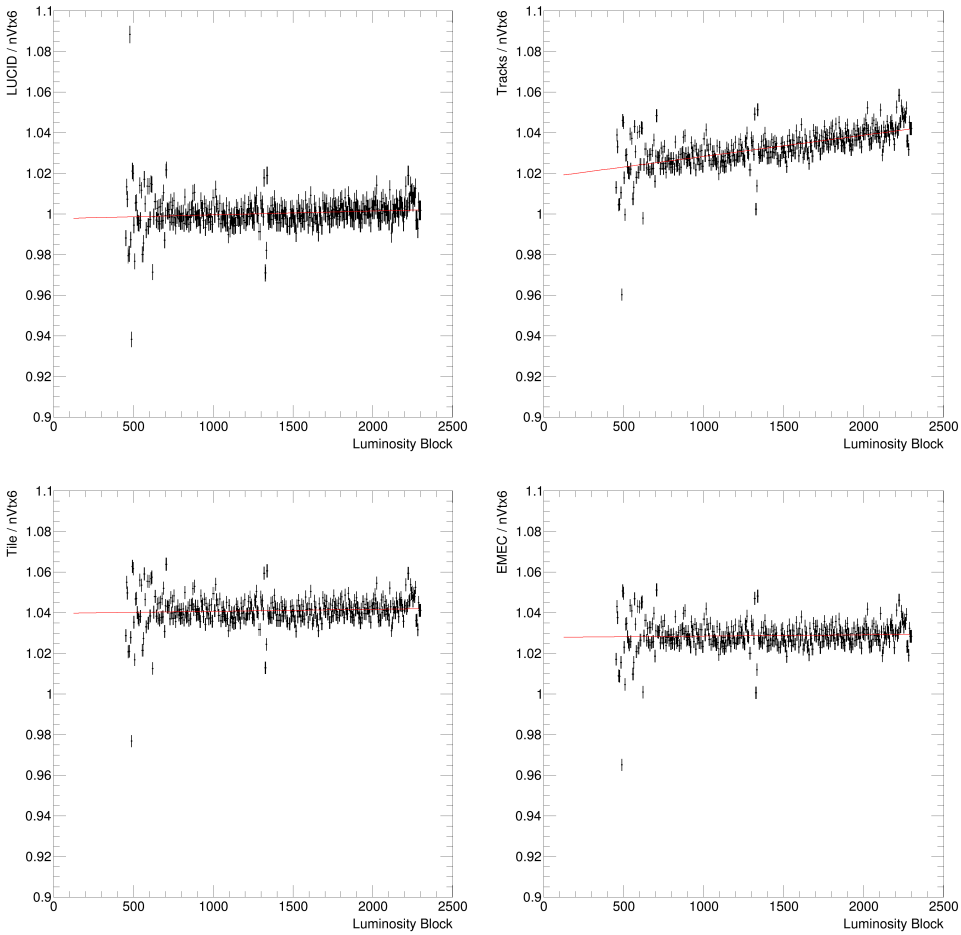

FIGURE 6.13: External stability ratios with respect to `nVtx6_1200`. The other algorithms shown in this plot are LUCID (top left), Tracks (top right), Tile (bottom left) and EMEC (bottom right). The ratio in this figure is for the run number 299584.

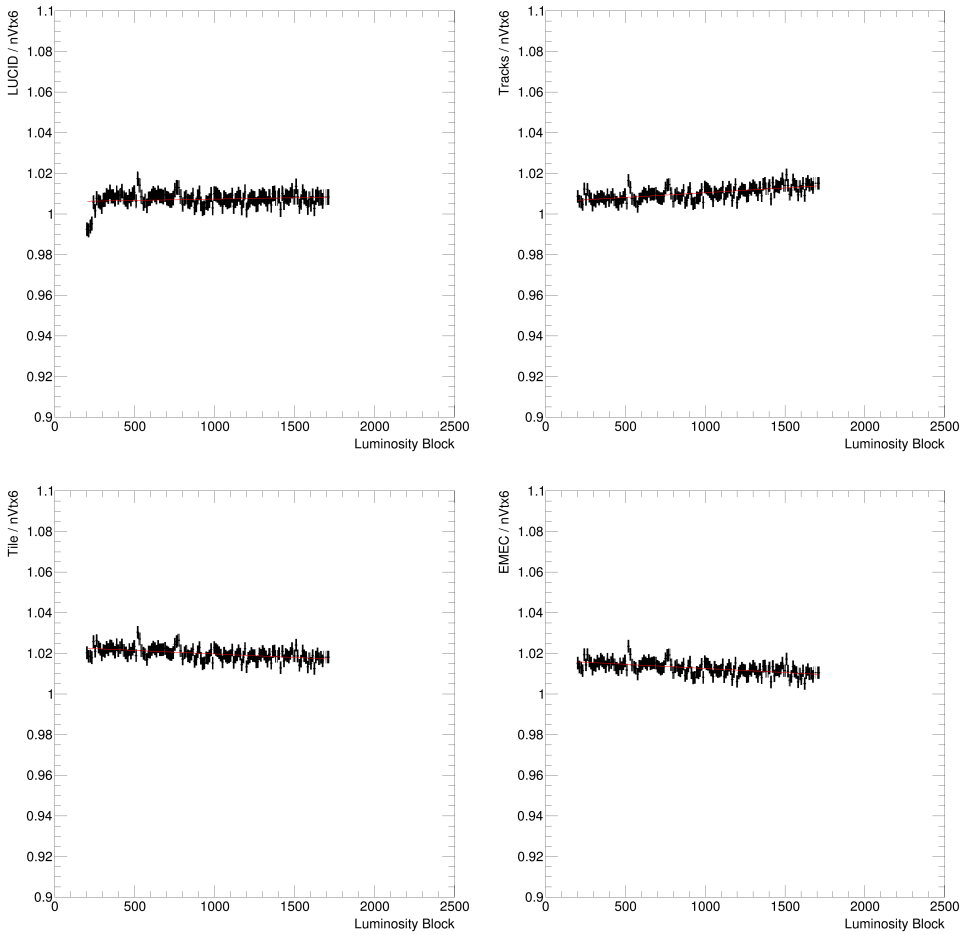

FIGURE 6.14: External stability ratios with respect to `nVtx6_1200`. The other algorithms shown in this plot are LUCID (top left), Tracks (top right), Tile (bottom left) and EMEC (bottom right). The ratio in this figure is for the run number 302300.

6.11 Statistical and systematic uncertainties

The uncertainties listed in this section are specific to the vertex counting algorithm. However, as the vertex algorithm is calibrated in a long physics run it is required to account for the systematic error that arises from this calibration process and this is covered at the end of the section. When uncertainties refer to the maximal difference for all WPs, the WP `nVtx2` and `nVtx3` have been excluded as they do not have MC closure as shown in section 6.7.

6.11.1 Statistical uncertainty

There are four sources of statistical uncertainty that effect the vertex counting algorithm. Three of these sources are the determination of each of the three pileup corrections and the final source is the number of vertices reconstructed in a 10 LB period.

The statistical error on the split and fake corrections are negligible as the number of events in the MC datasets used to determine these corrections is high. Furthermore, the optimisation procedure for the WP cuts does not allow the statistical error on the value of P_{merge} to be greater than 0.1%. This value, however, is used multiple times in the determination of f_{merge}. To determine the impact on f_{merge} the value of P_{merge} was shifted up and down by 0.1%. It was found that the resulting effect on f_{merge} was maximally 1.2%. As the correction f_{merge} is maximally of the order 10%, the impact on μ_{vis} is 0.12%.

The determination of the average number of reconstructed vertices can be approximated using Gaussian statistics. In a 10 LB period there are approximately 100000 events with which to calculate this average. The error on the mean is proportional to $1/\sqrt{N_{events}}$ and so the error will be of the order of 0.1%.

6.11.2 Determination of P_{merge}

Section 6.5.4 covers the determination of the probability that two vertices merge. In this section when $f_{exp}(|\Delta z|)$ is fitted to $f_{obs}(|\Delta z|)$ the region $\Delta z \geq 50$ mm is excluded. A systematic is assigned to the change in the value of P_{merge} when the the excluded region is widened. To test the sensitivity to this exclusion region, P_{merge} was determined again using an exclusion region of $\Delta z \geq 100$ mm. The maximal difference between f_{merge} calculated using the normal exclusion (50 mm) and the new exclusion (100 mm) region was 2.0% and so a systematic of 0.2% is assigned using the same argument as the previous systematic.

6.11.3 Symmetrizing Δz

Symmetrizing the Δz distribution effectively doubles the number of available statistics to perform the calculation of P_{merge}. The difference in the calculation of P_{merge} with and without taking the modulus of Δz was calculated for all WPs for the quiescent period in the vdM scan with run number 299390 and it was found that the maximal difference resulted in a systematic of 0.1% using the same logic as the previous two sections. This is due to the slight normalisation difference of $f_{exp}(|\Delta z|)$ between the two methods due to statistics.

6.11.4 Luminous region width impact on fake correction

The width of the luminous region in the MC is not the same as what is typically observed in data along the $\hat{z}$ axis. The number of fakes is expected to be influenced by the density of of the vertices in the detector. Thereby, for the same value of μ a run with a narrower distribution along the $\hat{z}$ axis should have a larger fake correction. To first order this correction will be linearly proportional to the difference in the root mean square z (RMS(Z)) values between the luminosity blocks where the fake correction is being applied and the MC where the fake correction was evaluated. This can be expressed as:

$$\mu_{fake}^{corrected} = \frac{\mathrm{RMS}(z)^{MC}}{\mathrm{RMS}(z)^{Data}} \times \mu_{fake}. \tag{6.32}$$

When this additional correction is applied to this algorithm it was found that the maximal difference between the corrected luminosity predictions was 0.42%.

6.11.5 μ dependence

Comparisons of the vertex counting to other algorithms in section 6.10 show that there is still a remaining μ dependence. A systematic of the size 1% is assigned to cover this μ dependence.

6.11.6 μ_{MC} linearity

As demonstrated in section 6.6.1 μ_{MC} is not perfectly linear with μ_{truth}. Although this problem is greatly reduced with the optimisation of the p_{T} cut, it is not entirely removed. To account for the remaining non-linearity a systematic of the size 0.2% is applied.

6.11.7 Algorithm calibration

There is a systematic error associated with the process by which the vertex counting algorithm is calibrated using the prediction of LUCID in the run 299584. The systematic errors that effect the LUCID algorithm's prediction are given in table 6.2. The total systematic associated with the calibration is 1.9%.

6.11.8 Summary of errors

Table 6.3 summarises all of the errors previously covered in this section. The total error on the luminosity prediction of the vertex counting algorithm in a 10 LB period is 2.2%.

Source	Uncertainty [%]
DCCT calibration	0.2
FBCT bunch-by-bunch fractions	0.1
Scan curve fit model	0.5
Background subtraction	0.2
Orbit-drift correction	0.1
Beam position jitter	0.3
Beam-beam effects	0.3
Emittance growth correction	0.2
Non-factorisation effects	0.4
Length-scale calibration	0.3
ID length scale	0.1
Bunch-by-bunch σ_{vis} consistency	0.2
Scan-to-scan reproducibility	0.5
Reference specific luminosity	0.2
Subtotal for absolute vdM calibration	1.1
Calibration transfer	1.6
Afterglow and beam-halo subtraction	0.1
Total	1.9

TABLE 6.2: Summary of the systematic errors on the determination of the calibration of algorithms using the LUCID detector. The table summarises the breakdown of the contributions to the vdM calibration as well as the calibration transfer to physics running. The table was obtained from [119].

Source	Uncertainty [%]
Statistical: merged correction	0.12
Statistical: μ_{rec} determination	0.1
Sub-Total Statistical	0.16
Determination of P_{merge}	0.2
Symmetrizing Δz	0.1
Luminous region width impact on fakes	0.42
μ dependence	1.00
μ_{MC} linearity	0.2
Algorithm calibration	1.9
Sub-Total Systematic	2.2
Total	2.2

TABLE 6.3: This table summarises all of the statistical and systematic errors that affect the luminosity prediction of the vertex counting algorithm. All of the systematic errors in this table are correlated between each 10 LB measurement.

6.12 Conclusion and future prospects

The vertex counting algorithm has been updated to perform well on data collected by ATLAS in Run 2. It was validated using a MC closure test where all but two of the WPs were validated. The algorithm was calibrated using the long physics run 299584 with a comparison to the prediction from the LUCID algorithm. All of the WPs that passed the MC closure test were then demonstrated to have a good internal consistency, furthermore the same working points were also demonstrated to be consistent with `OR_BI_LUCID`, `Mean_EMEC`, `Mean_D5_TILE`, and `PIXELENHANCED2_TRACKS`. Finally the statistical and systematic errors were evaluated on the algorithm. It was found that the algorithm can predict the luminosity over a 10 LB time period with a precision of 2.2%.

The future of the vertex counting algorithm into Run 3 is going to be challenging. This is because the algorithm is strongly affected by pileup and with the even higher pileup conditions expected in Run 3 it is going to be difficult to model the pileup corrections to a sufficient accuracy. Increasing the p_{T} cuts on tracks can greatly reduce the impact of pileup. Thereby, if a low μ dataset with enough statistics to resolve the dip in the Δz vertex distribution at Δz~0 for higher p_{T} cuts were available this effect could be somewhat mitigated.

The main issue with the algorithm is that the fake correction is only evaluated in one Monte Carlo dataset with a fixed width of the luminous region in the $\hat{z}$ direction. This is accounted for by applying a systematic, however, this effect will be needed to be better studied for the higher pileup in Run 3. The other main issue is that the algorithm cannot provide a better time resolution than a period of 10 LBs. This is a fundamental limitation due to the statistical precision available. The final issue is that two of the eight working points did not have MC closure. The suspected reason for this is that the MC based corrections poorly describe these lower track vertices. These WPs were also seen to behave poorly in Run 1.

Chapter 7

Precision measurements of vector boson fusion

This chapter presents precision differential cross-section measurements for the electroweak production of a Z boson in association with two jets in a phase space designed to enhance the contribution of the electroweak Zjj process. Section 7.1 provides an introduction to the background of Zjj production. Then section 7.2 covers the data and MC samples used in this analysis. Section 7.3 covers basic event selection. Section 7.4 describes the corrections applied to the MC datasets. Section 7.5 contains comparisons of data and MC simulations, revealing a general mismodelling of the dominant background process. Section 7.6 summarises the method used to constrain the background modelling and to extract the electroweak signal. Section 7.7 illustrates the systematics and how they were evaluated. Section 7.8 shows the predicted uncertainties calculated using Asimov data. Section 7.9 presents the differential electroweak cross-section. Section 7.10 describes an alternative method to extract the electroweak signal along with comparisons to the method. Finally section 7.11 is a summary of the results.

7.1 Introduction

The majority of events at ATLAS containing the production of a Z boson in association with at least two jets are produced via the so-called "strong Z boson production" (strong-Zjj). In this process, the jets are produced via a strong force interaction, such as initial state QCD radiation from the incoming partons. An example of this is the Drell Yan process shown in the left hand side of figure 7.1. In strong-Zjj events, the two jets are colour-connected, and this produces an experimental signature of additional jet activity, produced predominantly in the rapidity interval between the two leading jets.

An alternative production mechanism for Zjj is quark-quark scattering mediated by the t-channel exchange of a weak gauge boson [131, 132]. This is referred to as the electroweak production of a Z boson in association with two jets (EW-Zjj). This is a purely electroweak process and so the rate is approximately $O(100)$ times lower than the strong-Zjj process. As covered in section 2.3.4, the structure constant for the $SU(2)_L$ group is the totally anti-symmetric tensor ϵ_{ijk}, which allows for self interaction between the photon and the W/Z boson. The result of this self interaction are triple (TGC) and quartic (QCG) gauge couplings. In the SM the allowed TGCs are the $WW\gamma$ and the WWZ vertex. The WWZ vertex is referred to as vector boson fusion (VBF) and is shown on the right hand side of figure 7.1.

The VBF process is of great interest to the ATLAS Collaboration because it is sensitive to new physics via anomalous triple gauge couplings [133] and the fact it

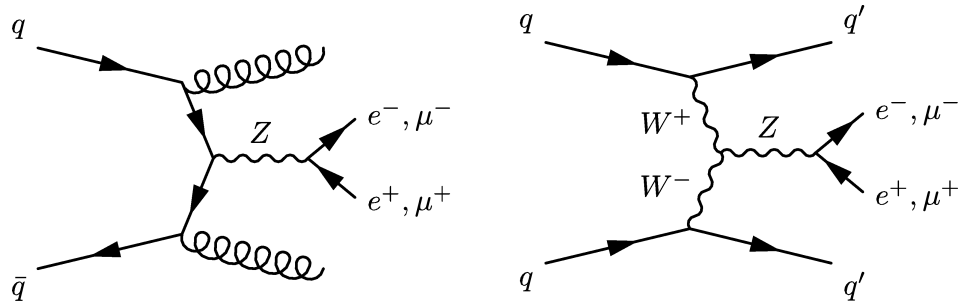

FIGURE 7.1: Feynman diagrams depicting the production mechanism of a Z boson in association with jets. These diagrams depict the special cases where: (left) the additional jets arise as the result of radiated gluons (strong-Zjj), and (right) a t-channel exchange of an electroweak gauge boson (EW-Zjj). Figure obtained from [130].

is similar to the VBF production of the Higgs boson. Furthermore, VBF is not the only mechanism for the EW-Zjj production. Figure 7.8 depicts most of the tree level diagrams for EW-Zjj production.

Di-boson production VV ($V = W, Z$) is another sub-dominant source of Zjj events if one of the bosons decays hadronically. Figure 7.9 shows this process for both the s- and t-channels. Although this is also a purely electroweak process it is not considered part of the definition of EW-Zjj due to the fact it does not have a t-channel exchange of a weak gauge boson.

The first observation and cross-section measurement of EW-Zjj in pp collisions was at the ATLAS detector at a centre-of-mass energy of $\sqrt{s} = 8$ TeV [134]. The predictions using the Powheg-box event generator [135–137] were in good agreement with the measured fiducial cross-section and this allowed limits to be placed on the anomalous triple gauge couplings on the WWZ vertex. A separate cross-section measurement was also performed at the centre-of-mass energy of $\sqrt{s} = 13$ TeV [130], and the resulting EW-Zjj cross-section as a function of the centre-of-mass energy can be seen in figure 7.10. The CMS collaboration has also measured the EW-Zjj production cross-section at both centre of mass energies [138]. A summary of $\sqrt{s} = 7$ TeV and $\sqrt{s} = 8$ TeV measurements of both EW-Zjj and EW-Wjj cross-sections can be seen in figure 7.11.

In this chapter, a data-driven method is used to extract the EW-Zjj contribution. This measurement is performed using proton-proton collision data collected by the ATLAS experiment during the years 2015-2018. The methodology is quite similar to the previous EW-Vjj ($V = W, Z$) measurements [130, 134, 139]. The main differences to these analyses is that for the first time differential cross-section measurements of EW-Zjj are performed. Previously differential measurements were performed only for inclusive[1] Zjj using Run 1 data [134]. Additionally this analysis uses more sophisticated statistical methods and the full Run 2 dataset which has more than ~40 times the statistics of the previous Run 2 measurement [130].

The differential cross-section measurements are performed on four key observables: the di-jet invariant mass, m_{jj}; the rapidity separation of the leading two jets, Δy_{jj}; the transverse momentum of the di-lepton system, p_{T}^{Z}, and the signed azimuthal angle between the two leading jets, $\Delta\phi_{jj}^{\mathrm{signed}}$[2].

[1] Inclusive Zjj is the combination of strong-Zjj and EW-Zjj.

[2] The direction of the sign is that the lower p_{T} jet's azimuthal angle is subtracted from the higher p_{T} jet.

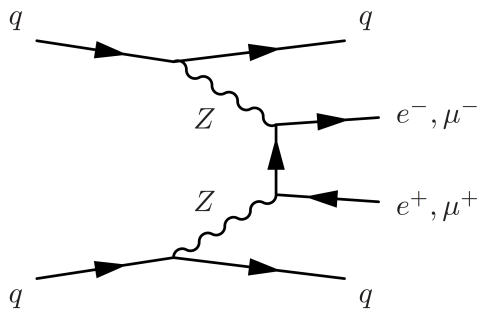

FIGURE 7.2: Non-resonant Via Z

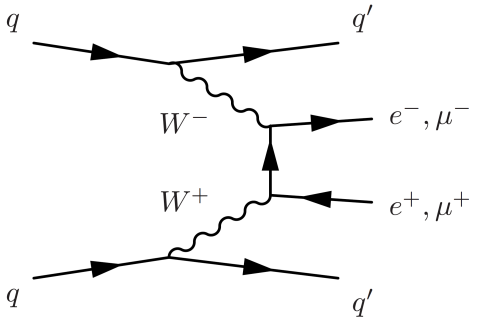

FIGURE 7.3: Non-resonant Via W

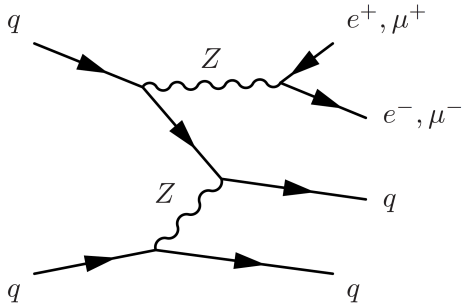

FIGURE 7.4: Z and t-channel (via Z)

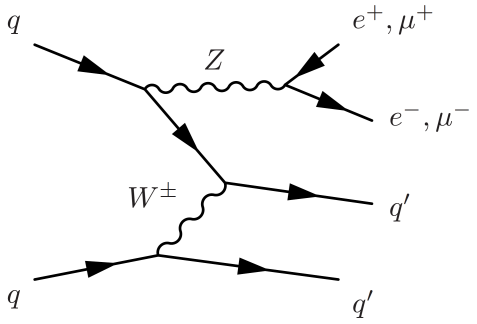

FIGURE 7.5: Z and t-channel (via W)

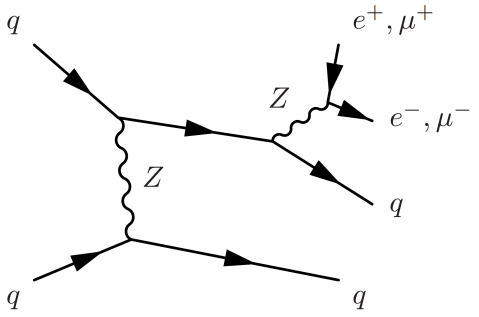

FIGURE 7.6: t-channel (via Z) and Z

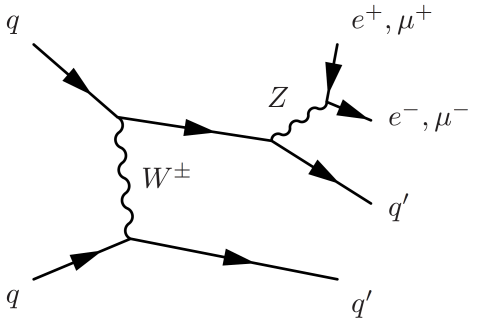

FIGURE 7.7: t-channel (via W) and Z

FIGURE 7.8: Feynman diagrams for EW-Zjj production at the LHC. Figure obtained from Ref. [43].

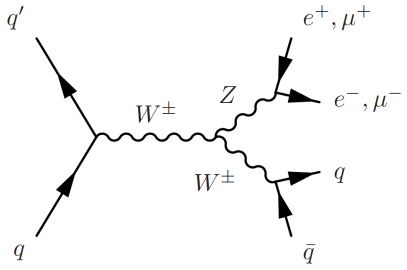

(a) s-channel diboson.

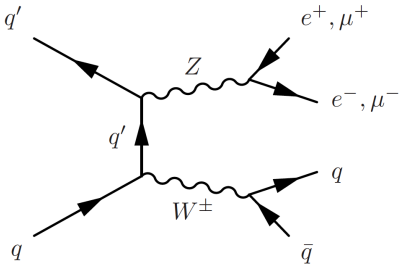

(b) t-channel diboson.

FIGURE 7.9: Feynman diagrams for EW-Zjj di-boson production at the LHC for both the (a) t-and (b) s-channel [43].

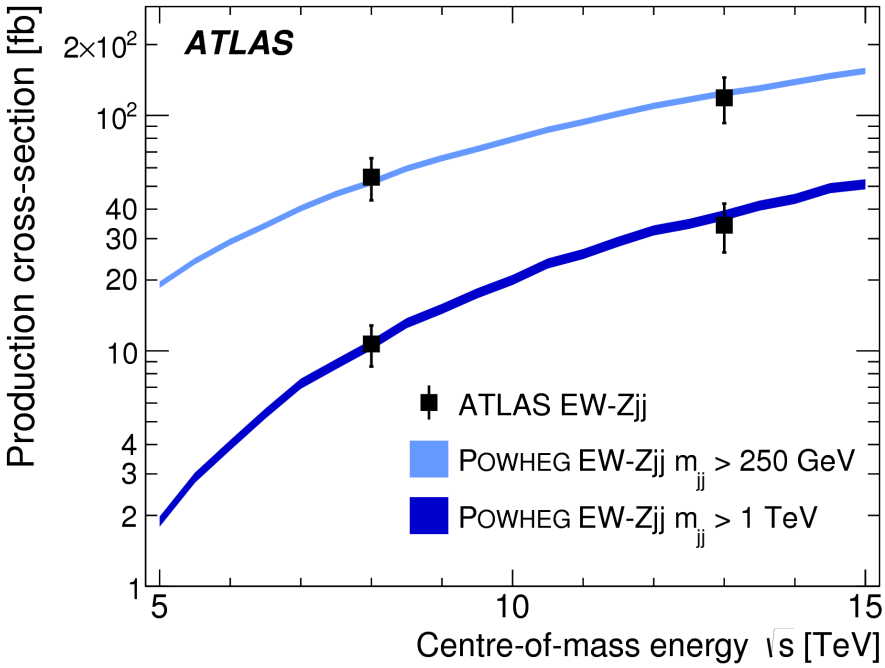

FIGURE 7.10: The EW-Zjj cross-sections for the centre-of-mass energies of $\sqrt{s} = 8$ and 13 TeV, for two different value of di-jet invariant mass ($m_{jj} \geq 0.25$ and 1 TeV) [138]. The error bars represent the total uncertainty on the measurement. Additionally predictions from the POWHEG event generator are shown with their uncertainty bands.

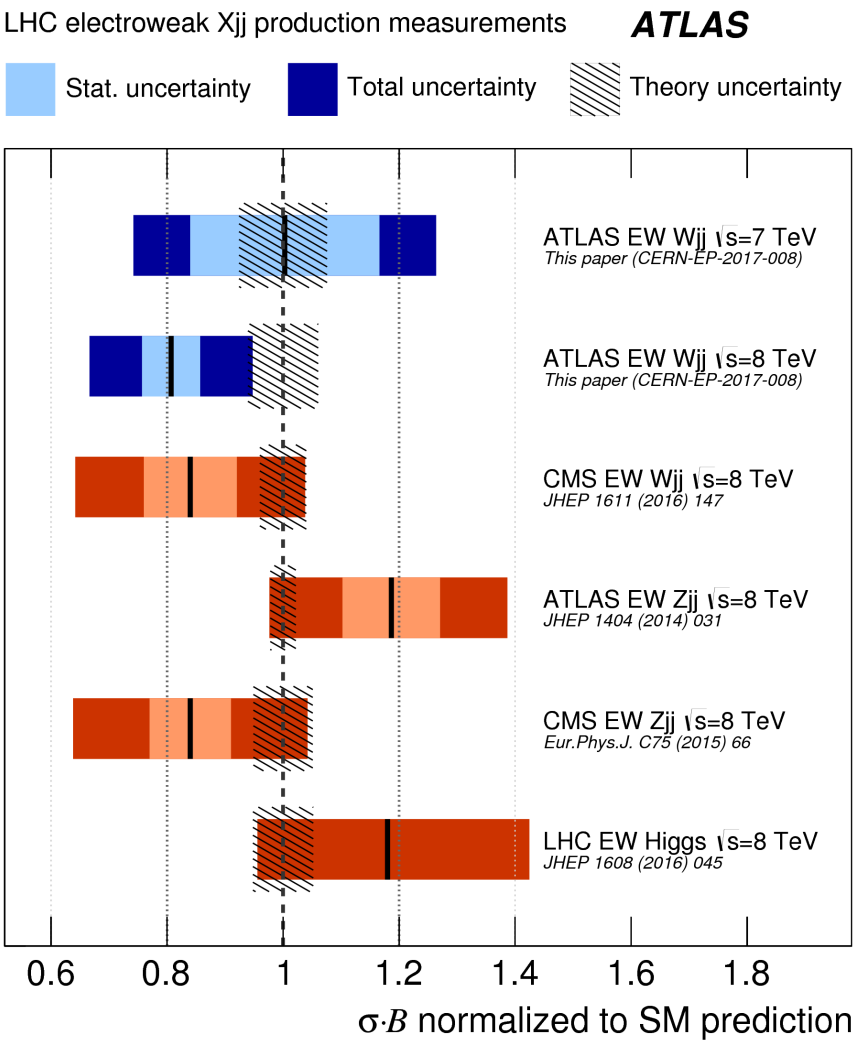

FIGURE 7.11: A summary of measurements of the cross-section multiplied by the branching fractions divided by the SM predictions of the EW production of a single W, Z or Higgs boson at a high di-jet invariant mass. The statistical error is marked by the lighter shaded band and the outer darker band is the total measurement uncertainty. The shaded regions that are centred at 1 represent the theoretical predictions which are POWHEG+PYTHIA8 for ATLAS, MADGRAPH+PYTHIA8 for CMS, and POWHEG+PYTHIA8 for the LHC combination [138].

7.2 Data and MC samples

The analysis is performed on data taken from 2015 to 2018 with a proton bunch spacing of 25 ns. For data collected during 2015 and 2016, an integrated luminosity of 35.7 fb^{-1} was collected. The 2017 data sample corresponds to an integrated luminosity of 44.3 fb^{-1} and the 2018 data has 58.5 fb^{-1}. The full Run 2 dataset hence corresponds to 138.42 fb^{-1}, with a total uncertainty of 1.7% [119]. The measurement of the integrated luminosity is covered in Chapter 5. The GRID datasets used are listed in Appendix C.2.

Monte Carlo event samples are used to estimate the contributions of different physics processes and to estimate the contribution from background events. Since the pileup conditions were quite different between the years, dedicated MC samples were produced within so-called MC campaigns with pileup and detector conditions set to match that of the data. The MC16a campaign matches the data collected in 2015-2016, MC16d corresponds to 2017 data and MC16e to 2018 data. The MC samples within a given campaign are normalised to the luminosity of the dataset they correspond to, and objects are reconstructed and calibrated according to the recommendations from the ATLAS combined performance groups, which often differ from year-to-year. Thereafter, an identical event selection is applied (see section 7.3.4) to the three datasets and the samples are merged prior to the end of the analysis.

EW-Zjj production has been simulated using the VBF_W-Z process in POWHEG-BOX [135–137]. Divergences from Born contributions are avoided by imposing a p_{T} cut on the two tagging jets of $p_T^j > 20$ GeV . There is also a di-lepton mass cut of $m_{ll} > 60$ GeV applied at the generator level. The renormalisation and factorisation scales in the calculation were set to the constant value of the vector boson's mass. The samples used the CT10nlo PDF set and were showered using PYTHIA 8 with the AZNLO tune for multiple parton interactions and the underlying event. This POWHEG process omits the di-boson contributions from the EW-Zjj final state. This assumes that the EWK and di-boson processes are independent with negligible interference.

EW-Zjj production has also been simulated using the SHERPA v.2.2.1 generator [140], and the CKKW method is used to combine the various final-state topologies and match to the parton shower [141]. The SHERPA EW-Zjj sample also omits the di-boson contributions from the EW-Zjj final state by using the min_n_tchannel option from SHERPA and setting it to 1. The SHERPA sample is generated with a $m_{ll} > 40$ GeV cut and a $p_T^j > 15$ cut on the leading two jets. The matrix elements were merged with the SHERPA parton shower [142] using the ME+PS@NLO prescription [143]. However, the resulting MC sample suffers from the so-called colour-flow bug [144, 145], which, as the name suggests, means that the QCD colour charge flow was incorrectly assigned during the event generation. This results in a lower overall cross-section, but more importantly, too much hadronic activity in the VBF gap region. The same issues were present in the Run 1 analysis, where it also was noticed that the scale and CKKW merging scale variations are much larger than expected (see figures 47 and 48 of reference [146]). Because of the known serious issues with this sample, it is only used for cross checks, and for a very conservative EW-Zjj shape systematic.

Strong-Zjj production has been simulated using two different generators: MADGRAPH5_aMC@NLO v2.2.2 [147] and SHERPA 2.2.1. Having different samples for the same process allowed cross-checks to be performed of the behaviour of the QCD

contribution to Zjj production and helped assess the theoretical modelling uncertainty.

The MADGRAPH5_aMC@NLO v2.2.2 (MADGRAPH) generator uses explicit matrix elements for up to four partons at LO. The parton shower for this sample was obtained from PYTHIA v8.186 [148], with the A12 tune and NNPDF23LO PDF set [149]. For the Strong-Zjj SHERPA sample, matrix elements were calculated for up to two partons at next-to-leading-order (NLO) and up to four additional partons at LO using the Comix [150] and OpenLoops [151] matrix element generators.

The background processes relevant to this analysis come from semi-leptonic diboson decays, W+jets events, $t\bar{t}$ and single-top production, and di-bosons production. The di-boson processes were simulated using SHERPA v2.2.1 and v2.2.2. The samples for $t\bar{t}$ and single-top production were generated with the POWHEG-BOX v2 generator and PYTHIA 8 [148]. Finally, W+jets events were simulated with SHERPA v2.1.1. All the SHERPA samples were produced using the CT10 [152] parton distribution functions (PDFs) and the default generator tune for underlying event activity.

All the MC samples above are passed through the GEANT 4 simulator [153] for a full simulation of the ATLAS detector [154]. The effect of pileup interactions in the same or nearby bunch crossings is also simulated using PYTHIA v8.186 with the A2 tune [155] and the MSTW2008LO PDF set [156] and overlaid on the hard scatter event of interest. The MC samples used are re-weighted so that the distribution of $\langle\mu\rangle$ matches what was observed in data in each production year.

The data and MC samples used are passed through the STDM3 derivation production which preselects events with two off-line leptons (muons or electrons) with $p_T > 15$ GeV that also pass a loose quality criteria.

An overview of the signal and background samples used in this analysis is shown in table 7.1 along with their total production cross-section, including higher order QCD corrections and their respective uncertainties where available. A detailed list of all these samples can be found in Appendix C.2.

Physics process	Generator	σ [pb]	$\sigma_{\ell\ell}$ [pb]	σ_{baseline} [fb]
EW-Zjj	POWHEG+PYTHIA8	1.535	0.412	153
EW-Zjj	SHERPA v2.2.0	1.267	0.292	85.0
Z + jets	MADGRAPH+PYTHIA8	4,223	781	3630
Z + jets	SHERPAv2.2.1	4,183	756	3121
VV	SHERPA v2.2.X	106	0. 889	22.9
$t\bar{t}$	POWHEG+PYTHIA8	452	0.451	11.8
single top	POWHEG+PYTHIA8	145	0.040	0.7
W+jets	POWHEG+PYTHIA8	39,178	0.006	0.0
$(Z \to \tau\tau)$+jets	POWHEG+PYTHIA8	1901	0.019	0.0

TABLE 7.1: Signal and background MC samples with the associated event generators and production cross-sections multiplied by the relevant branching ratios. The EW and strong-Zjj(first four) samples are generated separately for $Z \to e^-e^+$ and $Z \to \mu^-\mu^+$. The column labelled σ reports the total cross-section, and the next two present the cross-section multiplied by a selection efficiency taken from MC samples, averaged over years and channels. The di-lepton cross-section $\sigma_{\ell\ell}$ requires two good leptons, and the baseline cross-section σ_{baseline} accounts for the selection efficiency of the baseline section described in section 7.3.4.

7.3 Event selection for baseline region

This section will cover the process used to select events for a "baseline region". This region is then later split into search and control regions to extract the EW-Zjj process, and this is covered in section 7.6.2.

7.3.1 Event pre-selection

The event level pre-selections placed on the Run 2 data are:

- To be part of the standard ATLAS good run list.
- To reject events with tile calorimeter, liquid argon system or silicon tracker problems.
- To remove events with missing information due to a restart of the timing, trigger and control system.
- To remove events that fail the "Loose" event cleaning criteria, this cut is also applied to the MC simulation (see section 7.3.3.3).

These detector level problems affect a small number of events and so the impact on the total integrated luminosity is negligible. Additionally, there is another event level cleaning cut that affects jets in the forward region in the 2016 data known as the "BadBatMan" problem in the electromagnetic end-cap calorimeter. This cut is also implemented as a decoration[3] in the derivation framework and applying it removes 1.66% of the 2016 data. The integrated luminosity for 2016 is adjusted accordingly.

7.3.2 Trigger requirements

Each event needs to pass a di-lepton trigger, the recommended trigger is different for each data period and lepton channel. The applied triggers are listed in table 7.2 and all the triggers used are un-prescaled. The trigger selections are also applied to the MC simulations.

Data,MC period	electron channel	muon channel
Data 15	`HLT_2e12_lhloose_L12EM10VH`	`HLT_mu18_mu8noL1`
Data 16, MC16a	`HLT_2e17_lhvloose_nod0`	`HLT_mu22_mu8noL1`
Data 17+18, MC16d, MC16e	`HLT_2e24_lhvloose_nod0`	`HLT_mu22_mu8noL1`

TABLE 7.2: Overview of the trigger requirements used for each of the data-taking periods.

7.3.3 Object definitions

7.3.3.1 Electron definition

Electron reconstruction is covered in section 4.3. In this analysis, candidate electrons must pass the Medium likelihood electron identification working point. They are calibrated using the latest recommendations released in December 2018.

[3] A decoration is an additional piece of information added to the files.

The electron isolation requires that the candidate electron satisfies the Gradient isolation working point provided by the `IsolationSelectionTool`. This working point uses a cone of radius $R = 0.2$ around the object to define the activity near the electron. The working point targets an efficiency rather than a specific fixed energy cut. The isolation efficiency is 90% for an electron with $p_{\mathrm{T}} > 25$ GeV and 99% for an electron with $p_{\mathrm{T}} > 60$ GeV.

The electrons selected in this analysis are required to have $p_{\mathrm{T}} > 25$ GeV, $|\eta| < 2.47$. Additionally electrons that fall into $1.37 < |\eta| < 1.52$ are removed as this region corresponds to the calorimeter crack and so has poor resolution and reconstruction efficiency.

7.3.3.2 Muon definition

Muon reconstruction is covered in section 4.4. Muons are pre-selected by the use of the `MuonSelectionTool` with the Medium quality working point. Candidate muons need also satisfy the same Gradient isolation working point as the electrons and are required to have $p_{\mathrm{T}} > 25$ GeV and $|\eta| < 2.4$.

7.3.3.3 Jet definition

Jet reconstruction is covered in section 4.6. All jets are required to have a calibrated transverse momentum of $p_{\mathrm{T}} > 25$ GeV and rapidity $|y| < 4.4$. To remove jets originating from different pp collisions in the same bunch crossing, the jet vertex tagger (JVT) is used. In this analysis, the Medium JVT working point (JVT > 0.59) is applied to jets with $|\eta| < 2.5$ and $p_{\mathrm{T}} < 120$ GeV. Events are rejected if a jet fails to fulfil the "LooseBad" quality of the `EventCleaningTool`. For this event-level veto, only jets with $p_{\mathrm{T}} > 20$ GeV and $|\eta| < 2.8$ that pass both JVT and overlap removal are used.

7.3.3.4 Overlap removal

Electrons are always reconstructed as jets due to the signature in the calorimeter, so before selecting jets it is important to ensure that each jet does not coincide with a good electron. Overlap removal (OR) is applied to veto objects where the selected objects are not well separated. It is applied in two stages.

The first stage is applied to jets that pass a minimal pre-selection ($p_{\mathrm{T}} > 25$ GeV, $|y| < 4.4$). A jet is removed if it is within a radius $R < 0.2$ of a good electron. A jet is removed if it is within a radius $R < 0.2$ of a good muon if either of the following additional criteria are met. The first criteria is that the number of tracks within the jet of $p_T > 500$ MeV must be less than 3. The second criteria is that the ratio of the jet's p_{T} with respect to that of the muon must be less than two. This first stage of the OR is applied to pre-selected jets because the efficiency scale factor of the JVT cut can only be calculated after OR.

The second stage of OR is after the leptons and jets have been selected. Any lepton that is within a radius $R < 0.4$ of a selected jet is removed. This is essentially an additional isolation cut on the selected leptons.

7.3.4 Final selection

The event selection is very similar to the previous EW-Zjj analyses detailed both in the papers [130, 134, 139] and in the support note [146]. The event selection is designed to reject various backgrounds while retaining the EW-Zjj signal process

such that the signal-to-background ratio is enhanced. The selection criteria is summarised in table 7.3 and is referred to as the baseline region. This is applied on top of the basic object selection outlined in section 7.3.3. A detailed description is given below.

Event selection	Description
Trig+DQ	di-lepton trigger. Lumiblock flagged good by GRL. Data quality flags.
di-lepton	Two opposite sign leptons e^+e^- or $\mu^+\mu^-$ with $m_{\ell\ell} \in (81, 111)$ GeV.
di-jet	At least two jets where the leading two have $p_{\mathrm{T}}^{\mathrm{j1}} > 85$ GeV and $p_{\mathrm{T}}^{\mathrm{j2}} > 80$ GeV.
Baseline	$p_{\mathrm{T}}^{Z} > 20$ GeV, $p_{\mathrm{T}}^{\mathrm{bal}} < 0.15$, $m_{jj} > 1000$ GeV, $\Delta y_{jj} > 2$, $\xi_Z < 1.0$

TABLE 7.3: Overview of the event selection. The criteria are applied cumulatively.

The leading two jets are denoted $j1$ and $j2$ and their four momentum sum defines the di-jet system, denoted jj. The invariant mass of this system is the di-jet invariant mass, m_{jj} and the rapidity separation between $j1$ and $j2$ is denoted Δy_{jj}. Any jet that has rapidity in the rapidity interval of the two leading jets (i.e. between y_{j1} and y_{j2}) is defined as a gap jet. The number of such jets, denoted $N_{\mathrm{jets}}^{\mathrm{gap}}$, is a key observable of the analysis.

The Z candidate Z bosons are selected by requiring two oppositely charged same-flavour leptons with $81 < m_{\ell\ell} < 111$ GeV. The di-jet system is selected by requiring the leading and sub-leading jets have a p_{T} of $p_{\mathrm{T}}^{\mathrm{j1}} > 85$ GeV and $p_{\mathrm{T}}^{\mathrm{j2}} > 80$ respectively. Finally the baseline region is selected by requiring that the di-lepton system has a $p_{\mathrm{T}}^{Z} > 20$ GeV and that the di-jet system has a invariant mass of $m_{jj} > 1000$ GeV and di-jet rapidity separation of $\Delta y_{jj} > 2$. The final cut is on the p_{T}-balance of the system of $p_{\mathrm{T}}^{\mathrm{bal}} < 0.15$. The p_{T}-balance observable is defined as

$$p_{\mathrm{T}}^{\mathrm{bal}} \equiv \left|\sum \vec{p}_{\mathrm{T}}\right| / \sum p_{\mathrm{T}}, \tag{7.1}$$

where the sum runs over the two leptons and the leading two jets, and the leading gap jet, if such a jet exists. Finally, the Z centrality observable, ξ_Z, is defined by

$$\xi_Z = \frac{|y_{\ell\ell} - (y_{\mathrm{j1}} + y_{\mathrm{j2}})/2|}{\Delta y_{jj}}, \tag{7.2}$$

and it describes the absolute difference in rapidity of the di-lepton and di-jet systems divided by the rapidity separation of the two leading jets.

Tables 7.4 and 7.5 present the observed and predicted event yields of the $Z \to ee$ and $Z \to \mu\mu$ channels, respectively, after the different event selection critera. They make the motivation for each selection criteria quite clear. The jet p_{T} and p_{T}^{Z} requirement significantly reduces the strong Z background, while the $p_{\mathrm{T}}^{\mathrm{bal}}$ requirement significantly reduces contributions from $t\bar{t}$ and single top.

7.3.5 Normalisation regions

The normalisation region follows an identical selection process to that for the baseline region with the exception that the cut on the di-jet invariant mass is now required to satisfy $500 < m_{jj} < 750$ GeV. These normalisation regions are used as part of the data-driven constraint and are covered in more detail in section 7.6.3.

$Z \to ee$ channel	Selection								
Sample	None	Trig+DQ	Dilepton	Jets	Δy_{jj}	m_{jj}	p_{T}^{Z}	$p_{\mathrm{T}}^{\mathrm{balance}}$	ζ_Z
Data 2015+2016	330.0M	31.2M	13.1M	93.4k	26.2k	26.1k	24.4k	18.4k	17.3k
Sherpa strong Zjj	74.7M	25.5M	13.1M	86.1k	27.1k	27.0k	25.3k	18.9k	17.8k
Madgraph strong Zjj	75.6M	26.4M	13.5M	103k	29.5k	29.4k	27.7k	22.2k	21.1k
$t\bar{t}$	3.3M	306k	16.2k	3.1k	741	738	683	196	193
Diboson	357k	77.6k	24.5k	2.2k	484	483	463	278	265
Single top	445k	32.5k	1.4k	112	32	31	29	9.4	9.4
Powheg EW Zjj	27.4k	14.2k	7.1k	2.6k	1.8k	1.8k	1.7k	1.5k	1.5k
Total MC (MG)	79.7M	26.8M	13.5M	111k	32.5k	32.4k	30.6k	24.2k	23.1k
Total MC (Sherpa)	78.8M	25.9M	13.1M	94.2k	30.2k	30.1k	28.2k	20.9k	19.8k
Data 2017	281.6M	27.6M	14.5M	107k	30.0k	29.9k	27.8k	20.9k	19.7k
Sherpa strong Zjj	92.7M	27.1M	15.0M	103k	32.5k	32.4k	30.2k	22.4k	21.1k
Madgraph strong Zjj	93.7M	27.9M	15.4M	123k	35.2k	35.1k	32.9k	26.3k	25.0k
$t\bar{t}$	4.0M	251k	18.6k	3.6k	872	870	802	243	240
Diboson	451k	77.1k	28.4k	2.6k	588	586	563	342	327
Single top	557k	25.1k	1.7k	133	29	29	26	10	9.7
Powheg EW Zjj	34.0k	14.8k	8.3k	3.1k	2.1k	2.1k	2.0k	1.8k	1.8k
Total MC (MG)	98.8M	28.3M	15.4M	132k	38.8k	38.7k	36.3k	28.7k	27.4k
Total MC (Sherpa)	97.8M	27.4M	15.0M	112k	36.1k	36.0k	33.6k	24.8k	23.5k
Data 2018	313.8M	37.4M	19.3M	141k	39.7k	39.5k	36.8k	27.7k	26.1k
Sherpa strong Zjj	122.3M	36.1M	19.9M	136k	43.2k	43.1k	40.2k	30.0k	28.0k
Madgraph strong Zjj	123.8M	37.3M	20.5M	163k	46.6k	46.5k	43.7k	34.8k	33.1k
$t\bar{t}$	5.1M	345k	25.0k	4.9k	1.2k	1.2k	1.1k	310	303
Diboson	566k	103k	37.7k	3.4k	779	777	745	453	436
Single top	688k	34.4k	2.2k	188	50	50	49	16	16
Powheg EW Zjj	44.8k	19.8k	11.2k	4.2k	2.9k	2.9k	2.7k	2.5k	2.4k
Total MC (MG)	130.2M	37.8M	20.6M	175k	51.5k	51.4k	48.3k	38.0k	36.3k
Total MC (Sherpa)	128.8M	36.6M	20.0M	149k	48.0k	47.9k	44.8k	33.2k	31.2k

TABLE 7.4: $Z \to ee$ channel data event yields and predicted yields from MC at various stages of the event selection. The cuts in this table are the same as listed in table 7.3.

$Z \to \mu\mu$ channel	Selection								
Sample	None	Trig+DQ	Dilepton	Jets	Δy_{jj}	m_{jj}	p_{T}^{Z}	$p_{\mathrm{T}}^{\mathrm{balance}}$	ξ_Z
Data 2015+2016	330.0M	96.1M	14.8M	99.7k	28.3k	28.3k	26.2k	19.9k	18.5k
Sherpa strong Zjj	74.5M	31.1M	15.1M	91.0k	29.6k	29.5k	27.4k	20.5k	19.1k
Madgraph strong Zjj	75.2M	32.3M	15.6M	110k	31.9k	31.8k	29.7k	23.8k	22.5k
$t\bar{t}$	3.3M	1.1M	17.2k	3.1k	740	738	683	210	209
Diboson	357k	113k	27.5k	2.2k	496	495	475	286	273
Single top	445k	142k	1.5k	114	31	30	29	8.7	8.7
Powheg EW Zjj	27.4k	17.6k	8.0k	2.8k	1.9k	1.9k	1.8k	1.6k	1.6k
Total MC (MG)	79.2M	33.6M	15.6M	118k	35.0k	34.9k	32.6k	25.9k	24.6k
Total MC (Sherpa)	78.6M	32.5M	15.1M	99.2k	32.8k	32.7k	30.4k	22.6k	21.2k
Data 2017	281.6M	109.5M	16.3M	112k	32.1k	32.0k	29.7k	22.4k	20.9k
Sherpa strong Zjj	92.6M	38.8M	17.1M	108k	34.8k	34.7k	32.1k	23.8k	22.2k
Madgraph strong Zjj	93.1M	40.2M	17.7M	129k	38.1k	38.0k	35.5k	28.2k	26.6k
$t\bar{t}$	4.0M	1.3M	19.8k	3.6k	835	833	771	228	225
Diboson	451k	141k	31.9k	2.6k	587	585	564	338	323
Single top	557k	180k	1.8k	119	32	32	31	11	11
Powheg EW Zjj	34.0k	21.9k	9.3k	3.2k	2.2k	2.2k	2.1k	1.9k	1.9k
Total MC (MG)	98.2M	41.9M	17.7M	138k	41.7k	41.6k	38.9k	30.6k	29.1k
Total MC (Sherpa)	97.7M	40.5M	17.2M	117k	38.5k	38.4k	35.5k	26.2k	24.7k
Data 2018	313.8M	144.1M	21.5M	148k	42.6k	42.4k	39.4k	29.7k	27.7k
Sherpa strong Zjj	122.2M	51.1M	22.8M	142k	45.9k	45.8k	42.6k	31.4k	29.3k
Madgraph strong Zjj	123.1M	53.0M	23.5M	173k	50.7k	50.6k	47.3k	37.6k	35.5k
$t\bar{t}$	5.1M	1.8M	26.2k	4.6k	1.1k	1.1k	1.0k	324	321
Diboson	566k	186k	42.5k	3.4k	782	780	748	443	423
Single top	688k	236k	2.4k	188	50	49	47	12	12
Powheg EW Zjj	44.9k	29.0k	12.5k	4.3k	2.9k	2.9k	2.8k	2.5k	2.5k
Total MC (MG)	129.5M	55.2M	23.6M	185k	55.6k	55.5k	51.9k	40.9k	38.8k
Total MC (Sherpa)	128.7M	53.3M	22.9M	154k	50.8k	50.7k	47.2k	34.7k	32.6k

TABLE 7.5: $Z \to \mu\mu$ channel data event yields and predicted yields from MC at various stages of the event selection. The cuts in this table are the same as listed in table 7.3.

7.4 Simulation corrections

The corrections detailed in this section are applied to the MC simulations to account for differences in the detector response and environment between the simulations and the data. Generally they are applied on a per-event or per-object basis.

7.4.1 Pileup re-weighting

The MC simulations are produced each year before ATLAS has finished data taking. This results in the ATLAS data and MC simulations having a different distribution of the average number of pileup interactions, μ, per event. The `PileupReweightingTool` calculates weights that can be applied per event in simulation in order to preserve the cross-section of each sample whilst correcting the μ distribution to match the data. The tool is provided with a pileup re-weighting configuration file for each MC sample that contains the average μ distributions for that sample. The tool is also provided a "Lumicalc" file for each data period; these files contain the average μ distributions for data and can be generated for a given trigger. As this analysis strictly uses un-prescaled triggers, the tool can be provided with centrally available Lumicalc files that correspond to the official Good Run Lists (GRL).

In addition to providing per event weights, the tool also corrects the μ values in simulation by a constant factor to account for a known effect where the μ distribution in simulation is too hard. The MC16 samples used in this analysis require the MC simulations to be scaled down by $1/1.03$ before calculating the pileup weights.

7.4.2 Lepton scale factors

The lepton identification, reconstruction and isolation efficiencies are measured with J/ψ and $Z \to ee$ events in data using a tag-and-probe method. One lepton must pass the tightest identification requirements (the tag) for the event to be tagged, then the second lepton (the probe) can be selected with very loose identification. This is done to avoid a bias on the measured quantities of the second lepton. The probe electron can then be used to measure the efficiencies, such as the electron identification efficiency. This method is used to calculate scale factors dependent on η and/or p_T and they are applied on a per-event basis. This is done in both data and simulation and the ratio of $\epsilon_{data}/\epsilon_{simulation}$ provides a p_T and η dependent scale factor that is applied on a per-object basis for each simulation. The net effect is to correct the simulation to reflect the real efficiency of the detector in data.

7.4.3 Trigger scale factors

The efficiency of the applied di-lepton triggers, given in section 7.3.2, are also inconsistent between data and MC, thus a trigger scale factor is required that accounts for this difference. The di-electron triggers applied are symmetric, requiring 2 electrons each with a given p_{T}, i.e `HLT_2e24_lhvloose_nod0`. As such the two electrons in an event are effectively identical in terms of calculating the trigger scale factor. In contrast, the di-muon triggers such as `HLT_mu22_mu8noL1` place different p_{T} requirements on each muon and since one cannot know which of the reconstructed muons

satisfied each requirement the trigger scale factor is computed in a more sophisticated manner. The efficiency is computed as follows for both data and simulation

$$\begin{aligned}\epsilon = \epsilon_{\text{leg1}}(\mu_1)\epsilon_{\text{leg1}}(\mu_2) + \epsilon_{\text{leg1}}(\mu_1)\left[1-\epsilon_{\text{leg1}}(\mu_2)\right]\epsilon_{\text{leg2}}(\mu_2) \\ + \epsilon_{\text{leg1}}(\mu_2)\left[1-\epsilon_{\text{leg1}}(\mu_1)\right]\epsilon_{\text{leg2}}(\mu_1)\end{aligned} \tag{7.3}$$

where leg 1 and leg 2 are each half of the di-muon trigger and μ_1 and μ_2 are the leading and sub-leading muon respectively. Again, the trigger scale factor is the ratio of the efficiency calculated in data, to that calculated in simulation.

7.5 Background modelling in the baseline region

This section provides a comparison of data and simulation in the baseline region using SHERPA as the strong-Zjj sample. Figure 7.12 depicts the variables m_{jj} and m_{ll} and it can be seen that the simulations over predict the event yield by nearly a factor of two. How this poor modelling is corrected is covered in section 7.6. For now it is sufficient to note that the simulation is over predicted and increasingly so for higher values of m_{jj}. In all the remaining plots in this chapter the electron and muon channels are merged. This is because the mismodelling was seen to be consistent between the two channels and merging them reduces the statistical error on the data-driven corrections described in section 7.6.

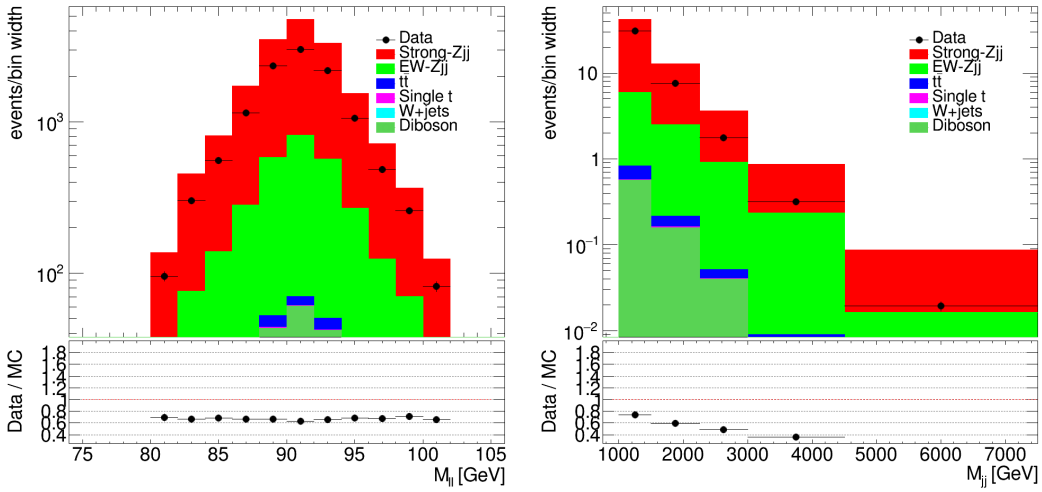

FIGURE 7.12: A comparison of data and simulation in the baseline region for the combination of the electron and muon channels where SHERPA is used for the strong-Zjj prediction. The distributions shown are $m_{\ell\ell}$ (left) and m_{jj} (right).

Figure 7.13 shows a comparison of data and simulation for the leading and sub-leading lepton p_{T}. It can be seen that apart from the normalisation of the simulation that the agreement is quite good as indicated by a flat data/MC ratio.

Figure 7.14 contains a comparison of data and simulation for the leading and sub-leading jet p_{T}. It can be seen that again the simulation over predicts the number of events for high values of jet p_{T}. This is to be expected after seeing this behaviour for the variable m_{jj}.

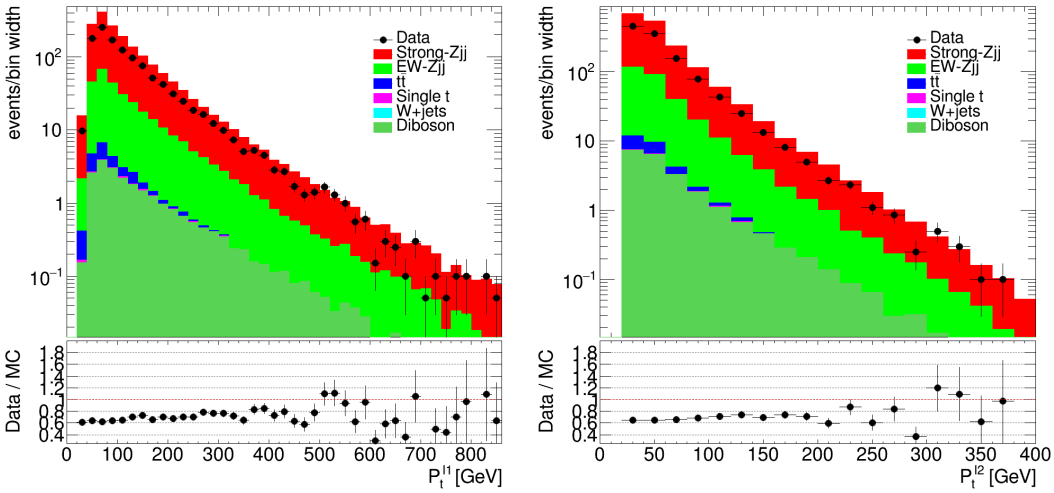

FIGURE 7.13: A comparison of data and simulation in the baseline region for the combination of the electron and muon channels using where SHERPA is used for the strong-Zjj prediction. The distributions shown are leading lepton p_{T} (left) and sub-leading lepton p_{T} (right).

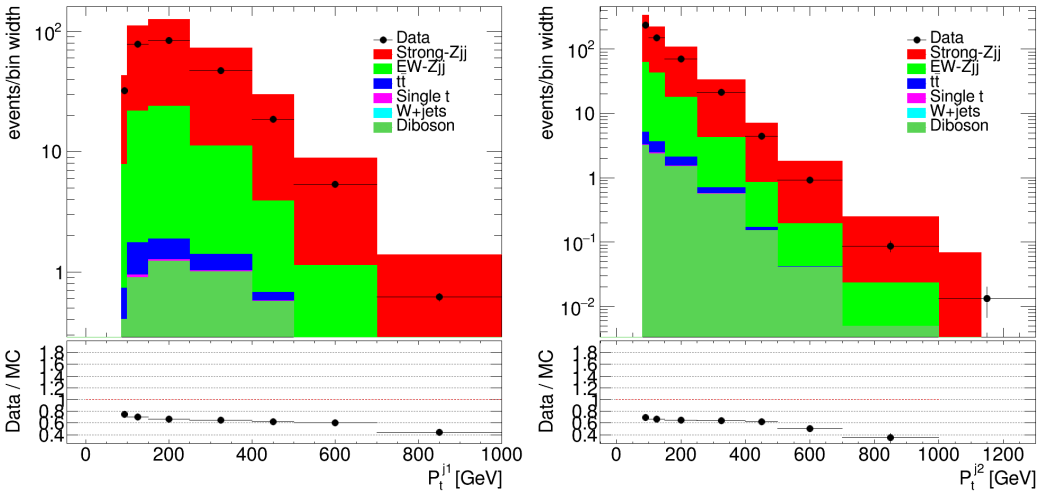

FIGURE 7.14: A comparison of data and simulation in the baseline region for the combination of the electron and muon channels using where SHERPA is used for the strong-Zjj prediction. The distributions shown are leading jet p_{T} (left) and sub-leading jet p_{T} (right).

The number of gap jets is defined to be the number of additional jets in the rapidity interval with the two leading jets that pass the basic jets selection outlined in section 7.3.3.3. Figure 7.15 depicts a comparison of data and simulation for the number of gap jets and the transverse momentum of the Z boson. It can be seen that again the number of gap jets is poorly modelled by the strong-Zjj MC simulation.

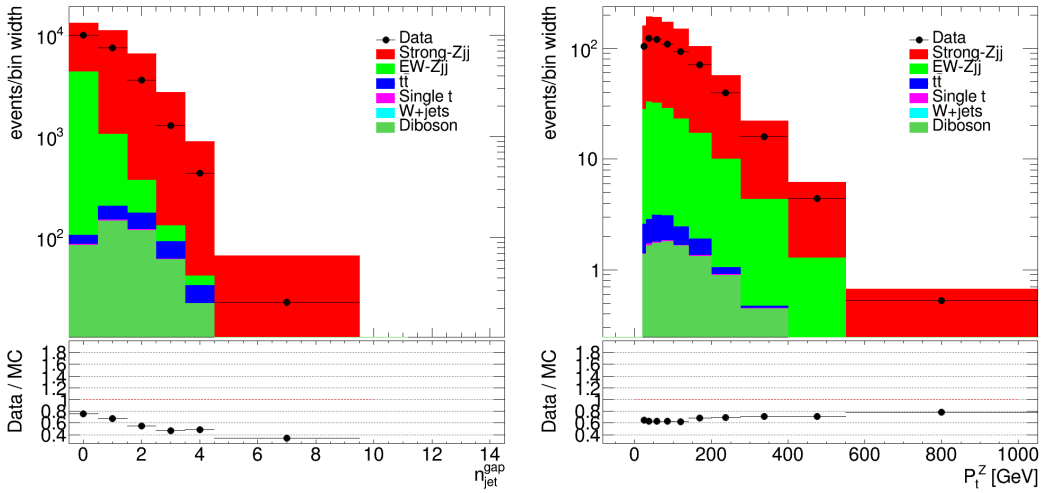

FIGURE 7.15: A comparison of data and simulation in the baseline region for the combination of the electron and muon channels using where SHERPA is used for the strong-Zjj prediction. The distributions shown are the number of gap jets (left) and p_{T}^{Z} (right).

Figure 7.16 depicts a comparison of data and simulation for the variables Δy_{jj} and $\Delta\phi_{jj}^{\text{signed}}$. It can be seen that while these variables are better modelled than the jet p_{T}, the agreement between Data/MC is again poor. In summary the normalisation

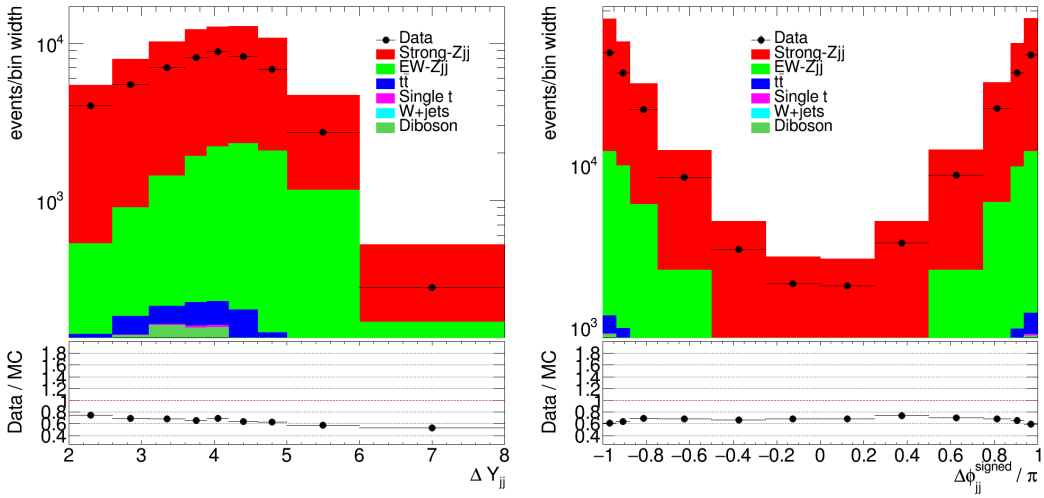

FIGURE 7.16: A comparison of data and simulation in the baseline region for the combination of the electron and muon channels using SHERPA for the strong-Zjj prediction. The distributions shown are Δy_{jj} (left) and $\Delta\phi_{jj}^{\text{signed}}$ (right).

of the strong-Zjj is approximately ~25% too high in the baseline region. Furthermore, for the variables involving the jet transverse momentum the strong-Zjj MC simulation increasingly over-predicts the number of events for higher values of p_{T}. How the normalisation and shape of the strong-Zjj is constrained is covered in the following section.

7.6 Extraction of the electroweak signal

This section covers the method used to extract the electroweak signal. The mismodelling of the simulation shown in the previous section means that the simulation for backgrounds cannot be simply subtracted from the data. Instead, a data-driven approach is used. Three control regions and a signal region are defined from the baseline region. The control regions are used to derive and validate a data-driven constraint on the strong-Zjj background that is then applied to the strong-Zjj template in the signal region.

7.6.1 Blinding the analysis

The signal region in this analysis was blinded [4] while the analysis method was being developed. To determine the effectiveness of the data-driven constraint it was derived in one control region and applied to the remaining two control regions. Any non closure of this constraint is taken to be a systematic and is covered in section 7.6.6. Additionally all the systematics were first predicted using an Asimov dataset and this is covered in section 7.8.

7.6.2 Signal and control region definitions

The event selection in the signal and control regions follow the baseline event selection outlined in section 7.3.4. The events are then divided into four orthogonal subregions. The Signal Region (SR) is defined by $N_{\text{jets}}^{\text{gap}} < 1$ and $\xi_Z \leq 0.5$ and is the region with the largest relative contribution from EW-Zjj production. Three EW-suppressed control regions (CR) are then defined by reversing these cuts: CR A is defined as $N_{\text{jets}}^{\text{gap}} \geq 1$ and $\xi_Z \leq 0.5$; CR B is defined as $N_{\text{jets}}^{\text{gap}} \geq 1$ and $\xi_Z > 0.5$ and CR C is defined as $N_{\text{jets}}^{\text{gap}} < 1$ and $\xi_Z > 0.5$. These signal and control region definitions are depicted in figure 7.17. The variables $N_{\text{jets}}^{\text{gap}}$ and ξ_Z that are used to define the SR and the 3 CRs are chosen as they are not correlated with each other. This is shown in figure 7.18 for both data and the strong-Zjj SHERPA prediction, with correlation coefficients of ~0.05 and ~0.07 respectively. Additionally these cuts suppress the contribution of EW-Zjj in the CRs.

[4] In this context blinded means that the data in the signal region is not looked at for any reason until the analysis method is finalised.

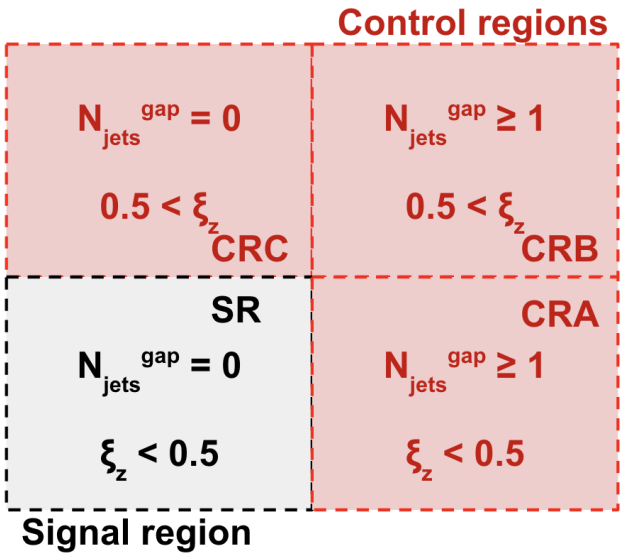

FIGURE 7.17: Diagram depicting how the control and search regions are defined for the extraction of the electroweak signal differentially. These cuts are applied on top of those for the baseline region.

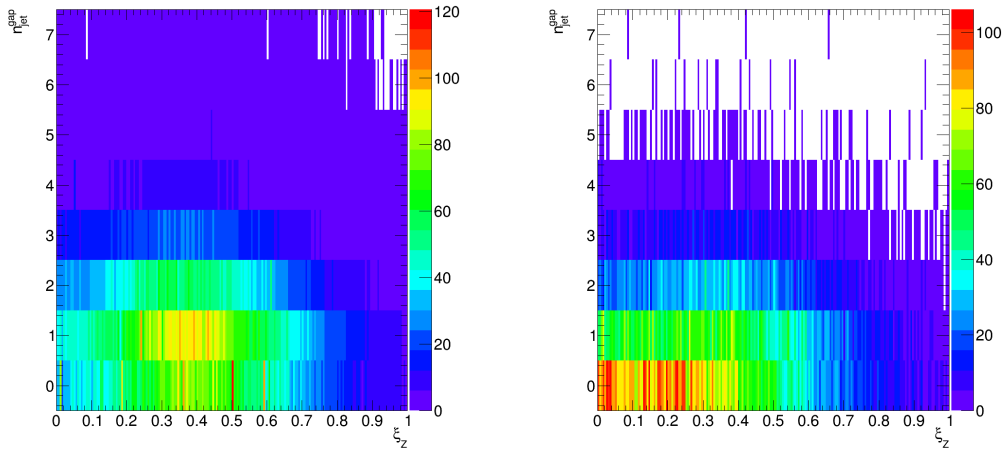

FIGURE 7.18: Correlation between the ξ_Z and $N_{\text{jets}}^{\text{gap}}$ observables in the baseline fiducial region, determined from data (left) and SHERPA strong-Zjj (right). The correlation coefficients are -0.051 for data and 0.072 for SHERPA.

7.6.3 Mathematical formalism

The differential cross-section for EW-Zjj production as a function of a variable x is defined in each bin i of the distribution in a signal region by,

$$\frac{d\sigma_i^{\text{EW}}}{dx} = \frac{\hat{N}_{\text{SR},i}^{\text{EW}}}{\Delta x_i \, \mathcal{L}\mathcal{C}_i^{EW}} = \frac{N_{\text{SR},i}^{\text{data}} - N_{\text{SR},i}^{\text{strong}} - N_{\text{SR},i}^{\text{non-Z}}}{\Delta x_i \, \mathcal{L}\mathcal{C}_i^{EW}}, \tag{7.4}$$

where $\mathcal{L}$ is the integrated luminosity of the dataset, and Δx_i is the width of the bin. $\mathcal{C}_i^{EW}$ is a bin-by-bin correction factor applied to the observed background-subtracted data that accounts for experimental efficiency and detector resolution effects. It is derived from EW-Zjj MC simulation as outlined in section 7.9. The $\hat{N}_{\text{SR},i}^{\text{EW}}$ term is the estimated number of EW-Zjj events, defined as the data minus the non-EW Zjj background, i.e.

$$\hat{N}_{\text{SR},i}^{\text{EW}} = N_{\text{SR},i}^{\text{data}} - N_{\text{SR},i}^{\text{strong}} - N_{\text{SR},i}^{\text{non-Z}}. \tag{7.5}$$

The small non-Zjj contribution ($N_{\text{SR},i}^{\text{non-Z}}$) comes primarily from di-boson and $t\bar{t}$ processes and is taken from MC predictions normalised to the best available cross-sections, as documented in section 7.2. The largest background contribution comes from strong-Zjj production, which is estimated using a partially data-driven approach as outlined below. The number of strong-Zjj events in the SR, $N_{\text{SR},i}^{\text{strong}}$, is defined by

$$N_{\text{SR},i}^{\text{strong}} = k \, r_{\text{CR},i} \, N_{\text{SR},i}^{\text{strong,MC}}, \tag{7.6}$$

where in the ith bin of a differential distribution; $N_{\text{SR},i}^{\text{strong,MC}}$ is the number of strong-Zjj events predicted by MC simulation in the SR; $r_{\text{CR},i}$ is a bin-by-bin re-weighting function derived in a CR and k is an additional normalisation factor that accounts for data/MC mismodelling in the relative normalisation of the SR and CR. Both $r_{\text{CR},i}$ and k are derived in CRs and combine to constrain the strong-Zjj prediction in the SR. This method determines the strong-Zjj constraints in sequential steps. Firstly the $r_{\text{CR},i}$ factors are determined, and then k. Finally these constraints are applied to strong-Zjj template in the SR.

The re-weighting function, $r_{\text{CR},i}$ is defined in each bin of the differential distribution by

$$r_{\text{CR},i} = \frac{N_{\text{CR},i}^{\text{data}} - N_{\text{CR},i}^{\text{non-strong}}}{N_{\text{CR},i}^{\text{strong,MC}}}, \tag{7.7}$$

where $N_{\text{CR},i}^{\text{data}}$ is the number of events measured in data in the CR of bin i, and $N_{\text{CR},i}^{\text{strong,MC}}$ and $N_{\text{CR},i}^{\text{non-strong}}$ are the number of predicted strong-Zjj and non-strong-Zjj events predicted by MC simulations respectively. Then $r_{\text{CR},i}$ is parametrised using a function which depends on the kinematic variable that is being measured. Table 7.6 gives the parametrisations used, along with the alternative parametrisations for the systematic evaluation (which is covered in section 7.7.2).

The normalisation factor, k, accounts for the relative data/MC normalisation difference between the search and CR. For the measurement of $d\sigma/dm_{jj}$, the normalisation factor is defined as,

$$k = \frac{N_{\text{SR},0}^{\text{data}} - N_{\text{SR},0}^{\text{non-strong}}}{N_{\text{CR},0}^{\text{data}} - N_{\text{CR},0}^{\text{non-strong}}} \frac{N_{\text{CR},0}^{\text{strong-MC}}}{N_{\text{SR},0}^{\text{strong-MC}}}, \tag{7.8}$$

Variable	$r_{\mathrm{CR},i}$ parametrisation	$r_{\mathrm{CR},i}$ alt parametrisation
m_{jj}	$r_{\mathrm{CR},i} = e^{a+b(m_{jj})}$	$r_{\mathrm{CR},i} = a + (m_{jj})^b$
Δy_{jj}	$r_{\mathrm{CR},i} = a + b(\Delta y_{jj})$	$r_{\mathrm{CR},i} = a + b(\Delta y_{jj}) + c(\Delta y_{jj})^2$
p_{T}^{Z}	$r_{\mathrm{CR},i} = a + b(p_{\mathrm{T}}^{Z})$	$r_{\mathrm{CR},i} = a + b(p_{\mathrm{T}}^{Z}) + c(p_{\mathrm{T}}^{Z})^2$
$\Delta\phi_{jj}^{\mathrm{signed}}$	$r_{\mathrm{CR},i} = a + c(\Delta\phi_{jj}^{\mathrm{signed}})^2$	$r_{\mathrm{CR},i} = a + c(\Delta\phi_{jj}^{\mathrm{signed}})^2 + +c(\Delta\phi_{jj}^{\mathrm{signed}})^4$

TABLE 7.6: Parametrisation of $r_{\mathrm{CR},i}$ for the 4 different variables.

where 0 labels a normalisation region. The normalisation regions used in equation 7.8 have an identical selection criteria to the signal and CRs given in figure 7.17 with the exception of the m_{jj} cut. The signal and CRs use $m_{jj} > 1000$ GeV and the normalisation regions use 500 GeV$< m_{jj} <$ 750 GeV (This is the "zero bin" in equation 7.8). The choice of normalisation region at low m_{jj} is motivated by the fact that the number of strong events dominate the number of electroweak events and so the electroweak template has little impact on the strong-Zjj normalisation.

For the measurement as a function of Δy_{jj}, p_{T}^{Z} and $\Delta\phi_{jj}^{\mathrm{signed}}$, the normalisation of the strong-Zjj template in the search region is taken from the integral of the constrained m_{jj} strong-Zjj template. This integral is taken over the range $m_{jj} > 1000$ GeV. This ensures that strong-Zjj template has the same number of events in it for each of the 4 measured variables.

Finally as there are two strong-Zjj predictions (SHERPA and MADGRAPH), the analysis is repeated independently for each MC simulation and the final strong-Zjj prediction is taken to be the average of the two results, with an error equal to the spread of the two.

7.6.4 Choice of control region to constrain strong-Zjj in signal region

For the measurement of the differential cross-section as a function of m_{jj}, the CR used to define the re-weighting function in equation 7.7 is taken to be CR C. The motivation for using CR C is given in figure 7.19, which shows the double ratio of MADGRAPH to SHERPA's event-yield ratio N_{SR}/N_i (where $i = A, B, C$) for strong-Zjj production. To avoid large systematic uncertainties related to event generator modelling, a flat double ratio is needed between the different generators as it implies that they are consistent with each other. As shown in figure 7.19, the flattest double ratio is obtained for event-yield ratios between the SR and CR C.

Other kinematic variables have different CRs with the flattest double ratio and so not all variables derive the re-weighting function in the same CR. Figure 7.19 shows the double ratios for the other kinematic variables and table 7.7 summarises which CR is to be used to derive $r_{\mathrm{CR},i}$. In figure 7.19 the statistical errors in the double ratio as a function of m_{jj} appear larger as it is a more steeply falling distribution and so most of the events are in the first two bins.

Variable	Default CR
m_{jj}	C
p_{T}^{Z}	A
Δy_{jj}	C
$\Delta\phi_{jj}^{\mathrm{signed}}$	A

TABLE 7.7: Summary of the CR used to derive the data-driven constraint. The CR chosen is the one that produces the flattest double ratio of strong-Zjj event yields for different phase space regions, N_i/N_{SR} with respect to SHERPA. These ratios can be seen in figure 7.19. A flat double ratio implies that the difference between the search and CR is the same for both MADGRAPH and SHERPA, and so the systematic error will be lower.

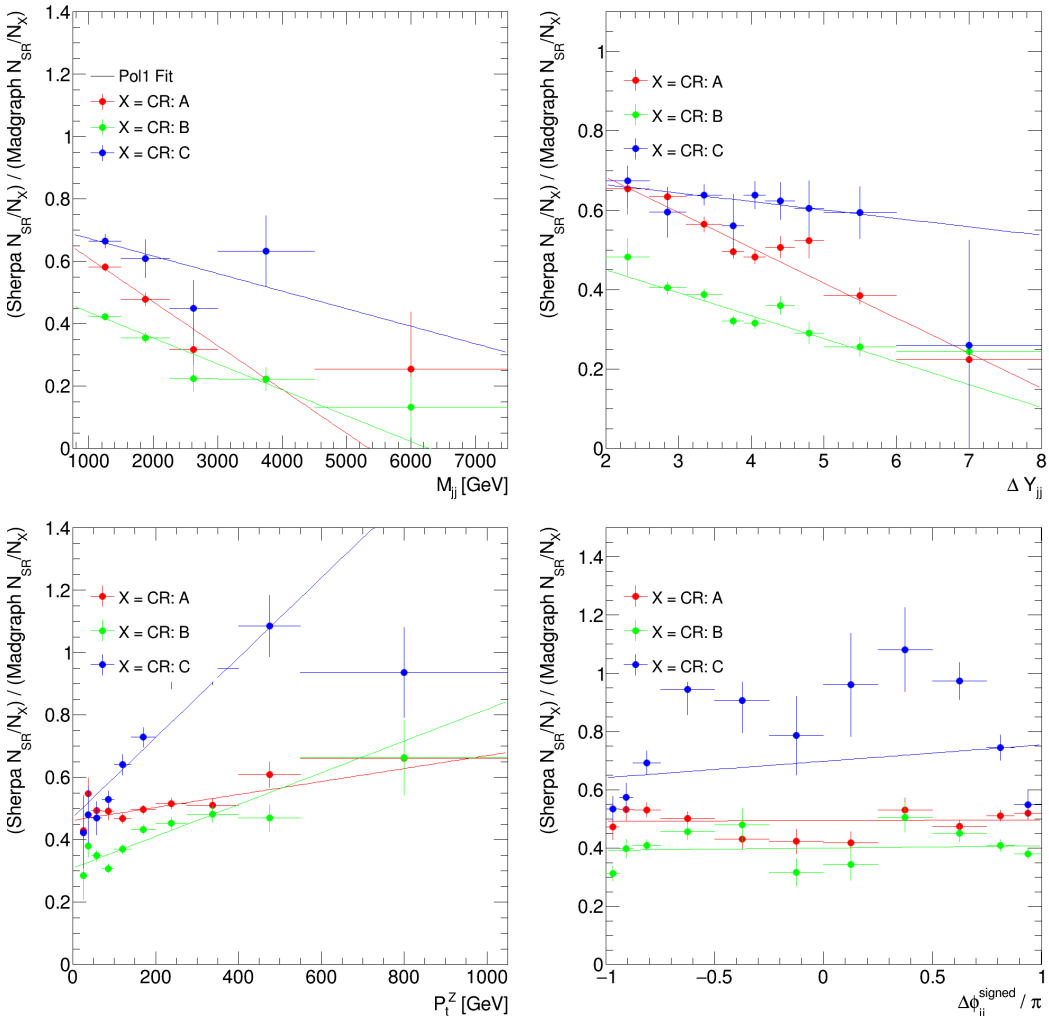

FIGURE 7.19: Double ratio of event yields in different CRs for (top-left) m_{jj}, (top-right) Δy_{jj}, (bottom-left) $p_{\mathrm{T}}^{Z}$and (bottom-right) $\Delta\phi_{jj}^{\mathrm{signed}}$, N_{SR}/N_i with respect to SHERPA, (where $i = A, B, C$) for strong-Zjj production as calculated with MADGRAPH and SHERPA. A flat double ratio implies that the difference between the search and CR is the same for both MADGRAPH and SHERPA, and so the systematic error will be lower.

7.6.5 Derivation of data-driven constraint on strong-Zjj

The parametrisation of $r_{\mathrm{CR},i}$ is given in table 7.6 along with the alternate parametrisations used to estimate the systematic impact of the parametrisation, which is covered in section 7.7.2. A comparison of data and simulation in the default CRs for the four key variables is given in figure 7.20. Figure 7.21 shows the data-driven constraint, $r_{\mathrm{CR},i}$, for both strong-Zjj templates for each of the four variables. The constraints are derived in dedicated CRs that suppress the EW-Zjj contribution as outlined in section 7.6.4 and for each of the MC event generators used to simulate strong-Zjj production.

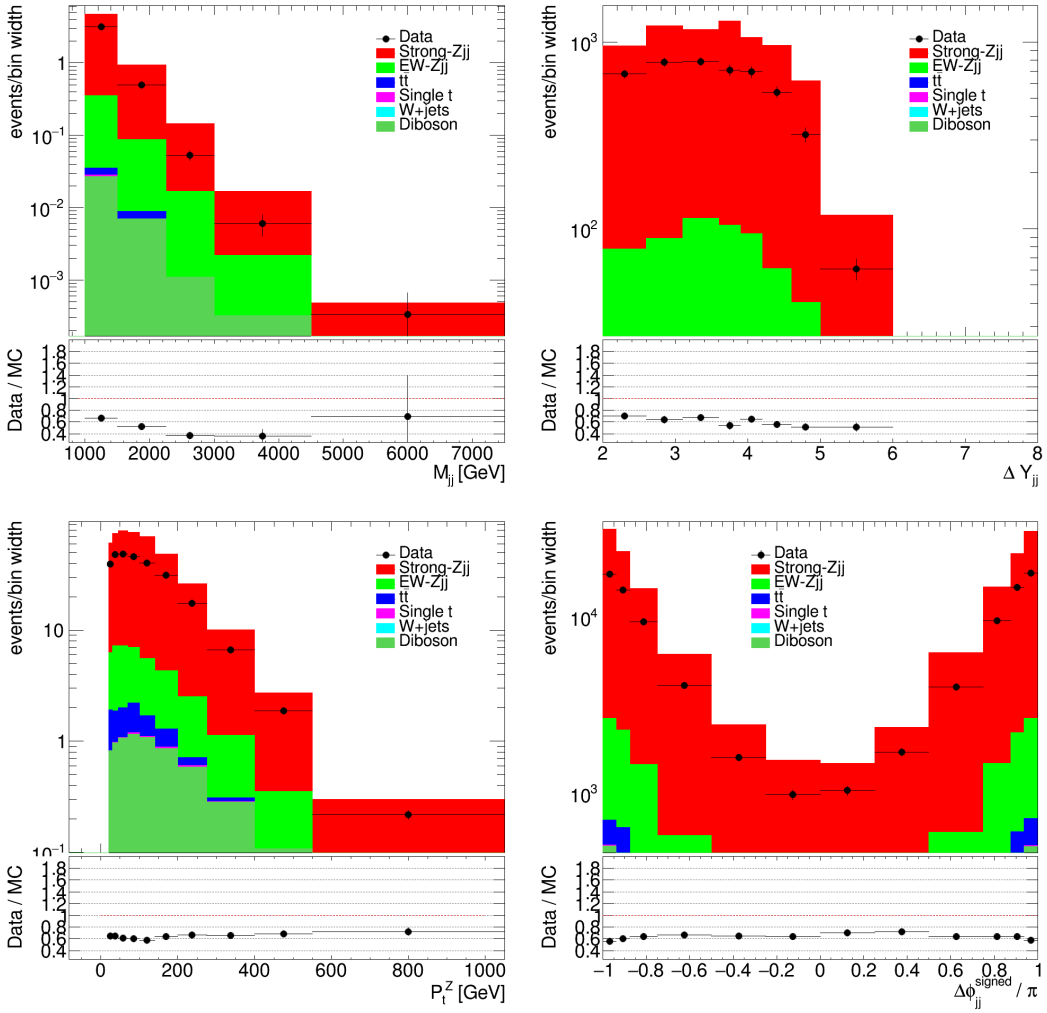

FIGURE 7.20: A comparison of data and simulation for CR used to derive the SR for the four key variables. The chosen CR is the one that has the flattest double ratio from figure 7.19. These plots use the combination of the electron and muon channels and use SHERPA for the strong-Zjj prediction. The distributions shown are m_{jj}(CR C), Δy_{jj}(CR C), p_{T}^{Z}(CR A) and $\Delta\phi_{jj}^{\mathrm{signed}}$(CR A).

The re-weighting functions derived in the other CRs or using the alternate parametrisations given in table 7.6 are shown in Appendix F. For the variable $\Delta\phi_{jj}^{\mathrm{signed}}$ no CP violation is expected and so the linear term in the second order polynomial has been removed. If the linear term is kept in the fit, the value of the constant is within one

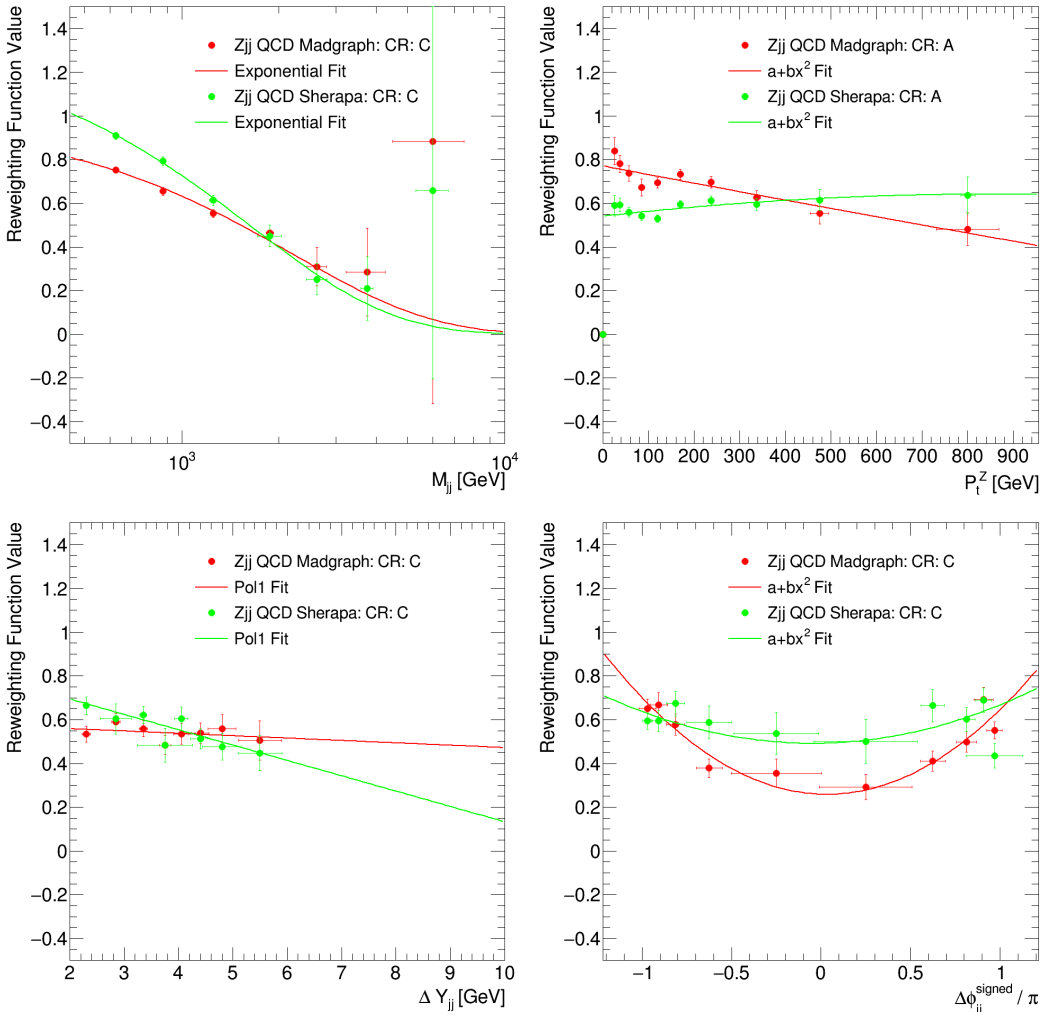

FIGURE 7.21: Data-driven constraint on strong-Zjj production as a function of (top-left) m_{jj}, (top-right) Δy_{jj}, (bottom-left) $p_{\mathrm{T}}^{Z}$and (bottom-right) $\Delta\phi_{jj}^{\mathrm{signed}}$. The constraints are derived in dedicated CRs (as outlined in section 7.6.4) and shown separately for the MADGRAPH, and SHERPA event generators. These constraints are then used to constrain the strong-Zjj in the search region.

standard deviation of zero. It is worth noting that as the re-weighting function is describing a mismodelling effect, one can have a linear term without CP violation. The same logic can be applied to the cubic term for the alternative parametrisation. The additional normalisation factor, k, (equation 7.8) that accounts for data/MC mismodelling in the relative normalisation of the SR and CR of the Strong-Zjj, is derived separately for each distribution using the phase space regions defined in section 7.6.4 and separately for each MC event generator prediction.

7.6.6 Closure test of constraints and normalisation factors

The SR is defined as $N_{\mathrm{jets}}^{\mathrm{gap}} < 1$ and $\zeta_Z \leq 0.5$ and the CRs used to derive the data-driven constraint are listed in table 7.7. For this data-driven constraint to work effectively the data/MC mismodelling must be similar between the CR and the SR. This can be explicitly tested in the two EW-suppressed CRs that are not used to constrain

the strong-Zjj template in the SR. This is illustrated in figure 7.22 for the m_{jj} case. In the full analysis, CR C is used to constrain the strong-Zjj template in the SR. This can be validated using two EW-suppressed regions CR B and CR A. Specifically, a re-weighting function derived in CR B can be used to correct the strong-Zjj template in CR A and validated against the data. If a different CR other than C is used to obtain the re-weighting function that constrains the SR, the other two CRs can still be used to test the method in an analogous manner.

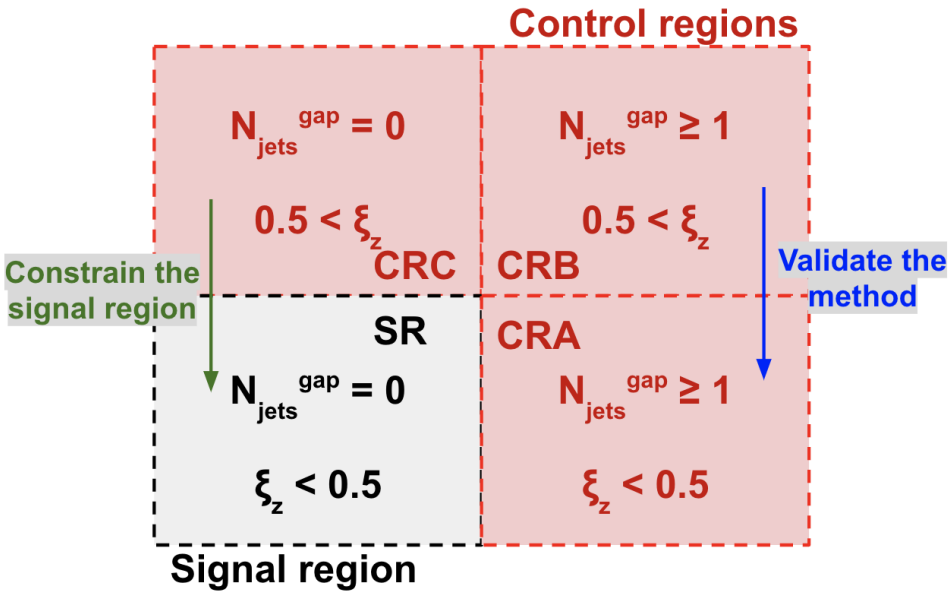

FIGURE 7.22: Diagram depicting how the control and search regions are defined for the extraction of the electroweak signal differentially and how the validation procedure is performed for the m_{jj} variable. The arrows' origin is where that data-driven correction is derived and it points to where the correction is applied.

Figure 7.23 shows the result of using a data-driven constraint derived in a CR to constrain the SHERPA strong-Zjj prediction in another CR. It can be seen that the agreement between data and simulation is improved for each of the measured variables. The agreement is not perfect, however, as the data/MC ratio after the data-driven constraint has been applied is not perfectly flat at 1. A non closure systematic is taken as the data/MC ratio in this validation CR, as described in section 7.7.2. This systematic accounts for the fact that the data/MC mismodelling is not exactly the same in all regions.

The additional normalisation factor, k, (equation 7.8) that accounts for data/MC mismodelling in the relative normalisation of the strong-Zjj template between the two regions can also be checked. A summary of these normalisations can be found in table 7.8 for both the validation and for constraining the search region. These tables show that the normalisation factors derived in a CR to another CR are very similar to moving from a CR to the search region. As the normalisation is derived outside of the SR this check does not look at the data inside the SR itself and thereby was performed before unblinding.

The reason for the variation in these k-factors between the SHERPA and MADGRAPH shown in table 7.8 is due to the fact that the data-driven constraint happens in two steps. The first step is the shape correction $r_{CR,i}$ which does not preserve the integral of the strong-Zjj template. The second step is when the normalisation factor

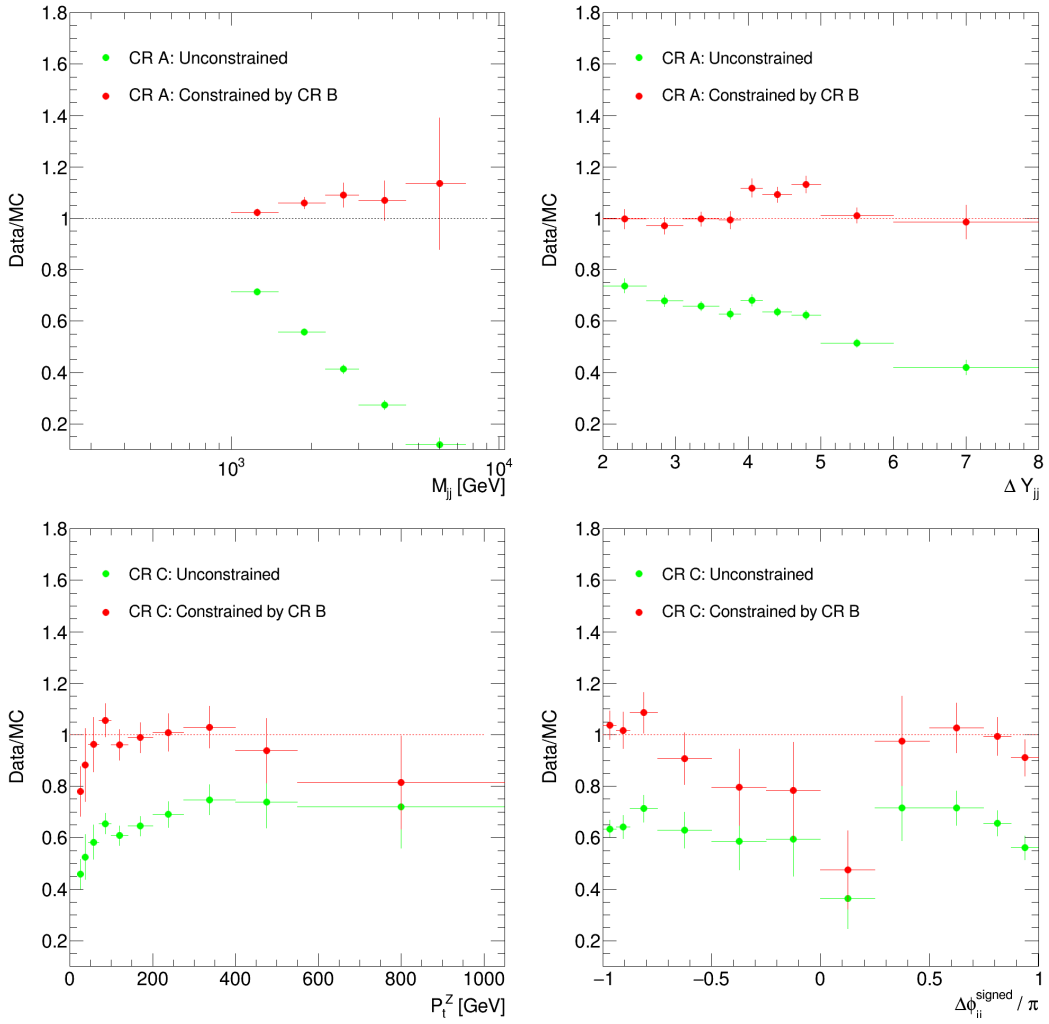

FIGURE 7.23: Data/MC ratios for CR A&C before and after the data-driven constraint has been applied having been derived in CR B for (top-left) m_{jj}, (top-right) Δy_{jj}, (bottom-left) $p_{\mathrm{T}}^{Z}$and (bottom-right) $\Delta\phi_{jj}^{\mathrm{signed}}$. The constraints are derived in dedicated CRs (as outlined in section 7.6.4) and shown only for the SHERPA event generators.

k is applied. As the first step does not preserve the normalisation of the strong-Zjj template, the k-factor is then a little different for each MC generator.

Variable Name	Derived In	Applied To	Value of k SHERPA	Value of k MADGRAPH
m_{jj}	CR B	CR A	1.14	0.81
m_{jj}	CR C	SR	1.11	0.79
p_{T}^{Z}	CR B	CR C	1.21	0.83
p_{T}^{Z}	CR A	SR	1.21	0.82
Δy_{jj}	CR B	CR A	1.18	0.85
Δy_{jj}	CR C	SR	1.19	0.82
$\Delta\phi_{jj}^{\mathrm{signed}}$	CR B	CR A	1.17	0.84
$\Delta\phi_{jj}^{\mathrm{signed}}$	CR C	SR	1.20	0.87

TABLE 7.8: Comparison of the normalisation k values derived between the different CR/SR combinations. These values are expected to be similar between the same strong-Zjj MC for both the CR and the SR.

7.6.7 The strong-Zjj template in the SR

The final strong-Zjj prediction in the SR used in the measurement is taken to be an average of the SHERPA and MADGRAPH constrained templates as there is no argument to be made that one is more accurate than the other. Figure 7.24 shows a comparison of the SHERPA and MADGRAPH templates in the SR after the data-driven constraints have been applied. It can be seen that after the data-driven constraint is applied there is a relatively good agreement between the two generator predictions.

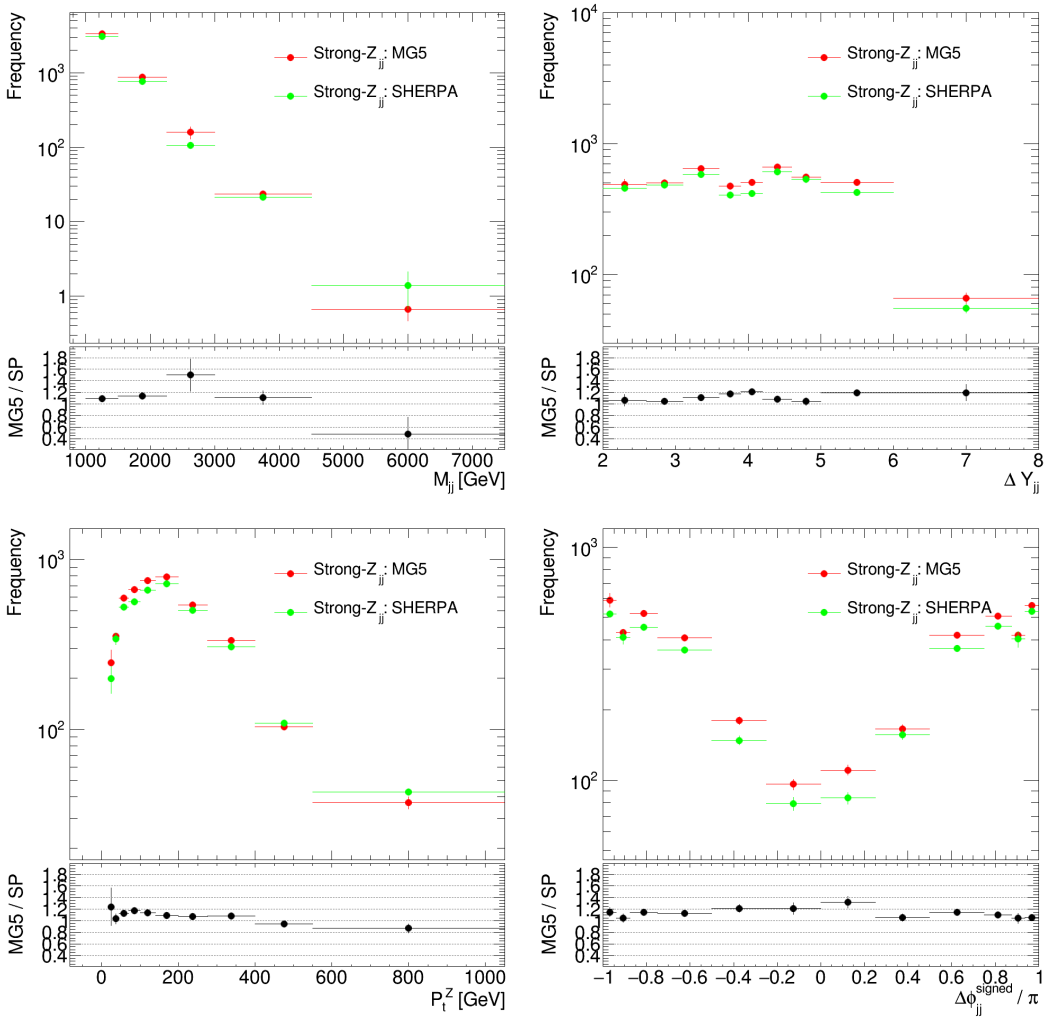

FIGURE 7.24: Predictions for the constrained strong-Zjj template in the SR for both SHERPA and MADGRAPH for (top-left) m_{jj}, (top-right) Δy_{jj}, (bottom-left) $p_{\mathrm{T}}^{Z}$and (bottom-right) $\Delta\phi_{jj}^{\text{signed}}$. The constraints are derived in dedicated CRs (as outlined in section 7.6.4).

7.7 Statistical and systematic uncertainty

In this section, the method used to evaluate the experimental and theoretical systematic uncertainties on the measurement of the electroweak differential cross-section are discussed.

7.7.1 Statistical uncertainties

The impact of the statistical error of both the CR and the SR are calculated for both the MC and the data separately. The statistical error from the CR affects the calculated number of electroweak events as it is used to derive the data-driven constraint as detailed in section 7.6.

The MC simulations' statistical uncertainty can be sizeable. The statistical variance of the MC prediction ($\sum w$) in a bin is given by $\sum w^2$ of the events in the bin, where w denotes the event weight, that includes the $\sigma\,\mathcal{L}$ normalisation to the luminosity and all corrections accounting for shortcomings in the simulation (the pileup

re-weighting and all lepton and jet efficiency scale factors). The fractional statistical uncertainty of a predicted MC event yield n_j in bin j is hence $\Delta n_j = \sqrt{\sum_j w^2} / \sum_j w$. The primary reason this uncertainty sometimes is large for the analysis is due to the fact that the strong-Zjj sample is produced in slices of H_{T}. The analysis is dominated by high H_{T} events, but events from low H_{T} slices occasionally pass the event selection. These events have a very large cross-section normalisation weight, and have a large contribution to $\sum w$ and $\sum w^2$.

To calculate the impact of the statistics a bootstrap method is used. For the data, the analysis is repeated 2000 times: 1000 times where the SR is varied and the same for the CR. For each repetition, the bin yield in a given distribution is varied by shifting the bin yield by random numbers pulled from a Poisson distribution of mean equal to the yield in the bin. Then the full analysis is repeated, i.e. the data-driven constraint from the CR is applied in the SR to the strong-Zjj template and the number of electroweak events is extracted. The standard deviation of the extracted number of electroweak events is taken from the toy experiments to be the statistical error from data in the bin.

For the MC simulations the analysis is again repeated 2000 times in an analogous manner to the data. For each repetition the bin yields are varied by a random number pulled from a Gaussian distribution of mean equal to the value in the bin and standard deviation equal to the error in the bin. Then the full analysis is repeated. The standard deviation of the spread of predictions of the number of electroweak events is taken to be the statistical error for the MC simulations in the bin.

7.7.2 Modelling of Strong-Zjj

The normalisation and shape of the strong-Zjj background is constrained using the data-driven method outlined in section 7.6. In this method, a re-weighting function, $r_{\mathrm{CR},i}$, for the strong-Zjj background is derived in a CR. It is then subsequently used to re-weight the background template in the SR, after accounting for data/MC differences in the relative normalisation of the SR and CR (i.e. the additional normalisation factor k). The change in the strong-Zjj background template due to any experimental or theory systematic uncertainty can be defined in each bin as,

$$N^{\text{strong}}_{\mathrm{SR},i}(\text{shift}) = \frac{k_{\text{shift}}}{k_{\text{nom}}} \frac{r^{\text{shift}}_{\mathrm{CR},i}}{r^{\text{nom}}_{\mathrm{CR},i}} N^{\text{strong}}_{\mathrm{SR},i}(\text{nom}) \tag{7.9}$$

where k and $r_{\mathrm{CR},i}$ are defined by equations 7.7 and 7.8, "$shift$" and "nom" label the systematic-shifted and nominal templates. In the case of changes to only the strong-Zjj background (i.e. the modelling uncertainty), the values of k and $r_{\mathrm{CR},i}$ simplify to

$$\frac{k_{\text{shift}}}{k_{\text{nom}}} = \frac{N^{\text{strong-MC}}_{\mathrm{CR},0}(\text{shift})\, N^{\text{strong-MC}}_{\mathrm{SR},0}(\text{nom})}{N^{\text{strong-MC}}_{\mathrm{CR},0}(\text{nom})\, N^{\text{strong-MC}}_{\mathrm{SR},0}(\text{shift})}, \tag{7.10}$$

and

$$\frac{r^{\text{shift}}_{\mathrm{CR},i}}{r^{\text{nom}}_{\mathrm{CR},i}} = \frac{N^{\text{strong,MC}}_{\mathrm{CR},i}(\text{nom})}{N^{\text{strong,MC}}_{\mathrm{CR},i}(\text{shift})}. \tag{7.11}$$

For each source of uncertainty, the values of k_{shift}/k_{nom} and $r^{shift}_{\mathrm{CR},i}/r^{nom}_{\mathrm{CR},i}$ are determined. These are then propagated to the strong-Zjj template in the SR using equation 7.9.

The envelope of theory modelling variations is taken as a $\pm 1\sigma$ theoretical uncertainty band.

7.7.2.1 MC generator scales

The change in the strong-Zjj prediction due to the choice of factorisation and renormalisation is taken as a modelling systematic. Four variations are defined by using new SHERPA strong-Zjj predictions with either the factorisation or the renormalisation scale shifted up or down by a factor of two. The full analysis is repeated with the shifted strong-Zjj prediction and the number of electroweak events in each bin of the SR is obtained. The difference between nominal and shifted is taken as a systematic and is called QCD Scale.

7.7.2.2 Choice of Strong-Zjj generator

The theoretical modelling uncertainty due to the choice of event generator is determined using SHERPA and MADGRAPH. Figure 7.19 shows the double ratio of strong-Zjj event yields in the SRs and CRs for each of these generators in each bin m_{jj}, Δy_{jj}, $\xi_Z$and $N_{\text{jets}}^{\text{gap}}$ with respect to SHERPA. The double ratios are then fitted with a first order polynomial and used to predict $k_{\text{shift}}/k_{\text{nom}}$ and $r_{\text{CR},i}^{\text{shift}}/r_{\text{CR},i}^{\text{nom}}$. The exception to this is $\Delta\phi_{jj}^{\text{signed}}$ which uses a second order polynomial. Applying these fits as an additional re-weighting allows one to to estimate a systematic associated with the choice of strong-Zjj generator. The change in the extracted electroweak yield is taken to be a systematic called the QCD modelling systematic.

7.7.2.3 Re-weighting function parametrisation

A systematic is assigned to the parametrisation of the re-weighting function, $r_{\text{CR},i}$. Here, the full analysis is repeated using a different parametrisation and the difference in the extracted electroweak yield between this and the nominal case is taken as a systematic and is called ReW parametrisation systematic. These alternate parametrisations can be found in table 7.6.

7.7.2.4 Non closure of closure test

The closure test of the data-driven constraint is covered in section 7.6.6 and it quantifies the non closure of the method in two EW-suppressed CRs. This non closure is shown in figure 7.25 for each strong-Zjj MC simulation and is applied as an additional re-weighting on the SR. This difference between the EW yields obtained between the variation and the nominal re-weighting is taken as the systematic. This systematic is called the QCD Non Closure systematic.

The non closure on the validation of the data-driven constraint is parametrised by re-calculating the data-driven constraint, $r_{\text{CR},i}$ (equation 7.7), and applying it as an additional re-weighting on the SR. The difference between this and the nominal case is taken as the systematic. The size of these non closures can be seen in figure 7.23. Additionally the non closure fits are shown in figure 7.25, where all the fits are first order polynomials with the exception of $\Delta\phi_{jj}^{\text{signed}}$which uses a second order polynomial.

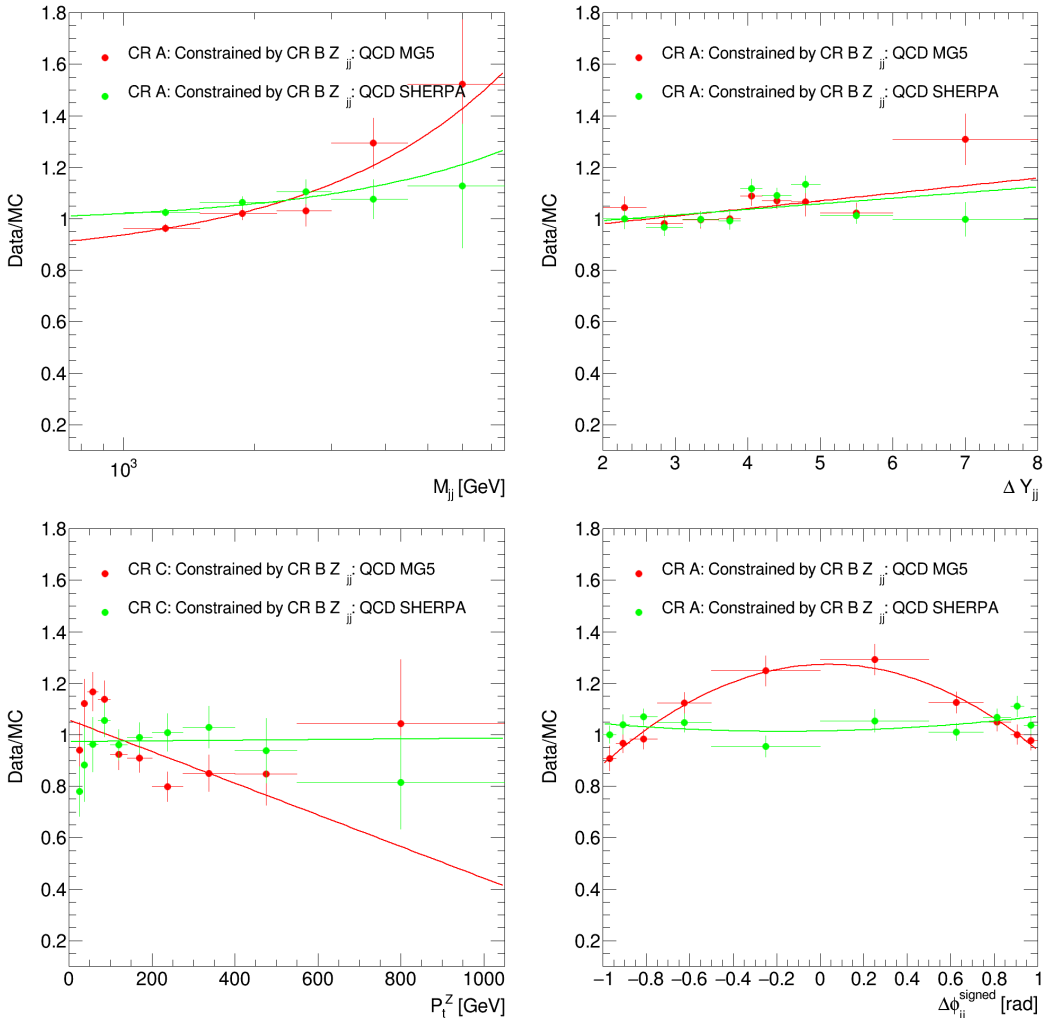

FIGURE 7.25: Fitted Data/MC ratios for CR A&C after the data-driven constraint has been applied having been derived in CR B for (top-left) m_{jj}, (top-right) Δy_{jj}, (bottom-left) p_{T}^{Z} and (bottom-right) $\Delta\phi_{jj}^{\mathrm{signed}}$. The constraints are derived in dedicated CRs (as outlined in section 7.6.4). All fits with the exception of $\Delta\phi_{jj}^{\mathrm{signed}}$ are first order polynomials and $\Delta\phi_{jj}^{\mathrm{signed}}$ are second order polynomials.

7.7.3 Theoretical modelling of electroweak Zjj

The shape and normalisation of the EW-Zjj simulation impacts on the analysis as it is subtracted from the data in the CRs when determining k and $r_{\mathrm{CR},i}$ for the data-driven constraint on the strong-Zjj background. Although these constraints are derived in EW-suppressed regions, they still can result in a relatively large uncertainty on the extracted EW yield.

7.7.3.1 Electroweak template shape

The uncertainty associated with the shape of the EW-Zjj template is determined by using SHERPA and POWHEG+PYTHIA8. This is done after normalising the EW templates to the POWHEG+PYTHIA8 prediction in the baseline region, which is accurate to NLO in QCD. The difference in shape between the two templates are shown in figure 7.26 for the default CRs used for each measured distribution. This systematic is called EWK Shape.

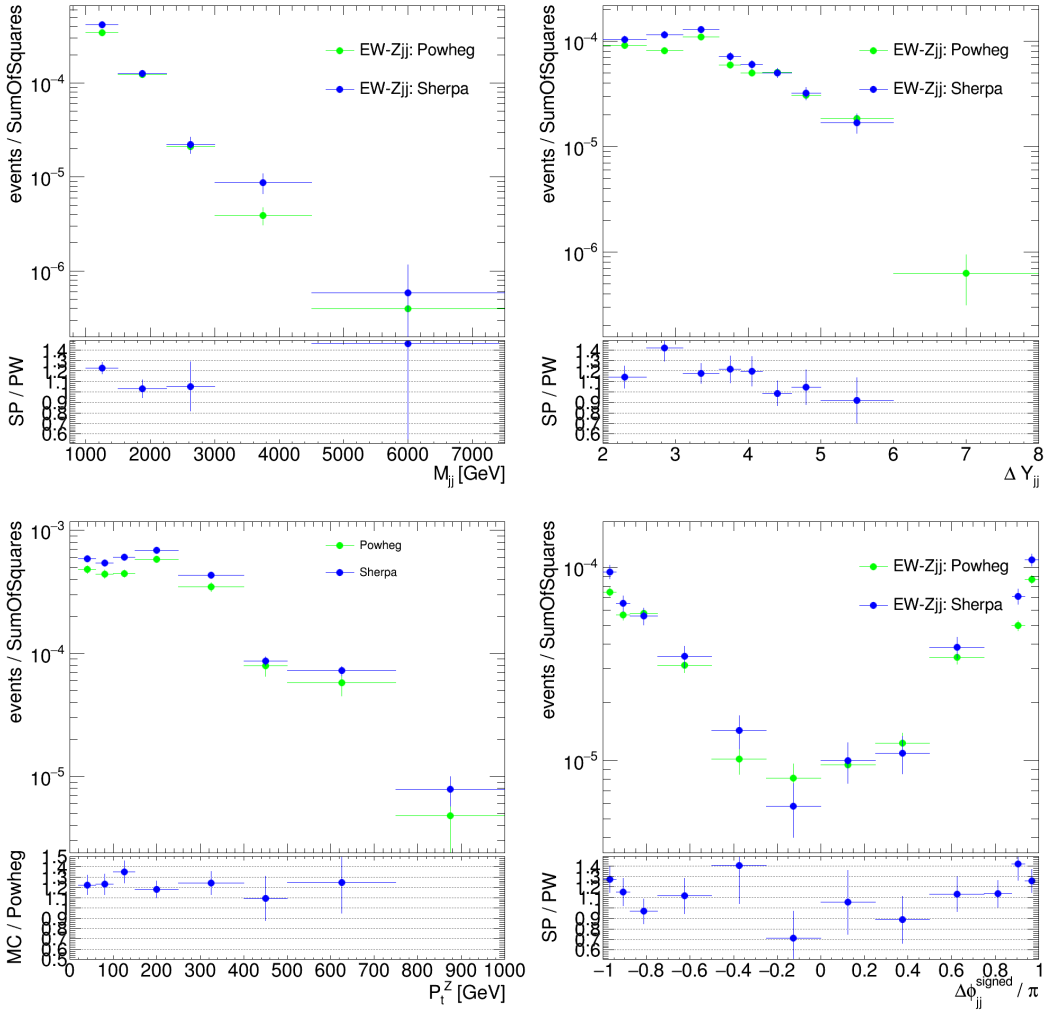

FIGURE 7.26: Ratio of electroweak templates predicted by SHERPA and POWHEG+PYTHIA8 in the CR used to constrain the SR for each measured distribution: (top-left) m_{jj}, (top-right) Δy_{jj}, (bottom-left) p_{T}^{Z} and (bottom-right) $\Delta\phi_{jj}^{\mathrm{signed}}$

7.7.3.2 Electroweak normalisation

The uncertainty associated with the normalisation of the EW template is estimated by varying the contribution by $\pm 20\%$, which is consistent with the previously measured fiducial cross-sections using ATLAS data at $\sqrt{s} = 8$ TeV and $\sqrt{s} = 13$ TeV. The analysis is repeated using the shifted templates and the difference between this and the nominal case is taken as a systematic.

7.7.4 Jet and lepton systematics

The impact of the jet energy scale (JES), jet energy resolution (JER) and lepton systematics is calculated for each of the MC simulation samples used in this analysis. The method to calculate this is slightly different for the strong-Zjj, EW-Zjj, and non-Z_{jj} samples and this section will cover each of these 3 cases in turn. The systematics shifts are applied separately to the MC16a, MC16d and MC16e MCs and then the 3 shifted MC simulation predictions are summed together to create a single systematic-shifted template.

For the strong-Zjj a method can be used analogously to equations 7.7.2 and 7.7.2 to evaluate effect of the JES and JER on the strong-Zjj template. The same double ratio is calculated and applied to the strong-Zjj template in the SR.

For the EW-Zjj and the Non-Zjj the treatment is identical: the systematic shifts are applied to events in both the SR and CR. This is because the data-driven constraint is affected by these templates in the CR. Both the EW-Zjj and the non-Zjj affect the calculation of the normalisation as given in equations 7.7.2 and 7.7.2. Furthermore, the non-Zjj components enter into the final calculation of equation 7.8.

7.7.4.1 Lepton systematics

As described in sections 7.4.2, so-called scale factors are applied to account for shortcomings in the simulated lepton reconstruction, identification and triggering efficiency. These scale factors have associated systematic uncertainties.

For the electrons there is one systematic source each for the identification, isolation and reconstruction and two for the triggers. For the muons, there are 2 isolation systematics, 4 reconstruction systematics, 2 for track to vertex association (TTVA), 2 for trigger statistical uncertainty, 2 for identification, 2 for the sagita bias and one for the scale. Furthermore, muons have associated uncertainties on both the momentum scale and resolutions in the muon spectrometer and the tracking systems. All uncertainty sources are considered uncorrelated and are varied separately. A list of all lepton systematics is given in Appendix E. The Lepton systematics, however, were found to have a negligible impact on this analysis.

7.7.4.2 Jet systematics

Systematic uncertainties associated to jet reconstruction are split into two broad categories, jet energy scale (JES) and jet energy resolution (JER). The complete list of JES/JER systematics is roughly 130 total nuisance parameters (NPs), investigating each separately is only necessary for the most sensitive analyses so the jet performance group offers various configurations that reduce the number of NPs to a manageable number. This analysis uses the so-called "category reduction" for JES systematics which reduces the number of NPs to 29, leaving enough information so

that a combination with CMS is possible, and for JER systematics the "full JER" reduction is used to reduce the number of NPs from 34 to 13. The JES uncertainties are broken down by category as follows:

- 5 η intercalibration NPs (1 modelling, 3 non closure, 1 statistical)
- 2 flavour NPs (flavour response and flavour composition)
- 1 b jet response NP
- 4 pileup NPs
- 1 punch through NP
- 1 extremely high p_{T} single particle NP
- 2 detector NPs
- 4 modelling NPs
- 6 statistical NPs
- 3 mixed NPs

JES uncertainties come from a variety of primary sources most of which are the jet calibration procedures such as η intercalibration, Z+jet balance and multi-jet balance. Other primary sources are MC non closure, jet flavour and pileup. Each of the 29 NPs are evaluated separately and for JES and JER the important NPs are given in Appendix E.

Note that since the in situ jet calibration is derived to a large extent using γ+jet and $Z \to ee$ events, the systematic uncertainties associated with the scale are correlated with the electron scale uncertainties. However, since all in situ JES and the electron or muon scale uncertainties are found to be negligible, this is of no concern to the analysis.

The per-jet efficiency to satisfy the jet vertex fraction requirement is measured in $(Z \to \ell\ell)$+jet events in data and simulation, selecting separately events enriched in hard-scatter jets and events enriched in jets from other proton interactions in the same bunch crossing (pileup). The corresponding uncertainty is evaluated in the analysis by changing the nominal JVF cut value, of 0.59 by ± 0.05 and repeating the full analysis using the modified cut value. Additionally there is 1 NP associated to the efficiency difference in data and MC of the default JVT requirement that is applied as part of the jet definition, see section 7.3.3.3.

7.8 Predicted uncertainties in the SR with Asimov data

Asimov data is where one adds up all of the MC simulations used in the analysis to make a set of "expected" data. This "expected" data is then used to to test the method is behaving as expected.

7.8.0.1 Constraining the Asimov to look more like data

As it can be seen in figure 7.21 both the strong-Zjj samples SHERPAand MADGRAPH greatly over predict the number of events at high m_{jj}. If one were to use the "stock" Asimov (i.e. without modification) one would have a large over-prediction in the size of the systematics on the extracted EW yield, simply because the ratio of N_{EWK}/N_{Strong} is too small. The ratio of N_{EWK}/N_{Strong} events is very important to this analysis. To account for this, the strong-Zjj component of the Asimov is constrained using data in the default CR for each variable in exactly the same method as illustrated in section 7.6.3.

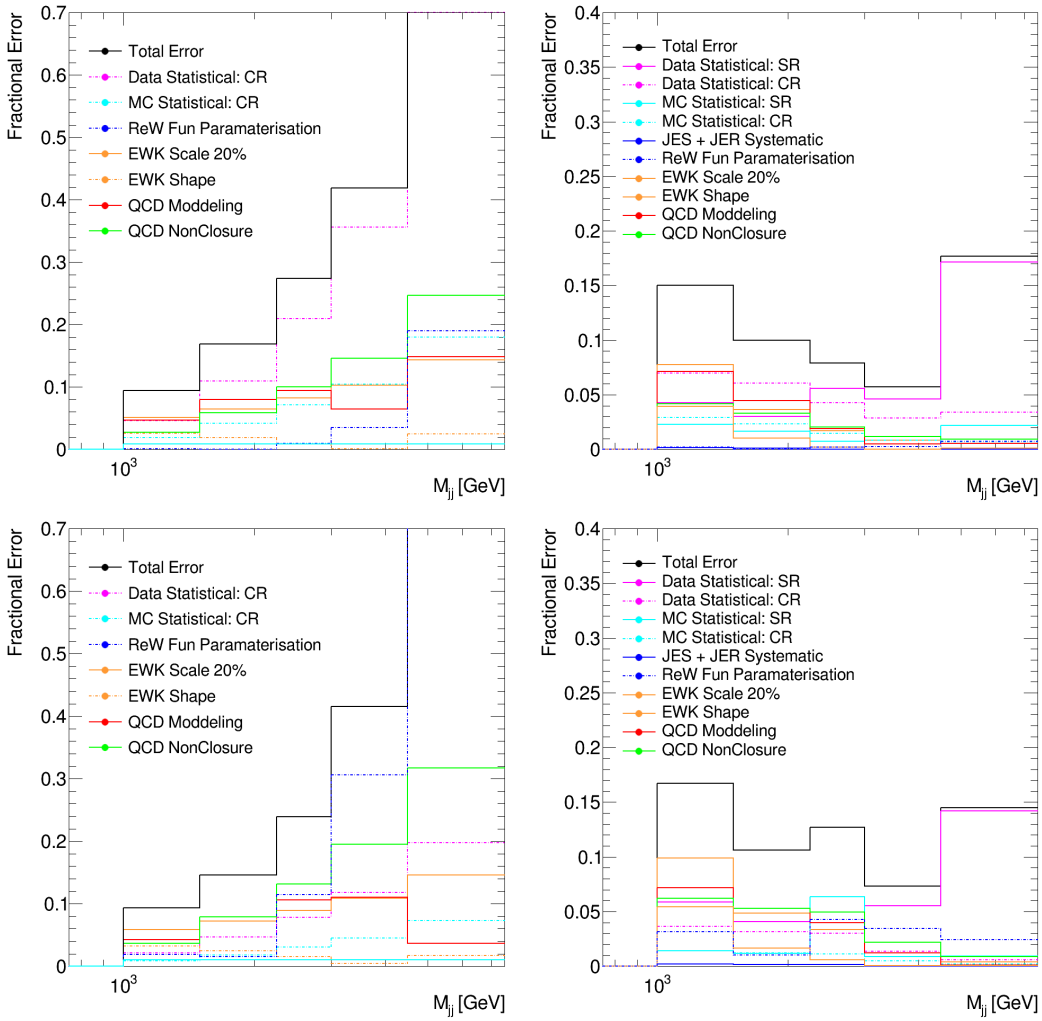

FIGURE 7.27: Depicted here are predicted systematic and statistical errors for m_{jj} using Asimov data for the strong-Zjj (left) and the number of electroweak events (right) and for SHERPA(top) and MADGRAPH (bottom).

7.8.0.2 Predicted Statistical and systematic errors.

The Asimov corrected data was used pre-unblinding to calculate the estimated systematic and statistical errors per bin on the strong-Zjj template as well as the expected uncertainties on the extracted electroweak yield. Figure 7.27 shows the expected uncertainties for both MADGRAPH and SHERPA for m_{jj}. The expected uncertainties on the other three variables are given in Appendix G.

Figure 7.27 clearly demonstrates the relationship between the uncertainty on the strong-Zjj template and the extracted EW-Zjj. As m_{jj} increases the ratio of N_{EWK}/N_{Strong} becomes larger, and so the fractional uncertainty on the strong-Zjj template becomes less impactful on the extracted number of electroweak events. This can be clearly seen by the fact the fractional error on the strong-Zjj increases with m_{jj} but the same behaviour is not seen for the extracted EW-Zjj yield. Instead, for EW-Zjj the uncertainty is largest at low m_{jj} values due to the electroweak errors, as they affect the normalisation factor k. At high values statistical uncertainties dominate. The uncertainty on the extracted electroweak yield is lowest in the mid-range of m_{jj}.

7.9 Electroweak cross-sections

This section contains the extracted electroweak differential cross-sections in the SR along with a comparison to a theory prediction from the POWHEG generator. The differential cross-section, which is described in section 7.6.3, is given by,

$$\frac{d\sigma_i^{\text{EW}}}{dx} = \frac{\hat{N}_{\text{SR},i}^{\text{EW}}}{\Delta x_i \, \mathcal{LC}_i^{EW}} = \frac{N_{\text{SR},i}^{\text{data}} - N_{\text{SR},i}^{\text{strong}} - N_{\text{SR},i}^{\text{non-Z}}}{\Delta x_i \, \mathcal{LC}_i^{EW}}. \tag{7.12}$$

Using the method covered in section 7.6 the quantity $\hat{N}_{\text{SR},i}^{\text{EW}}$ can be calculated by subtracting the constrained number of strong-Zjj and non-Z events from that of the data per bin. The integrated luminosity of the data analysed in this section is 138.42 ($\pm$1.7%) fb^{-1}[119]. The correction factor accounts for experimental efficiency and detector resolution effects and can be parametrised per-bin as,

$$\mathcal{C}_i^{EW} = \frac{N_i^{\text{reco}}}{N_i^{\text{truth}}}, \tag{7.13}$$

where N^{reco} is the number of reconstructed events that enter into the SR predicted by the MC simulations. The quantity N^{truth} is calculated by applying the normal selection criteria for the SR but now using the MC truth information. The correction factor for the SR was computed using the SHERPA and the POWHEG predictions for EW-Zjj. As SHERPA is known to suffer from the colour flow bug described in section 7.2 the value obtained from POWHEG is used. The difference between the predictions of SHERPA and POWHEG is taken as a systematic. Additionally the jet and lepton systematics covered in section 7.7.4 are applied in the same method as previously described. They constitute an additional systematic on the quantity N^{reco} per bin. Figure 7.28 gives the correction factors, $\mathcal{C}$, for all four key variables along with their associated statistical and systematic error. It was found that the difference between the predictions of the SHERPA and POWHEG generators was found to dominate the systematic error.

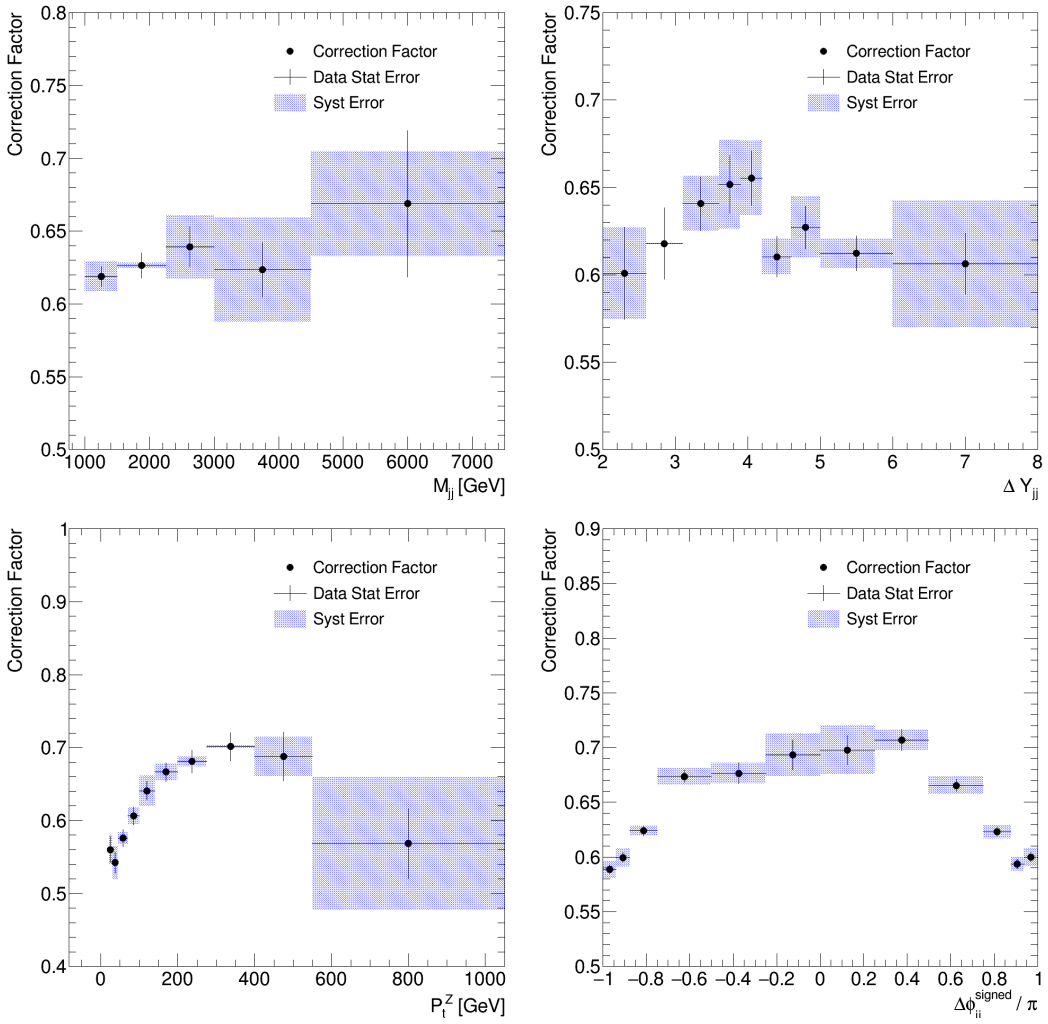

FIGURE 7.28: Depicted here are correction factors m_{jj} (top-left), Δy_{jj} (top-right), p_{T}^{Z} (bottom-left) and $\Delta\phi_{jj}^{\mathrm{signed}}$ (bottom-right).

7.9.1 Differential electroweak cross-sections

This section presents the combination of the measurements of EW-Zjj using SHERPA and MADGRAPH to model the Strong-Zjj for the combined channel (electrons+muons). They are compared to the EW-Zjj prediction by the POWHEG generator. The hashed blue region represents the systematic error and the size of the error bar on the data point represents the statistical error. Additionally the breakdown of the systematic errors for each variable can be found in figures in Appendix H.

Figure 7.29 shows the differential electroweak measurement for the four key variables. Each of the four measurements predicts approximately ~6% fewer events than the POWHEG prediction. The measured m_{jj} distribution shows tension with the prediction from POWHEG for high values of m_{jj} with data showing 20% fewer events than simulation. For Δy_{jj} this is reflected as a 20% deficit at large values of Δy_{jj}. It is worth noting that the disagreement for high m_{jj} and Δy_{jj} is approximately the same, which is to be expected as these two variables are correlated. The result for p_{T}^{Z} shows a better agreement than the previous two observables, with POWHEG slightly over-predicting the number of events for low values of p_{T}^{Z}. Finally $\Delta\phi_{jj}^{\mathrm{signed}}$ shows that POWHEG over-predicts the number of events for $\Delta\phi_{jj}^{\mathrm{signed}}$~0.

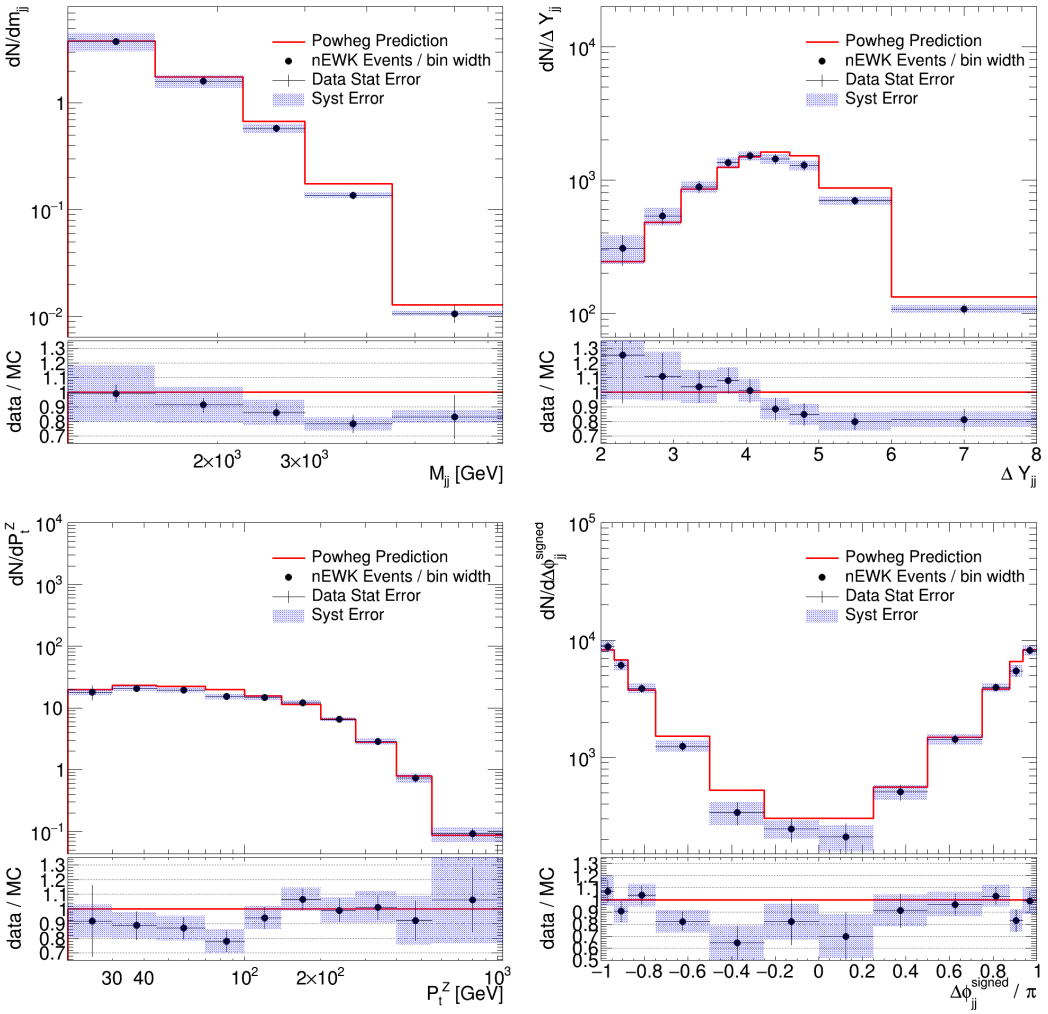

FIGURE 7.29: Measured differential electroweak Zjj cross-sections as a function of m_{jj} (top-left), Δy_{jj} (top-right), p_{T}^{Z} (bottom-left) and $\Delta\phi_{jj}^{\mathrm{signed}}$ (bottom-right). The data is compared to the NLO QCD prediction provided by POWHEG.

7.9.2 Fiducial electroweak cross-sections

The fiducial electroweak cross-section is calculated by taking the integral of the electroweak template in the SR. Table 7.9 gives the extracted number of electroweak events for each of the four distributions. It can be seen that they are in good agreement with each other and all lie ~6% below the POWHEG prediction. As the integral of the strong-Zjj template is the same for all variables and no constraints are applied to the non-Z MC simulations the extracted yield is the same for all variables. The statistical uncertainty is significantly higher for m_{jj} than for the other three variables. This is due to the fact that the ratio of N_{EWK}/N_{Strong} is smaller in the first two bins of the m_{jj} distribution than for any of the bins for the other variables. This results in the uncertainty on the strong-Zjj template having a significantly larger effect for this variable. As the results are comparable with each other, p_{T}^{Z} was used to measure the fiducial electroweak cross-section as it has the lowest systematic error. Table 7.10 gives a breakdown of the statistical and systematic errors on Δy_{jj}.

Variable	Extracted electroweak events	POWHEG prediction
m_{jj}	3760.75 ± 130 (stat) ± 369 (syst)	4017.34
Δy_{jj}	3759.73 ± 124 (stat) ± 99 (syst)	4017.34
p_{T}^{Z}	3759.79 ± 118 (stat) ± 95 (syst)	4017.34
$\Delta\phi_{jj}^{\mathrm{signed}}$	3760.73 ± 110 (stat) ± 113 (syst)	4017.34

TABLE 7.9: text

Source	Uncertainty [%]
Statistical: Data SR	2.5
Statistical: Data CR	1.2
Statistical: MC SR	1.5
Statistical: MC SR	0.8
Sub-Total Statistical	3.3
ReW Fun Parametrisation	0.4
EWK Scale 20%	0.2
EWK Shape	0.8
QCD Moddeling	1.1
QCD NonClosure	1.1
C-factor	0.1
Luminosity	1.7
Sub-Total Systematic	2.5
Total	4.1

TABLE 7.10: This table summarises all of the statistical and systematic errors that effect the fiducial measurement of EW-Zjjusing the variable Δy_{jj}.

The integrated luminosity of the data analysed in this section is 138.42 ($\pm$1.7%) fb^{-1}[119]. Using this in combination with the correction factor given in figure 7.28 gives the measured EW-Zjj cross-section in the SR as:

$$\sigma^{EW} = 43.40 \pm 1.43 \text{ (stat)} \pm 1.01 \text{ (syst) fb.} \tag{7.14}$$

The prediction from POWHEG is

$$\sigma^{EW}_{Powheg} = 46.7 \pm 0.78 \text{ (lumi) fb.} \tag{7.15}$$

Thereby the measured fiducial EW-Zjj cross-section is in agreement with the theory prediction from POWHEG to within its errors.

7.10 Comparison to alternative method

This section will provide a comparison to an alternative method to obtain the differential electroweak measurement. The alternative method was implemented by another ATLAS member. The two results were implemented pre-unblinding and serve as a cross-check of the method.

7.10.1 Alternative method to extract EW-Zjj

The alternative method uses an extended profile likelihood fit in which the same three CRs and the SR described in figure 7.17) enter to constrain the strong-Zjj prediction in the SR. The likelihood function is

$$\log L = -\sum_i \nu_i + \sum_i N_i^{\text{data}} \log \nu_i - \sum_j \log \mathcal{N}_j, \tag{7.16}$$

where i ranges over the bins of the distribution being fitted, j is an index corresponding to an uncertainty source with an associated nuisance parameter θ_j and an uncertainty amplitude in each bin λ_{ij}. The penalty term $\log \mathcal{N}_j = \theta_j^2/2$ is a Gaussian constraint on each nuisance parameter. Finally, ν_i represents the prediction in bin i, composed of signal and background predictions as

$$\begin{aligned} \nu_i &= \mu_{\text{SR},i}^{\text{EW}} N_{\text{SR},i}^{\text{EW,MC}} + N_{\text{SR},i}^{\text{strong}} + N_{\text{SR},i}^{\text{non-Z}} && i \in \text{SR}, \\ \nu_i &= N_i^{\text{EW}} + N_i^{\text{strong}} + N_i^{\text{non-Z}} && i \notin \text{SR}. \end{aligned} \tag{7.17}$$

The $\mu_{\text{SR},i}^{\text{EW}}$ are the parameters of interest to be measured as they are the electroweak signal strength per bin. The electroweak prediction $N_{\text{SR},i}^{\text{EW,MC}}$ is constant in the SR set to the Standard Model prediction. All other N_i in eq. 7.17 are constrained by nuisance parameters and allowed to float in the fit. The number of strong-Zjj events in the SR is defined by

$$\begin{aligned} N_i^{\text{strong}} &= k(x)\, r_{\text{CR},i}\, N_i^{\text{strong,MC}} && i \in \text{SR} \cup \text{VR}, \\ N_i^{\text{strong}} &= r_{\text{CR},i}\, N_i^{\text{strong,MC}} && i \in \text{CR}, \end{aligned} \tag{7.18}$$

where $N_i^{\text{strong,MC}}$ is the number of strong-Zjj events predicted by MC simulation, $r_{\text{CR},i}$ is a bin-by-bin data driven constraint fit in a pair of regions, one with at least one gap jet (CRA and CRB) and one with zero gap jets (CRC and the SR). $k(x)$ is an additional shape function dependent on the measurement variable x (e.g m_{jj}) that extrapolates the strong template from CRC to the SR. Equation 7.18 differs from equation 7.6 in that the constant scale factor k has been replaced by a function that depends on m_{jj}. The transfer function k is a linear function for three of the measurement variables, m_{jj}, Δy_{jj} and p_{T}^Z. Since $\Delta\phi_{jj}^{\text{signed}}$ is a signed variable, a linear transfer function is not appropriate so one reverts to the constant k factor which performs adequately in this variable. To summarize, $k(x)$ is defined as follows:

$$k(x) = p_0 + p_1 x, \qquad x = m_{jj}, \Delta y_{jj} \text{ or } p_{\text{T}}^Z \tag{7.19}$$

$$k(x) = p_0, \qquad x = \Delta\phi_{jj}^{\text{signed}} \tag{7.20}$$

where p_0 and p_1 are free parameters in the likelihood fit.
The likelihood fit is performed using the TRooFit package.[5]

[5] TRooFit: https://gitlab.cern.ch/will/TRooFit, an extension of RooFit developed by Will Buttinger.

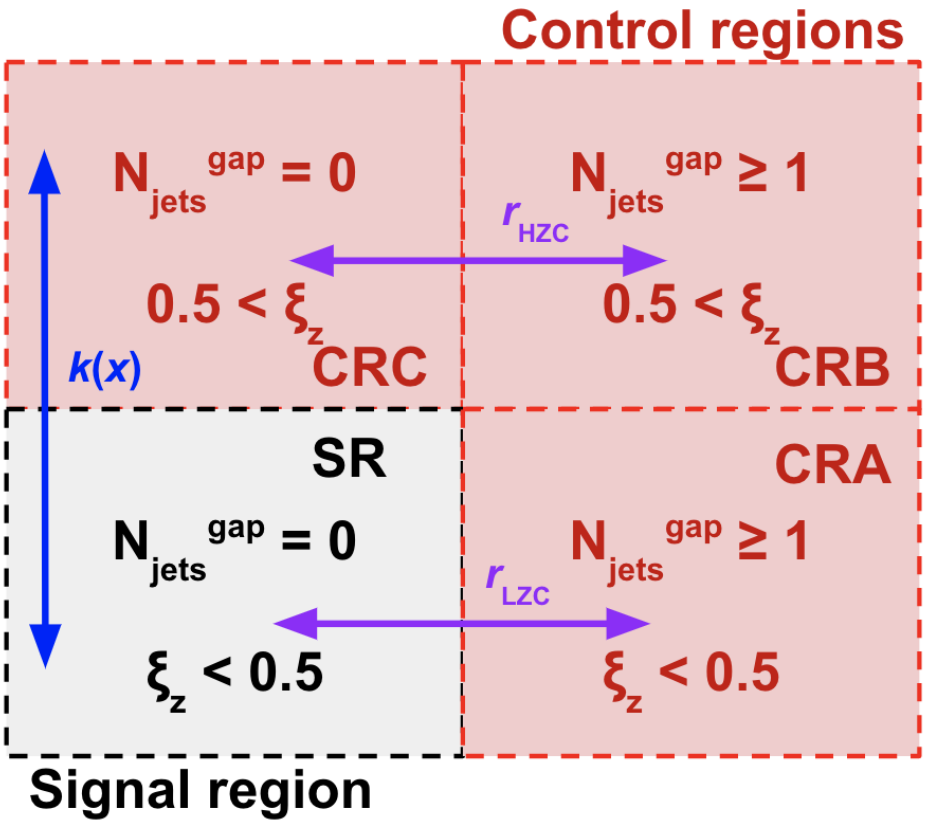

FIGURE 7.30: Diagram depicting how the $r_{\mathrm{CR},i}$ constraints and k transfer function are defined for the second method of extracting the electroweak signal. r_{HZC} are a set of bin-by-bin fit parameters between pairs of bins in each of the "High-Z-Centrality" regions (CRB and CRC) and similarly r_{LZC} are fit to bins in the "Low-Z-Centrality" regions (CRA and the SR).

7.10.2 Comparison plots

Figure 7.31 depicts the ratio of the measured differential electroweak spectrum compared to the prediction using the alternative method. It can be seen that all 4 variables are in good agreement with each other.

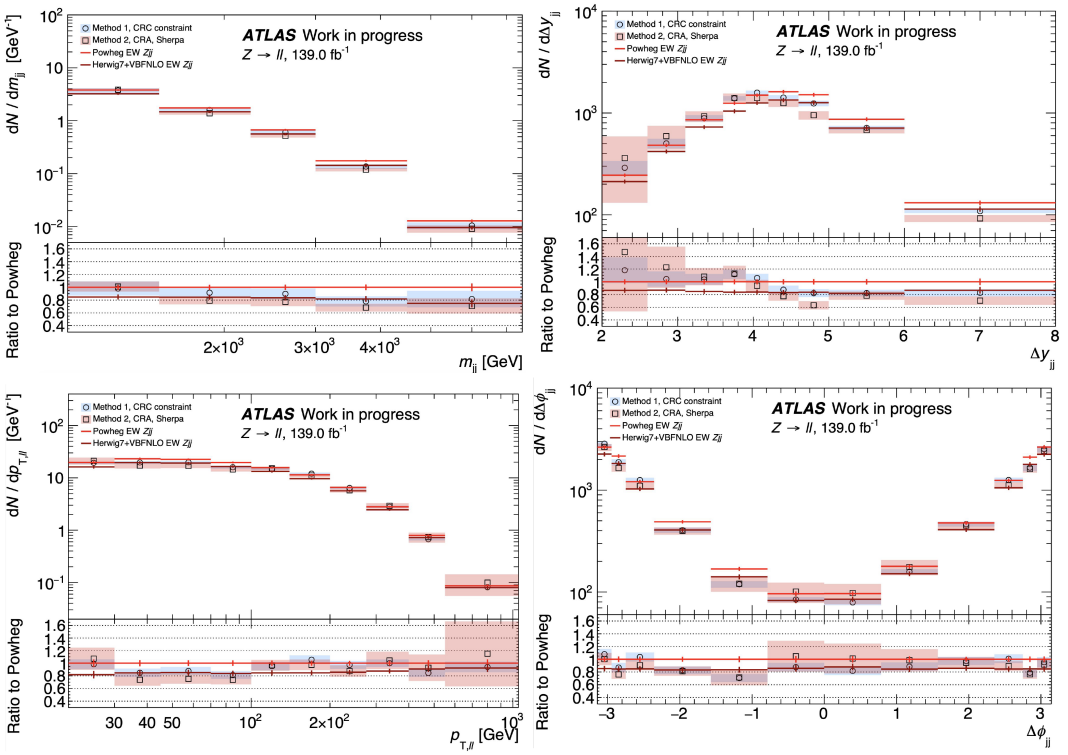

FIGURE 7.31: Depicted here are differential electroweak cross-sections for m_{jj} (top-left), Δy_{jj} (top-right), p_{T}^{Z} (bottom-left) and $\Delta\phi_{jj}^{\mathrm{signed}}$ (bottom-right).The red line is the prediction from POWHEG.

7.11 Conclusion and future prospects

This chapter presented the first differential measurement of the electroweak production of a Z boson in association with jets along with a fiducial measurement in the same fiducial region. Firstly a closure test was performed where a CR was used to constrain itself. The method was optimised by requiring the CR that constrains the SR to be the one with the flattest double ratio of strong-Zjj event yields in the SRs and CRs. After this, the method was validated by using a CR to constrain another in an analagous manner to the CR designated to constrain the SR. A non closure systematic was then applied to account for the fact that this validation was not perfect. The errors were then predicted using Asimov data which demonstrated it would be possible to extract the electroweak signal before unblinding.

A comparison was made to a prediction from the POWHEG-BOX generator. The fiducial measurement is in good agreement with the prediction from theory and with each other. The measured fiducial cross-section was $\sigma^{EW} = 39.9 \pm 1.32\,(\mathrm{stat}) \pm 1.00\,(\mathrm{syst})$ fb. The largest contribution to the systematic error was the QCD modelling and the non closure of the validation. This suggests that the limiting factor to improving this measurement is the accuracy of the strong-Zjj MCs used for this analysis.

The goal of the analysis in this chapter was to give the first differential measurement of the EW-Zjj process in ATLAS. This has been achieved for the four key variables m_{jj}, Δy_{jj}. p_{T}^{Z} and $\Delta\phi_{jj}^{\mathrm{signed}}$. This measurement is going to be part of a paper summarising the measurements of EW-Zjj production in Run 2 at ATLAS.

Chapter 8

Conclusion

This thesis presented the implementation and utilisation of an algorithm that calculates the luminosity delivered to the ATLAS detector during proton-proton collisions at the Large Hadron Collider. Firstly a closure test was performed to validate the pileup corrections applied to the number of reconstructed vertices. Then this algorithm was demonstrated to be both internally and externally consistent for all the WPs that passed the closure test. The algorithm is able to predict the luminosity over a 10 LB period with a precision of 2.2%.

The measurement of the electroweak production of a Z boson in association with jets was performed both differentially and inclusively. It was performed with 138.42 ($\pm$1.7%) fb^{-1} of data that was collected by the ATLAS detector between 2015-2018. All of the data used in this thesis was collected with a centre of mass collision energy of $\sqrt{s} = 13$ TeV. The four different variables gave inclusive cross-sections that were consistent with each other and with a prediction from POWHEG. This measurement is will to be part of a paper summarising the measurements of EW-Zjjproduction in Run 2 at ATLAS.

Appendix A

Vertex counting radial cut motivation

This appendix covers the motivation behind adding a constraint on the radial position of the vertex with respect to the centre of the luminous region. Figure A.1 depicts the Δz distributions for the WP `nVtx5_900` with and without radial cut of $R < 0.3$ mm applied. It can be clearly seen that when the radial cut is not applied there is a poor fit of $f_{exp}(\Delta z)$ (red) to $f_{obs}(|\Delta z|)$ (black) for the region $5 < |\Delta z| < 20$ mm. This is believed to be due to secondary vertices being reconstructed.

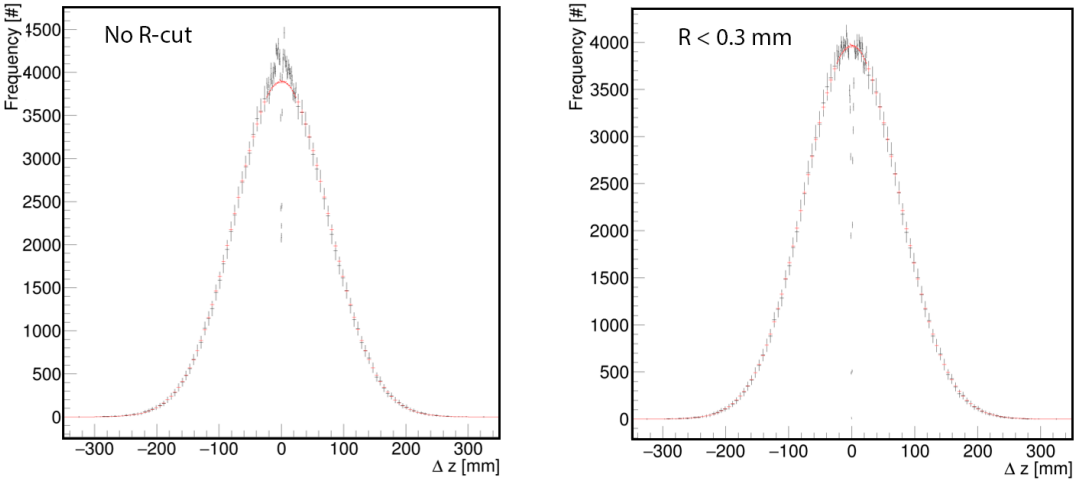

FIGURE A.1: In black are the Δz distributions for the WP `nVtx5_900` with and without radial cut of $R < 0.3$ mm applied. The red line the fit of $f_{exp}(\Delta z)$ to $f_{obs}(|\Delta z|)$ as described in section 6.5.4. The data used in this plot is from the quiescent period of the vdM scan 330875.

In this context a secondary vertex is reconstructed when particles produced in an initial proton-proton scatter decay a non-negligible distance away from the original interaction. They are counted as primary vertices by the vertex counting algorithm because it cannot distinguish these from a true primary vertex. As far as the reconstruction algorithm can see, the secondary vertex appears to have several tracks pointing back to a unique point, which is the criteria for a vertex to be reconstructed.

If one applies the R cut as an additional constraint on the WPs it removes the secondary vertices as most of them lie outside of this radial value. This allows the data-driven vertex merging correction described in section 6.5.4 to be performed.

This effect was not seen previously in Run 1. It is believed that this is due to the fact that the addition of the IBL in Run 2 increased the resolution enough to allow for more secondary decays to be reconstructed. The IBL is covered in section 3.2.4.1. Furthermore the vertex reconstruction algorithm was updated for Run

2, these changes improved the efficiency of finding vertexes and thereby also secondary vertices.

Appendix B

Vertex truth matching

This Appendix will cover the logic used to identify the split and fake vertices using the truth information contained in the MC simulation files. Before one can identify these vertices firstly it is required to match the reconstructed vertices (R-vertices) to the truth vertices (T-vertices).

The MCs used to evaluate these corrections do not provide a direct mapping from R-vertex to T-vertex, so instead one has to use the tracks associated to the vertices. Each truth track (T-track) can be mapped onto a reconstructed track (R-track) by using the truth information provided in the MC. There are a few fringe cases involved in using the truth information and this is covered in section B.3. However, in general one proceeds as follows:

1. Iterate over all R-tracks associated to R-vertices.
2. Map the R-track to the T-track and from this the T-vertex.
3. Create a list of which R-tracks are associated with each T-vertex.
4. Map the R-vertex to the T-vertex that has the largest number of associated R-tracks.

If two or more R-vertices have the same number of R-tracks associated to a T-vertex then the R-vertex with the highest sum of p_t^2 of R-tracks associated to that T-vertex is chosen and the others are classified as merged. Additionally it is possible for two of more T-vertices to be mapped to a single R-vertex. This is, however, not a problem as this is expected due to vertex merging, where two ore more vertices are reconstructed as the same vertex. Additionally there is no radial constraint on the T-vertices considered for this matching procedure as otherwise it is possible for complications to arise where the R-vertex is just inside the radial cut and the T-vertex to lie outside.

The R-track to T-track mapping is not a perfect process, there is a very small μ dependent fraction of T-tracks that can not be matched to a R-track that is associated with a R-vertex. As this fraction of T-tracks is always of order 0.1% or lower its effect is negated in this algorithm. The primary reason for the matching to fail is that the R-track has been badly reconstructed due to the track reconstruction algorithm being "confused" by other nearby hits in the ID. Track reconstruction is covered in section 4.1.

B.1 Identifying split vertices

The procedure for identifying a split vertex is performed per WP as it is possible for a vertex to be classified as split for one WP and not for another. For example,

consider the case where there is a single 12 track vertex in the event that splits into a 9 track and a 3 track vertex when reconstructed. For `nVtx3` this would be seen as a split vertex as the vertex counting algorithm would count two vertices. On the other hand the WP `nVtx5` would not classify this as a split vertex as this WP does not "see" the 3 track vertex.

After all the T-vertices have been matched to R-vertices a vertex is classified as split if two or more[1] R-vertices are mapped to the same T-vertex and the R-vertices pass the selection criteria for the WP. In the rare case the vertex is split into three vertices that pass the selection criteria two splits are counted.

B.2 Identifying fake vertices

Like for split vertices the procedure for identifying a fake vertex is performed per WP as it is possible for a vertex to be classified as fake for one WP and not for another. A R-vertex is classified as fake if less then N associated tracks are matched to the same T-vertex, where N is the cut on the number of associated tracks.

B.3 Edge cases

There are two edge cases that can come up with the truth classification of vertices due to the fact that the merging correction is data-driven, and so it does not have access to the truth information available to the other two correction.

B.3.1 Fake and merged vertex pairs

Using the above classifications it is technically possible for two vertices to be classified as both fake and merged. Consider the case where we have an event with two 4-track vertices A and B that during the reconstruction process "swap" a track. Thereby vertex A has one R-track associated from vertex B and B has one R-track associated from A. Additionally both of the vertices have 3 R-tracks correctly associated. For the WP `nVtx4` both A and B would be classified as fake vertices as they only have 3 correctly assigned tracks. Additionally these two vertices should be classified as merged as they lost a track to another vertex,and so they should fail the WP's criteria. As the vertex merging algorithm does not use truth information it does not 'see" this type of vertex merging as both of the vertices were still reconstructed and so they enter into the Δz distribution. Using equations 6.3 and 6.4 results in,

$$\mu_{vis} = 2(\text{reco}) - 2(\text{fake}) - 0(\text{split}) + 0(\text{merged}) = 0, \tag{B.1}$$

which is an incorrect result as $\mu_{vis} = 2$ for the `nVtx4` WP as there was two vertices that could have been reconstructed. Thereby the fake algorithm should also not count this type of merged and fake vertex due to the fact that the data-driven vertex merging correction does not "see" it. Removing this case from the fake vertex correction "balances" out the merged vertex correction,

$$\mu_{vis} = 2(\text{reco}) - 0(\text{fake}) - 0(\text{split}) + 0(\text{merged}) = 2, \tag{B.2}$$

which leads to the correct result.

[1] Vertex splitting into three verticies happens O(0.01%) of al vertex splits

B.3.2 Split and merged vertex pairs

It is possible for a vertex pair to be both split an merged in an analogous manner to the fake and merged pair described in the section above. Consider an event with two vertices: vertex A is a 12 track vertex that has split during reconstruction into a 8 and a 4 track vertex called A_8 and A_4, vertex B was a 3 track vertex that has merged with vertex A_4. The result of this are two reconstructed vertices where the first is simply the 8-track vertex A_8 and the second is the combination of A_4 and vertex B which results in a 7 track vertex being reconstructed. For the WP `nVtx4` this is classified as both a split and a merged vertex. Using the same logic as the previous section this type of split vertex is not counted.

Appendix C

Datasets

C.1 MC samples for the vertex counting algorithm

```
mc15_13TeV.159000.ParticleGenerator_nu_E50.recon.DAOD_IDTRKLUMI.e3711_s2576_s2132_r8204
mc15_13TeV.159000.ParticleGenerator_nu_E50.recon.DAOD_IDTRKLUMI.e3711_s2576_s2132_r8205
mc15_13TeV.159000.ParticleGenerator_nu_E50.recon.AOD.e3711_s2576_s2132_r8904
mc15_13TeV.159000.ParticleGenerator_nu_E50.recon.AOD.e3711_s2576_s2132_r7380
```

C.2 Data and MC samples for VBF analysis

C.2.1 Data

```
data15_13TeV.periodD.physics_Main.PhysCont.DAOD_STDM3.grp15_v11_p3372_p3388_p3402
data15_13TeV.periodE.physics_Main.PhysCont.DAOD_STDM3.grp15_v11_p3372_p3388_p3402
data15_13TeV.periodF.physics_Main.PhysCont.DAOD_STDM3.grp15_v11_p3372_p3388_p3402
data15_13TeV.periodG.physics_Main.PhysCont.DAOD_STDM3.grp15_v11_p3372_p3388_p3402
data15_13TeV.periodH.physics_Main.PhysCont.DAOD_STDM3.grp15_v11_p3372_p3388_p3402
data15_13TeV.periodJ.physics_Main.PhysCont.DAOD_STDM3.grp15_v11_p3372_p3388_p3402

data16_13TeV.periodA.physics_Main.PhysCont.DAOD_STDM3.grp15_v11_p3372_p3388_p3402
data16_13TeV.periodB.physics_Main.PhysCont.DAOD_STDM3.grp15_v11_p3372_p3388_p3402
data16_13TeV.periodC.physics_Main.PhysCont.DAOD_STDM3.grp15_v11_p3372_p3388_p3402
data16_13TeV.periodD.physics_Main.PhysCont.DAOD_STDM3.grp15_v11_p3372_p3388_p3402
data16_13TeV.periodE.physics_Main.PhysCont.DAOD_STDM3.grp15_v11_p3372_p3388_p3402
data16_13TeV.periodF.physics_Main.PhysCont.DAOD_STDM3.grp15_v11_p3372_p3388_p3402
data16_13TeV.periodG.physics_Main.PhysCont.DAOD_STDM3.grp15_v11_p3372_p3388_p3402
data16_13TeV.periodI.physics_Main.PhysCont.DAOD_STDM3.grp15_v11_p3372_p3388_p3402
data16_13TeV.periodK.physics_Main.PhysCont.DAOD_STDM3.grp15_v11_p3372_p3388_p3402
data16_13TeV.periodL.physics_Main.PhysCont.DAOD_STDM3.grp15_v11_p3372_p3388_p3402

data17_13TeV.periodB.physics_Main.PhysCont.DAOD_STDM3.grp15_v11_p3372_p3388_p3402
data17_13TeV.periodC.physics_Main.PhysCont.DAOD_STDM3.grp15_v11_p3372_p3388_p3402
data17_13TeV.periodD.physics_Main.PhysCont.DAOD_STDM3.grp15_v11_p3372_p3388_p3402
data17_13TeV.periodE.physics_Main.PhysCont.DAOD_STDM3.grp15_v11_p3372_p3388_p3402
data17_13TeV.periodF.physics_Main.PhysCont.DAOD_STDM3.grp15_v11_p3372_p3388_p3402
data17_13TeV.periodH.physics_Main.PhysCont.DAOD_STDM3.grp15_v11_p3372_p3388_p3402
data17_13TeV.periodI.physics_Main.PhysCont.DAOD_STDM3.grp15_v11_p3372_p3388_p3402
data17_13TeV.periodK.physics_Main.PhysCont.DAOD_STDM3.grp15_v11_p3372_p3388_p3402

data18_13TeV.periodB.physics_Main.PhysCont.DAOD_STDM3.grp18_v01
data18_13TeV.periodC.physics_Main.PhysCont.DAOD_STDM3.grp18_v01
data18_13TeV.periodD.physics_Main.PhysCont.DAOD_STDM3.grp18_v01
data18_13TeV.periodF.physics_Main.PhysCont.DAOD_STDM3.grp18_v01
data18_13TeV.periodI.physics_Main.PhysCont.DAOD_STDM3.grp18_v01
data18_13TeV.periodK.physics_Main.PhysCont.DAOD_STDM3.grp18_v01
data18_13TeV.periodL.physics_Main.PhysCont.DAOD_STDM3.grp18_v01
data18_13TeV.periodM.physics_Main.PhysCont.DAOD_STDM3.grp18_v01
data18_13TeV.periodO.physics_Main.PhysCont.DAOD_STDM3.grp18_v01
data18_13TeV.periodQ.physics_Main.PhysCont.DAOD_STDM3.grp18_v01
```

C.2.2 Powheg EW-Zjj

```
# TO BE REPLACED - SKIMMED BY MISTAKE

# MC16a (2016+2016 data conditions)
mc16_13TeV.344265.PhPy8EG_CT10nloME_AZNLOC6L1_VBFZee.deriv.DAOD_STDM3.e5208_e5984_s3126_r9364_r9315_p3552
mc16_13TeV.344266.PhPy8EG_CT10nloME_AZNLOC6L1_VBFZmumu.deriv.DAOD_STDM3.e5208_e5984_s3126_r9364_r9315_p3552

# MC16d (2017 data conditions)
mc16_13TeV.344265.PhPy8EG_CT10nloME_AZNLOC6L1_VBFZee.deriv.DAOD_STDM3.e5208_e5984_s3126_r10201_r10210_p3552
mc16_13TeV.344266.PhPy8EG_CT10nloME_AZNLOC6L1_VBFZmumu.deriv.DAOD_STDM3.e5208_e5984_s3126_r10201_r10210_p3552

# MC16e (2018 data conditions)
mc16_13TeV.344265.PhPy8EG_CT10nloME_AZNLOC6L1_VBFZee.deriv.DAOD_STDM4.e5208_e5984_s3126_r10724_r10726_p3598
mc16_13TeV.344266.PhPy8EG_CT10nloME_AZNLOC6L1_VBFZmumu.deriv.DAOD_STDM4.e5208_e5984_s3126_r10724_r10726_p3598
```

C.2.3 Sherpa EW-Zjj

```
# MC16a (2016+2016 data conditions)
mc16_13TeV.308092.Sherpa_221_NNPDF30NNLO_Zee2jets_Min_N_TChannel.deriv.DAOD_STDM3.e5767_e5984_s3126_r9364_r9315_p3552
mc16_13TeV.308093.Sherpa_221_NNPDF30NNLO_Zmm2jets_Min_N_TChannel.deriv.DAOD_STDM3.e5767_e5984_s3126_r9364_r9315_p3552

# MC16d (2017 data conditions)
mc16_13TeV.308092.Sherpa_221_NNPDF30NNLO_Zee2jets_Min_N_TChannel.deriv.DAOD_STDM3.e5767_e5984_s3126_r10201_r10210_p3526
mc16_13TeV.308093.Sherpa_221_NNPDF30NNLO_Zmm2jets_Min_N_TChannel.deriv.DAOD_STDM3.e5767_e5984_s3126_r10201_r10210_p3526

# MC16e (2018 data conditions)
mc16_13TeV.308092.Sherpa_221_NNPDF30NNLO_Zee2jets_Min_N_TChannel.deriv.DAOD_STDM3.e5767_e5984_s3126_r10724_r10726_p3598
mc16_13TeV.308093.Sherpa_221_NNPDF30NNLO_Zmm2jets_Min_N_TChannel.deriv.DAOD_STDM3.e5767_e5984_s3126_r10724_r10726_p3598
```

C.2.4 Sherpa Strong Z+jets

```
# MC16a (2016+2016 data conditions)
mc16_13TeV.364114.Sherpa_221_NNPDF30NNLO_Zee_MAXHTPTV0_70_CVetoBVeto.deriv.DAOD_STDM3.e5299_s3126_r9364_r9315_p3526
mc16_13TeV.364115.Sherpa_221_NNPDF30NNLO_Zee_MAXHTPTV0_70_CFilterBVeto.deriv.DAOD_STDM3.e5299_s3126_r9364_r9315_p3526
mc16_13TeV.364116.Sherpa_221_NNPDF30NNLO_Zee_MAXHTPTV0_70_BFilter.deriv.DAOD_STDM3.e5299_s3126_r9364_r9315_p3526
mc16_13TeV.364117.Sherpa_221_NNPDF30NNLO_Zee_MAXHTPTV70_140_CVetoBVeto.deriv.DAOD_STDM3.e5299_s3126_r9364_r9315_p3526
mc16_13TeV.364118.Sherpa_221_NNPDF30NNLO_Zee_MAXHTPTV70_140_CFilterBVeto.deriv.DAOD_STDM3.e5299_s3126_r9364_r9315_p3526
mc16_13TeV.364119.Sherpa_221_NNPDF30NNLO_Zee_MAXHTPTV70_140_BFilter.deriv.DAOD_STDM3.e5299_s3126_r9364_r9315_p3526
mc16_13TeV.364120.Sherpa_221_NNPDF30NNLO_Zee_MAXHTPTV140_280_CVetoBVeto.deriv.DAOD_STDM3.e5299_s3126_r9364_r9315_p3526
mc16_13TeV.364121.Sherpa_221_NNPDF30NNLO_Zee_MAXHTPTV140_280_CFilterBVeto.deriv.DAOD_STDM3.e5299_s3126_r9364_r9315_p3526
mc16_13TeV.364122.Sherpa_221_NNPDF30NNLO_Zee_MAXHTPTV140_280_BFilter.deriv.DAOD_STDM3.e5299_s3126_r9364_r9315_p3526
mc16_13TeV.364123.Sherpa_221_NNPDF30NNLO_Zee_MAXHTPTV280_500_CVetoBVeto.deriv.DAOD_STDM3.e5299_s3126_r9364_r9315_p3526
mc16_13TeV.364124.Sherpa_221_NNPDF30NNLO_Zee_MAXHTPTV280_500_CFilterBVeto.deriv.DAOD_STDM3.e5299_s3126_r9364_r9315_p3526
mc16_13TeV.364125.Sherpa_221_NNPDF30NNLO_Zee_MAXHTPTV280_500_BFilter.deriv.DAOD_STDM3.e5299_s3126_r9364_r9315_p3526
mc16_13TeV.364126.Sherpa_221_NNPDF30NNLO_Zee_MAXHTPTV500_1000.deriv.DAOD_STDM3.e5299_s3126_r9364_r9315_p3526
mc16_13TeV.364127.Sherpa_221_NNPDF30NNLO_Zee_MAXHTPTV1000_E_CMS.deriv.DAOD_STDM3.e5299_s3126_r9364_r9315_p3526
mc16_13TeV.364100.Sherpa_221_NNPDF30NNLO_Zmumu_MAXHTPTV0_70_CVetoBVeto.deriv.DAOD_STDM3.e5271_s3126_r9364_r9315_p3526
mc16_13TeV.364101.Sherpa_221_NNPDF30NNLO_Zmumu_MAXHTPTV0_70_CFilterBVeto.deriv.DAOD_STDM3.e5271_s3126_r9364_r9315_p3526
mc16_13TeV.364102.Sherpa_221_NNPDF30NNLO_Zmumu_MAXHTPTV0_70_BFilter.deriv.DAOD_STDM3.e5271_s3126_r9364_r9315_p3526
mc16_13TeV.364103.Sherpa_221_NNPDF30NNLO_Zmumu_MAXHTPTV70_140_CVetoBVeto.deriv.DAOD_STDM3.e5271_s3126_r9364_r9315_p3526
mc16_13TeV.364104.Sherpa_221_NNPDF30NNLO_Zmumu_MAXHTPTV70_140_CFilterBVeto.deriv.DAOD_STDM3.e5271_s3126_r9364_r9315_p3526
mc16_13TeV.364105.Sherpa_221_NNPDF30NNLO_Zmumu_MAXHTPTV70_140_BFilter.deriv.DAOD_STDM3.e5271_s3126_r9364_r9315_p3526
mc16_13TeV.364106.Sherpa_221_NNPDF30NNLO_Zmumu_MAXHTPTV140_280_CVetoBVeto.deriv.DAOD_STDM3.e5271_s3126_r9364_r9315_p3526
mc16_13TeV.364107.Sherpa_221_NNPDF30NNLO_Zmumu_MAXHTPTV140_280_CFilterBVeto.deriv.DAOD_STDM3.e5271_s3126_r9364_r9315_p3526
mc16_13TeV.364108.Sherpa_221_NNPDF30NNLO_Zmumu_MAXHTPTV140_280_BFilter.deriv.DAOD_STDM3.e5271_s3126_r9364_r9315_p3526
mc16_13TeV.364109.Sherpa_221_NNPDF30NNLO_Zmumu_MAXHTPTV280_500_CVetoBVeto.deriv.DAOD_STDM3.e5271_s3126_r9364_r9315_p3526
mc16_13TeV.364110.Sherpa_221_NNPDF30NNLO_Zmumu_MAXHTPTV280_500_CFilterBVeto.deriv.DAOD_STDM3.e5271_s3126_r9364_r9315_p3526
mc16_13TeV.364111.Sherpa_221_NNPDF30NNLO_Zmumu_MAXHTPTV280_500_BFilter.deriv.DAOD_STDM3.e5271_s3126_r9364_r9315_p3526
mc16_13TeV.364112.Sherpa_221_NNPDF30NNLO_Zmumu_MAXHTPTV500_1000.deriv.DAOD_STDM3.e5271_s3126_r9364_r9315_p3526
mc16_13TeV.364113.Sherpa_221_NNPDF30NNLO_Zmumu_MAXHTPTV1000_E_CMS.deriv.DAOD_STDM3.e5271_s3126_r9364_r9315_p3526

# MC16d (2017 data conditions)
mc16_13TeV.364114.Sherpa_221_NNPDF30NNLO_Zee_MAXHTPTV0_70_CVetoBVeto.deriv.DAOD_STDM3.e5299_s3126_r10201_r10210_p3526
mc16_13TeV.364115.Sherpa_221_NNPDF30NNLO_Zee_MAXHTPTV0_70_CFilterBVeto.deriv.DAOD_STDM3.e5299_e5984_s3126_r10201_r10210_p3526
mc16_13TeV.364116.Sherpa_221_NNPDF30NNLO_Zee_MAXHTPTV0_70_BFilter.deriv.DAOD_STDM3.e5299_e5984_s3126_r10201_r10210_p3526
mc16_13TeV.364117.Sherpa_221_NNPDF30NNLO_Zee_MAXHTPTV70_140_CVetoBVeto.deriv.DAOD_STDM3.e5299_e5984_s3126_r10201_r10210_p3526
mc16_13TeV.364118.Sherpa_221_NNPDF30NNLO_Zee_MAXHTPTV70_140_CFilterBVeto.deriv.DAOD_STDM3.e5299_e5984_s3126_r10201_r10210_p3526
mc16_13TeV.364119.Sherpa_221_NNPDF30NNLO_Zee_MAXHTPTV70_140_BFilter.deriv.DAOD_STDM3.e5299_e5984_s3126_r10201_r10210_p3526
mc16_13TeV.364120.Sherpa_221_NNPDF30NNLO_Zee_MAXHTPTV140_280_CVetoBVeto.deriv.DAOD_STDM3.e5299_e5984_s3126_r10201_r10210_p3526
mc16_13TeV.364121.Sherpa_221_NNPDF30NNLO_Zee_MAXHTPTV140_280_CFilterBVeto.deriv.DAOD_STDM3.e5299_e5984_s3126_r10201_r10210_p3526
mc16_13TeV.364122.Sherpa_221_NNPDF30NNLO_Zee_MAXHTPTV140_280_BFilter.deriv.DAOD_STDM3.e5299_e5984_s3126_r10201_r10210_p3526
mc16_13TeV.364123.Sherpa_221_NNPDF30NNLO_Zee_MAXHTPTV280_500_CVetoBVeto.deriv.DAOD_STDM3.e5299_e5984_s3126_r10201_r10210_p3526
mc16_13TeV.364124.Sherpa_221_NNPDF30NNLO_Zee_MAXHTPTV280_500_CFilterBVeto.deriv.DAOD_STDM3.e5299_e5984_s3126_r10201_r10210_p3526
mc16_13TeV.364125.Sherpa_221_NNPDF30NNLO_Zee_MAXHTPTV280_500_BFilter.deriv.DAOD_STDM3.e5299_e5984_s3126_r10201_r10210_p3526
mc16_13TeV.364126.Sherpa_221_NNPDF30NNLO_Zee_MAXHTPTV500_1000.deriv.DAOD_STDM3.e5299_e5984_s3126_r10201_r10210_p3526
mc16_13TeV.364127.Sherpa_221_NNPDF30NNLO_Zee_MAXHTPTV1000_E_CMS.deriv.DAOD_STDM3.e5299_e5984_s3126_r10201_r10210_p3526
mc16_13TeV.364100.Sherpa_221_NNPDF30NNLO_Zmumu_MAXHTPTV0_70_CVetoBVeto.deriv.DAOD_STDM3.e5271_s3126_r10201_r10210_p3526
mc16_13TeV.364101.Sherpa_221_NNPDF30NNLO_Zmumu_MAXHTPTV0_70_CFilterBVeto.deriv.DAOD_STDM3.e5271_s3126_r10201_r10210_p3526
mc16_13TeV.364102.Sherpa_221_NNPDF30NNLO_Zmumu_MAXHTPTV0_70_BFilter.deriv.DAOD_STDM3.e5271_s3126_r10201_r10210_p3526
mc16_13TeV.364103.Sherpa_221_NNPDF30NNLO_Zmumu_MAXHTPTV70_140_CVetoBVeto.deriv.DAOD_STDM3.e5271_s3126_r10201_r10210_p3526
mc16_13TeV.364104.Sherpa_221_NNPDF30NNLO_Zmumu_MAXHTPTV70_140_CFilterBVeto.deriv.DAOD_STDM3.e5271_s3126_r10201_r10210_p3526
mc16_13TeV.364105.Sherpa_221_NNPDF30NNLO_Zmumu_MAXHTPTV70_140_BFilter.deriv.DAOD_STDM3.e5271_s3126_r10201_r10210_p3526
mc16_13TeV.364106.Sherpa_221_NNPDF30NNLO_Zmumu_MAXHTPTV140_280_CVetoBVeto.deriv.DAOD_STDM3.e5271_s3126_r10201_r10210_p3526
mc16_13TeV.364107.Sherpa_221_NNPDF30NNLO_Zmumu_MAXHTPTV140_280_CFilterBVeto.deriv.DAOD_STDM3.e5271_s3126_r10201_r10210_p3526
mc16_13TeV.364108.Sherpa_221_NNPDF30NNLO_Zmumu_MAXHTPTV140_280_BFilter.deriv.DAOD_STDM3.e5271_s3126_r10201_r10210_p3526
mc16_13TeV.364109.Sherpa_221_NNPDF30NNLO_Zmumu_MAXHTPTV280_500_CVetoBVeto.deriv.DAOD_STDM3.e5271_s3126_r10201_r10210_p3526
mc16_13TeV.364110.Sherpa_221_NNPDF30NNLO_Zmumu_MAXHTPTV280_500_CFilterBVeto.deriv.DAOD_STDM3.e5271_s3126_r10201_r10210_p3526
mc16_13TeV.364111.Sherpa_221_NNPDF30NNLO_Zmumu_MAXHTPTV280_500_BFilter.deriv.DAOD_STDM3.e5271_s3126_r10201_r10210_p3526
mc16_13TeV.364112.Sherpa_221_NNPDF30NNLO_Zmumu_MAXHTPTV500_1000.deriv.DAOD_STDM3.e5271_s3126_r10201_r10210_p3526
mc16_13TeV.364113.Sherpa_221_NNPDF30NNLO_Zmumu_MAXHTPTV1000_E_CMS.deriv.DAOD_STDM3.e5271_s3126_r10201_r10210_p3526

# MC16e (2017 data conditions)
mc16_13TeV.364114.Sherpa_221_NNPDF30NNLO_Zee_MAXHTPTV0_70_CVetoBVeto.deriv.DAOD_STDM3.e5299_e5984_s3126_r10724_r10726_p3598
mc16_13TeV.364115.Sherpa_221_NNPDF30NNLO_Zee_MAXHTPTV0_70_CFilterBVeto.deriv.DAOD_STDM3.e5299_e5984_s3126_r10724_r10726_p3598
mc16_13TeV.364116.Sherpa_221_NNPDF30NNLO_Zee_MAXHTPTV0_70_BFilter.deriv.DAOD_STDM3.e5299_e5984_s3126_r10724_r10726_p3598
mc16_13TeV.364117.Sherpa_221_NNPDF30NNLO_Zee_MAXHTPTV70_140_CVetoBVeto.deriv.DAOD_STDM3.e5299_e5984_s3126_r10724_r10726_p3598
mc16_13TeV.364118.Sherpa_221_NNPDF30NNLO_Zee_MAXHTPTV70_140_CFilterBVeto.deriv.DAOD_STDM3.e5299_e5984_s3126_r10724_r10726_p3598
mc16_13TeV.364119.Sherpa_221_NNPDF30NNLO_Zee_MAXHTPTV70_140_BFilter.deriv.DAOD_STDM3.e5299_e5984_s3126_r10724_r10726_p3598
mc16_13TeV.364120.Sherpa_221_NNPDF30NNLO_Zee_MAXHTPTV140_280_CVetoBVeto.deriv.DAOD_STDM3.e5299_e5984_s3126_r10724_r10726_p3598
mc16_13TeV.364121.Sherpa_221_NNPDF30NNLO_Zee_MAXHTPTV140_280_CFilterBVeto.deriv.DAOD_STDM3.e5299_e5984_s3126_r10724_r10726_p3598
mc16_13TeV.364122.Sherpa_221_NNPDF30NNLO_Zee_MAXHTPTV140_280_BFilter.deriv.DAOD_STDM3.e5299_e5984_s3126_r10724_r10726_p3598
mc16_13TeV.364123.Sherpa_221_NNPDF30NNLO_Zee_MAXHTPTV280_500_CVetoBVeto.deriv.DAOD_STDM3.e5299_e5984_s3126_r10724_r10726_p3598
mc16_13TeV.364124.Sherpa_221_NNPDF30NNLO_Zee_MAXHTPTV280_500_CFilterBVeto.deriv.DAOD_STDM3.e5299_e5984_s3126_r10724_r10726_p3598
mc16_13TeV.364125.Sherpa_221_NNPDF30NNLO_Zee_MAXHTPTV280_500_BFilter.deriv.DAOD_STDM3.e5299_e5984_s3126_r10724_r10726_p3598
mc16_13TeV.364126.Sherpa_221_NNPDF30NNLO_Zee_MAXHTPTV500_1000.deriv.DAOD_STDM3.e5299_e5984_s3126_r10724_r10726_p3598
mc16_13TeV.364127.Sherpa_221_NNPDF30NNLO_Zee_MAXHTPTV1000_E_CMS.deriv.DAOD_STDM3.e5299_e5984_s3126_r10724_r10726_p3598
mc16_13TeV.364100.Sherpa_221_NNPDF30NNLO_Zmumu_MAXHTPTV0_70_CVetoBVeto.deriv.DAOD_STDM3.e5271_e5984_s3126_r10724_r10726_p3598
mc16_13TeV.364101.Sherpa_221_NNPDF30NNLO_Zmumu_MAXHTPTV0_70_CFilterBVeto.deriv.DAOD_STDM3.e5271_e5984_s3126_r10724_r10726_p3598
mc16_13TeV.364102.Sherpa_221_NNPDF30NNLO_Zmumu_MAXHTPTV0_70_BFilter.deriv.DAOD_STDM3.e5271_e5984_s3126_r10724_r10726_p3598
mc16_13TeV.364103.Sherpa_221_NNPDF30NNLO_Zmumu_MAXHTPTV70_140_CVetoBVeto.deriv.DAOD_STDM3.e5271_e5984_s3126_r10724_r10726_p3598
```

mc16_13TeV.364104.Sherpa_221_NNPDF30NNLO_Zmumu_MAXHTPTV70_140_CFilterBVeto.deriv.DAOD_STDM3.e5271_e5984_s3126_r10724_r10726_p3598
mc16_13TeV.364105.Sherpa_221_NNPDF30NNLO_Zmumu_MAXHTPTV70_140_BFilter.deriv.DAOD_STDM3.e5271_e5984_s3126_r10724_r10726_p3598
mc16_13TeV.364106.Sherpa_221_NNPDF30NNLO_Zmumu_MAXHTPTV140_280_CVetoBVeto.deriv.DAOD_STDM3.e5271_e5984_s3126_r10724_r10726_p3598
mc16_13TeV.364107.Sherpa_221_NNPDF30NNLO_Zmumu_MAXHTPTV140_280_CFilterBVeto.deriv.DAOD_STDM3.e5271_e5984_s3126_r10724_r10726_p3598
mc16_13TeV.364108.Sherpa_221_NNPDF30NNLO_Zmumu_MAXHTPTV140_280_BFilter.deriv.DAOD_STDM3.e5271_e5984_s3126_r10724_r10726_p3598
mc16_13TeV.364109.Sherpa_221_NNPDF30NNLO_Zmumu_MAXHTPTV280_500_CVetoBVeto.deriv.DAOD_STDM3.e5271_e5984_s3126_r10724_r10726_p3598
mc16_13TeV.364110.Sherpa_221_NNPDF30NNLO_Zmumu_MAXHTPTV280_500_CFilterBVeto.deriv.DAOD_STDM3.e5271_e5984_s3126_r10724_r10726_p3598
mc16_13TeV.364111.Sherpa_221_NNPDF30NNLO_Zmumu_MAXHTPTV280_500_BFilter.deriv.DAOD_STDM3.e5271_e5984_s3126_r10724_r10726_p3598
mc16_13TeV.364112.Sherpa_221_NNPDF30NNLO_Zmumu_MAXHTPTV500_1000.deriv.DAOD_STDM3.e5271_e5984_s3126_r10724_r10726_p3598
mc16_13TeV.364113.Sherpa_221_NNPDF30NNLO_Zmumu_MAXHTPTV1000_E_CMS.deriv.DAOD_STDM3.e5271_e5984_s3126_r10724_r10726_p3598

C.2.5 MadGraph Strong Z+jets

MC16a (2016+2016 data conditions)
mc16_13TeV.363147.MGPy8EG_N30NLO_Zee_Ht0_70_CVetoBVeto.deriv.DAOD_STDM3.e4866_s3126_r9364_r9315_p3526
mc16_13TeV.363148.MGPy8EG_N30NLO_Zee_Ht0_70_CFilterBVeto.deriv.DAOD_STDM3.e4866_s3126_r9364_r9315_p3526
mc16_13TeV.363149.MGPy8EG_N30NLO_Zee_Ht0_70_BFilter.deriv.DAOD_STDM3.e4866_s3126_r9364_r9315_p3526
mc16_13TeV.363150.MGPy8EG_N30NLO_Zee_Ht70_140_CVetoBVeto.deriv.DAOD_STDM3.e4866_s3126_r9364_r9315_p3526
mc16_13TeV.363151.MGPy8EG_N30NLO_Zee_Ht70_140_CFilterBVeto.deriv.DAOD_STDM3.e4866_s3126_r9364_r9315_p3526
mc16_13TeV.363152.MGPy8EG_N30NLO_Zee_Ht70_140_BFilter.deriv.DAOD_STDM3.e4866_s3126_r9364_r9315_p3526
mc16_13TeV.363153.MGPy8EG_N30NLO_Zee_Ht140_280_CVetoBVeto.deriv.DAOD_STDM3.e4866_s3126_r9364_r9315_p3526
mc16_13TeV.363154.MGPy8EG_N30NLO_Zee_Ht140_280_CFilterBVeto.deriv.DAOD_STDM3.e4866_s3126_r9364_r9315_p3526
mc16_13TeV.363155.MGPy8EG_N30NLO_Zee_Ht140_280_BFilter.deriv.DAOD_STDM3.e4866_s3126_r9364_r9315_p3526
mc16_13TeV.363156.MGPy8EG_N30NLO_Zee_Ht280_500_CVetoBVeto.deriv.DAOD_STDM3.e4866_s3126_r9364_r9315_p3526
mc16_13TeV.363157.MGPy8EG_N30NLO_Zee_Ht280_500_CFilterBVeto.deriv.DAOD_STDM3.e4866_s3126_r9364_r9315_p3526
mc16_13TeV.363158.MGPy8EG_N30NLO_Zee_Ht280_500_BFilter.deriv.DAOD_STDM3.e4866_s3126_r9364_r9315_p3526
mc16_13TeV.363159.MGPy8EG_N30NLO_Zee_Ht500_700_CVetoBVeto.deriv.DAOD_STDM3.e4866_s3126_r9364_r9315_p3526
mc16_13TeV.363160.MGPy8EG_N30NLO_Zee_Ht500_700_CFilterBVeto.deriv.DAOD_STDM3.e4866_s3126_r9364_r9315_p3526
mc16_13TeV.363161.MGPy8EG_N30NLO_Zee_Ht500_700_BFilter.deriv.DAOD_STDM3.e4866_s3126_r9364_r9315_p3526
mc16_13TeV.363162.MGPy8EG_N30NLO_Zee_Ht700_1000_CVetoBVeto.deriv.DAOD_STDM3.e4866_s3126_r9364_r9315_p3526
mc16_13TeV.363163.MGPy8EG_N30NLO_Zee_Ht700_1000_CFilterBVeto.deriv.DAOD_STDM3.e4866_s3126_r9364_r9315_p3526
mc16_13TeV.363164.MGPy8EG_N30NLO_Zee_Ht700_1000_BFilter.deriv.DAOD_STDM3.e4866_s3126_r9364_r9315_p3526
mc16_13TeV.363165.MGPy8EG_N30NLO_Zee_Ht1000_2000_CVetoBVeto.deriv.DAOD_STDM3.e4866_s3126_r9364_r9315_p3526
mc16_13TeV.363166.MGPy8EG_N30NLO_Zee_Ht1000_2000_CFilterBVeto.deriv.DAOD_STDM3.e4866_s3126_r9364_r9315_p3526
mc16_13TeV.363167.MGPy8EG_N30NLO_Zee_Ht1000_2000_BFilter.deriv.DAOD_STDM3.e4866_s3126_r9364_r9315_p3526
mc16_13TeV.363168.MGPy8EG_N30NLO_Zee_Ht2000_E_CMS_CVetoBVeto.deriv.DAOD_STDM3.e4866_s3126_r9364_r9315_p3526
mc16_13TeV.363169.MGPy8EG_N30NLO_Zee_Ht2000_E_CMS_CFilterBVeto.deriv.DAOD_STDM3.e4866_s3126_r9364_r9315_p3526
mc16_13TeV.363170.MGPy8EG_N30NLO_Zee_Ht2000_E_CMS_BFilter.deriv.DAOD_STDM3.e4866_s3126_r9364_r9315_p3526
mc16_13TeV.363123.MGPy8EG_N30NLO_Zmumu_Ht0_70_CVetoBVeto.deriv.DAOD_STDM3.e4649_s3126_r9364_r9315_p3526
mc16_13TeV.363124.MGPy8EG_N30NLO_Zmumu_Ht0_70_CFilterBVeto.deriv.DAOD_STDM3.e4649_s3126_r9364_r9315_p3526
mc16_13TeV.363125.MGPy8EG_N30NLO_Zmumu_Ht0_70_BFilter.deriv.DAOD_STDM3.e4649_s3126_r9364_r9315_p3526
mc16_13TeV.363126.MGPy8EG_N30NLO_Zmumu_Ht70_140_CVetoBVeto.deriv.DAOD_STDM3.e4649_s3126_r9364_r9315_p3526
mc16_13TeV.363127.MGPy8EG_N30NLO_Zmumu_Ht70_140_CFilterBVeto.deriv.DAOD_STDM3.e4649_s3126_r9364_r9315_p3526
mc16_13TeV.363128.MGPy8EG_N30NLO_Zmumu_Ht70_140_BFilter.deriv.DAOD_STDM3.e4649_s3126_r9364_r9315_p3526
mc16_13TeV.363129.MGPy8EG_N30NLO_Zmumu_Ht140_280_CVetoBVeto.deriv.DAOD_STDM3.e4649_s3126_r9364_r9315_p3526
mc16_13TeV.363130.MGPy8EG_N30NLO_Zmumu_Ht140_280_CFilterBVeto.deriv.DAOD_STDM3.e4649_s3126_r9364_r9315_p3526
mc16_13TeV.363131.MGPy8EG_N30NLO_Zmumu_Ht140_280_BFilter.deriv.DAOD_STDM3.e4649_s3126_r9364_r9315_p3526
mc16_13TeV.363132.MGPy8EG_N30NLO_Zmumu_Ht280_500_CVetoBVeto.deriv.DAOD_STDM3.e4649_s3126_r9364_r9315_p3526
mc16_13TeV.363133.MGPy8EG_N30NLO_Zmumu_Ht280_500_CFilterBVeto.deriv.DAOD_STDM3.e4649_s3126_r9364_r9315_p3526
mc16_13TeV.363134.MGPy8EG_N30NLO_Zmumu_Ht280_500_BFilter.deriv.DAOD_STDM3.e4649_s3126_r9364_r9315_p3526
mc16_13TeV.363135.MGPy8EG_N30NLO_Zmumu_Ht500_700_CVetoBVeto.deriv.DAOD_STDM3.e4649_s3126_r9364_r9315_p3526
mc16_13TeV.363136.MGPy8EG_N30NLO_Zmumu_Ht500_700_CFilterBVeto.deriv.DAOD_STDM3.e4649_s3126_r9364_r9315_p3526
mc16_13TeV.363137.MGPy8EG_N30NLO_Zmumu_Ht500_700_BFilter.deriv.DAOD_STDM3.e4649_s3126_r9364_r9315_p3526
mc16_13TeV.363138.MGPy8EG_N30NLO_Zmumu_Ht700_1000_CVetoBVeto.deriv.DAOD_STDM3.e4649_s3126_r9364_r9315_p3526
mc16_13TeV.363139.MGPy8EG_N30NLO_Zmumu_Ht700_1000_CFilterBVeto.deriv.DAOD_STDM3.e4649_s3126_r9364_r9315_p3526
mc16_13TeV.363140.MGPy8EG_N30NLO_Zmumu_Ht700_1000_BFilter.deriv.DAOD_STDM3.e4649_s3126_r9364_r9315_p3526
mc16_13TeV.363141.MGPy8EG_N30NLO_Zmumu_Ht1000_2000_CVetoBVeto.deriv.DAOD_STDM3.e4649_s3126_r9364_r9315_p3526
mc16_13TeV.363142.MGPy8EG_N30NLO_Zmumu_Ht1000_2000_CFilterBVeto.deriv.DAOD_STDM3.e4649_s3126_r9364_r9315_p3526
mc16_13TeV.363143.MGPy8EG_N30NLO_Zmumu_Ht1000_2000_BFilter.deriv.DAOD_STDM3.e4649_s3126_r9364_r9315_p3526
mc16_13TeV.363144.MGPy8EG_N30NLO_Zmumu_Ht2000_E_CMS_CVetoBVeto.deriv.DAOD_STDM3.e4649_s3126_r9364_r9315_p3526
mc16_13TeV.363145.MGPy8EG_N30NLO_Zmumu_Ht2000_E_CMS_CFilterBVeto.deriv.DAOD_STDM3.e4649_s3126_r9364_r9315_p3526
mc16_13TeV.363146.MGPy8EG_N30NLO_Zmumu_Ht2000_E_CMS_BFilter.deriv.DAOD_STDM3.e4649_s3126_r9364_r9315_p3526

MC16d (2017 data conditions)
mc16_13TeV.363147.MGPy8EG_N30NLO_Zee_Ht0_70_CVetoBVeto.deriv.DAOD_STDM3.e4866_s3126_r10201_r10210_p3526
mc16_13TeV.363148.MGPy8EG_N30NLO_Zee_Ht0_70_CFilterBVeto.deriv.DAOD_STDM3.e4866_s3126_r10201_r10210_p3526
mc16_13TeV.363149.MGPy8EG_N30NLO_Zee_Ht0_70_BFilter.deriv.DAOD_STDM3.e4866_s3126_r10201_r10210_p3526
mc16_13TeV.363150.MGPy8EG_N30NLO_Zee_Ht70_140_CVetoBVeto.deriv.DAOD_STDM3.e4866_s3126_r10201_r10210_p3526
mc16_13TeV.363151.MGPy8EG_N30NLO_Zee_Ht70_140_CFilterBVeto.deriv.DAOD_STDM3.e4866_s3126_r10201_r10210_p3526
mc16_13TeV.363152.MGPy8EG_N30NLO_Zee_Ht70_140_BFilter.deriv.DAOD_STDM3.e4866_s3126_r10201_r10210_p3526
mc16_13TeV.363153.MGPy8EG_N30NLO_Zee_Ht140_280_CVetoBVeto.deriv.DAOD_STDM3.e4866_s3126_r10201_r10210_p3526
mc16_13TeV.363154.MGPy8EG_N30NLO_Zee_Ht140_280_CFilterBVeto.deriv.DAOD_STDM3.e4866_s3126_r10201_r10210_p3526
mc16_13TeV.363155.MGPy8EG_N30NLO_Zee_Ht140_280_BFilter.deriv.DAOD_STDM3.e4866_s3126_r10201_r10210_p3526
mc16_13TeV.363156.MGPy8EG_N30NLO_Zee_Ht280_500_CVetoBVeto.deriv.DAOD_STDM3.e4866_s3126_r10201_r10210_p3526
mc16_13TeV.363157.MGPy8EG_N30NLO_Zee_Ht280_500_CFilterBVeto.deriv.DAOD_STDM3.e4866_s3126_r10201_r10210_p3526
mc16_13TeV.363158.MGPy8EG_N30NLO_Zee_Ht280_500_BFilter.deriv.DAOD_STDM3.e4866_s3126_r10201_r10210_p3526
mc16_13TeV.363159.MGPy8EG_N30NLO_Zee_Ht500_700_CVetoBVeto.deriv.DAOD_STDM3.e4866_s3126_r10201_r10210_p3526
mc16_13TeV.363160.MGPy8EG_N30NLO_Zee_Ht500_700_CFilterBVeto.deriv.DAOD_STDM3.e4866_s3126_r10201_r10210_p3526
mc16_13TeV.363161.MGPy8EG_N30NLO_Zee_Ht500_700_BFilter.deriv.DAOD_STDM3.e4866_s3126_r10201_r10210_p3526
mc16_13TeV.363162.MGPy8EG_N30NLO_Zee_Ht700_1000_CVetoBVeto.deriv.DAOD_STDM3.e4866_s3126_r10201_r10210_p3526
mc16_13TeV.363163.MGPy8EG_N30NLO_Zee_Ht700_1000_CFilterBVeto.deriv.DAOD_STDM3.e4866_s3126_r10201_r10210_p3526
mc16_13TeV.363164.MGPy8EG_N30NLO_Zee_Ht700_1000_BFilter.deriv.DAOD_STDM3.e4866_s3126_r10201_r10210_p3526
mc16_13TeV.363165.MGPy8EG_N30NLO_Zee_Ht1000_2000_CVetoBVeto.deriv.DAOD_STDM3.e4866_s3126_r10201_r10210_p3526
mc16_13TeV.363166.MGPy8EG_N30NLO_Zee_Ht1000_2000_CFilterBVeto.deriv.DAOD_STDM3.e4866_s3126_r10201_r10210_p3526
mc16_13TeV.363167.MGPy8EG_N30NLO_Zee_Ht1000_2000_BFilter.deriv.DAOD_STDM3.e4866_s3126_r10201_r10210_p3526
mc16_13TeV.363168.MGPy8EG_N30NLO_Zee_Ht2000_E_CMS_CVetoBVeto.deriv.DAOD_STDM3.e4866_s3126_r10201_r10210_p3526
mc16_13TeV.363169.MGPy8EG_N30NLO_Zee_Ht2000_E_CMS_CFilterBVeto.deriv.DAOD_STDM3.e4866_s3126_r10201_r10210_p3526
mc16_13TeV.363170.MGPy8EG_N30NLO_Zee_Ht2000_E_CMS_BFilter.deriv.DAOD_STDM3.e4866_s3126_r10201_r10210_p3526
mc16_13TeV.363123.MGPy8EG_N30NLO_Zmumu_Ht0_70_CVetoBVeto.deriv.DAOD_STDM3.e4649_s3126_r10201_r10210_p3526
mc16_13TeV.363124.MGPy8EG_N30NLO_Zmumu_Ht0_70_CFilterBVeto.deriv.DAOD_STDM3.e4649_s3126_r10201_r10210_p3526
mc16_13TeV.363125.MGPy8EG_N30NLO_Zmumu_Ht0_70_BFilter.deriv.DAOD_STDM3.e4649_s3126_r10201_r10210_p3526
mc16_13TeV.363126.MGPy8EG_N30NLO_Zmumu_Ht70_140_CVetoBVeto.deriv.DAOD_STDM3.e4649_s3126_r10201_r10210_p3526
mc16_13TeV.363127.MGPy8EG_N30NLO_Zmumu_Ht70_140_CFilterBVeto.deriv.DAOD_STDM3.e4649_s3126_r10201_r10210_p3526
mc16_13TeV.363128.MGPy8EG_N30NLO_Zmumu_Ht70_140_BFilter.deriv.DAOD_STDM3.e4649_s3126_r10201_r10210_p3526
mc16_13TeV.363129.MGPy8EG_N30NLO_Zmumu_Ht140_280_CVetoBVeto.deriv.DAOD_STDM3.e4649_s3126_r10201_r10210_p3526

mc16_13TeV.363130.MGPy8EG_N30NLO_Zmumu_Ht140_280_CFilterBVeto.deriv.DAOD_STDM3.e4649_s3126_r10201_r10210_p3526
mc16_13TeV.363131.MGPy8EG_N30NLO_Zmumu_Ht140_280_BFilter.deriv.DAOD_STDM3.e4649_s3126_r10201_r10210_p3526
mc16_13TeV.363132.MGPy8EG_N30NLO_Zmumu_Ht280_500_CVetoBVeto.deriv.DAOD_STDM3.e4649_s3126_r10201_r10210_p3526
mc16_13TeV.363133.MGPy8EG_N30NLO_Zmumu_Ht280_500_CFilterBVeto.deriv.DAOD_STDM3.e4649_s3126_r10201_r10210_p3526
mc16_13TeV.363134.MGPy8EG_N30NLO_Zmumu_Ht280_500_BFilter.deriv.DAOD_STDM3.e4649_s3126_r10201_r10210_p3526
mc16_13TeV.363135.MGPy8EG_N30NLO_Zmumu_Ht500_700_CVetoBVeto.deriv.DAOD_STDM3.e4649_s3126_r10201_r10210_p3526
mc16_13TeV.363136.MGPy8EG_N30NLO_Zmumu_Ht500_700_CFilterBVeto.deriv.DAOD_STDM3.e4649_s3126_r10201_r10210_p3526
mc16_13TeV.363137.MGPy8EG_N30NLO_Zmumu_Ht500_700_BFilter.deriv.DAOD_STDM3.e4649_s3126_r10201_r10210_p3526
mc16_13TeV.363138.MGPy8EG_N30NLO_Zmumu_Ht700_1000_CVetoBVeto.deriv.DAOD_STDM3.e4649_s3126_r10201_r10210_p3526
mc16_13TeV.363139.MGPy8EG_N30NLO_Zmumu_Ht700_1000_CFilterBVeto.deriv.DAOD_STDM3.e4649_s3126_r10201_r10210_p3526
mc16_13TeV.363140.MGPy8EG_N30NLO_Zmumu_Ht700_1000_BFilter.deriv.DAOD_STDM3.e4649_s3126_r10201_r10210_p3526
mc16_13TeV.363141.MGPy8EG_N30NLO_Zmumu_Ht1000_2000_CVetoBVeto.deriv.DAOD_STDM3.e4649_s3126_r10201_r10210_p3526
mc16_13TeV.363142.MGPy8EG_N30NLO_Zmumu_Ht1000_2000_CFilterBVeto.deriv.DAOD_STDM3.e4649_e5984_s3126_r10201_r10210_p3526
mc16_13TeV.363143.MGPy8EG_N30NLO_Zmumu_Ht1000_2000_BFilter.deriv.DAOD_STDM3.e4649_e5984_s3126_r10201_r10210_p3526
mc16_13TeV.363144.MGPy8EG_N30NLO_Zmumu_Ht2000_E_CMS_CVetoBVeto.deriv.DAOD_STDM3.e4649_e5984_s3126_r10201_r10210_p3526
mc16_13TeV.363145.MGPy8EG_N30NLO_Zmumu_Ht2000_E_CMS_CFilterBVeto.deriv.DAOD_STDM3.e4649_e5984_s3126_r10201_r10210_p3526
mc16_13TeV.363146.MGPy8EG_N30NLO_Zmumu_Ht2000_E_CMS_BFilter.deriv.DAOD_STDM3.e4649_s3126_r10201_r10210_p3526

MC16e (2018 data conditions)
mc16_13TeV.363147.MGPy8EG_N30NLO_Zee_Ht0_70_CVetoBVeto.deriv.DAOD_STDM3.e4866_e5984_s3126_r10724_r10726_p3598
mc16_13TeV.363148.MGPy8EG_N30NLO_Zee_Ht0_70_CFilterBVeto.deriv.DAOD_STDM3.e4866_e5984_s3126_r10724_r10726_p3598
mc16_13TeV.363149.MGPy8EG_N30NLO_Zee_Ht0_70_BFilter.deriv.DAOD_STDM3.e4866_e5984_s3126_r10724_r10726_p3598
mc16_13TeV.363150.MGPy8EG_N30NLO_Zee_Ht70_140_CVetoBVeto.deriv.DAOD_STDM3.e4866_e5984_s3126_r10724_r10726_p3598
mc16_13TeV.363151.MGPy8EG_N30NLO_Zee_Ht70_140_CFilterBVeto.deriv.DAOD_STDM3.e4866_e5984_s3126_r10724_r10726_p3598
mc16_13TeV.363152.MGPy8EG_N30NLO_Zee_Ht70_140_BFilter.deriv.DAOD_STDM3.e4866_e5984_s3126_r10724_r10726_p3598
mc16_13TeV.363153.MGPy8EG_N30NLO_Zee_Ht140_280_CVetoBVeto.deriv.DAOD_STDM3.e4866_e5984_s3126_r10724_r10726_p3598
mc16_13TeV.363154.MGPy8EG_N30NLO_Zee_Ht140_280_CFilterBVeto.deriv.DAOD_STDM3.e4866_e5984_s3126_r10724_r10726_p3598
mc16_13TeV.363155.MGPy8EG_N30NLO_Zee_Ht140_280_BFilter.deriv.DAOD_STDM3.e4866_e5984_s3126_r10724_r10726_p3598
mc16_13TeV.363156.MGPy8EG_N30NLO_Zee_Ht280_500_CVetoBVeto.deriv.DAOD_STDM3.e4866_e5984_s3126_r10724_r10726_p3598
mc16_13TeV.363157.MGPy8EG_N30NLO_Zee_Ht280_500_CFilterBVeto.deriv.DAOD_STDM3.e4866_e5984_s3126_r10724_r10726_p3598
mc16_13TeV.363158.MGPy8EG_N30NLO_Zee_Ht280_500_BFilter.deriv.DAOD_STDM3.e4866_e5984_s3126_r10724_r10726_p3598
mc16_13TeV.363159.MGPy8EG_N30NLO_Zee_Ht500_700_CVetoBVeto.deriv.DAOD_STDM3.e4866_e5984_s3126_r10724_r10726_p3598
mc16_13TeV.363160.MGPy8EG_N30NLO_Zee_Ht500_700_CFilterBVeto.deriv.DAOD_STDM3.e4866_e5984_s3126_r10724_r10726_p3598
mc16_13TeV.363161.MGPy8EG_N30NLO_Zee_Ht500_700_BFilter.deriv.DAOD_STDM3.e4866_e5984_s3126_r10724_r10726_p3598
mc16_13TeV.363162.MGPy8EG_N30NLO_Zee_Ht700_1000_CVetoBVeto.deriv.DAOD_STDM3.e4866_e5984_s3126_r10724_r10726_p3598
mc16_13TeV.363163.MGPy8EG_N30NLO_Zee_Ht700_1000_CFilterBVeto.deriv.DAOD_STDM3.e4866_e5984_s3126_r10724_r10726_p3598
mc16_13TeV.363164.MGPy8EG_N30NLO_Zee_Ht700_1000_BFilter.deriv.DAOD_STDM3.e4866_e5984_s3126_r10724_r10726_p3598
mc16_13TeV.363165.MGPy8EG_N30NLO_Zee_Ht1000_2000_CVetoBVeto.deriv.DAOD_STDM3.e4866_e5984_s3126_r10724_r10726_p3598
mc16_13TeV.363166.MGPy8EG_N30NLO_Zee_Ht1000_2000_CFilterBVeto.deriv.DAOD_STDM3.e4866_e5984_s3126_r10724_r10726_p3598
mc16_13TeV.363167.MGPy8EG_N30NLO_Zee_Ht1000_2000_BFilter.deriv.DAOD_STDM3.e4866_e5984_s3126_r10724_r10726_p3598
mc16_13TeV.363168.MGPy8EG_N30NLO_Zee_Ht2000_E_CMS_CVetoBVeto.deriv.DAOD_STDM3.e4866_e5984_s3126_r10724_r10726_p3598
mc16_13TeV.363169.MGPy8EG_N30NLO_Zee_Ht2000_E_CMS_CFilterBVeto.deriv.DAOD_STDM3.e4866_e5984_s3126_r10724_r10726_p3598
mc16_13TeV.363170.MGPy8EG_N30NLO_Zee_Ht2000_E_CMS_BFilter.deriv.DAOD_STDM3.e4866_e5984_s3126_r10724_r10726_p3598
mc16_13TeV.363123.MGPy8EG_N30NLO_Zmumu_Ht0_70_CVetoBVeto.deriv.DAOD_STDM3.e4649_e5984_s3126_r10724_r10726_p3598
mc16_13TeV.363124.MGPy8EG_N30NLO_Zmumu_Ht0_70_CFilterBVeto.deriv.DAOD_STDM3.e4649_e5984_s3126_r10724_r10726_p3598
mc16_13TeV.363125.MGPy8EG_N30NLO_Zmumu_Ht0_70_BFilter.deriv.DAOD_STDM3.e4649_e5984_s3126_r10724_r10726_p3598
mc16_13TeV.363126.MGPy8EG_N30NLO_Zmumu_Ht70_140_CVetoBVeto.deriv.DAOD_STDM3.e4649_e5984_s3126_r10724_r10726_p3598
mc16_13TeV.363127.MGPy8EG_N30NLO_Zmumu_Ht70_140_CFilterBVeto.deriv.DAOD_STDM3.e4649_e5984_s3126_r10724_r10726_p3598
mc16_13TeV.363128.MGPy8EG_N30NLO_Zmumu_Ht70_140_BFilter.deriv.DAOD_STDM3.e4649_e5984_s3126_r10724_r10726_p3598
mc16_13TeV.363129.MGPy8EG_N30NLO_Zmumu_Ht140_280_CVetoBVeto.deriv.DAOD_STDM3.e4649_e5984_s3126_r10724_r10726_p3598
mc16_13TeV.363130.MGPy8EG_N30NLO_Zmumu_Ht140_280_CFilterBVeto.deriv.DAOD_STDM3.e4649_e5984_s3126_r10724_r10726_p3598
mc16_13TeV.363131.MGPy8EG_N30NLO_Zmumu_Ht140_280_BFilter.deriv.DAOD_STDM3.e4649_e5984_s3126_r10724_r10726_p3598
mc16_13TeV.363132.MGPy8EG_N30NLO_Zmumu_Ht280_500_CVetoBVeto.deriv.DAOD_STDM3.e4649_e5984_s3126_r10724_r10726_p3598
mc16_13TeV.363133.MGPy8EG_N30NLO_Zmumu_Ht280_500_CFilterBVeto.deriv.DAOD_STDM3.e4649_e5984_s3126_r10724_r10726_p3598
mc16_13TeV.363134.MGPy8EG_N30NLO_Zmumu_Ht280_500_BFilter.deriv.DAOD_STDM3.e4649_e5984_s3126_r10724_r10726_p3598
mc16_13TeV.363135.MGPy8EG_N30NLO_Zmumu_Ht500_700_CVetoBVeto.deriv.DAOD_STDM3.e4649_e5984_s3126_r10724_r10726_p3598
mc16_13TeV.363136.MGPy8EG_N30NLO_Zmumu_Ht500_700_CFilterBVeto.deriv.DAOD_STDM3.e4649_e5984_s3126_r10724_r10726_p3598
mc16_13TeV.363137.MGPy8EG_N30NLO_Zmumu_Ht500_700_BFilter.deriv.DAOD_STDM3.e4649_e5984_s3126_r10724_r10726_p3598
mc16_13TeV.363138.MGPy8EG_N30NLO_Zmumu_Ht700_1000_CVetoBVeto.deriv.DAOD_STDM3.e4649_e5984_s3126_r10724_r10726_p3598
mc16_13TeV.363139.MGPy8EG_N30NLO_Zmumu_Ht700_1000_CFilterBVeto.deriv.DAOD_STDM3.e4649_e5984_s3126_r10724_r10726_p3598
mc16_13TeV.363140.MGPy8EG_N30NLO_Zmumu_Ht700_1000_BFilter.deriv.DAOD_STDM3.e4649_e5984_s3126_r10724_r10726_p3598
mc16_13TeV.363141.MGPy8EG_N30NLO_Zmumu_Ht1000_2000_CVetoBVeto.deriv.DAOD_STDM3.e4649_e5984_s3126_r10724_r10726_p3598
mc16_13TeV.363142.MGPy8EG_N30NLO_Zmumu_Ht1000_2000_CFilterBVeto.deriv.DAOD_STDM3.e4649_e5984_s3126_r10724_r10726_p3598
mc16_13TeV.363143.MGPy8EG_N30NLO_Zmumu_Ht1000_2000_BFilter.deriv.DAOD_STDM3.e4649_e5984_s3126_r10724_r10726_p3598
mc16_13TeV.363144.MGPy8EG_N30NLO_Zmumu_Ht2000_E_CMS_CVetoBVeto.deriv.DAOD_STDM3.e4649_e5984_s3126_r10724_r10726_p3598
mc16_13TeV.363145.MGPy8EG_N30NLO_Zmumu_Ht2000_E_CMS_CFilterBVeto.deriv.DAOD_STDM3.e4649_e5984_s3126_r10724_r10726_p3598
mc16_13TeV.363146.MGPy8EG_N30NLO_Zmumu_Ht2000_E_CMS_BFilter.deriv.DAOD_STDM3.e4649_e5984_s3126_r10724_r10726_p3598

C.2.6 $t\bar{t}$

MC16a (2016+2016 data conditions)
mc16_13TeV.410470.PhPy8EG_A14_ttbar_hdamp258p75_nonallhad.deriv.DAOD_STDM3.e6337_e5984_s3126_r9364_r9315_p3517

MC16d (2017 data conditions)
mc16_13TeV.410470.PhPy8EG_A14_ttbar_hdamp258p75_nonallhad.deriv.DAOD_STDM3.e6337_e5984_s3126_r10201_r10210_p3517

MC16e (2018 data conditions)
mc16_13TeV.410470.PhPy8EG_A14_ttbar_hdamp258p75_nonallhad.deriv.DAOD_STDM3.e6337_e5984_s3126_r10724_r10726_p3613

C.2.7 Diboson

MC16a (2016+2016 data conditions)
mc16_13TeV.364250.Sherpa_222_NNPDF30NNLO_llll.deriv.DAOD_STDM3.e5894_s3126_r9364_r9315_p3517
mc16_13TeV.364253.Sherpa_222_NNPDF30NNLO_lllv.deriv.DAOD_STDM3.e5916_s3126_r9364_r9315_p3517
mc16_13TeV.364254.Sherpa_222_NNPDF30NNLO_llvv.deriv.DAOD_STDM3.e5916_s3126_r9364_r9315_p3517
mc16_13TeV.364255.Sherpa_222_NNPDF30NNLO_lvvv.deriv.DAOD_STDM3.e5916_s3126_r9364_r9315_p3517
mc16_13TeV.363494.Sherpa_221_NNPDF30NNLO_vvvv.deriv.DAOD_STDM3.e5332_s3126_r9364_r9315_p3517
mc16_13TeV.363355.Sherpa_221_NNPDF30NNLO_ZqqZvv.deriv.DAOD_STDM3.e5525_s3126_r9364_r9315_p3517
mc16_13TeV.363356.Sherpa_221_NNPDF30NNLO_ZqqZll.deriv.DAOD_STDM3.e5525_s3126_r9364_r9315_p3517
mc16_13TeV.363357.Sherpa_221_NNPDF30NNLO_WqqZvv.deriv.DAOD_STDM3.e5525_s3126_r9364_r9315_p3517
mc16_13TeV.363358.Sherpa_221_NNPDF30NNLO_WqqZll.deriv.DAOD_STDM3.e5525_s3126_r9364_r9315_p3517
mc16_13TeV.363359.Sherpa_221_NNPDF30NNLO_WpqqWmlv.deriv.DAOD_STDM3.e5583_s3126_r9364_r9315_p3517
mc16_13TeV.363360.Sherpa_221_NNPDF30NNLO_WplvWmqq.deriv.DAOD_STDM3.e5983_s3126_r9364_r9315_p3517

mc16_13TeV.363489.Sherpa_221_NNPDF30NNLO_WlvZqq.deriv.DAOD_STDM3.e5525_s3126_r9364_r9315_p3517

MC16d (2017 data conditions)
mc16_13TeV.364250.Sherpa_222_NNPDF30NNLO_llll.deriv.DAOD_STDM3.e5894_e5984_s3126_r10201_r10210_p3552
mc16_13TeV.364253.Sherpa_222_NNPDF30NNLO_lllv.deriv.DAOD_STDM3.e5916_e5984_s3126_r10201_r10210_p3552
mc16_13TeV.364254.Sherpa_222_NNPDF30NNLO_llvv.deriv.DAOD_STDM3.e5916_e5984_s3126_r10201_r10210_p3552
mc16_13TeV.364255.Sherpa_222_NNPDF30NNLO_lvvv.deriv.DAOD_STDM3.e5916_e5984_s3126_r10201_r10210_p3552
mc16_13TeV.363494.Sherpa_221_NNPDF30NNLO_vvvv.deriv.DAOD_STDM3.e5332_e5984_s3126_r10201_r10210_p3552
mc16_13TeV.363355.Sherpa_221_NNPDF30NNLO_ZqqZvv.deriv.DAOD_STDM3.e5525_e5984_s3126_r10201_r10210_p3552
mc16_13TeV.363356.Sherpa_221_NNPDF30NNLO_ZqqZll.deriv.DAOD_STDM3.e5525_s3126_r10201_r10210_p3552
mc16_13TeV.363357.Sherpa_221_NNPDF30NNLO_WqqZvv.deriv.DAOD_STDM3.e5525_e5984_s3126_r10201_r10210_p3552
mc16_13TeV.363358.Sherpa_221_NNPDF30NNLO_WqqZll.deriv.DAOD_STDM3.e5525_e5984_s3126_r10201_r10210_p3552
mc16_13TeV.363359.Sherpa_221_NNPDF30NNLO_WpqqWmlv.deriv.DAOD_STDM3.e5583_e5984_s3126_r10201_r10210_p3552
mc16_13TeV.363360.Sherpa_221_NNPDF30NNLO_WplvWmqq.deriv.DAOD_STDM3.e5983_e5984_s3126_r10201_r10210_p3552
mc16_13TeV.363489.Sherpa_221_NNPDF30NNLO_WlvZqq.deriv.DAOD_STDM3.e5525_e5984_s3126_r10201_r10210_p3552

MC16e (2018 data conditions)
mc16_13TeV.364250.Sherpa_222_NNPDF30NNLO_llll.deriv.DAOD_STDM3.e5894_e5984_s3126_r10724_r10726_p3596
mc16_13TeV.364253.Sherpa_222_NNPDF30NNLO_lllv.deriv.DAOD_STDM3.e5916_e5984_s3126_r10724_r10726_p3596
mc16_13TeV.364254.Sherpa_222_NNPDF30NNLO_llvv.deriv.DAOD_STDM3.e5916_e5984_s3126_r10724_r10726_p3596
mc16_13TeV.364255.Sherpa_222_NNPDF30NNLO_lvvv.deriv.DAOD_STDM3.e5916_e5984_s3126_r10724_r10726_p3596
mc16_13TeV.363494.Sherpa_221_NNPDF30NNLO_vvvv.deriv.DAOD_STDM3.e5332_e5984_s3126_r10724_r10726_p3596
mc16_13TeV.363355.Sherpa_221_NNPDF30NNLO_ZqqZvv.deriv.DAOD_STDM3.e5525_e5984_s3126_r10724_r10726_p3596
mc16_13TeV.363356.Sherpa_221_NNPDF30NNLO_ZqqZll.deriv.DAOD_STDM3.e5525_e5984_s3126_r10724_r10726_p3596
mc16_13TeV.363357.Sherpa_221_NNPDF30NNLO_WqqZvv.deriv.DAOD_STDM3.e5525_e5984_s3126_r10724_r10726_p3596
mc16_13TeV.363358.Sherpa_221_NNPDF30NNLO_WqqZll.deriv.DAOD_STDM3.e5525_e5984_s3126_r10724_r10726_p3596
mc16_13TeV.363359.Sherpa_221_NNPDF30NNLO_WpqqWmlv.deriv.DAOD_STDM3.e5583_e5984_s3126_r10724_r10726_p3596
mc16_13TeV.363360.Sherpa_221_NNPDF30NNLO_WplvWmqq.deriv.DAOD_STDM3.e5983_e5984_s3126_r10724_r10726_p3596
mc16_13TeV.363489.Sherpa_221_NNPDF30NNLO_WlvZqq.deriv.DAOD_STDM3.e5525_e5984_s3126_r10724_r10726_p3596

C.2.8 Single top

MC16a (2016+2016 data conditions)
mc16_13TeV.410642.PhPy8EG_A14_tchan_lept_top.deriv.DAOD_STDM3.e6536_e5984_a875_r9364_r9315_p3517
mc16_13TeV.410643.PhPy8EG_A14_tchan_lept_antitop.deriv.DAOD_STDM3.e6536_e5984_a875_r9364_r9315_p3517
mc16_13TeV.410644.PowhegPythia8EvtGen_A14_singletop_schan_lept_top.deriv.DAOD_STDM3.e6527_e5984_s3126_r9364_r9315_p3517
mc16_13TeV.410645.PowhegPythia8EvtGen_A14_singletop_schan_lept_antitop.deriv.DAOD_STDM3.e6527_e5984_s3126_r9364_r9315_p3517
mc16_13TeV.410646.PowhegPythia8EvtGen_A14_Wt_DR_inclusive_top.deriv.DAOD_STDM3.e6552_e5984_s3126_r9364_r9315_p3517
mc16_13TeV.410647.PowhegPythia8EvtGen_A14_Wt_DR_inclusive_antitop.deriv.DAOD_STDM3.e6552_e5984_s3126_r9364_r9315_p3517

MC16d (2017 data conditions)
mc16_13TeV.410642.PhPy8EG_A14_tchan_lept_top.deriv.DAOD_STDM3.e6536_e5984_a875_r10201_r10210_p3517
mc16_13TeV.410643.PhPy8EG_A14_tchan_lept_antitop.deriv.DAOD_STDM3.e6536_e5984_a875_r10201_r10210_p3517
mc16_13TeV.410644.PowhegPythia8EvtGen_A14_singletop_schan_lept_top.deriv.DAOD_STDM3.e6527_e5984_s3126_r10201_r10210_p3517
mc16_13TeV.410645.PowhegPythia8EvtGen_A14_singletop_schan_lept_antitop.deriv.DAOD_STDM3.e6527_s3126_r10201_r10210_p3517
mc16_13TeV.410646.PowhegPythia8EvtGen_A14_Wt_DR_inclusive_top.deriv.DAOD_STDM3.e6552_e5984_s3126_r10201_r10210_p3517
mc16_13TeV.410647.PowhegPythia8EvtGen_A14_Wt_DR_inclusive_antitop.deriv.DAOD_STDM3.e6552_e5984_s3126_r10201_r10210_p3517

MC16e (2018 data conditions)
mc16_13TeV.410658.PhPy8EG_A14_tchan_BW50_lept_top.deriv.DAOD_STDM3.e6671_e5984_s3126_s3136_r10724_r10726_p3596
mc16_13TeV.410659.PhPy8EG_A14_tchan_BW50_lept_antitop.deriv.DAOD_STDM3.e6671_e5984_s3126_s3136_r10724_r10726_p3596
mc16_13TeV.410644.PowhegPythia8EvtGen_A14_singletop_schan_lept_top.deriv.DAOD_STDM3.e6527_e5984_a875_r10724_r10726_p3596
mc16_13TeV.410645.PowhegPythia8EvtGen_A14_singletop_schan_lept_antitop.deriv.DAOD_STDM3.e6527_e5984_s3126_r10724_r10726_p3596
mc16_13TeV.410646.PowhegPythia8EvtGen_A14_Wt_DR_inclusive_top.deriv.DAOD_STDM3.e6552_e5984_a875_r10724_r10726_p3596
mc16_13TeV.410647.PowhegPythia8EvtGen_A14_Wt_DR_inclusive_antitop.deriv.DAOD_STDM3.e6552_e5984_a875_r10724_r10726_p3596

C.2.9 W+jets

MC16a (2016+2016 data conditions)
mc16_13TeV.361100.PowhegPythia8EvtGen_AZNLOCTEQ6L1_Wplusenu.deriv.DAOD_STDM3.e3601_s3126_r9364_r9315_p3517
mc16_13TeV.361101.PowhegPythia8EvtGen_AZNLOCTEQ6L1_Wplusmunu.deriv.DAOD_STDM3.e3601_s3126_r9364_r9315_p3517
mc16_13TeV.361103.PowhegPythia8EvtGen_AZNLOCTEQ6L1_Wminusenu.deriv.DAOD_STDM3.e3601_s3126_r9364_r9315_p3517
mc16_13TeV.361104.PowhegPythia8EvtGen_AZNLOCTEQ6L1_Wminusmunu.deriv.DAOD_STDM3.e3601_s3126_r9364_r9315_p3517

mc16_13TeV.361100.PowhegPythia8EvtGen_AZNLOCTEQ6L1_Wplusenu.deriv.DAOD_STDM3.e3601_e5984_s3126_r10201_r10210_p3526
mc16_13TeV.361101.PowhegPythia8EvtGen_AZNLOCTEQ6L1_Wplusmunu.deriv.DAOD_STDM3.e3601_e5984_s3126_r10201_r10210_p3526
mc16_13TeV.361103.PowhegPythia8EvtGen_AZNLOCTEQ6L1_Wminusenu.deriv.DAOD_STDM3.e3601_e5984_s3126_r10201_r10210_p3526
mc16_13TeV.361104.PowhegPythia8EvtGen_AZNLOCTEQ6L1_Wminusmunu.deriv.DAOD_STDM3.e3601_e5984_s3126_r10201_r10210_p3526

mc16_13TeV.361100.PowhegPythia8EvtGen_AZNLOCTEQ6L1_Wplusenu.deriv.DAOD_STDM3.e3601_e5984_s3126_r10724_r10726_p3596
mc16_13TeV.361101.PowhegPythia8EvtGen_AZNLOCTEQ6L1_Wplusmunu.deriv.DAOD_STDM3.e3601_e5984_s3126_r10724_r10726_p3596
mc16_13TeV.361103.PowhegPythia8EvtGen_AZNLOCTEQ6L1_Wminusenu.deriv.DAOD_STDM3.e3601_e5984_s3126_r10724_r10726_p3596
mc16_13TeV.361104.PowhegPythia8EvtGen_AZNLOCTEQ6L1_Wminusmunu.deriv.DAOD_STDM3.e3601_e5984_s3126_r10724_r10726_p3596

C.2.10 $Z \to \tau\tau$

mc16_13TeV.361108.PowhegPythia8EvtGen_AZNLOCTEQ6L1_Ztautau.deriv.DAOD_STDM3.e3601_s3126_r9364_r9315_p3517
mc16_13TeV.361108.PowhegPythia8EvtGen_AZNLOCTEQ6L1_Ztautau.deriv.DAOD_STDM3.e3601_e5984_s3126_r10201_r10210_p3526
mc16_13TeV.361108.PowhegPythia8EvtGen_AZNLOCTEQ6L1_Ztautau.deriv.DAOD_STDM3.e3601_e5984_s3126_r10724_r10726_p3596

Appendix D

Histogram binning

Differential cross section measurements are performed for the following four observables:

- Dijet invariant mass: m_{jj}
- Z boson transverse momentum defined as p_{T} of the dilepton system: p_{T}^{Z}
- Rapidity separation of the two leading jets: $\Delta y_{jj} \equiv |y_{\mathrm{j1}} - y_{\mathrm{j2}}|$
- Signed azimuthal separation between the two highest p_{T} jets: $\Delta\phi_{jj}^{\mathrm{signed}}$,

The binning used is presented in table D.1. The final bin in m_{jj} and Δy_{jj} have low statistics in some of the control regions described in section 7.6.2, so for some purposes the two last bins are merged.

Observable	Bin edges												
m_{jj} / GeV	750	1,000	1,500	2,250	3,000	4,500	7,500						
Δy_{jj}	2.0	2.6	3.1	3.6	3.9	4.2	4.6	5.0	6.0	8.0			
p_{T}^{Z} / GeV	20	30	45	70	100	140	200	275	400	550	1,050		
$\Delta\phi_{jj}^{\mathrm{signed}}$	$-\pi$	$-15\pi/16$	$-7\pi/8$	$-3\pi/4$	$-\pi/2$	$-\pi/4$	0	$\pi/4$	$\pi/2$	$3\pi/4$	$7\pi/8$	$15\pi/16$	π

TABLE D.1: Binning used for the Zjj differential cross section measurements. For Δy_{jj} p_{T}^{Z} and $\Delta\phi_{jj}^{\mathrm{signed}}$ an additional criterion of $m_{jj} > 1000$ GeV is applied. For the $\Delta\phi_{jj}^{\mathrm{signed}}$ binning, we use 4 digits precision.

Appendix E

VBF systematics

List of lepton systematics:

- MUON_EFF_ISO_STAT__1up
- MUON_EFF_ISO_SYS__1up
- MUON_EFF_RECO_STAT__1up
- MUON_EFF_RECO_STAT_LOWPT__1up
- MUON_EFF_RECO_SYS__1up
- MUON_EFF_RECO_SYS_LOWPT__1up
- MUON_EFF_TTVA_STAT__1up
- MUON_EFF_TTVA_SYS__1up
- MUON_EFF_TrigStatUncertainty__1up
- MUON_EFF_TrigSystUncertainty__1up
- MUON_ID__1up
- MUON_MS__1up
- EL_EFF_ID_TOTAL_1NPCOR_PLUS_UNCOR__1up
- EL_EFF_Iso_TOTAL_1NPCOR_PLUS_UNCOR__1up
- EL_EFF_Reco_TOTAL_1NPCOR_PLUS_UNCOR__1up
- EL_EFF_TriggerEff_TOTAL_1NPCOR_PLUS_UNCOR__1up
- EL_EFF_Trigger_TOTAL_1NPCOR_PLUS_UNCOR__1up
- MUON_SAGITTA_RESBIAS__1up
- MUON_SAGITTA_RHO__1up
- MUON_SCALE__1up

List of important/large jet systematics:

- EtaIntercalibration_Modelling
- EtaIntercalibration_TotalStat
- Flavor_Composition
- Flavor_Response
- Pileup_OffsetMu
- Pileup_OffsetNPV
- Pileup_PtTerm
- Pileup_RhoTopology

Appendix F

Re-weighting function fits

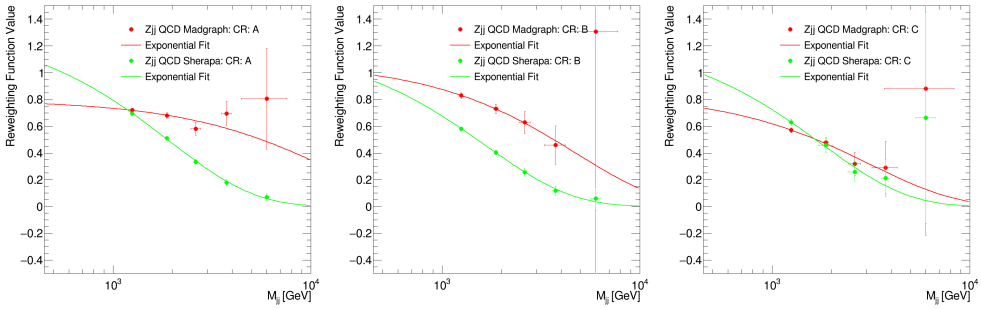

FIGURE F.1: Data driven constraint on strong-Zjj production for the variable $m_{jj}$for all control regions. The constraints are derived in dedicated control regions (as outlined in Section 7.6.4) and shown for the Madgraph, and Sherpa event generators. These constrains are then used to constrain the strong-Zjj in the search region.

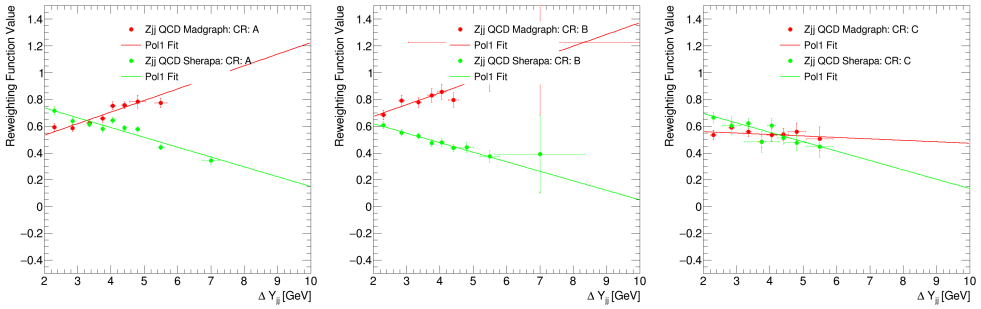

FIGURE F.2: Data driven constraint on strong-Zjj production for the variable $\Delta y_{jj}$for all control regions. The constraints are derived in dedicated control regions (as outlined in Section 7.6.4) and shown for the Madgraph, and Sherpa event generators. These constrains are then used to constrain the strong-Zjj in the search region.

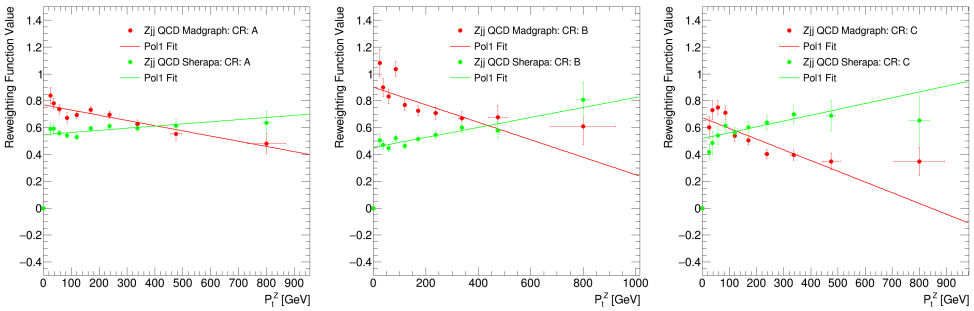

FIGURE F.3: Data driven constraint on strong-Zjj production for the variable $p_{\mathrm{T}}^{Z}$for all control regions. The constraints are derived in dedicated control regions (as outlined in Section 7.6.4) and shown for the Madgraph, and Sherpa event generators. These constrains are then used to constrain the strong-Zjj in the search region.

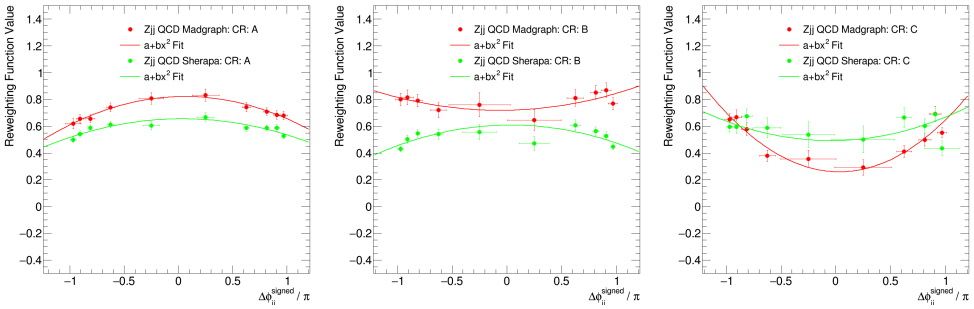

FIGURE F.4: Data driven constraint on strong-Zjj production for the variable $\Delta\phi_{jj}^{\mathrm{signed}}$for all control regions. The constraints are derived in dedicated control regions (as outlined in Section 7.6.4) and shown for the Madgraph, and Sherpa event generators. These constrains are then used to constrain the strong-Zjj in the search region.

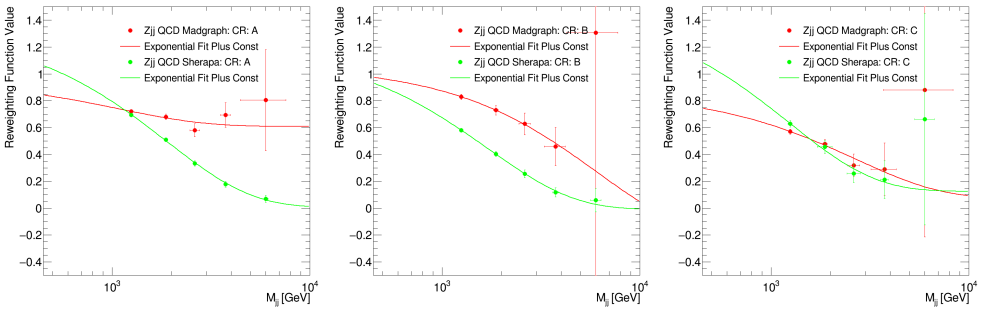

FIGURE F.5: Data driven constraint on strong-Zjj production for the variable $m_{jj}$for all control regions using the alternate paramaterisation given in table 7.6. The constraints are derived in dedicated control regions (as outlined in Section 7.6.4) and shown for the Madgraph, and Sherpa event generators. These constrains are then used to constrain the strong-Zjj in the search region.

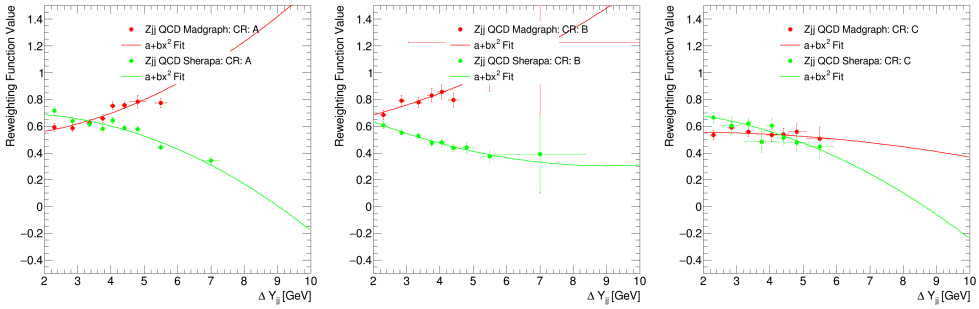

FIGURE F.6: Data driven constraint on strong-Zjj production for the variable $\Delta y_{jj}$for all control regions using the alternate paramaterisation given in table 7.6. The constraints are derived in dedicated control regions (as outlined in Section 7.6.4) and shown for the Madgraph, and Sherpa event generators. These constrains are then used to constrain the strong-Zjj in the search region.

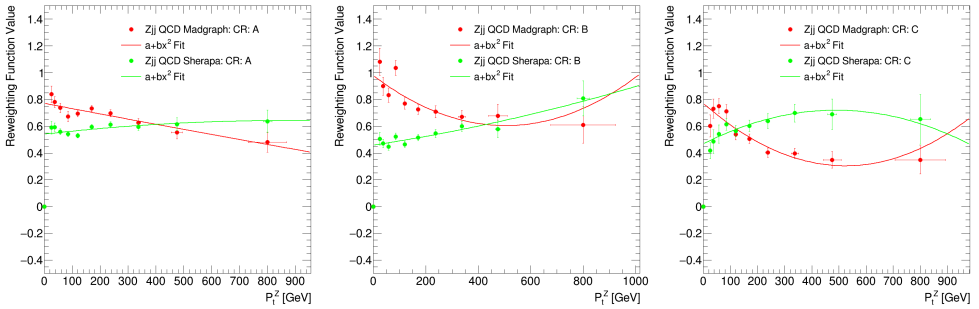

FIGURE F.7: Data driven constraint on strong-Zjj production for the variable $p_{\mathrm{T}}^{Z}$for all control regions using the alternate paramaterisation given in table 7.6. The constraints are derived in dedicated control regions (as outlined in Section 7.6.4) and shown for the Madgraph, and Sherpa event generators. These constrains are then used to constrain the strong-Zjj in the search region.

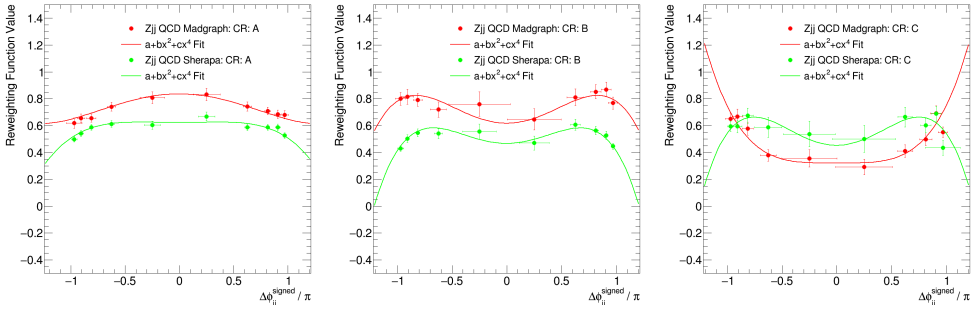

FIGURE F.8: Data driven constraint on strong-Zjj production for the variable $\Delta\phi_{jj}^{\mathrm{signed}}$for all control regions using the alternate paramaterisation given in table 7.6. The constraints are derived in dedicated control regions (as outlined in Section 7.6.4) and shown for the Madgraph, and Sherpa event generators. These constrains are then used to constrain the strong-Zjj in the search region.

Appendix G

Predicted errors on EW and Strong-Zjj using Asimov data

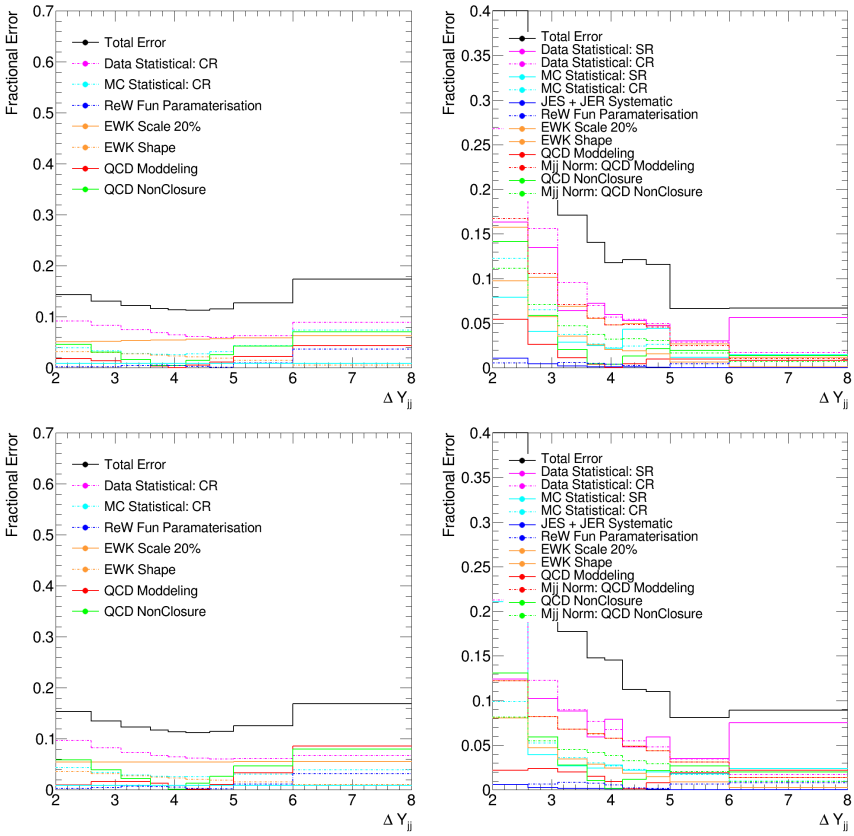

FIGURE G.1: Depicted here are the predicted systematic and statistical errors for ΔY_{jj} using Asimov data for the strong-Zjj (left) and the number of electroweak events (right) and for SHERPA(top) and MADGRAPH (bottom).

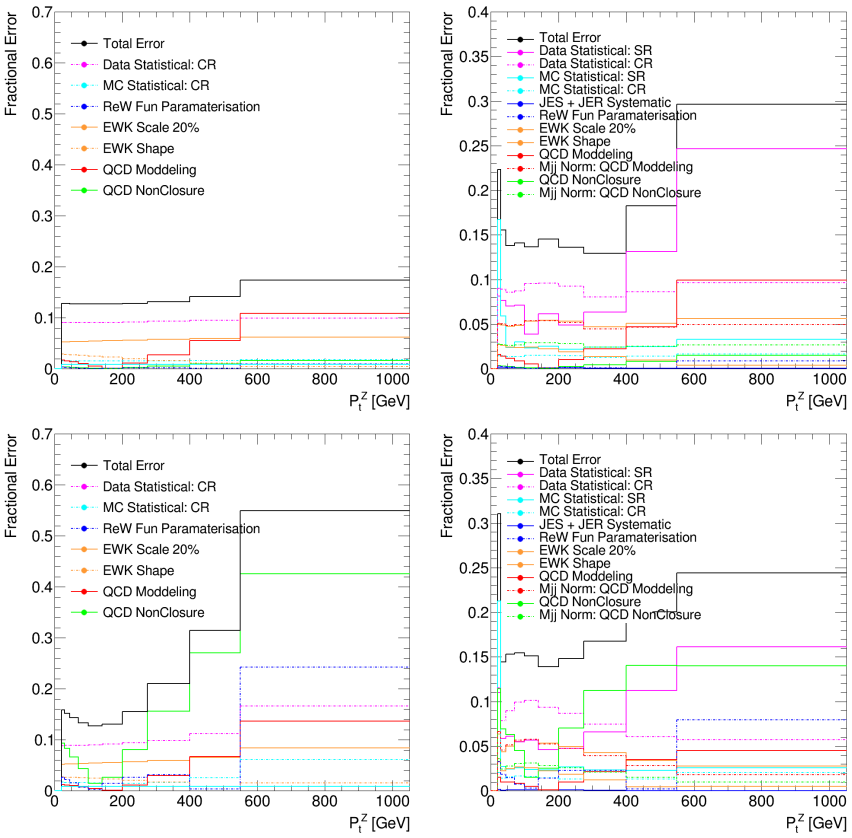

FIGURE G.2: Depicted here are the predicted systematic and statistical errors for p_T^Z using Asimov data for the strong-Zjj (left) and the number of electroweak events (right) and for SHERPA(top) and MADGRAPH (bottom).

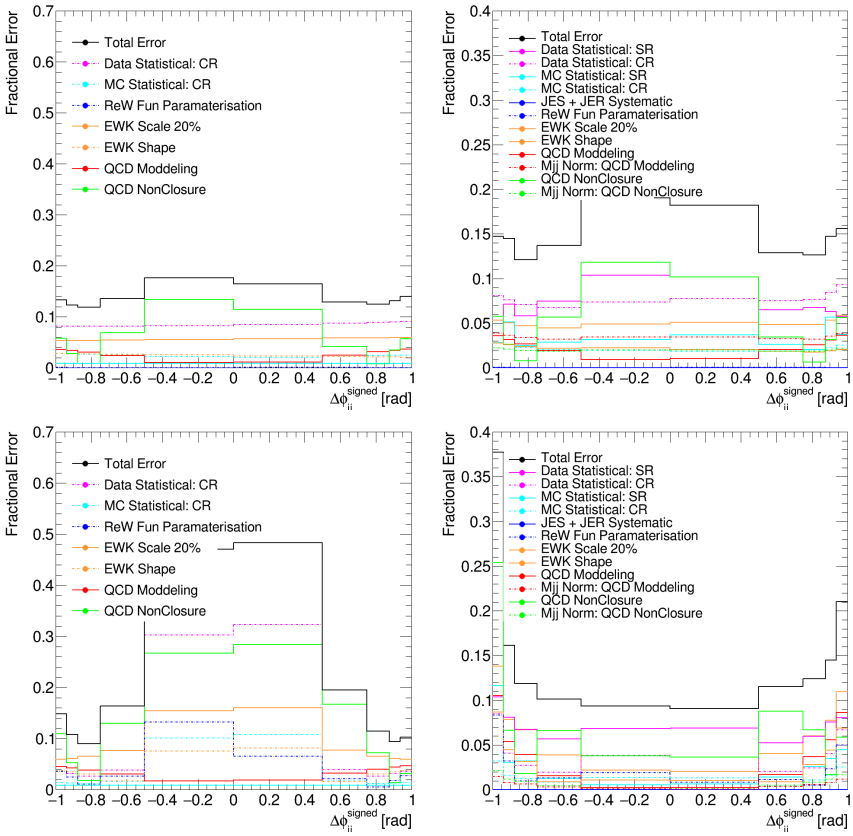

FIGURE G.3: Depicted here are the predicted systematic and statistical errors for $\Delta\phi_{jj}^{signed}$ using Asimov data for the strong-Zjj (left) and the number of electroweak events (right) and for SHERPA(top) and MADGRAPH (bottom).

Appendix H

Errors on EW and Strong-Zjj

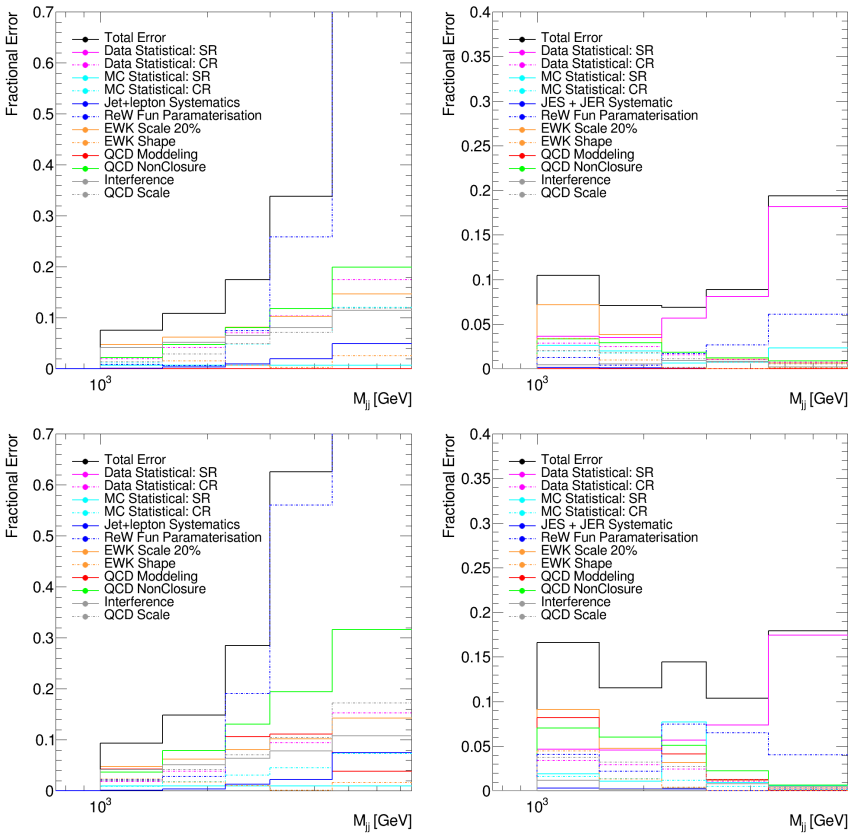

FIGURE H.1: Depicted here are the systematic and statistical errors for m_{jj} using real data for the strong-Zjj (left) and the number of electroweak events (right) and for SHERPA(top) and MADGRAPH (bottom).

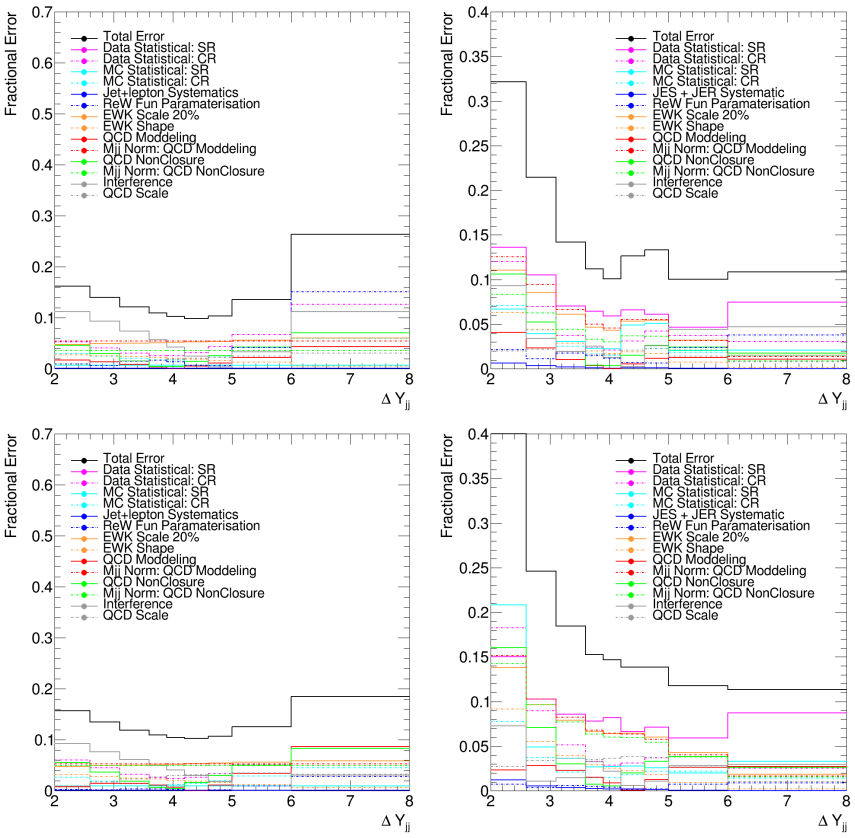

FIGURE H.2: Depicted here are the measured systematic and statistical errors for ΔY_{jj} for the strong-Zjj (left) and the number of electroweak events (right) and for SHERPA(top) and MADGRAPH (bottom). The statistical error is calculated using 1000 bootstraps.

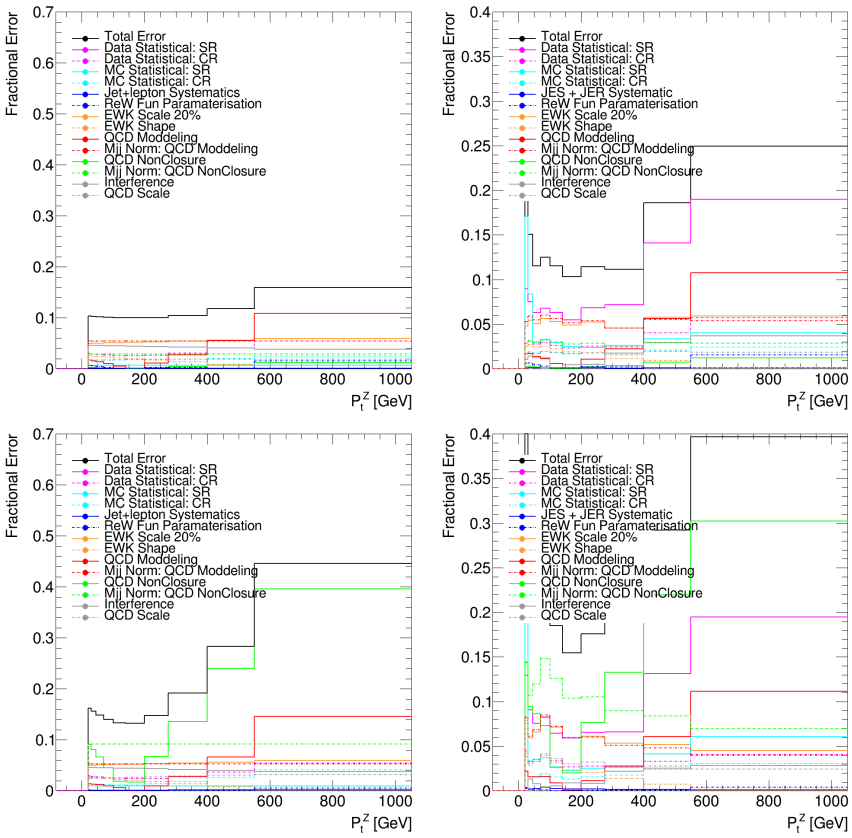

FIGURE H.3: Depicted here are the measured systematic and statistical errors for p_T^Z for the strong-Zjj (left) and the number of electroweak events (right) and for SHERPA(top) and MADGRAPH (bottom). The statistical error is calculated using 1000 bootstraps.

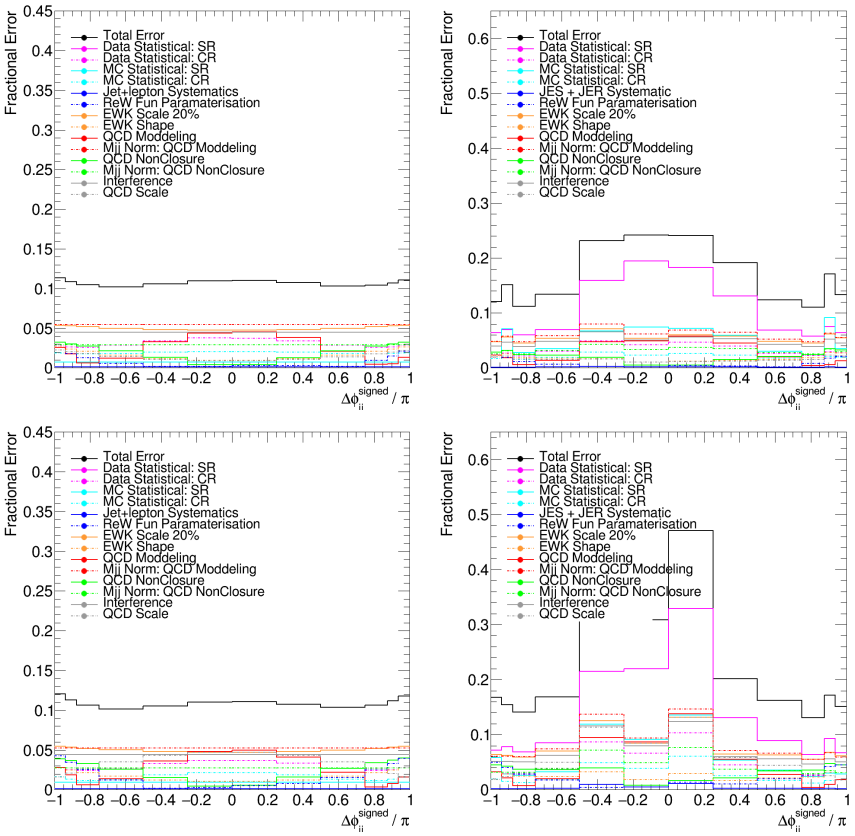

FIGURE H.4: Depicted here are the measured systematic and statistical errors for $\Delta\phi_{jj}^{signed}$ for the strong-Zjj (left) and the number of electroweak events (right) and for SHERPA(top) and MADGRAPH (bottom). The statistical error is calculated using 1000 bootstraps.

Bibliography

[1] D. J. Griffiths, *Introduction to quantum mechanics*, Cambridge University Press.

[2] A. Einstein, *Zur Elektrodynamik bewegter Karper [AdP 17, 891 (1905)]*, Annalen der Physik **14** () 194, eprint: https://onlinelibrary.wiley.com/doi/pdf/10.1002/andp.200590006, URL: https://onlinelibrary.wiley.com/doi/abs/10.1002/andp.200590006.

[3] Y. L.D.L. E. Lifshitz, *The Classical Theory of Fields 4th Ed*, elsevier.

[4] S. Weinberg, *A Model of Leptons*, Phys. Rev. Lett. **19** (21 1967) 1264, URL: https://link.aps.org/doi/10.1103/PhysRevLett.19.1264.

[5] P. W. Higgs, *Broken Symmetries and the Masses of Gauge Bosons*, Phys. Rev. Lett. **13** (16 1964) 508, URL: https://link.aps.org/doi/10.1103/PhysRevLett.13.508.

[6] The ATLAS Collaboration, *Observation of a new boson at a mass of 125 GeV with the CMS experiment at the LHC*, Physics Letters B **716** (2012) 30 , URL: http://www.sciencedirect.com/science/article/pii/S0370269312008581.

[7] The CMS Collaboration, *Observation of a new particle in the search for the Standard Model Higgs boson with the ATLAS detector at the LHC*, Physics Letters B **716** (2012) 1 , ISSN: 0370-2693, URL: http://www.sciencedirect.com/science/article/pii/S037026931200857X.

[8] M. Tanabashi et al., *Review of Particle Physics*, Phys. Rev. **D98** (2018) 030001.

[9] P. A. M. Dirac, *Quantum theory of emission and absorption of radiation*, Proc. Roy. Soc. Lond. **A114** (1927) 243.

[10] M. D. Schwartz, *Quantum Field Theory and the Standard Model*, Cambridge University Press, 2014, ISBN: 1107034736, 9781107034730.

[11] P. A. M. Dirac, *The quantum theory of the electron*, Proc. Roy. Soc. Lond. **A117** (1928) 610.

[12] S. Weinberg, *A Model of Leptons*, Phys. Rev. Lett. **19** (21 1967) 1264, URL: https://link.aps.org/doi/10.1103/PhysRevLett.19.1264.

[13] A. Salam, *Gauge unification of fundamental forces*, Rev. Mod. Phys. **52** (3 1980) 525, URL: https://link.aps.org/doi/10.1103/RevModPhys.52.525.

[14] A. Salam and J. N. C. Ward, *Weak and electromagnetic interactions*, (1958), URL: https://doi.org/10.1007/BF02726525.

[15] S. L. Glashow, *Partial-symmetries of weak interactions*, Nuclear Physics **22** (1961) 579 , ISSN: 0029-5582, URL: http://www.sciencedirect.com/science/article/pii/0029558261904692.

[16] T. D. Lee and C. N. Yang, *Question of Parity Conservation in Weak Interactions*, Phys. Rev. **104** (1 1956) 254, URL: https://link.aps.org/doi/10.1103/PhysRev.104.254.

[17] C. S. Wu, E. Ambler, R. W. Hayward, D. D. Hoppes, and R. P. Hudson, *Experimental Test of Parity Conservation in Beta Decay*, Phys. Rev. **105** (4 1957) 1413, URL: https://link.aps.org/doi/10.1103/PhysRev.105.1413.

[18] F. Yndurain, *The Theory of Quark and Gluon Interactions*, Springer.

[19] E. D. Bloom et al., *High-Energy Inelastic $e - p$ Scattering at 6 and 10*, Phys. Rev. Lett. **23** (16 1969) 930, URL: https://link.aps.org/doi/10.1103/PhysRevLett.23.930.

[20] S. Weinberg, *A Model of Leptons*, Phys. Rev. Lett. **19** (21) 1264, URL: https://link.aps.org/doi/10.1103/PhysRevLett.19.1264.

[21] S. L. Glashow, *Partial-symmetries of weak interactions*, Nuclear Physics **22** (1961) 579 , ISSN: 0029-5582, URL: http://www.sciencedirect.com/science/article/pii/0029558261904692.

[22] A. Salam, *Weak and Electromagnetic Interactions*, Conf. Proc. **C680519** (1968) 367.

[23] T. Nakano and K. Nishijima, *Charge Independence for V-particles*, Prog. Theor. Phys. **10** (1953) 581.

[24] M. Gell-Mann, *The interpretation of the new particles as displaced charge multiplets*, Nuovo Cim. **4** (1956) 848.

[25] N. Cabibbo, *Unitary Symmetry and Leptonic Decays*, Phys. Rev. Lett. **10** (12 1963) 531, URL: https://link.aps.org/doi/10.1103/PhysRevLett.10.531.

[26] M. Kobayashi and T. Maskawa, *CP Violation in the Renormalizable Theory of Weak Interaction*, Prog. Theor. Phys. **49** (1973) 652.

[27] Z. Maki, M. Nakagawa, and S. Sakata, *Remarks on the unified model of elementary particles*, Prog. Theor. Phys. **28** (1962) 870, [,34(1962)].

[28] F. Englert and R. Brout, *Broken Symmetry and the Mass of Gauge Vector Mesons*, Phys. Rev. Lett. **13** (9 1964) 321, URL: https://link.aps.org/doi/10.1103/PhysRevLett.13.321.

[29] P. W. Higgs, *Broken Symmetries and the Masses of Gauge Bosons*, Phys. Rev. Lett. **13** (16 1964) 508, URL: https://link.aps.org/doi/10.1103/PhysRevLett.13.508.

[30] G. S. Guralnik, C. R. Hagen, and T. W. B. Kibble, *Global Conservation Laws and Massless Particles*, Phys. Rev. Lett. **13** (20 1964) 585, URL: https://link.aps.org/doi/10.1103/PhysRevLett.13.585.

[31] J. Ellis, M. K. Gaillard, and D. V. Nanopoulos, *A Historical Profile of the Higgs Boson*, (2012), arXiv: 1201.6045 [hep-ph].

[32] F. Halzen and A. D. Martin, *Quarks and Leptons: An Introductory Course in Modern Particle Physics*, John Wiley Sons, 1984.

[33] *Results for the Global Electroweak Standard Model Fit*, project-gfitter.web.cern.ch/project-gfitter/Standard_Model/, Accessed: 07-12-2018.

[34] *Summary plots from the ATLAS Standard Model physics group, 2017*, https://atlas.web.cern.ch/Atlas/GROUPS/PHYSICS/CombinedSummaryPlots/SM/, Accessed: 07-12-2018.

[35] F. Zwicky, *On the Masses of Nebulae and of Clusters of Nebulae*, Astrophys. J. **86** (1937) 217.

[36] J. de Swart, G. Bertone, and J. van Dongen, *How Dark Matter Came to Matter*, (2017), [Nature Astron.1,0059(2017)], arXiv: 1703.00013 [astro-ph.CO].

[37] T. S. van Albada, J. N. Bahcall, K. Begeman, and R. Sancisi, *Distribution of dark matter in the spiral galaxy NGC 3198*, **295** (1985) 305.

[38] P. A. R. Ade et al., *Planck 2015 results. XIII. Cosmological parameters*, Astron. Astrophys. **594** (2016) A13, arXiv: 1502.01589 [astro-ph.CO].

[39] A. D. Sakharov, *Violation of CP Invariance, C asymmetry, and baryon asymmetry of the universe*, Pisma Zh. Eksp. Teor. Fiz. **5** (1967) 32, [Usp. Fiz. Nauk161,no.5,61(1991)].

[40] M. Kobayashi and T. Maskawa, *CP-Violation in the Renormalizable Theory of Weak Interaction*, Progress of Theoretical Physics **49** (1973) 652, URL: http://dx.doi.org/10.1143/PTP.49.652.

[41] P. Minkowski, *A review of neutrino properties Neutrino oscillations - a historical overview and its projection*, EPJ Web Conf. **182** (2018) 02087.

[42] R. P. Feynman, *QED: The Strange Theory of Light and Matter*, 1986, ISBN: 9780691024172.

[43] J. M. I. Ponce, "Vertex counting as a luminosity measure at ATLAS and determination of the electroweak Zjj production cross-section", PhD thesis: Manchester U., 2016-06-27.

[44] V. N. Gribov and L. N. Lipatov, *Deep inelastic e p scattering in perturbation theory*, Sov. J. Nucl. Phys. **15** (1972) 438, [Yad. Fiz.15,781(1972)].

[45] Y. L. Dokshitzer, *Calculation of the Structure Functions for Deep Inelastic Scattering and e+ e- Annihilation by Perturbation Theory in Quantum Chromodynamics.*, Sov. Phys. JETP **46** (1977) 641, [Zh. Eksp. Teor. Fiz.73,1216(1977)].

[46] G. Altarelli and G. Parisi, *Asymptotic Freedom in Parton Language*, Nucl. Phys. **B126** (1977) 298.

[47] S. Dulat et al., *New parton distribution functions from a global analysis of quantum chromodynamics*, Phys. Rev. **D93** (2016) 033006, arXiv: 1506.07443 [hep-ph].

[48] E. Schopf, N. Wermes, and I. Brock, "Search for the Higgs Boson Decay to Bottom and Charm Quarks", Presented 17 Jul 2018, 2018, URL: https://cds.cern.ch/record/2637125.

[49] P. Skands, "Introduction to QCD", *Proceedings, 2nd Asia-Europe-Pacific School of High-Energy Physics (AEPSHEP 2014): Puri, India, November 04?17, 2014*, [,63(2017)], 2013 341, arXiv: 1207.2389 [hep-ph].

[50] T Sjstrand, *Monte Carlo Generators*, (2006) 23 p, URL: http://cds.cern.ch/record/999717.

[51] T. Sjostrand, S. Mrenna, and P. Z. Skands, *A Brief Introduction to PYTHIA 8.1*, Comput. Phys. Commun. **178** (2008) 852, arXiv: 0710.3820 [hep-ph].

[52] J. Bellm et al., *Herwig 7.0/Herwig++ 3.0 release note*, Eur. Phys. J. **C76** (2016) 196, arXiv: 1512.01178 [hep-ph].

[53] M. Bähr et al., *Herwig++ physics and manual*, The European Physical Journal C **58** (2008) 639, ISSN: 1434-6052, URL: https://doi.org/10.1140/epjc/s10052-008-0798-9.

[54] T. Gleisberg et al., *Event generation with SHERPA 1.1*, JHEP **02** (2009) 007, arXiv: 0811.4622 [hep-ph].

[55] S. Alioli, P. Nason, C. Oleari, and E. Re, *A general framework for implementing NLO calculations in shower Monte Carlo programs: the POWHEG BOX*, JHEP **06** (2010) 043, arXiv: 1002.2581 [hep-ph].

[56] J. Alwall et al., *The automated computation of tree-level and next-to-leading order differential cross sections, and their matching to parton shower simulations*, JHEP **07** (2014) 079, arXiv: 1405.0301 [hep-ph].

[57] S. Frixione and B. R. Webber, *Matching NLO QCD computations and parton shower simulations*, JHEP **06** (2002) 029, arXiv: hep-ph/0204244 [hep-ph].

[58] G. Aad et al., *The ATLAS Simulation Infrastructure*, Eur. Phys. J. **C70** (2010) 823, arXiv: 1005.4568 [physics.ins-det].

[59] *Geant4—a simulation toolkit*, Nuclear Instruments and Methods in Physics Research Section A: Accelerators, Spectrometers, Detectors and Associated Equipment **506** (2003) 250 , ISSN: 0168-9002, URL: http://www.sciencedirect.com/science/article/pii/S0168900203013688.

[60] L. Evans and P. Bryant, *LHC Machine*, Journal of Instrumentation **3** (2008) S08001, URL: http://stacks.iop.org/1748-0221/3/i=08/a=S08001.

[61] F. Pastore, *ATLAS Run-2 status and performance*, Nuclear and Particle Physics Proceedings **270-272** (2016) 3 , 18th Montpellier International Conference on Quantum Chromodynamics (QCD 15), ISSN: 2405-6014, URL: http://www.sciencedirect.com/science/article/pii/S2405601416000031.

[62] The ALICE Collaboration, *The ALICE experiment at the CERN LHC*, Journal of Instrumentation **3** (2008) S08002, URL: http://stacks.iop.org/1748-0221/3/i=08/a=S08002.

[63] The ATLAS Collaboration, *The ATLAS Experiment at the CERN Large Hadron Collider*, Journal of Instrumentation **3** (2008) S08003, URL: http://stacks.iop.org/1748-0221/3/i=08/a=S08003.

[64] The CMS Collaboration, *The CMS experiment at the CERN LHC*, Journal of Instrumentation **3** (2008) S08004, URL: http://stacks.iop.org/1748-0221/3/i=08/a=S08004.

[65] The LHCb Collaboration, *The LHCb Detector at the LHC*, Journal of Instrumentation **3** (2008) S08005, URL: http://stacks.iop.org/1748-0221/3/i=08/a=S08005.

[66] *CERN, CERN Accelerator Complex.*, http://bigscience.web.cern.ch/bigscience/Objects/LHC/accelerator.jpg., Accessed: 09-07-2018.

[67] D. Boussard and T. Linnecar, *The LHC Superconducting RF System*, Adv. Cryog. Eng. **45A** (2000) 835.

[68] W. Bartmann et al., "Impact of LHC and SPS Injection Kicker Rise Times on Lhc Filling Schemes and Luminosity Reach", *Proc. of International Particle Accelerator Conference (IPAC'17), Copenhagen, Denmark, 14âĂŞ19 May, 2017*, (Copenhagen, Denmark), International Particle Accelerator Conference 8, JACoW, 2017 2043, ISBN: 978-3-95450-182-3, URL: http://jacow.org/ipac2017/papers/tupva007.pdf.

[69] O. S. Brüning et al., *LHC Design Report*, CERN Yellow Reports: Monographs, CERN, 2004, URL: http://cds.cern.ch/record/782076.

[70] ATLAS Collaboration, *Luminosity determination in pp collisions at $\sqrt{s}$ = 8 TeV using the ATLAS detector at the LHC*, Eur. Phys. J. **C76** (2016) 653, arXiv: 1608.03953 [hep-ex].

[71] *ATLAS inner detector: Technical Design Report, 1*, Technical Design Report ATLAS, CERN, 1997, URL: https://cds.cern.ch/record/331063.

[72] S Haywood, L Rossi, R Nickerson, and A Romaniouk, *ATLAS inner detector: Technical Design Report, 2*, Technical Design Report ATLAS, CERN, 1997, URL: https://cds.cern.ch/record/331064.

[73] J. D. Jackson, *Classical electrodynamics*, 3rd ed., Wiley, 1999, ISBN: 9780471309321, URL: http://cdsweb.cern.ch/record/490457.

[74] M. Aaboud et al., *Performance of the ATLAS Track Reconstruction Algorithms in Dense Environments in LHC Run 2*, Eur. Phys. J. **C77** (2017) 673, arXiv: 1704.07983 [hep-ex].

[75] *Track Reconstruction Performance of the ATLAS Inner Detector at $\sqrt{s} = 13$ TeV*, tech. rep. ATL-PHYS-PUB-2015-018, CERN, 2015, URL: http://cds.cern.ch/record/2037683.

[76] The ATLAS Collaboration, *Production and integration of the ATLAS Insertable B-Layer*, Journal of Instrumentation **13** (2018) T05008, URL: http://stacks.iop.org/1748-0221/13/i=05/a=T05008.

[77] *ATLAS Insertable B-Layer Technical Design Report Addendum Addendum*, (2012).

[78] The ATLAS TRT collaboration, *The ATLAS Transition Radiation Tracker (TRT) proportional drift tube: design and performance*, Journal of Instrumentation **3** (2008) P02013, URL: https://doi.org/10.1088%2F1748-0221%2F3%2F02%2Fp02013.

[79] The ATLAS TRT collaboration, Journal of Instrumentation **3** (2008) P02013, URL: https://doi.org/10.1088%2F1748-0221%2F3%2F02%2Fp02013.

[80] The ATLAS TRT collaboration, *The ATLAS TRT end-cap detectors*, Journal of Instrumentation **3** (2008) P10003, URL: https://doi.org/10.1088%2F1748-0221%2F3%2F10%2Fp10003.

[81] *ATLAS liquid-argon calorimeter: Technical Design Report*, Technical Design Report ATLAS, CERN, 1996, URL: https://cds.cern.ch/record/331061.

[82] *ATLAS tile calorimeter: Technical Design Report*, Technical Design Report ATLAS, CERN, 1996, URL: https://cds.cern.ch/record/331062.

[83] J. Pequenao, "Computer Generated image of the ATLAS calorimeter", 2008, URL: http://cds.cern.ch/record/1095927.

[84] *ATLAS muon spectrometer: Technical Design Report*, Technical Design Report ATLAS, CERN, 1997, URL: https://cds.cern.ch/record/331068.

[85] J. Pequenao, "Computer generated image of the ATLAS Muons subsystem", 2008, URL: http://cds.cern.ch/record/1095929.

[86] ATLAS Collaboration, *The ATLAS Experiment at the CERN Large Hadron Collider*, Journal of Instrumentation **3** (2008) S08003, URL: https://doi.org/10.1088%2F1748-0221%2F3%2F08%2Fs08003.

[87] D Caforio, *The ATLAS Forward Detectors - LUCID, ALFA and AFP: Past, Present and Future*, (2013), URL: https://cds.cern.ch/record/1514203.

[88] V Cindro et al., *The ATLAS Beam Conditions Monitor*, Journal of Instrumentation **3** (2008) P02004, URL: https://doi.org/10.1088%2F1748-0221%2F3%2F02%2Fp02004.

[89] M. Aaboud et al., *Performance of the ATLAS Trigger System in 2015*, Eur. Phys. J. **C77** (2017) 317, arXiv: 1611.09661 [hep-ex].

[90] G. Aad et al., *Technical Design Report for the Phase-I Upgrade of the ATLAS TDAQ System*, (2013).

[91] M. Abolins et al., *The ATLAS Data Acquisition and High Level Trigger system*, JINST **11** (2016) P06008.

[92] R. Fruhwirth, *Application of Kalman filtering to track and vertex fitting*, Nucl. Instrum. Meth. **A262** (1987) 444.

[93] T Cornelissen et al., *The new ATLAS track reconstruction (NEWT)*, J. Phys.: Conf. Ser. **119** (2008) 032014, URL: http://cds.cern.ch/record/1176900.

[94] ATLAS Colaboration, *Reconstruction of primary vertices at the ATLAS experiment in Run 1 proton–proton collisions at the LHC*, The European Physical Journal C **77** (2017) 332, ISSN: 1434-6052, URL: https://doi.org/10.1140/epjc/s10052-017-4887-5.

[95] G. Piacquadio, K. Prokofiev, and A. Wildauer, *Primary vertex reconstruction in the ATLAS experiment at LHC*, J. Phys. Conf. Ser. **119** (2008) 032033.

[96] *Vertex Reconstruction Performance of the ATLAS Detector at "$\sqrt{s} = 13$ TeV"*, tech. rep. ATL-PHYS-PUB-2015-026, CERN, 2015, URL: https://cds.cern.ch/record/2037717.

[97] M. Aaboud et al.,
Electron reconstruction and identification in the ATLAS experiment using the 2015 and 2016 LHC proton-proton collision data at $\sqrt{s}$ = 13 TeV,
Submitted to: Eur. Phys. J. (2019), arXiv: 1902.04655 [physics.ins-det].

[98] W Lampl et al., *Calorimeter Clustering Algorithms: Description and Performance*,
tech. rep. ATL-LARG-PUB-2008-002. ATL-COM-LARG-2008-003,
CERN, 2008, URL: https://cds.cern.ch/record/1099735.

[99] R. Frhwirth, *A Gaussian-mixture approximation of the Bethe-Heitler model of electron energy loss by bremsstrahlung*,
Somputer Physics Communications 154 (2003), URL: http://www.sciencedirect.com/science/article/pii/S0010465503002923..

[100] G. Aad et al., *Electron and photon energy calibration with the ATLAS detector using LHC Run 1 data*, Eur. Phys. J. **C74** (2014) 3071,
arXiv: 1407.5063 [hep-ex].

[101] M. Aaboud et al., *Electron and photon energy calibration with the ATLAS detector using 2015?2016 LHC proton-proton collision data*,
JINST **14** (2019) P03017, arXiv: 1812.03848 [hep-ex].

[102] *Electron efficiency measurements with the ATLAS detector using the 2015 LHC proton-proton collision data*, tech. rep. ATLAS-CONF-2016-024, CERN, 2016,
URL: https://cds.cern.ch/record/2157687.

[103] G. Aad et al., *Topological cell clustering in the ATLAS calorimeters and its performance in LHC Run 1*, Eur. Phys. J. **C77** (2017) 490,
arXiv: 1603.02934 [hep-ex].

[104] G. Aad et al., *Measurement of the muon reconstruction performance of the ATLAS detector using 2011 and 2012 LHC proton?proton collision data*,
Eur. Phys. J. **C74** (2014) 3130, arXiv: 1407.3935 [hep-ex].

[105] G. Aad et al., *Muon reconstruction performance of the ATLAS detector in proton–proton collision data at $\sqrt{s}$ =13 TeV*, Eur. Phys. J. **C76** (2016) 292,
arXiv: 1603.05598 [hep-ex].

[106] The ATLAS Collaboration,
ATLAS Muon Combined Performance with the full 2016 dataset,
https://atlas.web.cern.ch/Atlas/GROUPS/PHYSICS/PLOTS/MUON-2017-001/index.html, Accessed: 24-06-2019.

[107] *Measurement of the tau lepton reconstruction and identification performance in the ATLAS experiment using pp collisions at $\sqrt{s} = 13$ TeV*,
tech. rep. ATLAS-CONF-2017-029, CERN, 2017,
URL: https://cds.cern.ch/record/2261772.

[108] M. Hbner, *Measurement of the tau lepton reconstruction and identification performance in the ATLAS experiment using pp collisions at $\sqrt{(s)} = 13$ TeV*,
PoS **LHCP2018** (2018) 024.

[109] C. F. Galea, *Tau Lepton Reconstruction in ATLAS*,
Nucl. Part. Phys. Proc. **287-288** (2017) 111.

[110] M. Cacciari, G. P. Salam, and G. Soyez, *The anti-k_t jet clustering algorithm*,
JHEP **04** (2008) 063, arXiv: 0802.1189 [hep-ph].

[111] M. Cacciari, G. P. Salam, and G. Soyez, *FastJet User Manual*,
Eur. Phys. J. **C72** (2012) 1896, arXiv: 1111.6097 [hep-ph].

[112] M. Wobisch and T. Wengler,
"Hadronization corrections to jet cross-sections in deep inelastic scattering",
Monte Carlo generators for HERA physics. Proceedings, Workshop, Hamburg, Germany, 1998-1999, 1998 270, arXiv: hep-ph/9907280 [hep-ph].

[113] S. D. Ellis and D. E. Soper,
Successive combination jet algorithm for hadron collisions,
Phys. Rev. **D48** (1993) 3160, arXiv: hep-ph/9305266 [hep-ph].

[114] M. Aaboud et al., *Jet energy scale measurements and their systematic uncertainties in proton-proton collisions at $\sqrt{s} = 13$ TeV with the ATLAS detector*, Phys. Rev. **D96** (2017) 072002, arXiv: 1703.09665 [hep-ex].

[115] G. Aad et al., *Performance of pile-up mitigation techniques for jets in pp collisions at $\sqrt{s} = 8$ TeV using the ATLAS detector*, Eur. Phys. J. **C76** (2016) 581, arXiv: 1510.03823 [hep-ex].

[116] M. Aaboud et al., *Identification and rejection of pile-up jets at high pseudorapidity with the ATLAS detector*,
Eur. Phys. J. **C77** (2017) 580, [Erratum: Eur. Phys. J.C77,no.10,712(2017)], arXiv: 1705.02211 [hep-ex].

[117] *Optimisation of the ATLAS b-tagging performance for the 2016 LHC Run*, tech. rep. ATL-PHYS-PUB-2016-012, CERN, 2016, URL: https://cds.cern.ch/record/2160731.

[118] M. Aaboud et al., *Performance of missing transverse momentum reconstruction with the ATLAS detector using proton-proton collisions at $\sqrt{s}$ = 13 TeV*, Eur. Phys. J. **C78** (2018) 903, arXiv: 1802.08168 [hep-ex].

[119] *Luminosity determination in pp collisions at $\sqrt{s} = 13$ TeV using the ATLAS detector at the LHC*, tech. rep. ATLAS-CONF-2019-021, CERN, 2019, URL: http://cds.cern.ch/record/2677054.

[120] *ATLAS Collaboration: Public Results - Luminosity Public Results Run*, https://twiki.cern.ch/twiki/bin/view/AtlasPublic/LuminosityPublicResultsRun2/, Accessed: 22-05-2019.

[121] S. van der Meer, *Calibration of the Effective Beam Height in the ISR*, (1968).

[122] C. Rubbia, *Measurement of the luminosity of p−overlinep collider with a (generalized) Van der Meer Method*, tech. rep. CERN-p$\overline{p}$-Note-38, CERN, 1977, URL: http://cds.cern.ch/record/1025746.

[123] P. Grafström and W. Kozanecki, *Luminosity determination at proton colliders*, Progress in Particle and Nuclear Physics **81** (2015) 97 , ISSN: 0146-6410, URL: http://www.sciencedirect.com/science/article/pii/S0146641014000878.

[124] M. Venturini and W. Kozanecki,
Out-of-Plane Deflections as a Diagnostic Tool and Application to PEPII,
SLAC-PUB-8700 (2001), (), URL: http://slac.stanford.edu/pubs/slacpubs/8500/slac-pub-8700.pdf.

[125] G. Aad et al., *Improved luminosity determination in pp collisions at sqrt(s) = 7 TeV using the ATLAS detector at the LHC*, Eur. Phys. J. **C73** (2013) 2518, arXiv: 1302.4393 [hep-ex].

[126] ATLAS Luminosity Group, *Preliminary Luminosity Determination in pp Collisions at sqrt(s) = 8 TeV using the ATLAS Detector in 2012*, tech. rep. ATL-COM-LUM-2012-013, CERN, 2012, URL: https://cds.cern.ch/record/1494059.

[127] A. Sopczak, *Luminosity Monitoring in ATLAS with MPX Detectors*, JINST **9** (2014) C01027, arXiv: 1312.6296 [physics.ins-det].

[128] D Yu, S Pagan Griso, and B Heinemann, *Luminosity Measurement in pp Collisions at $\sqrt{s} = 7$ TeV using Vertex Counting with the ATLAS Detector in 2011*, tech. rep. ATL-COM-LUM-2013-016, CERN, 2013, URL: https://cds.cern.ch/record/1559846.

[129] D Berge, C Gabaldon, A Hoecker, A Messina, and G Piacquadio, *Determination of the absolute luminosity and the visible cross section from LHC van der Meer scans performed in October 2010, using events with MBTS triggers and with primary vertices*, tech. rep. ATL-COM-LUM-2011-003, CERN, 2011, URL: https://cds.cern.ch/record/1326897.

[130] ATLAS Collaboration, *Measurement of the cross-section for electroweak production of dijets in association with a Z boson in pp collisions at $\sqrt{s}$ = 13 TeV with the ATLAS detector*, Phys. Lett. **B775** (2017) 206, arXiv: 1709.10264 [hep-ex].

[131] C. Oleari and D. Zeppenfeld, *QCD corrections to electroweak $\updownarrow\nu_{\updownarrow}$jj and $\updownarrow^{+}\updownarrow^{-}$jj production*, Phys. Rev. D **69** (9 2004) 093004, URL: https://link.aps.org/doi/10.1103/PhysRevD.69.093004.

[132] J. Baglio et al., *VBFNLO: A Parton Level Monte Carlo for Processes with Electroweak Bosons – Manual for Version 2.7.0*, (2011), arXiv: 1107.4038 [hep-ph].

[133] U. Baur and D. Zeppenfeld, "Measuring three vector boson couplings in q q —> q q W at the SSC", *Workshop on Physics at Current Accelerators and the Supercollider Argonne, Illinois, June 2-5, 1993*, 1993 0327, arXiv: hep-ph/9309227 [hep-ph].

[134] The ATLAS Collaboration, *Measurement of the electroweak production of dijets in association with a Z-boson and distributions sensitive to vector boson fusion in proton-proton collisions at $\sqrt{s} = 8$ TeV using the ATLAS detector*, JHEP **04** (2014) 031, arXiv: 1401.7610 [hep-ex].

[135] P. Nason, *A new method for combining NLO QCD with shower Monte Carlo algorithms*, Journal of High Energy Physics **2004** (2004) 040, URL: http://stacks.iop.org/1126-6708/2004/i=11/a=040.

[136] S. Frixione, P. Nason, and C. Oleari, *Matching NLO QCD computations with parton shower simulations: the POWHEG method*, Journal of High Energy Physics **2007** (2007) 070, URL: http://stacks.iop.org/1126-6708/2007/i=11/a=070.

[137] O. C.e. a. Alioli S. Nason P., *A general framework for implementing NLO calculations in shower Monte Carlo programs: the POWHEG BOX*, Journal of High Energy Physics **2010** (), URL: https://doi.org/10.1007/JHEP06(2010)043.

[138] The CMS Collaborations, *Electroweak production of two jets in association with a Z boson in proton–proton collisions at $\sqrt{s} = 13$ TeV*, Eur. Phys. J. **C78** (2018) 589, arXiv: 1712.09814 [hep-ex].

[139] M. Aaboud et al., *Measurements of electroweak Wjj production and constraints on anomalous gauge couplings with the ATLAS detector*, Eur. Phys. J. **C77** (2017) 474, arXiv: 1703.04362 [hep-ex].

[140] T. Gleisberg et al., *Event generation with SHERPA 1.1*, JHEP **02** (2009) 007, arXiv: 0811.4622 [hep-ph].

[141] S. Catani et al., *QCD matrix elements + parton showers*, JHEP **11** (2001) 063, arXiv: hep-ph/0109231 [hep-ph].

[142] S. Schumann and F. Krauss, *A Parton shower algorithm based on Catani-Seymour dipole factorisation*, JHEP **03** (2008) 038, arXiv: 0709.1027 [hep-ph].

[143] S. Hoeche et al., *QCD matrix elements + parton showers: The NLO case*, JHEP **04** (2013) 027, arXiv: 1207.5030 [hep-ph].

[144] *Status of Sherpa event generator*, tech. rep. Talk at the MBI 2018 conference, 2018.

[145] *Modelling of the vector boson scattering process $pp \to W^{\pm}W^{\pm}jj$ in Monte Carlo generators in ATLAS*, tech. rep. ATL-PHYS-PUB-2019-004, CERN, 2019, URL: https://cds.cern.ch/record/2655303.

[146] *Measurement of the electroweak Z-boson plus dijet production cross section and distributions sensitive to the vector boson fusion production process in pp collisions at sqrts = 8 TeV with the ATLAS detector*, tech. rep. ATL-COM-PHYS-2013-331, 2015.

[147] J. Alwall et al., *The automated computation of tree-level and next-to-leading order differential cross sections, and their matching to parton shower simulations*, JHEP **07** (2014) 079, arXiv: 1405.0301 [hep-ph].

[148] T. Sjostrand, S. Mrenna, and P. Z. Skands, *A Brief Introduction to PYTHIA 8.1*, Comput. Phys. Commun. **178** (2008) 852, arXiv: 0710.3820 [hep-ph].

[149] R. D. Ball et al., *Parton distributions with LHC data*, Nucl. Phys. **B867** (2013) 244, arXiv: 1207.1303 [hep-ph].

[150] T. Gleisberg and S. Hoeche, *Comix, a new matrix element generator*, JHEP **12** (2008) 039, arXiv: 0808.3674 [hep-ph].

[151] F. Cascioli, P. Maierhofer, and S. Pozzorini, *Scattering Amplitudes with Open Loops*, Phys. Rev. Lett. **108** (2012) 111601, arXiv: 1111.5206 [hep-ph].

[152] H.-L. Lai et al., *New parton distributions for collider physics*, Phys. Rev. **D82** (2010) 074024, arXiv: 1007.2241 [hep-ph].

[153] S. Agostinelli et al., *GEANT4: A Simulation toolkit*, Nucl. Instrum. Meth. **A506** (2003) 250.

[154] G. Aad et al., *The ATLAS Simulation Infrastructure*, Eur. Phys. J. **C70** (2010) 823, arXiv: 1005.4568 [physics.ins-det].

[155] ATLAS Collaboration, *Summary of ATLAS Pythia 8 tunes*, ATL-PHYS-PUB-2012-003, 2012, URL: https://cds.cern.ch/record/1474107.

[156] A. D. Martin et al., *Parton distributions for the LHC*, Eur. Phys. J. **C63** (2009) 189, arXiv: 0901.0002 [hep-ph].